ISSN 0288-4534
CODEN:KONAE7

粉

KONA

POWDER AND PARTICLE

No. 10(1992)

Published by The Council of Powder Technology (JAPAN)

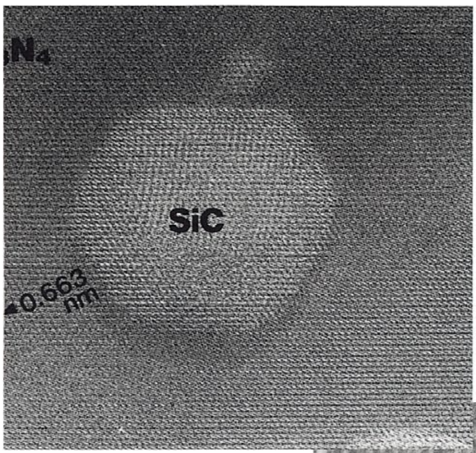

Nanodispersoid and Interface
in Sintered Si_3N_4-SiC Nanocomposites

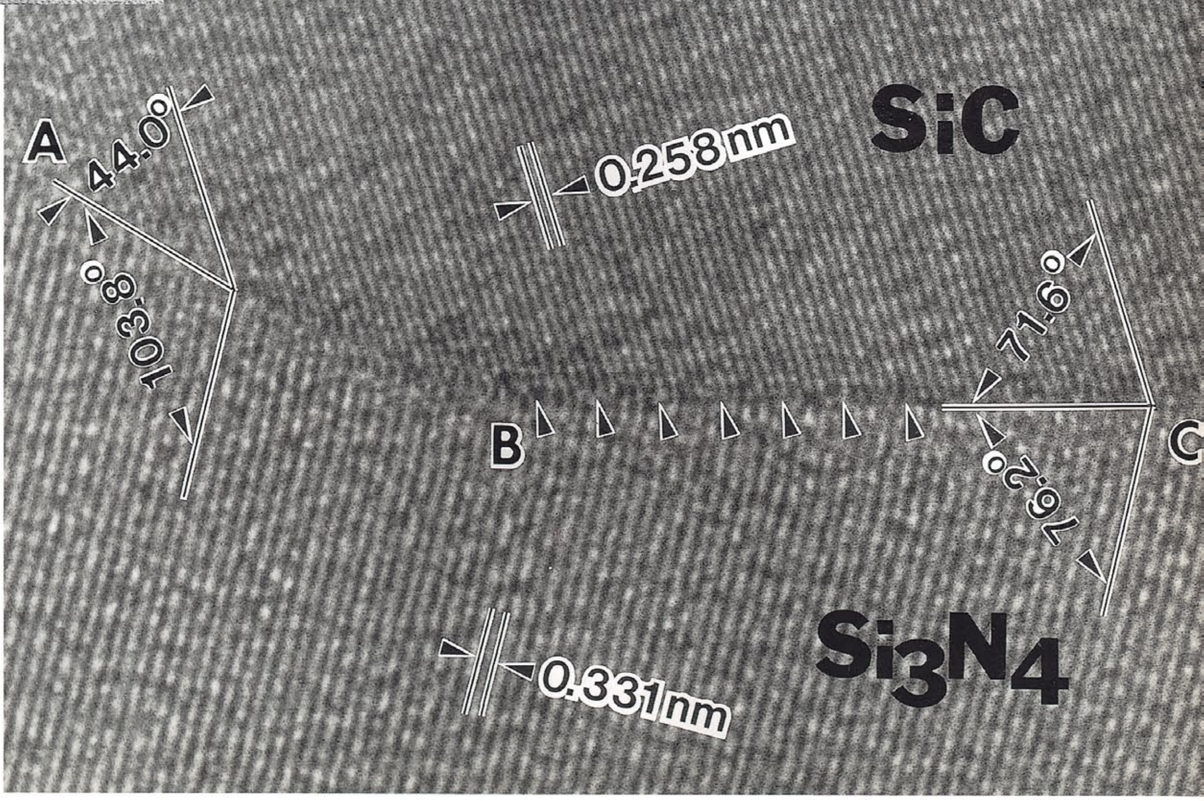

CORRECTION

Editorial Board

K. Miyanami	Editor in Chief (Univ. of Osaka Prefecture, JAPAN)
Asian Block	
Y. Kousaka	Block Vice Chairman (Univ. of Osaka Prefecture, JAPAN)
N. Yoshioka	(Okayama Univ. of Science, JAPAN)
G. Jimbo	(Nagoya Univ., JAPAN)
M. Arakawa	(Former Kyoto Institute of Tech., JAPAN)
T. Oshima	(Himeji Institute of Tech., JAPAN)
Y. Morikawa	(Osaka Sangyo Univ., JAPAN)
H. Masuda	(Kyoto Univ., JAPAN)
Y. Tsuji	(Osaka Univ., JAPAN)
H. Emi	(Kanazawa Univ., JAPAN)
Y. Kuwahara	(Government Industrial Research Institute, Nagoya,JAPAN)
P. Arnold	(Univ. of Wollongong, AUSTRALIA)
S. H. Kang	(Yeugnam Univ., KOREA)
W. Tanthapanichakoon	(Chulalongkorn Univ., THAILAND)
T. Yoshida	(Hosokawa Powder Tech. Foundation, JAPAN)
T. Yokoyama	(Hosokawa Micron Corp., JAPAN)
Secretariat	
T. Yokoyama	(Hosokawa Micron Corp., JAPAN)
F. Nakagawa	(Hosokawa Micron Corp., JAPAN)
European Block	
J. Schwedes	Block Chairman (Univ. Braunschweig, GERMANY)
B. Scarlett	Block Vice Chairman (Delft Univ. of Technology, THE NETHERLANDS)
K. Schönert	(Technische Univ. Clausthal, GERMANY)
F. Löffler	(Univ. Karlsruhe, GERMANY)
H. Schubert	(Bergakademie Freiberg, GERMANY)
E. Forssberg	(Univ. Lulea, SWEDEN)
S. R. de Silva	(Postec-Research A/S, NORWAY)
D. Ocepek	(Univ. Ljubljana, SLOVENIA)
J. F. Davidson	(Univ. of Cambridge, UNITED KINGDOM)
G. Ferrara	(Univ. di Trieste, ITALY)
J. F. Large	(Univ. de Tech. de Compiégne, FRANCE)
Secretariat	
D. Schwechten	(Alpine AG, GERMANY)
Americas Block	
M. McLaren	Block Chairman (State Univ. of Rutgers, U.S.A.)
T. P. Meloy	Block Vice Chairman (West Virginia Univ., U.S.A.)
J. P. Clark	(Massachusetts Institute of Tech., U.S.A.)
R. K. Rajamani	(Univ. of Utah, U.S.A.)
H. Herman	(State Univ. of New York, U.S.A.)
B. H. Kaye	(Laurentian Univ., CANADA)
L. Hixon	(Hosokawa Micron Inter., U.S.A.)
W. Gregg	(Hosokawa Micron Inter., U.S.A.)
Secretariat	
J. Van Cleef	(Hosokawa Micron Inter., U.S.A.)

KONA
GENERAL INFORMATION

HISTORY OF THE JOURAL

The Council of Power Technology (CPT), Japan, has been established on 1969 as a non-profit organization to enhance the activities of research and development on power sciences and technology in Japan. under the sponsorship of Hosokawa Micron Corporation. In 1983, the CPT has decided to issue an international journal, named "KONA", which publishes the exellent articles appeared in Japanese Journals concerning with powder sciences and technology, translated into English, throughout the world. After the seventh volume issued on 1989, the CPT han changed its policy to internationalize the "KONA" from the 8th issue (1990) on by incorporating the monographs originally written in English from the authors throughout the world.

AIMS AND SCOPE OF THE JOURNAL

KONA Journal is to publish the papers in a broad field of powder sciences and technology, ranging from fundamntal principles to practical applications. The papers discussing technological experiences and critical reviews of existing knowledge in specialized areas will be welcome.

These papers will be published only when they are judged, by the Editor, to be suitable for the progress of powder sceiences and technology, and are approved by each Block Editorial Committee. The paper submitted to the Editorial Secretariat should not have been previously published except the translated papers which would be selected by the Block Editorial Committees.

CATEGORY OF PAPERS

- Invited papers
  Original research and review papers invited by the Block KONA Editorial committees.
- Contributed papers
  Original research and review papers submitted to the Block KONA Editorial Committees, and refereed by the Editors.
- Tranalated papers
  Papers translated into English, previously published in other languages, selected by the Block KONA Editorial Committees with the permission of the authors and/or the copyright holder.

SUBMISSION OF PAPERS

Papers should be sent to each Block KONA Editorial Secretariat.

- Asian Block Editorial Secretariat
  T. Yokoyama or F. Nakagawa
  Hosokawa Micron Corporation Micromeritics Laboratory
  1-9, Shoudai Tajika, Hirakata. 573 JAPAN
- European Block Editorial Secretariat
  D. Schwechten
  Alpine AG
  Peter-Dörfler-Strasse 13-25
  Postfach 10 11 09
  D-8900 Augsburg 1, GERMANY
- American Block Editorial Secretariat
  J. Van Cleef
  Hosokawa Micron International Inc.,
  Micron Powder System Division
  10 Chatham Road Summit, NJ 07901, USA

FREQUENCY

KONA will be issued once each calender year.

SUBSCRIPTION

KONA is distributed free of charge to senior researchers at universities and laboratories as well as to institutions and libraries in the field throughout the world. The publisher is always glad to consider the addition of names of those who wish to obtain this journal regularly to the mailing list. Distribution of KONA is made by each Block Secretariat.

INSTRUCTIONS TO AUTHORS

(1) Manuscript format

- Two copies should be submitted to the Editorial Secretariat, in double-spaced typing on pages of uniform size.
- Authorship is to give author's names, and the mailing address where the work has been carried out on the title page.
- Abstract of 100-180 words should be given at the beginning of the paper.
- Nomenclature should appear at the end of each paper. Symbols and units are listed in alphabetical order with their definitions and dimensions in SI units.
- Literature references should be numbered and listed together at the end of paper, not in footnotes. Alphabetical order is accepted. Please give information as in the following examples :
  1) Carslaw, H. C. and J. C. Jaeger : "Conduction of Heat in Solids", 2nd ed., Clarendon Press, Oxford, England (1960).
  2) Howell, P. A.: US Patent, 3,334,603 (1963).
  3) Rushton, J. H., S. Nagata and D. L. Engle : AIChE J., 10. 298 (1964).
  4) Seborg, D. E.: Ph. D. Dissertation, Princeton Univ., N. J., U. S.A (1969).
- Original figures with each single copy should be submitted, on separate sheets. Authors' names and figure numbers are marked in the corner.
- Figure numbers and captions are listed on a separate sheet.
- Place of figure insertion is to be indicated in the margin of the manuscript.
- Tables should be typed on separate sheets.

(2) Reprints

- The authors shall receive 50 free reprints. Additional reprints will be furnished when ordered with return of galley proofs.

(3) Publication policy

- All papers submitted for publication become immediately the property of the CPT and remain so unless withdrawn by the author prior to acceptance for publication or unless released by the Editor. Papers are not to be reproduced or published in any form withont the written permission of the CPT.

KONA Powder and Particle No.10 (1992)

Contents

<Review>

<Original Research Paper>

<Translated Research Paper>

- Information Articles ……

See page 153 for description of cover photograph

Letter from the editor

After Professors Yoshioka and Jimbo, I have been nominated as the Editor-in-Chief of KONA journal from this issue on, by the Council of Powder Technology, Japan. First of all, I have to apologize to whom it may concern, for the numerous fatal and trivial mistakes appeared in the former issue of KONA No.9, the first internationalized edition. During the course of editing this second internationalized KONA, I have received many constructive suggestions from American and European Block Editorial Committees, my thanks due to them, and we have done our best to minimize embarrassing mistakes as few as possible. I still am afraid of, however, there being some.

Hopefully, we should be very glad if you would be generous enough to give us any criticism, opinion or suggestion for better international publication, and KONA journal could contribute to enhance the progress of powder sciences and technology in all the world. I will see that all goes well.

Kei Miyanami

Kei Miyanami
Editor in chief

Review

Tomography for Improving the Design and Control of Particulate Processing Systems †

F.J. Dickin, T.Dyakowski, S.L. McKee, R.A. Williams, R.C. Waterfall, C.G. Xie and M.S. Beck
*Process Tomography Group, UMIST**

Abstract

The ability to interrogate the dynamic internal characteristics of processing plants by using conventional instrumentation is severely limited for most practical conditions. The results of recent work, employing non-intrusive electrical sensors to obtain 2-dimensional images of component concentration profiles in cross-sections through process equipment, is making industry aware of new prospects for improving the design and control of many processes.

The range and status of sensing techniques and other enabling technology for the new subject of "Process Tomography" is outlined in this paper. This is followed by a discussion of the applications and future technical challenges which must be considered if process tomographic techniques are to find widespread application, with a particular emphasis on electrically-based sensor technology.

1. Introduction

Process tomography involves the use of instruments which provide cross-sectional profiles of the distribution of materials in a process vessel or pipeline. By analysing two suitably spaced images it is also feasible to measure the vector velocity profile[1,2]. Hence from this knowledge of material distribution and movement, internal models of the process can be derived and used as an aid to optimising the design of the process. This promises a substantial advance on present empirical methods of process design, often based on input/output measurements, with only a limited amount of information about the detailed internal behaviour of the process[3].

The process industry uses high-capital-cost plants which are often designed and operated on the basis of past experience and on models which usually assume time and space averaged parameters (e.g. 'well-mixed' reactors, 'completely' fluidised beds, etc.). The measurements made in such systems are also usually based on average parameters (temperature, mean flow velocity, chemical composition, etc). In some cases it has been possible to obtain microscale data (instantaneous temperature, velocity, composition, etc) at specific points in the process. However, complex experimental approaches (e.g. laser techniques involving sensing of microscale information) are not economically or practically feasible for many process design and operation needs. For these latter cases the 'process tomography' approach using simple external sensors has much to offer.

A process tomography system can be sub-divided into three sub-systems: the sensor, the data acquisition system, and the image reconstruction and display (**Fig. 1**). As with all measurement systems the sensor is probably the

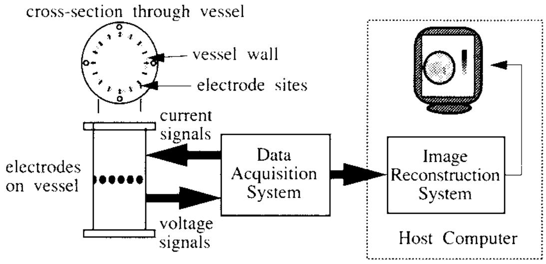

Fig. 1 Electrical Process Tomography System

---

* P.O. Box 88, Manchester M60 1QD, UNITED KINGDOM

† Received May 13, 1992

most critical part. The manner in which the sensor interrogates the process, and the quality of information obtained as a result of this, has a profound effect on the reliability and accuracy of the complete system. Practical considerations place a number of constraints on the sensor. Ideally it should be compact, non-intrusive, require minimum maintenance or calibration, and in many cases also be intrinsically safe.

Sensing techniques include electrical, ultrasound, nucleonic, and optical: a brief review of sensors appropriate to powder systems has been given elsewhere[4]. Most sensors can be categorised as having either a hard or a soft field. With 'hard-field' sensors, such as nucleonic, the sensor field sensitivity is not influenced by the distribution of materials in the process being imaged. However, with 'soft-field' sensors, such as capacitance and conductivity, the sensing field is altered by the component distribution and physical properties of the mixture being imaged. Although this limits the resolution compared with hard-field sensors, nevertheless the electronic sensing methods are often preferred for on-site process applications because of their low cost, safety, and speed.

2. Applications

Potential applications for process tomography embrace the three basic stages encountered in process engineering development:

Stage 1 Development of new process routes involving fundamentals of chemical process design (reaction kinetics, hydrodynamics etc.).

Stage 2 Implementation of the required process route by designing efficient industrial-scale equipment.

Stage 3 Routine process control, flow measurement and mass balancing functions, to enable operation under optimal conditions and to allow operational flexibility. Other applications exist for environmental monitoring of aqueous-based and gas-based mixtures.

At all three stages in the overall design of a process it is necessary to devise models (often based on a computational fluid dynamics approach) for the phenomena concerned, equipment characteristics and, ultimately, to simulate the entire process preferably in a dynamic sense. It is in this context that the use of tomographic techniques may offer a step-change in technology by enabling models to be verified with reference to tomographically measured internal process parameters. This is of some importance in the design of particulate processes.

Many process models have, hitherto, relied on theoretical computational fluid dynamics simulations whose model parameters are unquantifiably removed from the real process conditions, or whose predictions cannot always be adequately validated experimentally. For instance, the design of separation equipment holding concentrated solid/liquid dispersions that are optically opaque is often approached by estimating unit behaviour based on the (non-opaque) liquid phase only. The presence of multi-body particle-particle interactions often inhibits accurate prediction of the actual behaviour of the concentrated dispersion. Similarly, the modelling of process equipment frequently has to be based on empirical mass and population balance models derived from sampling the input and output streams to a given process (or so-called 'black-box' modelling). Such methods can be effective, but rely upon the availability of an adequate operational data-base to describe the behaviour of similar pieces of equipment handling similar components. As a consequence, such methods tend to be very system specific and rarely assist in providing any understanding of the fundamental mechanisms occurring within the process equipment. The net result is that considerable caution has to be exercised in scaling-up equipment design from the laboratory or pilot plant to full industrial scale. Potentially, the use of tomography would result in a more rigorous and confident design basis for process equipment. In some cases a modified equipment design would promote: safety, cost savings in capital equipment, floor space or overall productivity. Once a plant has been installed there are some obvious benefits in having the means to 'look inside' to investigate suspected malfunctions, wall wear, or poor performance. However, and more importantly, possibilities exist to perform accurate velocity, mass and component measurements. Such information could form part of the process control strategy.

3. Enabling Technology

The availability of efficient and low-cost integrated circuit components and digital signal processing systems has provided a foundation for rapid development of new tomographic imaging systems in the late 1980s and early 1990s. A brief resumé of the historical development of the enabling technology will be described.

Significant projects have been carried out in UK universities, in Norway, Germany and the USA, with emergent projects in two Chinese universities and by a Polish instrument manufacturer. Related technologies associated with electrical sensors were developed for geophysical applications in the early 1980s[5]).

3.1 Strategy for Sensor Design

Various sensing methods are needed for process tomography applications (**Table 1**). In the UK, a UMIST group has concentrated mainly on capacitive (section 3.1.1) and resistive (section 3.1.2) impedance sensing and on a new method of inductive sensing (section 3.1.3). Work on ultrasound sensing has been carried out at UMIST and Leeds University in the UK in association with Tianjin University in China and at Karlsruhe University in Germany (section 3.1.4). Optical sensing systems have been investigated at Bolton Institute of Higher Education in the UK, Hannover University in Germany and Micromath International in Poland (section 3.1.5). UK work on process imaging using gamma-ray tomography is featured at Surrey University[6]). Positron-based imaging is carried out at Birmingham University[7]). Extensive work on magnetic resonance imaging (MRI) using modified nuclear magnetic resonance (NMR) systems is being performed at Cambridge University and in the US.

A group of UK higher education establishments is collaborating on process tomography and is involved in instrumentation system modelling for solving the forward problem of field analysis, on which image reconstruction is based. It is becoming clear that process tomography instrument design could be aided by CAD packages for optimising the spatial sensitivity of the electrodes and for simulating the complete system, so that its performance can be assessed before commitment to detailed design. City University (London) is working on CAD and has already developed designs for capacitance tomography electrodes[8]).

In the following sections we will review the currently available methods which seem to be most suitable for providing 'real-time' (i.e. synchronised with process operation) tomographic images of process equipment.

3.1.1 Capacitive impedance tomography

A capacitive tomography system for imaging pipelines containing insulating mixtures (such as solids/gas and liquid/gas) is already delivering valuable images of powder/air and kerosene/nitrogen flows. It uses a charge-transfer capacitance transducer working at 15 volts with a noise level as low as 0.08 fF r.m.s. and a 6" pipeline twelve-electrode system[9,10,11]). It enables void fraction and the flow regime to be determined and is the first key stage in developing a non-invasive two-component mass flow meter. The oil industry is supporting early research; future work will be on gas/solids systems.

The Department of Energy in the USA is investigating the use of capacitance tomography for fluidised bed visualisation[12]). They use a 16-electrode system, with the electrodes energised at 500 volts to generate views of the dielectric constant of the bed.

3.1.2 Resistive impedance tomography

Resistive methods are suited to imaging aqueous systems including slurry conveyors, crystallisers, reactors, mixers, separators, and various kinds of porous media. Resistive tomography systems for medical use have been developed during the last few years, with major contributions by the Sheffield University Hospital group[13]). A tomography system designed for process use has recently been constructed at UMIST (up to 64 electrodes, frequency 75 Hz—150 kHz, excitation current up to 30 mA)[14]), and is being evaluated experimentally on process vessels, with particular attention being paid to metal-walled vessels to investigate any errors due to the conductivity of the walls. There are significant differences from the medical system because the human body is never in a steady state, so the medical systems are designed on a 'difference imaging' basis to examine relative changes over a short time scale, whereas proc-

Table 1 Features of sensing techniques used for process tomography

PRINCIPLE	PRACTICAL REALISATION	TYPICAL APPLICATIONS	GENERAL REMARKS	REMARKS ON RECONSTRUCTION ALGORITHMS
Modulation of beam of electromagnetic radiation by the dispersed components in the flowing fluid.	Optical techniques.	Many 2-component flows where the carrier phase is transparent to the radiation used.	Conceptually simple, high definition possible, fibre optic light guides can simplify optical arrangements. Images of central region poor if second phase concentration is high, due to absorption near walls.	Similar algorithms well established for medical CAT.
	Ionising radiation-x-ray and γ-rays.	Flows where there is a substantial density difference between the components.	Heavy shielding may be required to collimate beams and for safety.Photon statistical noise limits response time (only low-speed flows unless large sources are used).	
Reflection of external radiation.	Ultrasonic pulse echo systems.	2-component flows where reflections occur at boundaries e.g. liquid/gas flows.	Ultrasound, say 1 MHz pass through metal/liquid interface so a 'clip-on' system may be feasible for liquid flow. 'Ringing' of transmitter may cause difficulty in imaging discontinuities close to the pipe walls.	Similar to some NDT and medical applications.
Instantaneous measurement of electrical properties of the flowing fluid.	Electrical capacitance plates on walls of pipe detect the presence of the second component.	Oil/gas, oil/water, gas/solids flows etc.	Inexpensive and rugged. High definition not possible, but good for slug and annular flow, water separation measurements, dune and spiral flow patterns in pneumatic conveyors. Loss of definition near centre of pipe.	Sensor field is affected by distribution of second phase, so algorithms must allow for this.
	Conductivity sensing electrodes near wall of pipe.	Water/oil, water/gas, water/solid flows.	Similar to capacitance, but electrode polaritation, greasy deposits, etc. may need to be considered.	Similar to capacitance, similar methods used for some medical applications.

ess tomography systems must give results from absolute measurements of impedance which requires more precise instrumentation and image reconstruction algorithms. A number of process applications (mixing, separator design etc) are being investigated by UMIST[15,16]. Rensselaer Polytechnic Institute in the USA is also making noteworthy advances in resistive impedance tomography[17,18], using adaptive current excitation principles.

3.1.3 Electro-magnetic tomography

This method of imaging uses a sensor system with directional sensing coils for imaging materials which affect inductive fields projected over the cross-section of a process. It should enable the specific imaging of metals in the presence of substantial amounts of non-metallic materials, which is of interest in minerals processing and material recycling[19].

3.1.4 Ultrasonic tomography

Ultrasonic tomography has been extensively developed for medical applications. However, these systems require operator interpretation of results and are generally not suitable for high-speed process tomography. Designs for a system more suitable for process application, using specially developed wide-angle transmitters with transputers for image reconstruction have been suggested[20,21,22]. The wide-angle transmitters are combined with multiple receivers, and enable the image to be obtained with a small number of transmitters being "fired" in sequence, thus speeding-up the image frame-rate compared with systems where many narrow-angle transducers need to be fired in sequence. Work at Karlsruhe University has been concerned with vector tomography for velocity profile measurement[23], they have demonstrated the system on bubble columns. A large number of transmitters are used which enable good images to be obtained, but the frame rate is limited for the reasons given above.

3.1.5 Optical tomography

An optical tomography system using arrays of light-emitting diodes and photo-detectors for each projection has been constructed at Bolton Institute of Higher Education[24]. Optical systems for investigating mixing phenomena have been developed at Hannover University[25]. Future applications will employ optical techniques for calibration of other process tomography systems, and in some processes it is anticipated that optical access may be possible, thus enabling higher resolution than would be achieved using conventional electrical tomography.

Optical tomography is a useful way of teaching the basic principles of tomographic image reconstruction, a demonstration system using a simple optical bench has been made in Poland[26].

3.1.6 Tomography using ionising radiation

Gamma-ray tomography is very appropriate for imaging particulate systems[6], and since it is a 'hard' radiation, the image resolution can be better than it is when using electrical methods of tomography. However, the imaging speed is relatively slow because of the long averaging times required to reduce to acceptable levels the image flicker caused by the count rate limitations of gamma photon detection.

Positron emission tomography[7] is attractive because particular species of particles can be radio-labelled and their transit through a process can be imaged in 3 dimensions. However, the technique is inherently slow if a large number of particle trajectories has to be individually monitored, since only a small number of radio-labelled particles can be separately resolved at one time.

4. The Use of Tomographic Technology for Fluid-based Conveying Processes

Hydraulic and pneumatic conveying can be employed to transport solids over long distances, sometimes several hundred kilometres, which may offer a less expensive method than conventional transportation by road or rail. Design and modelling of these processes is of considerable importance, and this is a prime candidate for tomographic interrogation.

Considering the case of solid/liquid transportation, a range of flow regimes can occur, subject to process parameters such as phase volume fraction of solids, flow velocity, hydraulic pressure gradient and the physical properties of both the solid and the suspending liquid. The particle size of solids also has a significant effect upon the resultant flow regime produced.

Generally, a slurry is identified as being either homogeneous or heterogeneous. In the former, a high concentration of fine solids is suspended, while the latter is characterised by an asymmetric distribution of solids in the suspending liquid, with particles readily demonstrating a tendency to settle and form either a moving or a stationary bed of particles on the base of a horizontal pipeline. The velocity at which such a situation can arise is referred to as the critical deposition velocity, and represents a fundamental parameter in the design of slurry pipelines. Another phenomenon characteristic of a heterogeneous slurry is saltation, in which the suspension of particles due to turbulence is surpassed by gravitational force, and particles are subsequently suspended and deposited periodically on the surface of a moving or stationary bed.

In horizontal pneumatic conveying, the flow regimes encountered are largely dependent upon the suspending gas velocity. As the velocity is reduced, the trend is for the distribution of solid particles to become progressively less uniform. Eventually, a moving bed of particles can form coupled with a saltation effect similar to that described above. At sufficiently low velocity, the particle bed can build up to result in a blockage of the conveying line. Clearly, the flow velocity is significant and, as in the design of pipelines for hydraulic conveying, both the flow velocity and pipeline pressure drop represent essential design parameters. **Fig. 2** illustrates the change in pressure drop with superficial gas velocity, defined as the volumetric gas flowrate divided by the cross-sectional area of the pipe. The diagram also suggests a suitable range for the loading factor, LF, defined as the ratio of the mass flow of particles to the mass flow of gas. **Fig. 3** shows images obtained using a capacitance tomography instrument for different flow behaviours encountered in horizontal pneumatic conveying. These images illustrate the way that tomographic methods can be used to visualise process behaviour, to enable flow regimes to be identified, and for quantification of void fraction.

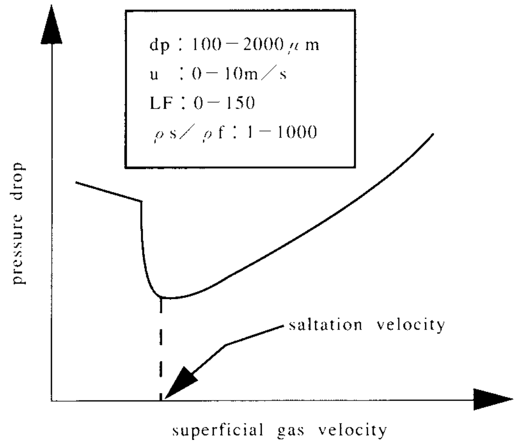

Fig. 2 Variation of pressure drop with gas velocity for horizontal pneumatic conveying

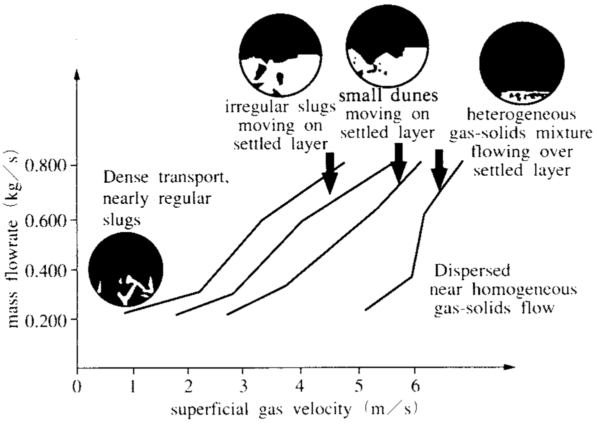

Fig. 3 Variation of mass flowrate with superficial gas velocitiy for horizontal pneumatic conveying

In vertical pneumatic conveying, it is found that as the LF decreases and the suspending gas velocity increases, the tendency is to encounter a uniform distribution of particles. In contrast, the choking velocity represents a gas velocity so low that a series of 'slugs' result. Generally, as the superficial gas velocity is decreased, a transition from dilute-phase to dense-phase will be observed. Pneumatic transport with low air velocity allows pressure drop to be minimized and as a consequence to reduce the amount of energy provided to the compressor. For vertical pneumatic transport, the relationship between pressure drop and superficial gas velocity is illustrated in **Fig. 4**: it clearly shows an optimum velocity for minimizing the pressure drop; this velocity depends on the flow regime which can be measured tomographically (**Fig. 3**).

A prime advantage in the application of process tomography to such systems is the ability to explore the spatial distribution of the contents of a vessel in an intrinsically safe manner, i.e. non-invasively. Further, electrical

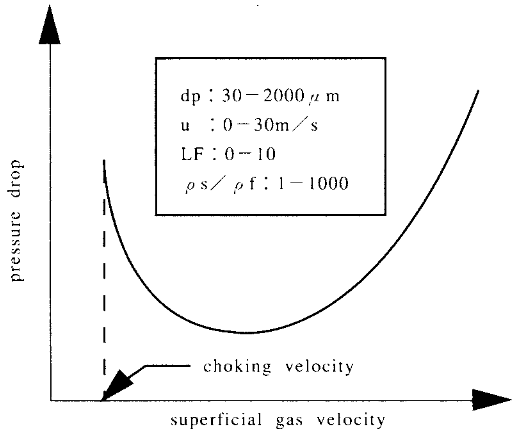

Fig. 4 Variation of pressure drop with gas velocity for vertical pneumatic conveying

tomography is an attractive method since it may prove to be less expensive, have a better dynamic response, and be more portable for routine use in process plant than radiation-based tomographic techniques such as positron emission, nuclear magnetic resonance, gamma photon emission, and X-ray tomography. Practical constraints such as the diameter of a large process vessel will render the direct application of radiation-based techniques difficult, and in this instance, electrical tomography would prove more advantageous.

Other process applications for tomography lie in the area of process control, in the detection of blockages in either full-scale pipelines or those of a pilot plant - to identify possible production difficulties would greatly enhance the efficiency of operation. The flow regimes discussed previously could be identified with ease and so further act as an aid to process control. In the case where flow velocity is below critical deposition velocity and a moving or stationary bed results, access to real-time images would allow a rapid response to be taken, thereby allowing the operation to continue without being further impaired.

The accurate determination of flow velocity, used in basic design equations for the design of both pipelines and pump power requirements, will enable a process engineer to refine the design of such equipment cost-effectively. Process tomography should also enhance an understanding of particle dynamics for both steady and unsteady flow and further, assist in the validation of fundamental design equations through accurate determination of parameters such as phase mass flowrate and flow velocity. The spatial variation of solids concentration and velocity should be readily determined, along with concentration profiles as a function of concentration, particle size distribution and flow velocity.

5. Current Developments and Future Challenges in Tomographic Instrumentation Using Electrical Sensors

Electrical field methods are emerging as robust, safe and relatively low-cost techniques for obtaining tomographic images of the contents of industrial equipment. Other sensor systems are available (e.g. gamma-ray and positron emission, section 3.1.6) which can produce higher resolution images than the electrical methods, but at the expense of ease of operation, speed and cost.

A medium-speed (ca. 100 frames per second) capacitive impedance tomography system is now ready for further development leading to industrial use (section 3.1.1), the application being mainly to the non-conducting fluids used in the oil industry. Although the existing instrument is suitable for oil well riser applications, there is a need to improve the sensitivity and speed for applications such as measuring flame front propagation. This most demanding requirement involves capacitively imaging flame fronts in a cylinder head. For engines running up to 6000 rpm this would involve increasing the image speed to 36,000 frames per second and using very small electrodes. A method of improving transducer sensitivity using replacement of existing charge transfer techniques by stray-free capacitance bridge measurements incorporating digital signal processing is being investigated27). A research group in Norway is investigating the use of dedicated silicon technology to make capacitance sensors of optimal design. Much of this technology is directly applicable to interrogation of dry powder processing.

The resistive impedance tomography method is suitable for use with electrically conducting systems (most chemical process applications). It forms the basis for model verification aimed to improve the design of industrial equipment. The use of impedance spectroscopy may in future provide a method for imaging specific components in a multi-component mixture, and is likely to be of interest for performing measurements in powder slurry systems.

Combined capacitive and resistive impedance transducers will have to be designed for applications where the measurement zone can change between being dominated by dielectric effects or by conductivity effects. The research challenges will be to identify the fluid transition, develop electrodes and electronics suitable for conducting and non-conducting fluids, and to design reconstruction algorithms suitable for imaging spaces where there are two different fluid states existing in the measurement zone.

There are a number of specific and rather fundamental challenges in process tomography which should be highlighted because their solution will need a considerable amount of research. One aspect is to define procedures for quantifying the performance of tomographic imaging systems; so far very few reports on this have been written[10,28]. This leads us into considering the following challenges:

a) Resolution. The attainable resolution is dependent on the correct placement, sizing and shielding of impedance electrodes and energising fields. This involves solving the forward problem as part of the design method using proprietary finite element design packages, and is particularly important in making cost-effective tomography installations. "Empirical" approaches to electrode sizing and placement relative to guards, interfering metalwork etc. are a costly and time-consuming process.

The image resolution (and fidelity) is also influenced by the type of algorithm used to solve the inverse problem of image reconstruction. Most work so far has involved using relatively straightforward backprojection and filtered backprojection methods. However, it is postulated that variations in the position of the field equipotentials due to the spatial distribution of material in the process could be compensated for by more advanced reconstruction techniques. Investigations have started on the use of iterative reconstruction algorithms such as a modified Newton - Raphson algorithm for quantitative impedance tomography[15].

Imaging industrial equipment with non-circular geometry will involve special challenges with electrode placement and with image reconstruction. Typical cases include plate separators and stirred tank reactors[29].

b) Speed. Data capture rates (aperture times) of 100 frames per second have already been achieved with electrical tomography systems where the measurement frequency is high (ca. 1 MHz for capacitive and inductive sensors and ca. 50 kHz for resistive sensors). Speed increases of up to, say 1000 frames per second should be attainable by parallel operation of sensing and signal processing systems, but will involve careful attention to the signal-to-noise ratio of the sensor electronics and elimination of cross - coupling by multifrequency methods. Operation at even higher speeds will probably require major developments in sensor electronics.

Data processing systems for reconstructing high-speed images fall into two general categories. For research applications it will often be sufficient to store the data and reprocess it at a lower speed. For real-time imaging concerned with some process monitoring, control and measurement applications, Transputer systems are already proving successful. Alternative configurations such as cellular array processors and the use of dedicated digital signal processing devices merit careful consideration.

c) Subject contrast. This term is used to denote the ratio in the process cross-section of the maximum to minimum density (for X-rays) or specific impedance (for electrical impedance tomography), and is an attempt to measure the 'sensitivity' of the tomographic instrument. In order to form a tomographic image, the sensor radiation or the field lines from the sensors must pass through all components of the object. With a penetrating radiation such as X-rays this is not usually a problem. (However, radiation methods are often unsuitable for process tomography because of the requirements for radiation containment, high cost and slow response.) Electrical field methods are relatively straightforward for insulating mixtures (e.g. gas/oil) where the dielectric constant ratio is low, so that electrical capacitance tomography is used, and for electrically conducting mixtures (e.g. most processes based on aqueous fluids and absorbent solids) where the specific conductivity ratio is low, so that low-frequency electrical impedance tomography is successful.

Although electrical methods are suitable for very many applications, there are cases where the presently available high-frequency capacitive impedance (1 MHz) and low-frequency (50 kHz) resistive impedance methods may not be fully suitable. Examples include imaging of flame structure and flame front propagation in internal combustion engines, where the flame is highly ionized and electrically conducting, whereas the zone in advance of the flame front is electrically insulating. Similarly, in oil industry separation process imaging, the oil-water mixture inversion means that combined capacitive and resistive impedance measurements are required. To cater for such a wide range of measurement conditions there is a need to develop multi-frequency sensor systems, measuring both resistive and reactive components.

d) Vector velocity. A full understanding of process behaviour requires a knowledge of the direction of material movement as well as its distribution. The velocities can be measured by cross-correlation of the image data. This is a computer-intensive operation; especially if the direction of the velocity vector is not known. Transputers with additional digital signal processors can be used for velocity imaging. Cellular array computers and electrically reconfigurable logic arrays should enable a higher data throughput than Transputer-based systems[1].

An alternative method for obtaining the velocity profiles is known as 'vector tomography'. This uses ultrasonic sensors to measure velocity data, from which the velocity profile is obtained by tomographic reconstruction. The potential of vector tomography is being investigated at Karlsruhe University (section 3.1.4).

e) Process control using tomographic image data. A tomographic image can provide the measurements at selected locations of internal process parameters which are critical to the optimal control of a process. Numerous opportunities for process control of plants exist and remain to be developed. For example, component control in pipelines, control of solids distribution in crystallisers, homogeneity of mixing processes, solids flow in bunkers. Thus, state variables directly associated with optimal operation could be used for process control, the state being actually measured rather than estimated from other measured parameters. Such measurements for process control would be based on localised information, so simplified tomographic measurement systems could be used.

f) Scale-up. Early applications of process tomography are to research and pilot scale plants of modest dimensions. An advantage of electrical field methods for tomographic imaging is that they are intrinsically able to be scaled-up (and down). Indeed, electrical conductivity imaging has been used on a terrestrial scale[5]. Optical and ionising radiation methods are also amenable to scale-up. Ultrasonic methods may be more problematic because the relatively low velocity of sound results in image frame-speed limitations (section 3.1.4).

6. Conclusions

Some process tomography systems (resistive and capacitive impedance) are available for immediate application to two-phase processes where the resolution and speed requirements are modest (say 1 in 20 of projection distance and 100 frames per second, respectively). For more stringent applications, sensors with improved signal-to-noise ratios need to be developed and more accurate image reconstruction algorithms need to be implemented. This work demands using the latest methods for sensor design and construction, and for interpreting the extensive range of mathematical techniques for image reconstruction into effective signal processing algorithms.

The techniques of process tomography are advancing rapidly in the early 1990s, and the subject is showing signs of providing a mature method suitable for low-cost visualisation of process behaviour. The application of process tomography will, no doubt, be 'user demand led' and the authors hope that this paper will assist teams of instrument and process engineers in exploring new applications to particulate processes.

References

1) Hayes D.G., Gregory I.A., and Beck M.S.: Velocity profile measurement in two-phase flows, Proc. European Concerted Action on Process Tomography, Manchester, 26-29 March 1992

2) Thorn R., Huang S.M., Xie C.G., Salkeld J. A., Hunt A., and Beck M.S.: Flow imaging for multi-component flow measurement, Flow Meas. Instrum., **1** (1990), 259-268

3) Dickin F.J., Hoyle B.S., Hunt A., Huang S. M., Ilyas O., Lenn C., Waterfall R.C., Williams R.A., Xie C.G., Beck M.S.: Tomographic imaging of industrial process equipment: techniques and applications, IEE Proc.-G, 139 (1992), 72-82

4) Williams R.A., Xie C.G., Dickin F.J., Simons S.J.R., and Beck M.S: Multi-phase flow measurements in powder processing - a review, Powder Technology, **66** (1991), 203-224

5) Dines K.A. and Lytle R.J.: Analysis of electrical conductivity imaging, Geophysics, **46** (1981), 1025-1036

6) Simons S.J.R., Seville J.P.K., Clift R., Gilboy W.B., and Hosseini-Ashrafi M.E.: Application of gamma-ray tomography to gas fluidised and spouted beds, Proc. European Concerted Action on Process Tomography, Manchester, 26-29 March 1992

7) Parker D.J., Hawkesworth M.R., Benyon T.D., and Bridgewater J.:Process engineering studies using positron-based imaging techniques, Proc. European Concerted Action on Process Tomography, Manchester, 26-29 March 1992

8) Khan S.H., and Abdullah F.: Validation of finite element modelling of multielectrode capacitive system for process tomography flow imaging, Proc. European Concerted Action on Process Tomography, Manchester, 26-29 March 1992

9) Huang S.M., Xie C.G., Thorn R., Snowden D., and Beck M.S.: Design of sensor electronics for electrical capacitance tomography, IEE Proc.-G, **139** (1992), 83-88

10) Huang S.M., Xie C.G., Vasina J., Lenn C., Zhang B.F., and Beck M.S.: Experimental evaluation of capacitance tomographic flow imaging systems using physical models, Proc. European Concerted Action on Process Tomography, Manchester, 26-29 March 1992

11) Xie C.G., Huang S.M., Hoyle B.S., Thorn R., Lenn C., Snowden D., and Beck M.S.: Electrical capacitance tomography for flow imaging: system model for development of image reconstruction algorithms and design of primary sensors, IEE Proc.-G, **139** (1992), 89-97

12) Fasching G.E. and Smith N.S.: A capacitive system for three-dimensional imaging of fluidized beds, Rev. Sci. Instrum., **62** (1991), 2243-2251

13) Barber D.C. & Brown B.H.: Applied potential tomography, J. Phys E, **17** (1984), 723-733

14) Wang M., Dickin F.J. and Beck M.S.: Improved electrical impedance tomography data collection system and measurement protocols, Proc. European Concerted Action on Process Tomography, Manchester, 26-29 March 1992

15) Abdullah M.Z., Quick S.V. & Dickin F.J.: Quantitative algorithm and computer architecture for real-time image reconstruction in process tomography, Proc. European Concerted Action on Process Tomography, Manchester, 26-29 March 1992

16) Williams R.A., Dickin F.J., Dyakowski, Ilyas O.M., Abdullah Z., and Beck M.S.: Looking into mineral process plant?, Minerals Engineering, **5** (1992) 867-881

17) Goble J.C. and Gallagher T.D.: A distributed architecture for medical instrumentation and electrical current computed tomograph, Proc. Annu. Int. Conf., IEEE Engineering in Medicine and Biology Society, **10** (1988), 285-286

18) Isaacson D.: Distinguishability of conductivities by electric current computed tomography, IEEE Trans. Medical Imaging, MI-**5** (1986), 91-95

19) Yu Z.Z., Conway W.F., Dickin F.J., Xie C. G., Beck M.S. and Xu L.A.: Field design for electromagnetic tomography systems, Proc. ICEMI 92 Conf., Tianjin University, China, 20-23 October 1992

20) Gai H., Li Y.C., Plaskowski A. and Beck M.S.: Ultrasonic flow imaging using time-resolved transmission mode tomography, IEE 3rd International Conf. on Image Processing and its Applications, Warwick University, 1989

21) Gai H., Beck M.S. and Flemons R.S.: An integral transducer/pipe structure for flow imaging, IEEE 3rd International Ultrasonic Symposium, Montreal, Canada , 1989

22) Weigand F. and Hoyle B.S.: Simulations for parallel processing of ultrasound reflection-mode tomography with applications to two-phase flow measurement, IEEE Trans. Ultrasonics, Ferroelectrics & Freq. Control, **36** (1989), 652-660

23) Wernsdörfer A.: Reconstruction from limited data with a-priori knowledge, Proc. European Concerted Action on Process Tomography, Manchester, 26-29 March 1992

24) Dugdale P., Green R.G., Hartley A.J., Jackson R.G., and Landauro J.: Optical sensors for process tomography, Proc. European Concerted Action on Process Tomography, Manchester, 26-29 March 1992

25) Mewes D. Fellhölter and Renz R.: Measurement of mixing phenomena in gas and liquid flow, Proc. European Concerted Action on Process Tomography, Manchester, 26-29 March 1992

26) Plaskowski A., Bukalski P., Habdas T. and Szuster K.: Application of the optical tomography for education and laboratory research, Proc. European Concerted Action on Process Tomography, Manchester, 26-29 March 1992

27) Yang W.Q. and Stott A.L.: Low value capacitance measurements for process tomography, Proc. European Concerted Action on Process Tomography, Manchester, 26-29 March 1992

28) Seagar A.D., Barber D.C. and Brown B.H.: Theoretical limits to sensitivity and resolution in impedance imaging, Clin. Phys. Physiol. Meas., **8** (1987), Suppl. A., 13-31

29) Lyon G.M. and Oakley J.P.: A digital signal processor based architecture for E I T data acquisition, Proc. European Concerted Action on Process Tomography, Manchester, 26-29 March 1992

Review

Mechanically Induced Reactivity of Solids †

Ursula Steinike
*Centre of Heterogeneaüs Catalysis of KAI e.V.**
Hans-Peter Hennig
WITEGA-Research GmbH

Abstract

The action of mechanical energy on solids effects changes to their structure. The resulting structural defects lead to a storage of energy in the solid, which may raise its chemical reactivity. Investigations on the mechanically induced reactivity of solids have been carried out with the specific aim of influencing reaction processes in order to obtain high yields, high reaction velocities or selective reactions. On the basis of detailed structural investigations on mechanically treated quartz and hydrargillite, the interaction of the stressed solid with the surroundings has been explored (titanite formation, zeolite formation, polymorphous transformation, gas adsorption, Na^+*-elimination and hydration of amorphous* Al_2O_3*).*

The investigations reveal that the size reduction which occurs during mechanical activation is not the decisive reason for reactivity enhancements, but that these are caused primarily by structural changes. Apart from the structural properties of solids, however, their chemical properties as well as those of the surroundings have an influence on their reactivity.

1. Introduction

People have known since ancient times that chemical reactions can be induced by mechanical energy, e.g. by friction or impact. Thus in prehistoric times, people generated light with the aid of flint stones. Also known are the effects of pressure and shear during geological epochs in the genesis of minerals, e.g. the formation of mica from feldspar by geotectonic movements. In 1911, Ostwald1) first used the term mechano-chemistry to describe the “influence” of mechanical energy on chemical reactions. The term “tribo-chemistry”, which is often regarded as a synonym, is, however, restricted to chemical and physico-chemical changes of solids under the influence of mechanical energy2).

In the 1920s, Tamman3) studied the influence of mechanical treatment on the reactivity of solids. In the 1930s it was primarily Fink4,5) and later Bowden and Tabor6), who investigated the effects of friction and abrasion on the oxidation reactions of metals and on their decomposition. They formulated the conception of “hot spots”. Up to the 1960s, progress was based on empiricism. Only in the 1970s were scientific investigations on the mechanism of the transfer of mechanical energy on solids begun7-11). The range of mechanically treated solid substances is very wide, comprises both inorganic and organic materials, and extends from oxides to phosphates and silicates, from metals to ores and raw materials, and is often used as a process step in the synthesis of compounds having great practical relevance12-25). Among organic substances, it is above all the polymers which aroused the interest of tribochemistry. But also, for example, the mechanical treatment of chloramphenicol-palmitate for the production of a physiologically active component is of importance26).

The influence of mechanical energy on solids induces a multitude of elementary physico-chemical micro and macroprocesses, which lead to a change of the structure, i.e. to the occurrence of structural defects such as changes of the surface, lattice distortions, conversion of long-range order distortions into short-range order and electronic defects. The processes taking place under the influence of mechanical energy are very complex, and depend on the kind and intensity of the mechanical stresses

---

* Rudower Chaussee 5, 0-1199 Berlin, GERMANY
† Recieved Feb. 19, 1992

and the specific properties of the solids based on their lattice structure and, of course, their chemical nature. The mechanical energy may be transferred, e.g. by the impact of solid particles or by the induction of tensile and compressive forces in the powder mass (**Fig. 1**).

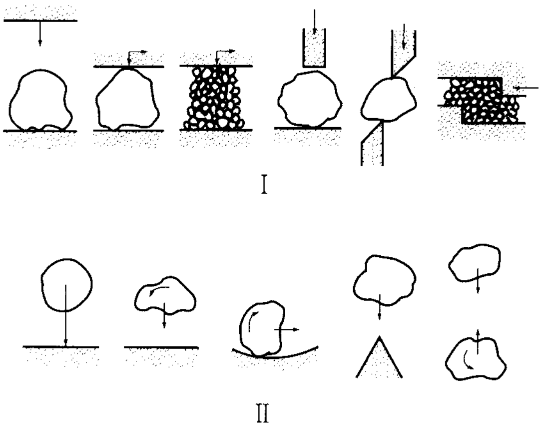

Fig. 1 Different stress mechanisms used in mechanically activating solid particles (2).
I stress between two surfaces (pressure and shearing stress)
II stressing by impact

Generally it has been established that with pressure and shear stresses, structural changes are concentrated at regions near the surface and diminish with increasing distance from the surface. With impact stresses, the size of the primary crystallite becomes smaller in the whole volume and the disturbance starts at the corners and borders[8,9].

Mechanical treatment leads to a storage of energy. According to theoretical investigations by Sigrist and Fichtner[27], it follows that apart from surface and inhomogeneous lattice distortions, homogeneous distortions may also contribute to this energy storage.

They applied their theory to experimental data from MgO and found maximum values of 30 J g^{-1} for inhomogeneous distortions, of 122 J g^{-1} for homogeneous and inhomogeneous distortions, and of 153 J g^{-1} for surface energy.

The reactivity of solids may often be considerably enhanced by mechanical treatment. Even such reactions as the formation of Au_2O_3 and C from Au and CO_2, the formation of CuO or Cu_2O and C from Cu and CO_2, which cannot be accomplished thermally as a result of extremely negative affinity, proceed under mechanical treatment with a measurable velocity[28].

Investigations on the mechanically changed reactivity of solids are being carried out with the aim of deliberately influencing the reaction processes of the solids concerned. For example, in chemical syntheses, the highest possible yield, and a high velocity and selectivity are aimed at. A specific influence on the reaction processes requires a knowledge of the relation between the real structure and kinetic parameters.

By means of some examples, the influence of the mechanical treatment on the structure and reactivity of solids will be demonstrated and some conclusions of general application are given.

2. Examples of Mechanical Activation

2.1 Reactivity of Mechanically-Treated Quartz

The effect of mechanical energy on the structure of quartz has been described in detail by Steinike et al.[8]. Mechanical activation leads to changes in the long and short-range order caused by lattice distortions and broken bonds. The mechanically-treated quartz is in a partially crystalline state. It still contains typical elements of the crystalline quartz structure and is characterized by the absence of long-range order (**Fig. 2**).

2.1.1 Formation of Titanite

Titanite ($CaTiSiO_5$) occurs in nature as a mineral and can be used for dielectric ceramics.

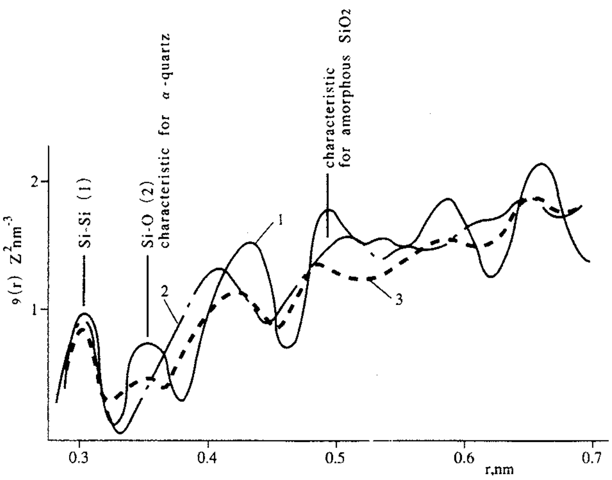

Fig. 2 Radial distribution function (RDF). 1=α-quartz, 2=amorphous SiO_2, 3=α-quartz after 70h of mechanical treatment, r=distance of an arbitrary atom from the origin (8).

There are indications that it may gain in significance in the fixation of radioactive waste[29,30]. There are various technical methods for the preparation of titanite[31,32]. According to Michailova et al.[33], the synthesis temperature is lowest if quartz sand is used as the SiO_2 component (**Fig. 3,a**). In the following it will be shown that in the production of titanite, quartz sand can be used and advantage may be taken of the reactivity-raising effect of its mechanical activation[34,35,36].

As the second reaction component, calcium titanate (synthetic perowskit) was used. With the use of calcium titanate and quartz sand the reaction at temperatures up to 1280°C leads to an incomplete transformation (**Fig. 3,b**). Higher temperatures bring about a complete transformation, but cannot be used because of the occurrence of disturbing sinter effects causing a hardening of the product. On the other hand, the use of mechanically-activated quartz sand leads to a complete titanite transformation already at 1250°C (**Fig. 3,c**). In this case, a temperature decrease of 30°C is not significant in itself, but the fact that the reaction is shifted to a temperature region in which no sinter effects occur is of critical importance.

$$\text{a}-CaCO_3+TiO_2+SiO_2\text{(quartz)}\xrightarrow{1250^\circ C}CaTiSiO_5+CO_2$$

(by Michailova)

$$\text{b}-CaTiO_3+SiO_2\text{(quartz)}\xrightarrow{>1280^\circ C}CaTiSiO_5$$

$$\text{c}-CaTiO_3+SiO_2\text{(mechan. activated quartz)}\xrightarrow{\approx 1250^\circ C}CaTiSiO_5$$

Fig. 3 Reaction equations for the formation of $CaTiSiO_5$ (36).

There are optimal conditions for the reaction with regard to the mechanically-generated disturbances. The specific surface area alone is not the decisive parameter (see **Table 1**). **Table 1** contains the temperatures at which the transformation to titanite is complete. The solid reaction starts at 1050°C and is completed at 1250°C, whereby the main quantity of $CaTiSiO_5$ — about 90% — is already formed at 1180°C. It was not possible by the transformation of quartz into a completely amorphous state or by the use of amorphous aerosil to further lower the reaction temperature of titanate under the given conditions.

Table 1 Dependence of the temperature T during a 100 percent transformation of titanate and quartz to titanite on the starting component.

Sample Name	t, h	s, m^2g^{-1}	X, %	T, °C
WQS/0	0	1	100	1280
WQS/0.5	0.5	3.2	92	1250
WQS/1	1	4.1	86	1250
WQS/3	3	7.4	84	1250
WQS/5	5	9.4	74	1250
WQS/10	10	11.6	71	1250
Aerosil	—	200	0	1280

t =time of mechanical treatment
s =specific surface of the SiO_2 component
X =crystallinity (measured by X-ray diffraction)
WQS =Weferlingen quartz sand (from deposit in Germany)

In the formation of titanite from quartz, cristobalite occurs as an intermediate product. The lower the temperature of the transformation of quartz into cristobalite, the lower the formation temperature of titanite. (The transformation temperature of mechanically-activated quartz is >1200°C, see section 2.1.2)

The crystallites of the initial products become covered by the reaction products (**Fig. 4**). In this figure, distinct growth regions with a layer-like structure are to be seen. The "layer" heights are of the order of some 10 nm. Titanite has grown upwards on the original titanate crystals during the reaction. The diffusion of the ions involved takes place through the cover layer. Ca and Ti could be detected by element analysis.

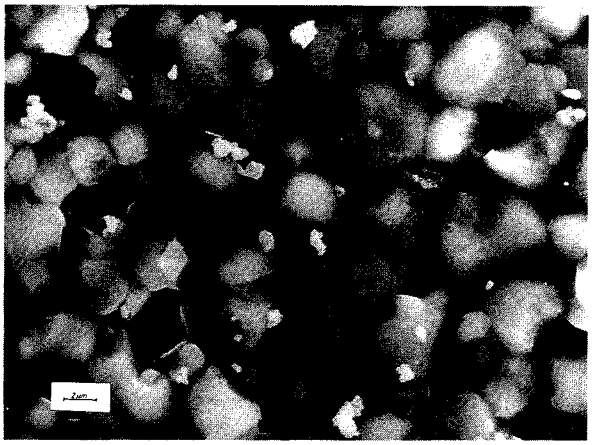

Fig. 4 Titanate formation on titanite crystals (1200°C, 1h halt) (36).

On the basis of the results, the formation of titanite is assumed to occur via a one-sided diffusion of cations (**Fig. 5**). The Ca^{2+} and Ti^{4+} ions or the corresponding oxygen-ion complexes diffuse into the quartz lattice which is in a reactive state of transformation into cristobalite. This transformation is a reconstructive one in which Si-O bonds have to be broken. The breakage of these Si-O bonds is facilitated by the mechanically-induced bond breakages and the generated distortions and deformations of the SiO_4-tetrahedrons with each other[8].

This also explains the formation of titanite at lower temperatures when mechanically-activated quartz is used. It is of decisive importance that the quartz lattice is in a state of transformation. The Si^{4-} ions or complexes being formed diffuse along the grain boundaries of the titanite crystallites being generated to the surface of titanate and react with titanate. From the crystal-chemical point of view, a diffusion into the titanate-lattice is not likely.

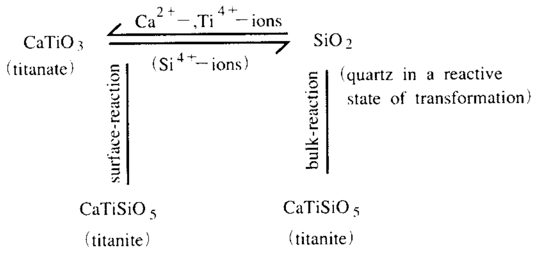

Fig. 5 Formation of titanite by one-sided diffusion of ions (36).

2.1.2 Polymorphous Quartz Transformation

Polymorphous intermediate transformations of SiO_2, which may occur during or as a result of a complete transformation, are of great importance for the reaction of silicates because of reactivity, as shown in the case of the titanite formation. It is known from literature that mechanical deformation processes may influence the velocity, as well as the mechanism of the modification transformations[37,38].

Without the influence of mechanical treatment, the polymorphous transformations of the most important SiO_2-modifications proceed according to Fenner[39], as shown in **Fig. 6**. Under the influence of mechanical treatment, the effect (degree) of the α-β- transformation decreases[49]. Strongly disturbed quartz is not transformable into the high-temperature form. The non-appearance of the transformation effect may be accounted for by a strong disturbance of the lattice. The α-β- transformation is based on insignificant displacements of the atom positions, a deformation of the lattice. In the case of the mechanically-activated quartz, however, a growing part of the 6-ring arrangement has already been destroyed. As a result of the mechanical activation the temperature of the quartz - cristobalite transformation is strongly reduced (**Fig. 6,b**). The quartz-cristobalite transformation is, as already mentioned, a reconstructive one in which the structures have to be completely reorganized and breakage of the Si-O bonds is necessary.

$$\text{(a)}\quad \alpha\text{-quartz} \xrightleftharpoons{573℃} \beta\text{-quartz} \xrightleftharpoons{870℃} \beta\text{-tridymite} \xrightleftharpoons{1470℃} \beta\text{-cristobalite}$$

$$\text{(b)}\quad \underset{\text{(mechan. activated)}}{\alpha\text{-quartz}} \xrightarrow{\geq 1200℃} \beta\text{-cristobalite}$$

Fig. 6 Polymorphous transformation of quartz. a) by Fenner (39), b) induced by mechanical treatment (40).

The breakage of Si-O bonds, and the relative distortion of the SiO_4 tetrahedrons facilitate the necessary disintegration of the structure, and play an essential role in the accelerated transformation at a lower temperature. The velocity constants k_1 and k_2 were determined from the time-dependence of the quartz-cristobalite transformation taking as a basis the mechanism derived by Mitra[41]. On the basis of its temperature-dependence, the activation energy A_E of both partial steps may be estimated to have the values shown in **Fig. 7**. The activation energy of both partial steps is reduced by a factor of two by mechanical activation. The activation energy of the transformation leading to cristobalite is slightly higher than that of the transformation quartz → transition phase. This fact can be explained by nucleation processes. The mechanically-induced elementary defects have no influence on the transformation quartz → transition phase, i.e. on the structure of the quartz lattice, but on the new formation of cristobalite, because the activation energies for both processes are considerably lowered. Accordingly, the produced defects must still be effective in the supposed transition phase, presumably in sub-microscopic small lattice regions no longer showing any diffraction[41].

$$\alpha-\text{quartz}\xrightarrow[(1)]{k_1}\text{transition phase}\xrightarrow[(2)]{k_2}\beta-\text{cristobalite}$$

Activation energies A_E, kJ mol^{-1}

	(1)	(2)
quartz (before mech.treatment)	≈ 405	≈ 426
quartz (mech.treated, 1and3h, resp.)	≈ 175	≈ 226

Fig. 7 Activation energies A_E for mechanically-induced quartz-cristobalite transformation (k_1, k_2 rate constants (40)).

2.1.3 Zeolite Formation

Zeolites are generally produced from solution containing alkaline silicates and aluminates via hydrothermal synthesis by precipitation or by a hydrogel procedure. The formation of zeolite by the reaction of quartz with aluminium oxide[42)] is also possible. In this case, the rate-determining step is the dissolution of quartz. The elementary step of the dissolution is influenced by lattice defects[43)], e.g. bond breakings, distortions and deformations normally associated with mechanical activation[44)].

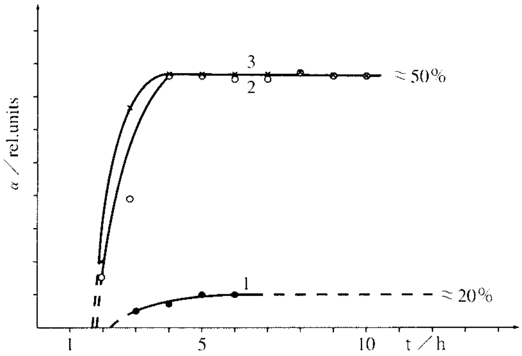

Fig. 8 Dependence of sodium A zeolite formation from mechanically-activated quartz and α-Al_2O_3 on the reaction time t. Experimental conditions: 2m NaOH, T=90°C, time of the mechanical mixing of quartz and α-Al_2O_3: 3h (45) (see **Table 2**). Mol ratio quartz: γ-Al_2O_3=2:1.

Fig. 8 and **Table 2** show the zeolite formation (NaA-zeolite) from mechanically-activated quartz and γ-Al_2O_3 as a function of reaction time[45)]. The transformation to zeolite first increases with mechanical activation but then remains constant. Essentially, the transformation as a whole increases with decreasing crystallinity of quartz. X-ray investigations reveal that only the disturbed, partially crystalline part of the quartz dissolves and reacts with γ-Al_2O_3 during the formation of NaA-zeolite. Under the chosen circumstances, the formation of NaA-zeolite is only possible to the extent that partially crystalline quartz is available, i.e. quartz which still contains the basic elements of a crystalline structure. With the use of amorphous SiO_2, e.g. aerosil, the species B is formed.

Table 2 Characterization of the samples for the zeolite formation.

	X, %	s_1, m^2g^{-1}	s_2, m^2g^{-1}	α, %
sample 1	100	<1	11.8	ca. 20
sample 2	50	10	25	ca. 50
sample 3	45	14	17	ca. 50

X =crystallinity (measured by X-ray diffraction) of quartz
s_1 =specific surface of quartz
s_2 =specific surface of quartz/$\gamma-Al_2O_3-$mixture
α =turnover to zeolite

2.1.4 Mechanically-Induced Adsorption of Quartz

An essential partial step in the reaction of a solid with the surroundings, e.g. a gas atmosphere, is its ability to ab- or adsorb gas. It appears that this process is also influenced by mechanical activation forces, and the structural changes of the solid associated with such activation[46)].

Generally, it can be stated that the amount of gas ab- and adsorbed increases with an increasing degree of the disturbance of quartz, but in a different way for the individual gases, as can be seen from **Fig. 9**. Highest is the adsorption of H_2, then follows that of CO_2 and O_2. Ar as a noble gas is not adsorbed at room temperature.

Mechanically-induced absorption primarily occurs during the action of energy. If the gas is added after the mechanical activation, there is only an adsorption at the surface and practically no diffusion of the gas molecules into the solid, i.e. the absorption is negligible.

It is assumed that during the treatment the pores are greater and that the whole lattice is loosened to a greater extent than the subsequent integral measurements reveal. The gases are absorbed both chemically and physically. The chemisorption occurs primarily on the basis of the Si-O bond breakages produced, which are determined by chemical gas-

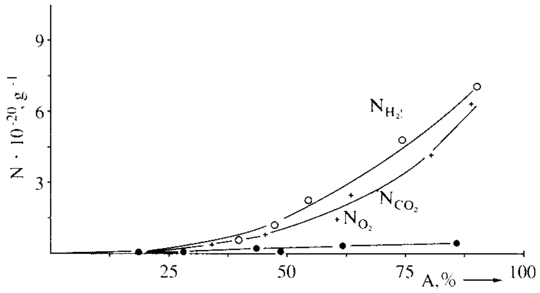

Fig. 9 Dependence of the number of adsorbed molecules N on the amorphous part A in mechanically-treated quartz (46).

interactions[8,46]. But far more molecules are taken up than correspond to the number of the measured centres[46], **Table 3**. The physical adsorption is mostly influenced by the following structural factors (**Table 3**).

Quartz, because of the small size of the micropores present, does not usually contain much gas, and only traces of H_2 can normally be detected. The gas kinetic diameter of H_2 is approximately comparable with the diameter of the quartz pores. That is why H_2 is also slightly absorbed by untreated quartz. On the other hand, the gas kinetic diameters of H_2, O_2 and Ar are all of the same order of magnitude as the pores in mechanically-activated material, but Ar is still not absorbed. Presuming that only the size of the pores has a decisive influence on the absorption, there should be no CO_2 absorption. While the structural changes and the resulting locally generated energy states at the surface and in the disturbed quartz layer are of decisive importance, they do not completely account for the differences in the amounts of the individual gases absorbed.

Thus it must be concluded that not only the structural properties of solids, but also the chemical properties of both solid and gas play important roles with regard to ab- and adsorption of gases.

2.2 Reactivity of Mechanically-Treated Hydrargillite

Aluminium oxides are one of the main components for the production of catalytic materials and adsorbents. The starting material for the technical production of surface-rich active aluminium oxides is hydrargillite. Aluminium oxides are produced via hydrargillite by a process of dissolving and precipitation. The short-time heating of mechanically-pretreated hydrargillite is another possibility to obtain active aluminium oxides free of Na^+.

The mechanical activation of hydrargillite has been the subject of several scientific investigations recently[47-49],and has in the last few years gained in significance in connection with a short-time heating[50-56].

The basic concept of this alternative procedure consists in the transformation of hydrargillite by short-time heating into a nearly X-ray amorphous aluminium oxide, being well washable regarding Na^+ ions. Synthetic hydrargillite always contains Na^+ ions as contamination caused during preparation, which adversely affect the catalytic properties of aluminum oxides, prepared from $Al(OH)_3$. Their removal is therefore necessary. The X-ray amorphous Al_2O_3 is transformed in the same washing process to pseudo-boehmite (AlOOH) by hydration. Hydrargillite is pretreated by a mechanical treatment for rapid disintegration.

Table 3 Mechanically-induced adsorption on quartz (period of time of mechanical treatment : 4h).

GA	s, $m^2 g^{-1}$	A, %	N. 10^{-20}, g^{-1}	Z. 10^{-18}, g^{-1}	N/Z	δ, nm
Ar	14	42	<0.1	5.9	—	0.37
H_2	10	48	11.3	0.9	1.10^2	0.28
O_2	14	44	0.24	14.0	2	0.36
CO_2	16	64	2.6	0.9	3.10^2	0.46

GA =Gas atmosphere
s =Specific surface of quartz
A =“Amorphous” content
N =Number of adsorbed gas molecules
Z =Number of radicals
δ =Diameter of the gas-molecule

Table 4 Dependence of Na^+—elimination of X-ray amorphous Al_2O_3 on mechanical and thermal^x activation.

Hydrargillite				X-ray amorphous AL_2O_3	
Sample	t , min	do, rel. units (±0.1)	s m^2/g (± 5%)	s m^2/g (± 5%)	$^cNa_2O$, mar% ±0.005
1	5	0.7	2.9	206	0.019
2	30	0.6	10.5	169	0.017
3	60	0.4	16.0	23	0.016
4	900	0.1	27.0	11	0.011

x = Conditions of thermal activation : 0.2s, 500°C
t = Mechanical pretreatment
do = Degree of order, measured by X-ray diffraction
s = Specific surface
$^cNa_2O$ = Na_2O content of the solid

The mechanical treatment of hydrargillite influences the thermal disintegration of hydrargillite[56,57]. Of special interest is the fact that after a mechanical and thermal short-time heating (550°C, residence time < 10s[55,56]) an aluminium oxide is formed, which is characterized by a very high reactivity. **Table 4** shows the Na^+-elimination from X-ray amorphous aluminium oxides as a function of the produced degree of order do (do measured in relative units from the X-ray determined intensity of the (100) reflex) and the specific surface after the short-time heating. The Na^+-elimination increases whereas the specific surface decreases.

Parallel to the Na^+-elimination, a rehydration takes place. The reaction of aluminium oxides with water at 90°C yields pseudo- boehmite, which differs from crystalline boehmite with regard to the Bragg-reflexes (profile and position) and the IR spectra[56]. The pseudo-boehmite content increases with the reaction time (**Fig. 10**) and reaches a final value after about 30 min. From this figure it also follows that the initial velocity of the pseudo-boehmite formation depends on the mechanical pretreatment.

The mechanical treatment of hydrargillite prior to the short-time heating increases the pseudo-boehmite yield. **Fig. 11** displays the dependence of the pseudo-boehmite-transformation on the duration of the mechanical pretreatment of hydrargillite and the degree of order do of the pretreated hydrargillite. The formation of pseudo-boehmite is also not dependent on the specific surface of aluminium oxide since it decreases in the same measure as the pseudo-boehmite content increases (**Fig. 11**

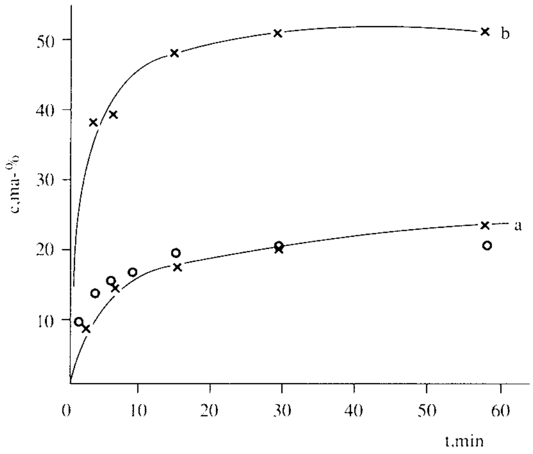

Fig. 10 Dependence of hydration of X-ray amorphous Al_2O_3 on the time t (different mechanically-treated hydrargillite, vibration mill), T = 90°C do = degree of order a: do = 0.73 b: do = 0.52 c = content of pseudo-boehmite (56).

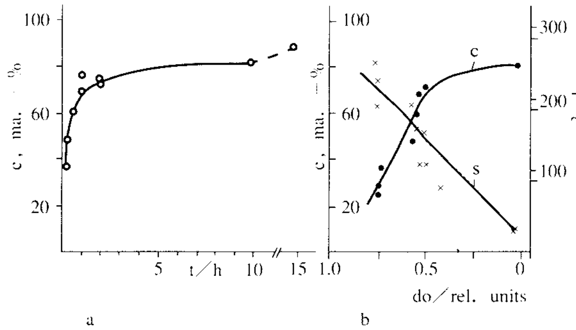

Fig. 11 Dependence of the content of pseudo-boehmite c (after short-time heating and hydration) on the duration of mechanical treatment t (a) and on the degree of order do (b, c) of hydrargillite, and the dependence of the specific surface s (after mechanical and thermal activation) on the degree of order do (b, s).

and **Table 4**). The reaction of aluminium oxide with H_2O also yields bayerite. The bayerite formation depends only slightly, however, on the mechanical pretreatment (the bayerite content rises with increased mechanical pretreatment from 0−5%). The bayerite formation is essentially determined by the temperature and reaction time. The aluminium oxides present are nearly X-ray amorphous and contain some χ-Al_2O_3 (**Table 5**). The short-range order was determined from the radial distribution function of the electron density by X-ray wide-angle investigations, **Fig. 12**[58]. The position of the 1st peak at 0.188 nm corresponds to the Al-O distance and is independent of the method of preparation. Also the position of the other peaks remain unchanged. However, beginning from the 2nd peak ($r > 0.3$ nm), there are differences in the intensities due to distortions of the coordination polyhedrons.

Table 5 Characterization of the samples after mechanical and thermal activation.

sample name	AL_2O_3-phase	c, %^{x}
1	X+r. a.^{xx}	40
2	X+r. a.	60
3	r. a+X	73
4	r. a+X	89

x x =X-ray amorphous
x =IR - spectroscopy, Dr. Geissler, Analytisches Zentrum Berlin
c =Degree of transformation to pseudo-boehmite

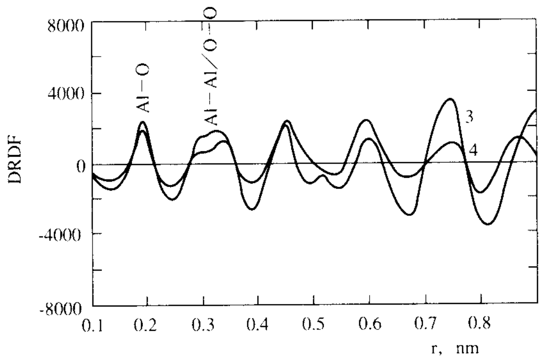

Fig. 12 Difference radial distribution function (DRDF). $DRDF=4\pi r^2 (\delta (r)-\delta_o)$ r=distance of an arbitrary atom from the origin (sample names see **Tables 4, 5**) (58).

The greater the distortion of the polyhedrons, the higher is the degree of rehydration of aluminium oxides. The energy stored as a result of mechanically-caused distortions facilitates the formation of boehmite from aluminum oxide and water ($Al_2O_3+H_2O \rightarrow Al(OOH)$). The reason for the distortion of the coordination polyhedrons is the mechanical pretreatment in connection with the subsequent short-time heating. The distortion increases with the length of time of the mechanical pretreatment[58].

3. Conclusions

Summarizing, it can be stated that under the influence of mechanical energy, solids undergo structural changes and structural defects which lead to an energy storage, which may result in an enhancement of chemical reactivity. Correlations exist between the mechanically-induced structural defects and the mechanism of the reactions.

The particle disintegration accomplished by mechanical activation and the resulting increase in surface area may be of importance for an increase of reactivity, but a number of publications have shown that the measured effect of the reactivity enhancement cannot be explained merely by these phenomena.

One of the cited examples even demonstrates that the reactivity enhancement may be inversely proportional to the increase in surface.

Table 6 contains a list of the investigated reactions as a function of structural defects. Apart from the structural properties of the solids, however, both the chemical properties of solids and those of the surroundings are of importance.

Table 6 The dependance of the reactivity of solids on their mechanically changed structure.

Reaction	Correlation with the changed structure
Solid-solid	
- α-β-quartz transformation 〔40〕	partially crystalline state 〔8,60〕
- quartz-cristobalite transformation 〔40〕	partially crystalline state, with broken Si-O bonds and distortions of the SiO_4-tetrahedrons
- titanite formation (mechanically-treated quartz+$CaTiO_3$) 〔45〕	quartz lattice being in a state transformation into cristobalite in connection with partially crystalline state
Solid-liquid	
- dissolution of quartz 〔44〕	partially crystalline state, with broken Si-O bonds and distortions of the SiO_4-tetrahedrons
- Zeolithe formation (mechanically - treated quartz+$\gamma-Al_2O_3+NaOH$) 〔45〕	− 〃 −
- CSH-formation (mechanically−treated quartz+$Ca(OH)_2+H_2O$) 〔59〕	− 〃 −
- rehydration of Al_2O_3 ($Al_2O_3+H_2O\cdots>$ AlOOH) 〔56, 58〕	distortions of the Al_2O_3-octrahedrons
Solid-gas	
mechanically-induced adsorption of quartz 〔46〕	partially cristalline state, broken Si-O bonds, radicals and chemical defects

References

1) Ostwald, W.: Handbuch der allg. Chemie I, Leipzig, 1919, 70
2) Heinicke, G.; Hennig, H.-P.; Linke, E.; Steinike, U.; Thiessen, K.P.: Tribochemistry, Akademie-Verlag Berlin 1984, Carl Hanser-Verlag, München 1984. Verlag Mir, Moskau 1987 (in Russian)
3) Tamman, G.: Z. Elektrochem., **35** (1929), 21
4) Fink, M.: Trans. Am. Soc. f. Steel Treating, **18** (1930), 1026
5) Fink, M.; Hoffmann, U.: Z. anorg. allg. Chemie, **210** (1933), 100
6) Bowden, F.F.; Tabor, D.: The friction and lubrication of solids, Oxford 1958.
7) Thiessen, P.A.: Abhandlungen der Dt. Akademie der Wissenschaften zu Berlin, Klasse f. Chemie, Geologie und Biologie, **5** (1966), 15
8) Steinike, U.; Kretzschmar, U.; Ebert, I.; Hennig, H.-P.; Barsova, L.I; Jurik, T.K.: Reactivity of Solids, **4** (1987), 1
9) Heegn, H.: Veränderung der Festkörpereigenschaften bei mechanischer Aktivierung und Feinzerkleinerung, Dissertation B, Akademie der Wissenschaften der DDR, Berlin (1986)
10) Soc. of Pow. Tech., Japan: Proceedings of the Second Japan-Soviet Symp. on Mechanochemistry, 22-24 March 1988, Tokyo
11) 5th Symp.: Theoretical and Technological Aspects of Comminution and Mech. Activation of Minerals: Tataraman 1988.
12) Gock, E.; Asiam,E.: in (11), 60.
13) Schulz, G.; Dietzel, W.: Abfall-Wirtschafts-Symp., 4-7 Dec. 1990, Berlin. I. Integrierte Abfallwirtschaftskonzepte, **3**, 265 (1990). EF-Verlag f. Energie und Umwelttechnik GmbH.
14) Schultz, L.; Hellster, E.; Zorn,G.: Z. phys. Chem., NF **157** (1988), 203
15) Ikeya, T.; Senna, M.: J. Non-Crystalline Solids, **113** (1989), 51
16) Pavlyukhin, Yu.T.; Medikov, Ya.Yu.; Boldyrev, V.V.: J. of Solid State Chemistry, **53** (1984), 155
17) Pavlyukhin, Yu.T.; Medikov, Ya.Yu.; Boldyrev, V.V.: Mat. Res. Bull. **18** (1983), 1317
18) Imamura, K.; Senǹa, M.: Mat. Res., Bull. 19 (1984), 59
19) Balaz, P.; Huhn, H.-J.; Tkacova, K.; Heegn,H.: Erzmetall, **41** (1988), 6
20) Tkacova, K.; Balaz, P.; Korneva, T.A.: J.

Therm. Anal., **34** (1988), 1031

21) Lin, I.J; Nadiv, S.; Groguian, D.J.M.: Minerals Sci. Engng., **7** (1975), 313

22) Tkacova, K.; Boldyrev, V.V.; Lyakhov, N.: Proc. Indian natn. Sa. Acad., 55A (1989), 778

23) Tkacova, K.; Balaz, P.; Bastl, Z.: Thermochimica Acta, **170** (1990), 277

24) Fubini, B.; Giamello, E.; Pugliese, L.; Volante, M.: Solid State Ionics, **32/33** (1989), 334

25) Giamello, E.; Fubini, B.; Volante, M.; Costa, D.: Colloids and Surface, **45** (1990), 155

26) Paudert, R. et al.: DD 222009.

27) Sigrist, K.; Fichtner,H.: Phys. Status Solidi, **95** (1985), 473

28) Thiessen, P.A.; Heinicke, G.; Schober, E.: Z. anorg. allg. Chem., **377** (1970), 28

29) Stäuble, J.; Bayer, G.: Schweiz. Mineral. Petr. Mit., **61** (1981), 361

30) White, T.J.; Segall, R.L.; Turner, P.S.: Angew. Chem., **97** (1985), 369

31) King, E.G.: Amer. Chem. Soc., **76** (1954), 4320

32) Völtzke, P.; Abicht, H.-P.; Müller, Th.; Richter, J.: Silikattechnik, **41** (1990), 306

33) Michailova, N.A.; Vinnikova, N.S.: Anorg. Werkstoffe, **15** (1979), 114

34) Köhler, Th.; Plötner, W.; Steinike, U.; Uecker, D.-Chr.; Schierhorn, E.: DD 263747

35) Plötner, W.; Köhler, Th.; Uecker, D.-Chr.; Steinike, U.: DD 254934

36) Steinike, U.; Uecker, D.-Chr.; Köhler, Th.; Plötner, W.; Schierhorn, E.; Jancke, K.; Hennig, H.-P.: Crystal. Res. Technol., 26 (1991)

37) Sigrist, K.; Heinicke, G.; Steinike, U.: Kristal und Technik, 8 (1973), 393

38) Senna, M.: KONA, **1** (1983), 48

39) Fenner, C.N.: Amer. J. Sci., **36** (1913), 331

40) Steinike, U.; Uecker, D.-Chr.; Sigrist, K.; Plötner, W.; Köhler, Th.: Crystal Res. Technol., **22** (1987), 1255

41) Mitra, S.: Trans. and J. Brit. Ceram. Soc., **76** (1977), 71

42) Cournager, R.A.; Kranich, W.L.; Sand, L. B.: J. of Phys. Chem., 79 (1975), 1578

43) Weyl, W.A.; Marboe, E.C.: Sprechsaal, **107** (1974), 1030

44) Steinike, U.; Hennig, H.-P.; Kretzschmar, U.; Richter-Mendau, J.: Crystal Res. Technol., **17** (1982), 1585

45) Wutzler, R.; Klevzov, D.; Steinike, U.; Hennig, H.-P.: Crystal Res. Technol., **26** (1991), 317

46) Steinike, U.; Hennig, H.-P.; Ebert, I.: Z. phys. Chem., Leipzig, **226** (1985), 302

47) Schrader, R.; Rump, H.; Sanner, G.: Z. anorg. allg. Chem., **350** (1967), 130

48) Pohl, K.; Haberecht, H.: DD 134365

49) Pohl, K.: Habilitationsschrift, TU Dresden, 1970

50) Vorobjev, Ju.K.; Schkrabina, R.A.; Moroz, T.D.; Fenelonov, V.B.; Zagrafskaja, R.V.; Kambarova, T.D.; Levickij, E.A.: Kinetika i kataliz, **22**, 6 (1981), 1595

51) Zolotovskij, B.P.; Schkarin, A.V.; Krivoruchko, O.P.; Kriger, T.A.; Bujanov, R.A.: Izv. Sib. Otd. Akad. Nauk SSSR, Ser. Chim. Nauk, **17** (392) 6, 36 (1984)

52) Bollmann, U.; Engels, S.; Haupt, K.; Kobelke, J.; Becker, K.; Neubauer, H.-D.: Z. Chem., **25** (1985), 273

53) Zolotovskij, B.P.; Paramzin, S.N., Krivoruchko, O.P.; Bujanov, R.A.: Izv. Sib. Otd. Akad. Nauk SSSR, Ser. Chim. Nauk **17** (446) 6, 80 (1987)

54) Steinike, U.; Becker, K.; Bollmann, U.: Spectrum, **7** (1988), 24

55) Bollmann, U.; Becker, K.; Berger, H.-J.; Birke, P.; Engels, S.; Gruhn, G.; Jancke, K.; Kraak, P.; Lange, R.; Steinike, U.: Cryst. Res. Technol., **23** (1988), 1303

56) Steinike, U.; Geissler, H.; Hennig, H.-P.; Jancke, K.; Jedamzik, J.; Kretzschmar, U.; Bollmann, U.: Z. anorg. allg. Chemie, **590** (1990), 213

57) Neissendorfer, F.; Steinike, U.; Tolochko, B.P.; Sheromov, M.A.: Nucl. instr. and methods in Physics Res., A 261 (1987), 219

58) Kretzschmar, U.; Steinike, U.; Bollmann, U.; Lausch, H.: Cryst. Res. Technol., in press

59) Jedamzik, J.: Dissertation, Akademie der Wissenschaften der DDR, Berlin, 1982.

60) Steinike, U.; Ebert, I.; Hennig, H.-P.; Müller, B.: Cryst. Res. Technol., **14** (1979), 1469

Review

Growth Forms of Crystals: Possible Implications for Powder Technology †

P. Bennema
RIM Laboratory of Solid State Chemistry
*University of Nijmegen, Toernooiveld**

Abstract

In this paper, a one-layer regular solution model for the interface crystal mother phase is treated from first principles. From this model, the concepts of thermal roughening and kinetic roughening are derived. These concepts correspond to a roughening transition under the influence of the temperature and a driving force for crystallization, respectively. The results of the simple theory are compared with recent advanced theories inspired by computer-simulation studies leading to the theory of roughening transition and kinetic roughening. It is shown how these theories can be integrated with the crystallographic morphological theory of Hartman and Perdok. Examples of mainly organic crystals are reviewed. Observed growth forms are interpreted by means of the theories discussed above.

1. Introduction

1.1 Concepts to describe shapes of crystals

In this paper, an introduction will be given on statistical-mechanical surface theories which are integrated with crystallographic-morphological theories. It will be shown how, in principle, growth forms of crystals can be predicted from these integrated theories. Growth forms of crystals result from a crystal growth process, caused by a non-equilibrium driving force. This may be a supersaturation for growth from solution or an undercooling for growth from the melt.

In most cases, crystal growth forms of single crystals are bounded by flat faces. The orientation of these faces is described with three integers (hkl). Crystal growth forms of a particular compound and crystal structure are in most cases characterized by combinations of forms of faces {hkl} . Such characteristic combinations of forms of different sizes are called habits of crystals. A form of faces indicated as {hkl} is a combination of faces such as (hkl), $(\bar{h}kl)$, $(h\bar{k}l)$, $(\bar{h}kl)$, which can be transformed into each other by the symmetry operations of the point group (in this case two mutual perpendicular mirror planes. Note that h means -h). Apart from the concept of habit, we will also use the concept of shape of a crystal or the concept of morphology of a crystal. Morphology implies first of all a theoretically predicted growth form. This is compared with the observed morphology or habit of single crystals. The shape of a crystal may correspond to a given form of a crystal. In this paper the concepts: morphology, habit, crystal growth from, and shape will be freely used without further definition. The meanings of these concepts will become clear from the context.

1.2 Aim and contents of the paper

Using the simplest possible statistical-mechanical, regular solution models of the interface crystal-mother phase as a heuristic and didactic tool, basic concepts like roughening transition and kinetic roughening of the interface will be introduced. Implications for crystal growth mechanisms will then be discussed. The results will be compared with results of recent theories on crystal surfaces and crystal growth.

Next, principles of classic crystallographic-morphological theories will be discussed and followed by a discussion of the crystallographic-morphological theory of Hartman and Perdok.

---

* 6525 ED Nijmegen THE NETHERLANDS

† Received May 20, 1992.

It will be shown how the statistical-mechanical models for the interface and the Hartman Perdok theory can be integrated. Next, a variety of successful predictions of the morphology of crystals will be reviewed. Recent research on shapes of organic crystals will be reviewed.

1.3 Practical implications of the morphology of crystals for powder technology

Separation processes of mother liquid from the crystallized mass of crystals using, among others, filtration processes may depend strongly on shapes of resulting crystals. The following example from the oil industry can be given[1]. During temperature lowering of about 10°C of gasoline, the high fraction of paraffins crystallizes as lozenge-shaped flat, platy crystals. The precipitate of these crystals blocks filters and pumps of storage tanks, trucks and cars. Adding specific tailor-made additives, platy paraffin crystals are changed into needle-like crystals, which no longer block filters.

Shapes of crystals which result from all kinds of crystallization production processes may play a crucial role in resulting properties of powders. So powders consisting of crystals with needle-like shapes, platy shapes, shapes of flat needles or blocks etc. will behave differently. One of the hot subjects of research in the field of (industrial) crystallization is currently: (i) to understand habits of crystals, and on this basis, (ii) finding ways to change crystal habits by varying solvents and designing specific tailor-made additives (for a survey see ref.[2]).

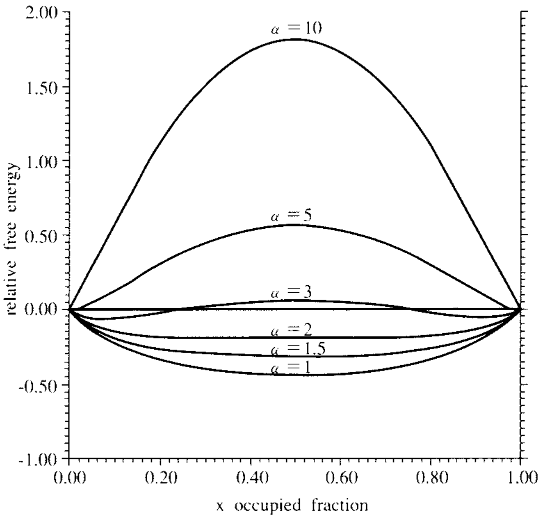

Fig. 1 Relative dimensionless free energy function f (x) (equation)) as a function of x the fraction of solid. For different values of α. (equation 15)
If $\alpha > 2$, two minima separated by a maximum occurs.
If $\alpha < 2$, only one minimum occurs.

2. Jackson's one-layer regular solution model for the crystal-mother phase interface

2.1 Principles of the model

In the original lattice-gas or regular-solution-like model of Jackson for the interface, the interface crystal-mother phase is partioned into equal cells[3] (for surveys and references see ref.[4-6], for regular solution see ref.[7]). In order to simplify our case we will use a tetragonal or square lattice with a fourfold axis perpendicular to the interface with the orientation (001). This gives square cells which are equal in size and shape. Following the tradition of so-called lattice gas or Ising models, the cells can have only two properties: solid or fluid. In original Ising models used in theories of magnetism, these properties are spin up or spin down[7]. In the simplest possible regular solution version of Jackson's solid-fluid interface model, the interface consists of only one mixed solid-fluid layer on top of a completely solid crystal (see also **Fig. 2** below). This first layer on top of the solid body can be considered as a square, mixed solid-fluid crystal. In the following, we will apply the usual formalism of regular solutions to this model (see also **Fig. 2**).

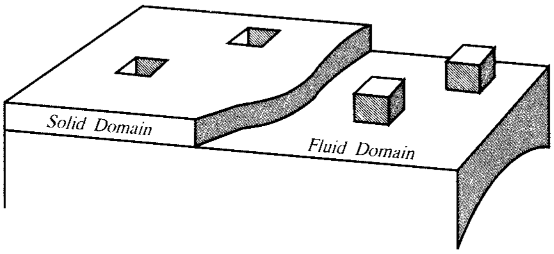

Fig. 2 Jackson's one-layer model Here, $\alpha > 2$, so that solid domains occur with fluid vacancies and fluid domains with solid adatoms.

2.2 Regular solution model

The mixed solid-fluid one-layer model can now be singled out and we will give the simplest possible statistical mechanical-thermodynamic treatment for this model[4-7].

As an artificial thermodynamic reference state, we start with a two-dimensional 100-percent-pure solid crystal and a 100-percent-pure fluid crystal. These pure reference crystals are mixed. We will calculate the change of free energy due to the mixing process. The pure solid crystal consists of N_s-solid cells or blocks and the pure fluid crystal of N_f-fluid blocks. Therefore, the original joint reference, free energy F^r of the two crystals, is given by

$$F^r=N_s\mu_s^*+N_f\mu_f^* \qquad (1)$$

μ_s^* and μ_f^* are the chemical potentials of one solid and one fluid cell. It is essential for lattice gas or Ising models that the internal rotational and vibrational degrees of freedom of solid and fluid cells do not change due to mixing. This implies that although solid-fluid bonds are formed which replace solid-solid and fluid-fluid bonds, the chemical potentials of solid and fluid cells do not change.

According to thermodynamics, the change in free energy is given by

$$\Delta F_{mix}=\Delta U_{mix}-T\Delta S_{mix} \qquad (2)$$

because F^r (equation (1)) remains unchanged. Here ΔU_{mix} and ΔS_{mix} are the energy of mixing and the entropy of mixing, respectively, resulting from mixing of the two pure reference crystals. According to the principles of regular solution theory, it is assumed that the entropy of mixing can be given in good approximation by the expression resulting from an ideal mixing process. According to Boltzmann, the statistical-mechanical expression for the entropy S is given by

$$S=klng \qquad (3)$$

Here, k is the Boltzmann constant and g the number of configurations of the system under consideration. For the reference state of the pure crystals g=1 and hence

$$S^r=0 \qquad (4)$$

After mixing the entropy becomes

$$S=kln\frac{N!}{N_e!N_f!} \qquad (5)$$

Using the well known Stirling approximation which is valid for large numbers N

$$lnN!\simeq NlnN-N \qquad (6)$$

equation (5) becomes

$$\Delta S_{mix}=S-S^r=-kTN(x_slnx_s+x_flnx_f) \qquad (7)$$

Here, N is the total number of cells in the two-dimensional mixed solid-fluid crystal or

$$N=N_s+N_f \qquad (8)$$

and x_s and x_f are the fractions of solid and fluid cells in the mixed solid-fluid crystal

$$x_s=\frac{N_s}{N},\quad x_f=\frac{N_f}{N} \qquad (9)$$

and

$$x_s+x_f=1 \qquad (10)$$

Equation (10) expresses that cells are either in a solid or a fluid state. We have now an expression for ΔS_{mix} given by equation (7).

In order to calculate ΔU_{mix}, the zeroth order mean field or Bragg Williams approximation is introduced, which is typical for regular solution models.

This zeroth order approximation implies that in the mixed solid-fluid crystal, a solid cell is generally surrounded by the same number of fluid and solid cells as the average composition of the mixed crystal. This implies that possible preferential clusterings of solid cells around a solid cell or fluid cells around a solid cell, and likewise for clusterings of fluid cells, are ruled out. Now, the average number of fluid cells surrounding one solid cell n_{sf} is given by

$$n_{sf}=zx_f \qquad (11)$$

Here, z is the coordination number of a solid cell. This is the number of the closest neighbouring cells. For our square lattice, z=4. The total average number of fluid cells N_{sf} surrounding the N_s solid cells is given by

$$N_{sf}=zN_sx_f \qquad (12)$$

N_{sf} corresponds to the total average number of solid - fluid closest - neighbouring - contacts between cells or bonds. In the pure solid and pure fluid crystal, only the closest neighbouring bond energies ss (solid-solid) and ff (fluid-fluid) occur. It can be said when using the zeroth order approach that due to the mixing process, normally N_{sf} ss bonds and ff bonds are replaced by N_{sf} sf bonds. For the formation of one sf bond, one half ss and one half ff bond energy must be broken. This can be demonstrated by the following. We start with a pure solid and a pure fluid crystal and exchange a solid and a fluid cell. Then in our square, two-dimensional crystals, 4 ss bonds are broken in 4 ff bonds. These are replaced by 8 sf bonds. So for the formation of one sf bond, 1/2 ss and 1/2 ff bond must be broken. It thus follows that the formation energy of one solid-fluid bond energy Φ referenced to a pure solid and a pure fluid crystal is given by

$$\Phi = \Phi^{sf} - \tfrac{1}{2}(\Phi^{ss} + \Phi^{ff}) \tag{13}$$

Here, Φ^{sf}, Φ^{ss} and Φ^{ff} are negative energies and the generalised energy, Φ, which plays a key role in the formalism to be developed is supposed to be positive. Substituting equation (13) into equation (12), writing according to equation (10) $x_f = 1 - x_s$, and dropping the index s in x_s, we obtain for ΔU_{mix} the expression

$$\Delta U_{mix} = NkTax(1-x) \tag{14}$$

Here, x is the fraction of solid cells in the mixed solid-fluid crystal and

$$a = z\frac{\Phi}{kT} \tag{15}$$

We recall that for our square lattice, $z=4$. Φ is for a square lattice with one type of closest neighbouring bond given by equation (13). Substituting the expressions for mixing entropy (equation (7)) and energy of mixing (equations (14,15) in equation (2)), the following expression for the free energy change due to the mixing process is obtained

$$\begin{aligned} F &= F^r + \Delta F_{mix} \\ &= NkTax(x-1) + NkT(xlnx + (1-x)\ln(1-x) \\ &\quad - N\Delta\mu^* + N\mu_f^* \end{aligned} \tag{16}$$

Here

$$\Delta\mu^* = \mu_f^* - \mu_s^* \tag{17}$$

The two last terms of equation (16) follow from equation (1) and equation (10).

In the case of thermodynamic equilibrium, the chemical potential of a solid cell has to be equal to the chemical potential of a fluid cell. Otherwise, growth or dissolution would occur. So

$$\mu_f^* = \mu_s^* \tag{18}$$

and equation (16) changes in

$$\begin{aligned} F &= kTax(1-x) + NkT(xlnx + (1-x)\ln(1-x) \\ &\quad + N\mu_f^* \end{aligned} \tag{19}$$

2.3 Implications of the model

If equation (19) is divided by NkT we get

$$f(x) = ax(1-x) + xlnx + (1-x)\ln(1-x) \tag{20}$$

In equation (20) we have omitted the term μ_f^* which is a constant for constant T. f(x) is given by

$$f(x) = \frac{F(x)}{NkT} \tag{21}$$

and has the meaning of the average free energy per solid and fluid cell in the mixed solid-fluid crystal divided by kT.

In **Fig. 1** we have plotted the function f(x) given by equation (20) in dependence of x for different α values. For values of $\alpha > 2$ two minima occur separated by a maximum for $x=0.5$. For values of $\alpha \leq 2$ only one minimum occurs for $x=0.5$.

The function f(x) results from adding the two functions: Δu_{mix} and $-T\Delta s_{mix}$. The dimensionless energy of mixing term Δu_{mix} is given by

$$\Delta u_{mix} = \frac{\Delta U_{mix}}{NkT} = -ax^2 + ax \tag{22}$$

Since α is supposed to be positive, this is a mountain parabola, with a maximum at $x=0.5$. The dimensionless entropy term $T\Delta s_{mix}$ is given by

$$-T\Delta s_{mix} = -\frac{T\Delta S_{mix}}{NkT} = xlnx + (1-x)\ln(1-x) \tag{23}$$

Taking the first derivative of equation (23) yields the following expression

$$-\frac{dT\Delta S_{mix}}{dx} = lnx - \ln(1-x) \tag{24}$$

It can be seen that this first derivative goes to $-\infty$ if $x \to 0$ and to $+\infty$ if $y \to 1$. Since the expressions xlnx and $(1-x)\ln(1-x)$ are negative, because x and $1-x$ are smaller than unity, the function $-T\Delta s_{mix}$ has the shape of a basin with infinite steep slopes for $x \to 0$ and $x \to 1$. By adding the basin function $-T\Delta s_{mix}$ and the mountain parabola function Δu_{mix}, two minima close to $x=0$ and $x=1$ occur separated by a maximum. This only holds if α is large enough. If α becomes smaller and smaller due to, for example, an increase in temperature (see equations (13,15)), the mountain parabola equation (22) shrinks. This implies that the maximum of the f(x) function decreases and that the minima shift towards the middle (**Fig. 1**). If α continues to decrease, a critical point is reached where the basin entropy function becomes dominant, which results in only one minimum for $x=0.5$. It will be shown below that the critical value for α is $\alpha^c=2$.

2.4 Physical interpretation of the model

Here Figure 2

In **Fig. 2**, a sketch is given of an interpretation of the two-dimensional regular solution model developed so far. It can be seen from **Fig. 1** that if $\alpha>2$, the two-dimensional mixed solid-fluid crystal will reach a minimum in the free energy by separating itself in a solid phase or solid domains with some fluid cells, and in a fluid phase or fluid domains with some solid cells. Then, two-dimensional domains will be separated by edges of steps with an edge-free energy larger than zero. If α decreases (or, keeping the bond energy Φ constant, by increasing the temperature), more and more solid cells will appear in the fluid domains as ad atoms on the surface, and more and more fluid cells will appear in the solid domains as surface vacancies. For $\alpha\approx2$, one phase or one domain occurs consisting of 50% solid cells and 50% fluid cells (see again **Fig. 1**).

The results of the two-dimensional regular solution model can now be given the following physical interpretation. If $\alpha>2$, a crystal face will be essentially flat because the surface will consist of large solid domains separated by steps with an edge free energy larger than zero. That surfaces which are flat over very large distances do occur can be demonstrated with the following argument. Assume that we have a very large surface consisting of one solid domain. Due to statistical fluctuations, only surface vacancies of fluid cells and ad atoms of solid cells can be formed. Large islands on top of the solid domains or large basins in the solid domains cannot be formed by statistical fluctuations, because the edge free energy of a step separating solid and fluid domains is larger than zero. If, however, $\alpha<2$, the possible edge free energies between (metastable) solid and fluid domains vanish and a surface may freely roughen up by statistical fluctuations. Then there is no need to maintain an overall flatness.

It follows from the considerations presented in this section that if α is larger than a critical value, a crystal surface is in essence flat, but if α is smaller than a certain critical value it is in essence rough. It can be seen from equations (13,15) that α is inversely proportional to the absolute temperature. We can therefore rephrase the statement given above in the following way: there exists for a crystal face a characteristic temperature T^R, to be called the roughening temperature, which is inversely proportional to α^c so that if
and if

$$\begin{aligned} &\alpha>\alpha^c \text{ or } T<T^R,\ \gamma>0 \\ &\quad \text{and if} \\ &\alpha\leq\alpha^c \text{ or } T\geq T^R,\ r=0 \end{aligned} \qquad (25)$$

γ is defined as the edge free energy per unit of length of a step. If $\alpha>\alpha^c$ or $T<T^R$, solid and fluid domains are separated by well-defined boundaries which correspond to steps with an edge free energy larger than zero. If $\alpha\leq\alpha^c$ or $T\geq T^R$, solid and fluid domains become one phase and edge free energies between (artificial) boundaries vanish. It thus follows that the change in the f(x) function from a function characterized by two minima corresponding to the solid and the fluid phases separated by a maximum, to one minimum corresponding to one mixed solid-fluid phase (see **Fig. 1**), can be given the preliminary interpretation of the roughening transition.

2.5 Kinetic roughening

In this section, the influence of a driving force for crystallization on the roughening transition will be studied. It was discussed above that in the case of thermodynamic equilibrium, $\Delta\mu^*=0$ (see equations (17,18)). It is, however, possible that the mother phase and the crystal surface under consideration are not in thermodynamic equilibrium and that, for example, μ_f the chemical potential of a fluid cell is larger than the chemical potential of a solid cell. In this case, a driving force for crystallization occurs. In case of growth from solution, the chemical potential of a fluid cell may be given by

$$\mu=\mu^{\theta}+kTlnx \qquad (26)$$

here, μ^{θ} is the standard chemical potential and x is the fraction of solute. In the case of thermodynamic equilibrium, the chemical potential of a solid cell is in principle equal to the chemical potential of a fluid cell, so that we can write

$$\mu_S=\mu^{\theta}+kTlnx_{eq} \qquad (27)$$

where now x_{eq} is the fraction of solute for a saturated solution in equilibrium with the solid phase. The driving force of crystallization is for relatively low supersaturations $\Delta\mu$ given by

$$\Delta\mu=\mu_f-\mu_S=kTln\frac{x}{x_{eq}}=kTln(1+\sigma)\simeq kT\sigma \qquad (28)$$

The dimensionless driving force β' is defined as:

$$\beta'=\frac{\Delta\mu}{kT}(\simeq\sigma) \qquad (28a\ )$$

It may also be interpreted as relative overpressure for growth from the vapour, relative undercooling for growth from the melt etc.. The general term $\Delta\mu$ can now be introduced in equation (16) in the following way:

$$F=NkT\alpha\times(1-x)+NkT(xlnx+(1-x)\ln(1-x)) \\ -Nx\Delta\mu-N\mu_f^* \qquad (29)$$

Dividing equation (29) again by NkT we get

$$f'(x)=\alpha x(1-x)+xlnx+(1-x)\ln(1-x)-\beta' x \qquad (30)$$

In equation (30), we distinguish between an f'(x) curve due to a driving force for crystallization and an f(x) curve corresponding to thermodynamic equilibrium (equation (29)).

In **Fig. 3**, relative free energy curves f(x) are plotted for α=3 and β'=0.1 and 0.5, respectively. Due to the non-equilibrium positive driving force β', a linear curve −xβ' with a negative slope −β' is added to the equilibrium curves f(x). It can be seen from **Fig. 3** that if β' is larger than a certain value we get the situation that only one minimum survives. This corresponds to the fact that the thermodynamically stable phase is the solid phase. This obviously occurs for an f'(x) curve with α=3 if β'=0.5. For the case that β'=0.1, the solid phase is also the stable phase, but the fluid phase is metastable. This means that still two domains occur: the thermodynamically-stable solid phase and the metastable fluid phase. Following the discussion of section 2.4 it can be said that the flatness is maintained. This is no longer the case when there is only one minimum, due to the (positive) driving force. In this case the surface will be roughened. The effect is the same as for roughening above the roughening temperature. The reason is, however, quite different. Roughening is now caused by a driving force for crystallization. This type of roughening is called kinetic roughening.

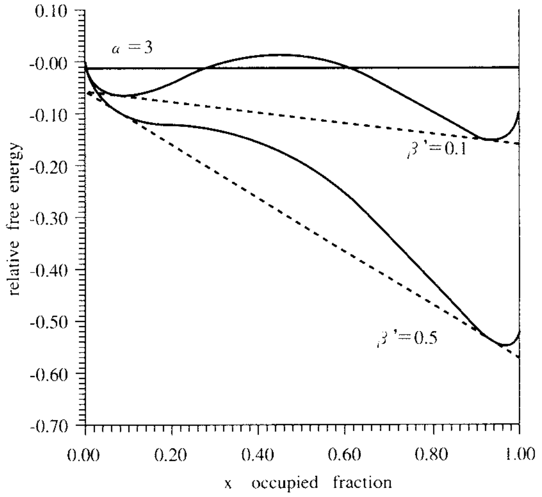

Fig. 3 The f' (x) function (equation (34)) is plotted as a function of x for β'=0.1 and β'=0.5, respectively.

2.6 Boundary between a flat surface and a kinetically roughened surface

It can be shown (see ref.[8]) that the boundary β'_{max} between the three extremes and the one extreme case is given by

$$\beta'_{max}=\pm\left\{\alpha\sqrt{1-\frac{2}{\alpha}}+\ln\frac{1-\sqrt{1-\frac{2}{\alpha}}}{1+\sqrt{1\pm\frac{2}{\alpha}}}\right\} \qquad (31)$$

Summarizing the discussion on kinetic roughening and the concept of (thermal) roughening, it can be stated that equation (25) implies that roughening transition or thermal roughening is defined as

$$\text{if } \alpha>\alpha^{R}(=2),\ \ \gamma>0\rightarrow \textit{flat surface}$$
$$\text{if } \alpha\leq\alpha^{R}\ \ \gamma=0\rightarrow \textit{rough surface} \tag{32}$$

and kinetic roughening implies

$$\text{if } |\beta'|>|\beta_{\max}| \text{ and } \alpha>\alpha^{R}\rightarrow \textit{kinetic roughening} \tag{33}$$

Note that for the one-layer mean field model $\alpha^{R}=2$. Due to the ad hoc mean field approximations and to a lesser extent the one-layer approach, this value differs by 60% from the proper value $\alpha^{R}=3.2$ which follows from computer simulations.

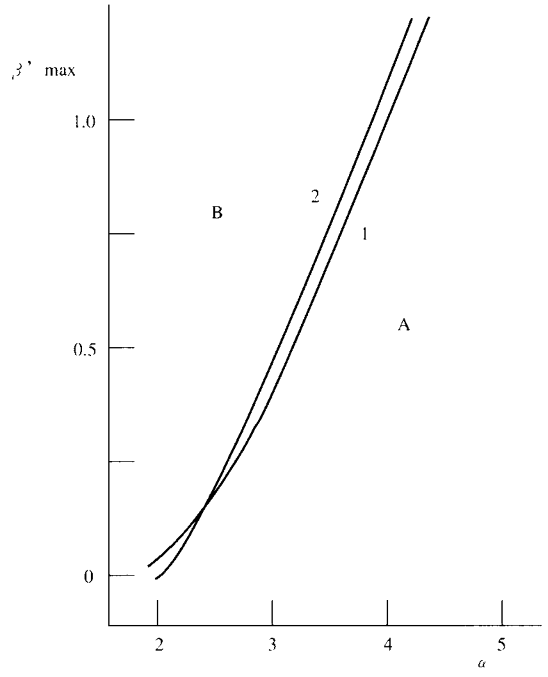

Fig. 4 Curve 2, $\beta'_{\max}$ curve according to equation (38) plotted as a function α. Curve unidy $\beta'_{\max}$ versus α curve for multilayer Temkin model.

In **Fig. 4** the $\beta'_{\max}$ versus α curve is presented (curve 2):. In region A, layer growth must occur, but region B corresponds to kinetic roughening. Curve 1 corresponds to the $\beta'_{\max}$ curve for a multilayer interface model introduced by Temkin (see for survey ref.[9] and included references). It can be seen that the one-layer Jackson model and the multilayer Temkin model give essentially the same results.

3. Thermal roughening; integration with Hartman Perdok theory and kinetic roughening

3.1 Monte Carlo Simulations

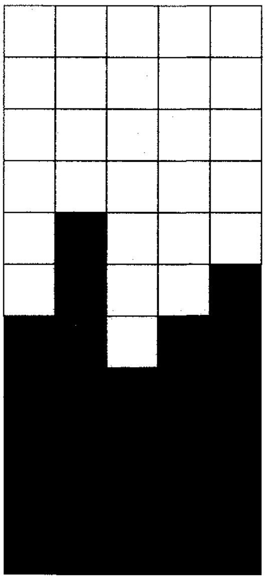

Fig. 5 Multilayer interface model, seen from the side Here, the solid-on-solid (SOS) condition is introduced. This condition implies that only solid blocks on top of solid blocks are permitted. So overhangs are ruled out and fluid vacancies in the solid body also.

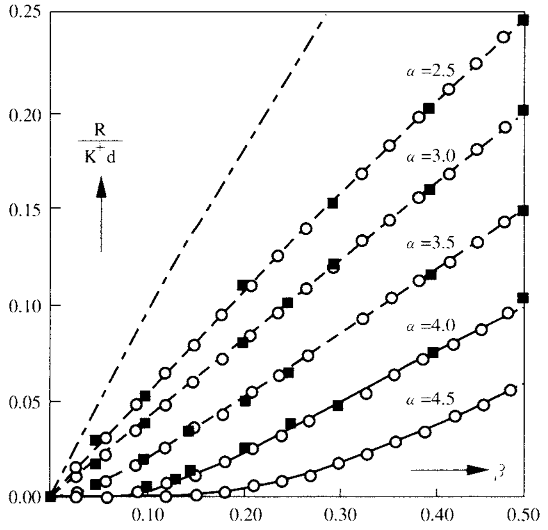

Fig. 6 Dimensionless growth rate $R/k^{+}d$ versus β', $o<\beta'<0.5$. k^{+} is the kinetic coefficient determined by the computer program used, d is the interplanar distance, and R the rate of growth of the (001) face. Solid lines are fitted with two-dimensional nucleation curves. The upper line is the maximum rate of growth acctrding to the so-called Wilson Frenkel law. Results of a general-purpose computer [11]. 0 results of a special-purpose computer [12].

The one-layer regular solution model of Jackson[3] has the advantage that it yields, in principle, essential concepts for the science of crystal growth such as thermal roughening and kinetic roughening. In addition, the regular solution model is easy to understand. The model, however, has its serious limitations. These are amongst others: (i) the limitation of the interface to one layer, and (ii) the application of mean field approximations. The last ad hoc approximation rules out preferential clusterings, which are essential for crystal growth.

Monte Carlo simulations have been carried out by Gilmer et al[11] and de Haan et al[12] for a multilayer so-called solid-on-solid model. Such a model is demonstrated in **Fig. 5**. An SOS model is defined as a (001) interface of a tetragonal crystal, as discussed above, where overhangs are ruled out. (See **Fig. 5**). As shown in refs[11,12], it is possible to simulate growth for different α (equation (15)), and β' (equations (28, 28a)) factors. In **Fig. (6)**, dimensionless rates of growth of the (001) surface in dependence of the dimensionless driving force β' are presented. These data result from Monte Carlo simulations obtained from a general and a special-purpose computer, respectively. It can be seen that at low α values a linear R(β') curve occurs, but at higher supersaturations a curved R(β') curve. For values of $\alpha \geq 4$ the curved curve could be fitted with a so-called two-dimensional nucleation curve, using the birth and spread version. This implies that two-dimensional nuclei are formed on the surface, which spread. On top of these spreading layers other two-dimensional nuclei are formed, etc. etc.

The change from a linear to a non-linear curve at a value of $\alpha \approx 3.2$ marks the roughening transition. If $\alpha < 3.2$, the edge free energy is zero, hence no two-dimensional nucleation barrier occurs and the crystal face will grow with a linear growth rate. Also, the crystallographic orientation (001) (or in general (hkl)) will not be maintained. If $\alpha > 3.2$, the edge free energy is larger than zero (equation (25)), and growth progresses with a two-dimensional nucleation mechanism leading to the non-linear curves R(β') of **Fig. 6**. For sufficiently high α values the growth rate is extremely slow, since the chance to form large critical nuclei is very low. In this case, growth may proceed via a spiral growth mechanism, induced by a screw dislocation. (We note that two conventions are used to define dimensionless energies or dimensionless temperatures which are expressed as xxx or kTxxx, respectively).

Inspired by the results of Monte Carlo simulations more than ten years ago, the concept of roughening transition on an SOS surface was clarified by experts on statistical-mechanical Ising models (see refs[4,5,6,8] for other references). It can be defined in the way carried out above, (see equations (25,32)), but the foundation of this concept is now much stronger compared to the ad hoc and loose intuitive arguments used above. As already mentioned, numerically the value of $\alpha^R = 2$ is 60% wrong. It follows from simulations that $\alpha^R = 3.6$.

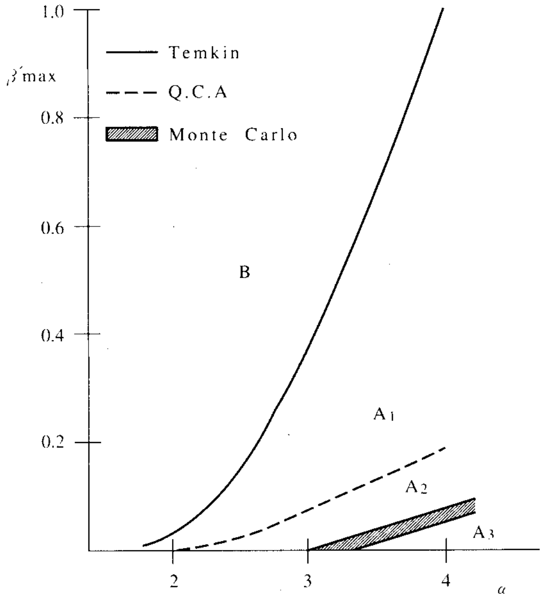

Fig. 7 $\beta'_{\max}$ versus α curves. Upper curve Temkin multilayer model, middle curve ; curve calculated van Leeuwen using a pair approximation [15] . Lowest band boundary of two-dimensional nucleation and kinetic roughening.

In **Fig. 7**, a $\beta'_{\max}$ versus α plot is presented. The upper curve corresponds to the multilayer mean field model of Temkin and was already presented in **Fig. 4** (curve 1). The lower curve results from a more refined mean field so-called pair approximation approach[15]. The lowest curve or band corresponds to the change from a two-dimensional nucleation regime to a regime where critical two-dimensional nucli are so small that they correspond to a few atoms or molecules. This occurs at some higher critical supersaturation. This is a modern way to define kinetic roughening. It can be seen that mean field models make the area for layer growth much too large. One can say that nature always finds clever fluctuations to reduce the resistance of growth on flat faces. In general, it can be said that the barriers such as those presented in **Fig. 1** resulting from mean field models are artificially high. The minima seem to be real. Notwithstanding the critisism on mean field models, these models retain their heuristic and didactic value.

3.2 Spiral growth

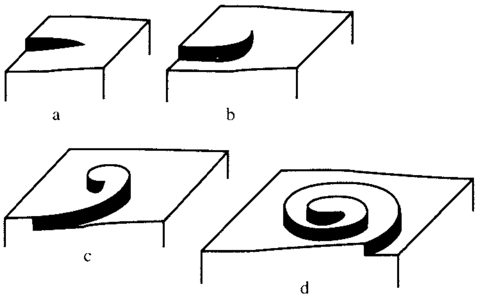

Fig. 8a, b, c, d
Development of aspiral on a crystal surface growing below its roughening temperature.

In order to explain how crystals can grow on flat faces (below the roughening temperature) at low driving forces (β'), Sir Charles Frank developed the brilliant theory of spiral growth. The mathematical theory was worked out in the famous paper of Burton, Cabrera and Frank in 1951. The idea of a growth spiral is demonstrated in **Fig 8 a,b,c,d**. Thanks to the fact that almost all crystals are not perfect, screw dislocations are present which are a source of steps. It can be proven from statistical mechanical SOS step models (one dimension lower than the SOS surface model) that steps are always rough up to the absolute zero temperature. So steps grow without a thermodynamic nucleation barrier. This is analogous to the advance velocity of a surface growing above its roughening temperature (see **Fig. 6**). The centre of the step source does not change, and the curvature at the centre also remains constant. This curvature is the same as the radius of the two-dimensional nucleus r*, which is given by

$$r^* = \frac{\gamma}{kT}\,\frac{\Omega}{\beta'} \qquad (34)$$

Here, γ is the edge free energy of a step expressed in energy per surface area and Ω is the molecular volume of an atom, molecule, etc. in the solid state. Thanks to the interaction of the step source, created by the screw dislocation, the edge free energy, which below the roughening temperature is larger than zero (equations (25,32)), and the driving force, which gives a curved step, a very special dissipative structure occurs: the growth spiral. Note that growth spirals are very flat hills. So the deviation of the orientations (hkl) is extremely small.

The concept of dissipative structure was introduced by Prigogine[14]. It is a structured pattern which develops due to non-linear effects under the influence of a thermodynamic driving force. A dissipative structure produces entropy.

3.2 Hartman Perdok theory and connected nets

So far, very simple lattice gas models were used leading to concepts of roughening transition, kinetic roughening and spiral growth. Real crystals may have very rich crystallograhic structures, and it has been shown that the world of statistical mechanical Ising models and the world of rich crystal structures, in principle at least, can be integrated.

The principles of the application of the integrated theory can be summarized as follows:
(i) first the bonds and bond energies between molecules must be determined. To determine the overall bond energies between molecules, the best available crystallographic data concerning mutual distances between molecules and their atoms are used and the best interatomic (for example, Buckingham) interaction potentials available.
(ii) Next, the molecules are reduced to points or centres of gravity and the so-called crystal graph is determined[1,4,5,6,8]. A crystal graph consists of a (infinite) set of points corresponding to the centres of gravity of molecules or growth units (or complexes) from which the crystal grows, and the relations or bonds between the centres of gravity. The relevant bonds of the crystal graph are the bonds corresponds to closest neighbouring bonds. The crystal graph fulfills the symmetry of the space group of the crystal structure.
(iii) In order to predict the slowest growing

faces, which will dominate the crystal growth form, from the crystal graph, the so-called connected nets have to be determined. A connected net is defined as a two-dimensional graph where all points are connected to each other. This means that one can go from any point in the connected net to any other point by an arbitrary uninterrupted path of bonds. In order to determine genuine connected nets, it must be possible to partition the whole crystal graph unambiguously in equal parallel stacks of connected nets with an overall thickness of the interplanar distance d_{hkl}, corrected for the extinction conditions of the space group.

In the concept of connected nets, the world of crystallography and the statistical-mechanical Ising models meet. Since in all crystallographic directions the edge energy of a connected net is larger than zero, connected nets show a roughening transition. So faces parallel to a connected net will have a high resistance against growth if they can grow below their roughening temperature with a layer mechanism. (This means spiral growth is in most cases dominant. Two-dimensional nucleation will occur rarely, if no screw dislocation emerges at the surface). Therefore, faces parallel to connected nets will dominate crystal habits.

Apart from connected nets, non-connected nets also occur. It is then not possible to connect within the thickness d_{hkl} the points of the crystal graph to each other, using bonds of the set of bonds of the crystal graph. For such a net, the edge energy in at least one direction is zero. A face parallel to such a net has a roughening temperature $T^R = 0K$. The concept used here was first developed by Hartman and Perdok more than 35 years ago[16]. A face parallel to a connected net was called an F (flat) face. Connected nets consist of at least two sets of parallel-connected uninterrupted chains of bonds of the crystal graph with a periodicity of the lattice of the crystal graph [uvw] . Such chains are called PBCs (Periodic Bond Chains).

A net containing at least two sets of connected PBCs is a connected net, and as already mentioned is parallel to an F face. A face parallel to an unconnected net consisting of only one set of parallel PBCs is called an S (stepped) face. A face parallel to an unconnected net without any PBCs is called a K (kined) face.

3.3 Order-disorder phase transition in two-dimensional connected net

Let us rephrase the theory of roughening transition summarized by equations (25, 39) in the following way

$$\begin{aligned} &\text{if } \theta < \theta^R \quad \gamma > 0 \\ &\text{if } \theta \geq \theta^R \quad \gamma = 0 \end{aligned} \qquad (32\,a)$$

Here, θ and θ^R are defined as dimensionless temperatures.

$$\theta = \frac{2kT}{\Phi_{str}} \qquad \theta^R = \left[\frac{2kT}{\Phi_{str}}\right]^R \qquad (35)$$

Φ_{str} is the strongest bond energy of a crystal graph. So, θ and θ^R are referenced to this bond energy. Φ_{str} has the shape as equation (13).

Onsager showed in 1944 that for a two-dimensional crystal or a connected net, an order disorder phase transisition occurs. Onsager was also able to calculate exactly the order-disorder phase transition temperature for simple nets with a given ratio of bond energies. This temperature is also known as the Ising temperature. So, using Onsagers approach and contrary to the regular solution theory, θ^c can be calculated exactly. Recently, a method was developed to apply this theory to real complex-connected nets[18]. Onsager's results and the new method can be summarized as follows.

$$\begin{aligned} &\text{if } \theta < \theta^C \quad \gamma > 0 \\ &\text{if } \theta \geq \theta^C \quad \gamma = 0 \end{aligned} \qquad (36)$$

Here, θ^c is the dimensionless Ising temperature using the same convention as eq (35). We note that equation (36) has the same meaning as equation (25,32a,b).

In the formalism developed in ref.[18], a probe step is introduced into the one-layer mixed solid-fluid crystal by forcing two screw dislocations of opposite sign, connected by a step, into this layer. (Note that when applied to magnetism the Ising temperature corresponds to the Curie temperature).

It was proposed to use the dimensionless Ising temperature θ^c, as a criterion for the relative morphological importance (MI) for a form of faces {hkl} on the crystal growth form[4,6,8]. It is then assumed that the higher the θ^c, the higher the MI. MI is defined as a (qualitative) statistical measure for the relative size and the relative frequency of occurrence of the faces of this form on the crystal growth form. The higher these quantities, the higher the MI.

We note that the reasons for using the Ising temperature of a two-dimensional connected net, instead of the more relevant roughening transition temperature in a multilayer interface as a criterion for the MI are the following:
(i) notwithstanding that the character of the roughening phase transition flat-rough is quite different from the character of an order-disorder phase transition in a connected net, it turns out that for simple models[4-6,8]:

$$\theta^R \simeq \theta^C \qquad (37)$$

So it is reasonable to assume that it also holds true for more complex models.
(ii) For more complex crystal structures θ^c contrary to θ^R, θ^c can be calculated, provided the connected nets are real planar nets (i.e. no crossing bonds and nets with more floors occur). However, in this latter case, good approximations are often possible[4-6,8].

3.4 Roughening and kinetic roughening

Assume that we have a sequence of Ising or roughening temperatures of the connected nets of a crystal graph:

$$\theta_1^C > \theta_2^C \cdots\cdots \theta_{m-2}^C > \theta_{m-1}^C > \theta_m^C \qquad (38)$$

If, at low supersaturations all faces grow below their roughening temperature as flat faces, it can be predicted that as the supersaturation increases, first face m will grow as a kinetically rough face and will become rounded, next faces m-1, etc. Or in other words: first the weakest faces with the lowest θ^c and, consequently lowest edge free energy, will grow as a kinetical rough face, next the next-weakest face, etc.

3.5 Proportionality condition

We recall that generalized bond energies Φ_i as used, for example, in eqs. (35) have the shape as given by equation (13).

Since sf and ff bond energies are generally unknown, the following ad hoc approximations are usually introduced to calculate bond-energies Φ_i
(i) the proportionality condition, implying that for two arbitrary bond energies Φ_i and Φ_j of the crystal graph, the following relation holds

$$\Phi_i : \Phi_j = \Phi_i^{ss} : \Phi_j^{ss} \qquad (39)$$

(ii) in order to calculate the actual bond energies, one other expression is needed, and the following approach has proved to be possible. Assume that the relative Ising or roughening temperatures are calculated for the connected nets or F faces of the faces 1, 2,...p,q... and that an order of decreasing θ^c values is obtained:

$$\theta_1^C > \theta_i^C \cdots\cdots > \theta_p^C > \theta_q^C > \cdots\cdots \qquad (40)$$

If it is observed that faces of the form p are flat, but faces of the form q are rough (or absent), then one may conclude that for the actual dimensionless temperature

$$\theta = \frac{2kT}{\Phi_{str}} \qquad (41)$$

according to the theory of roughening transition the following relation holds:

$$\theta_p^C > \theta > \theta_q^C \qquad (42)$$

We note that in all expressions for θ_p^c, θ, θ_q^c these values are referenced to the strongest bond energy Φ_{str}. Since the actual temperature T of the mother phase from which the crystal grows can be measured, Φ_{str} can be estimated from equations (41,42), and using eq. (39), all Φ_i's can be calculated[3-5,8]. In the following, some results of research on growth and morphology of organic and anorganic crystals will be mentioned.

5. Morphology of organic crystals

5.1 Cyclohexane

Cyclohexane, C_6H_{12}, forms plastic crystals with a cubic, closely-packed structure in which the C_6H_{12} molecules rotate almost freely and switch continuously from a chair to a bed configuration. The crystal graph can be considered as a cubic FCC lattice. Taking the closest neighbouring bonds, two types of connected nets, (111) and (100), can be identified.

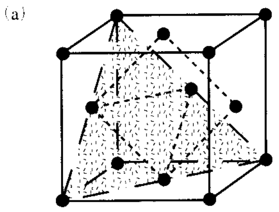

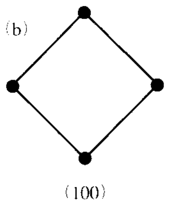

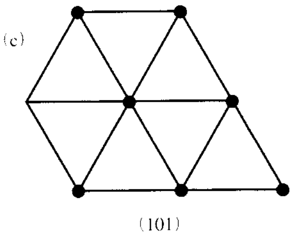

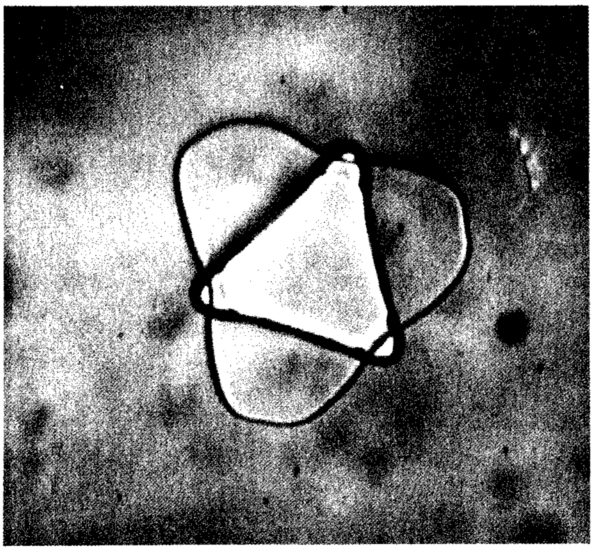

Fig. 9a Crystal graph of FCC structure.

Fig. 9b Connected net (100)

Fig. 9c Connected net (111)

Fig. 9d A cyclohexane crystal growing from the melt about 6°C of very low undercoolinng. From the rounded-off octahedron, six paralola like figurei are emitted. At the bottom of the growth cell the undercooling is higher than at the lower corner. This picture is taken from a TV screen. My thank's to R. Geertman.

This will lead to crystals having the shape of an octahedron. The corners may be cut off by cube faces. However, since the mobility of the cyclohexane molecules within the lattice close to the melting point of 6°C is very high, the enthalpy of melting ΔH^m is only 2.68 kJ mol^{-1}. This suggests that faces of cyclohexane crystals grow above their roughening temperatures with rounded-off rough faces from the melt, even at very low undercooling. This is indeed the case. It is interesting to see that the bond structure of the crystal graph still shows up in the anisotropy of the surface or growth rates. If the size of a growing crystal increases, the crystal form becomes unstable and dentritic growth starts with six branches, which are emitted from the rounded-off corners of the rounded-off pseudo-octahedron. (See **Fig. 9d**.) Instable crystal growth leading to dentritic or cellular growth will always occur if crystals grow above their roughening temperature.

5.2 Crystal of buckyball C_{60} molecules

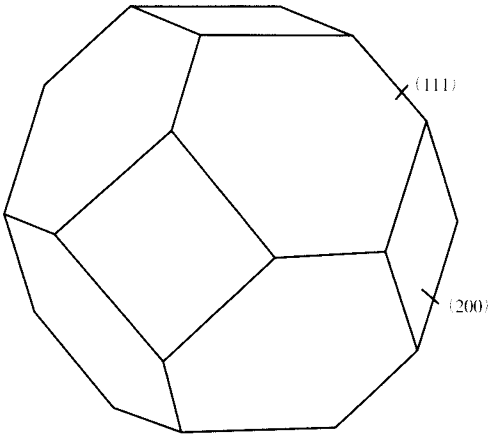

Fig. 10 Theoretical cubeoctahedron derived from the crystallo-graph fig. 10a. This is in agreement with the observed crystal forms.

Very recently, crystals of C_{60} were grown from the vapour phase. Now, $\Phi = -\frac{1}{2}\Phi^{ss}$ (equation (13)), since Φ^{sf} and Φ^{ff} are zero. The faces {111} and {100} are now growing below their roughening temperature and crystals in the shape of cube octahedrons are grown from the vapour phase (see schematic drawing **Fig. 10** and ref.[19]). Very recently, C_{70} crystals were also grown from the vapour phase. These show an HCP and FCC structure. Expected and observed morphologies for both crystal structures were in agreement with each other (work in progress).

5.3 Naphthalene and biphenyl

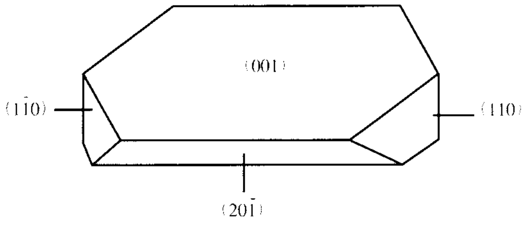

Fig. 11 Schematized naphthalene or biphenyl crystal.

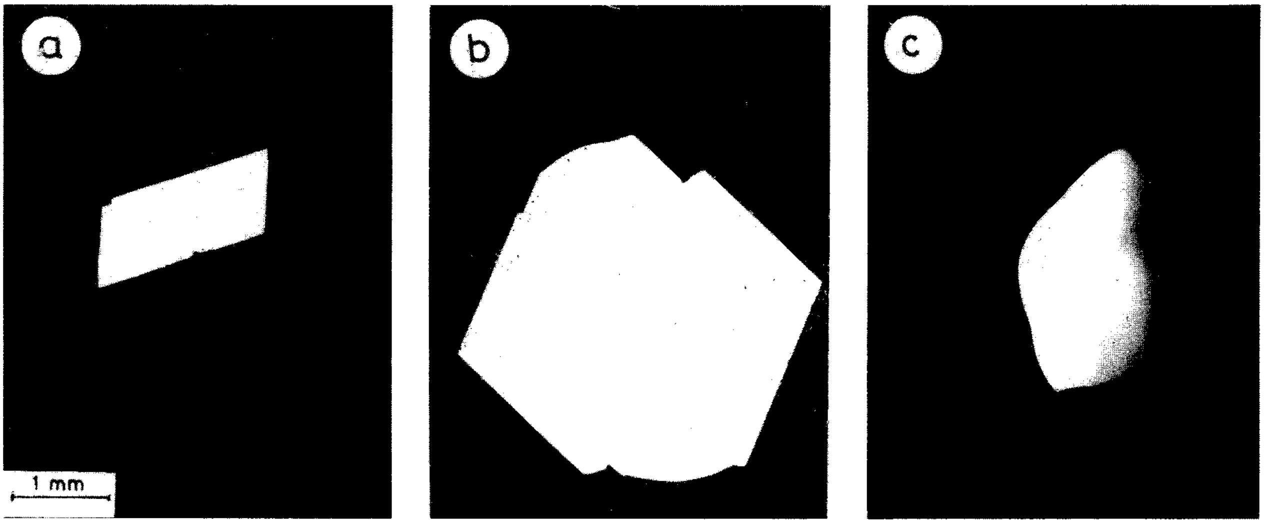

Fig. 12a, b, c,
Biphenyl in toluene observed with polarising microscopy.
(a) relative supersfturation $\sigma = 0.20\%$,
(b) $\sigma = \leq 27\%$ obviously {110} faces are flat. But for this value of σ {201} faces are kinetically roughened.
(c) for $\sigma = 99\%$ {110} faces are also kinetically roughened.

Extensive work has been done on naphthalene and biphenyl growing from different solvents and the melt. It can be predicted that naphthalene crystals will be dominated by two strong (001) F faces of the form {001} and also four F faces of the form {110} forming a parallelogram, and two F faces of the form {201} which will truncate the parallelogram (see **Fig. 11**).

Looking at the experimental growth forms of napht biphenyl Crgsbh growing from the organic solvent toluene, it can be seen that a crystal is indeed limited by the strongly dominant {001} faces and the four faces of the form {110} . Often faces of the form {201} occur. In **Fig. 12 a** and **b**, these are kinetically roughened (see further refs[4–6,8]).

5.4 Orthorhombic paraffin

It can be derived from the crystallograph of paraffin of the odd orthohombic structure that paraffin crystals will be limited by two large (001) faces, four faces of the form {110} , (and sometimes faces of the form {010}). (See **Fig. 13 a,b**.) In **Fig. 13 c**, a paraffin crystal with a number of 23 C atoms growing from a slightly supersaturated hexane solution is presented growing below the roughening temperature of the {110} faces. In **Fig. 13 d**, a C_{23} paraffin crystal is presented also growing from a hexane solution, but now above the roughening temperature. The roughening temperature turned out to be 10, 65 °C ± 0.5 °C and is low. This must be attributed to a strong interaction between solute and solvent molecules with the solid molecules. This makes the Φ_i^{sf} energies extra

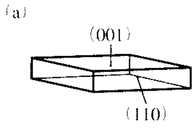

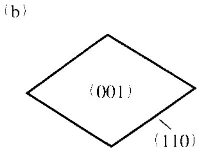

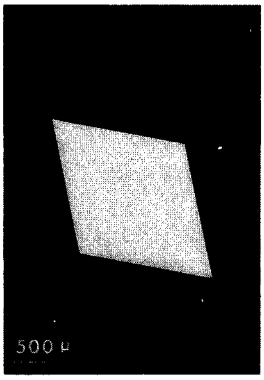

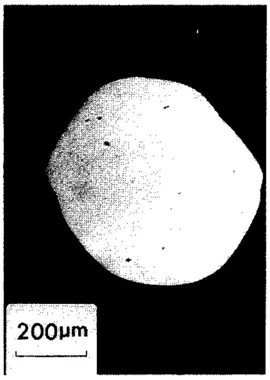

Fig. 13a A typical paraffin crystal limited by large faces of the from {001} , and four faces of the from {110} .
Fig. 13b Same crystal seen from above.
Fig. 13c A paraffin crystal with 23C atoms par molecules with straight {110} faces grtwing from an hexane solution below the roughening temperature of {110} faces at very low supersaturations.
Fig. 13d Paraffin crystal, but now growing above the roughening temperature.

negative, and as can be seen from equation (13), Φ_i low1). Very recently, a very special kind of kinetic roughening was observed; a so-called rough-flat-rough transition21).

5.5 Morphology of β-lactose

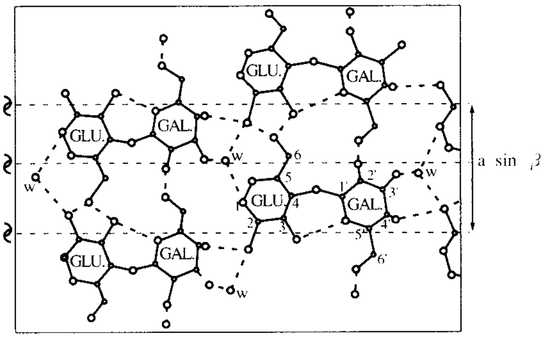

Fig. 14a

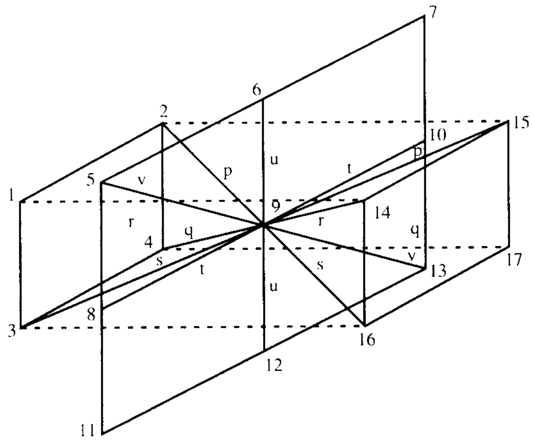

Fig. 14b

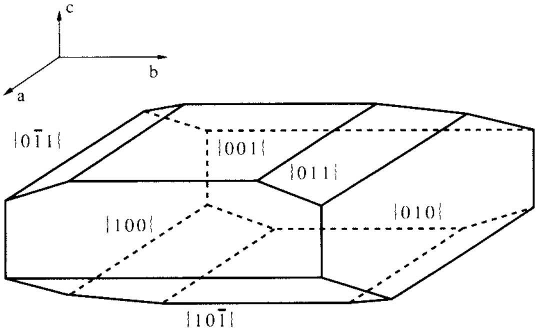

Fig. 14c

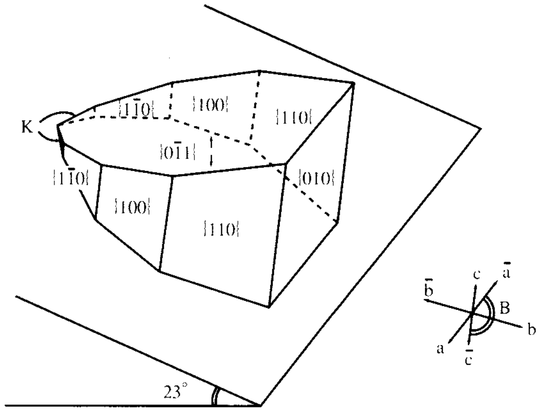

Fig. 14e

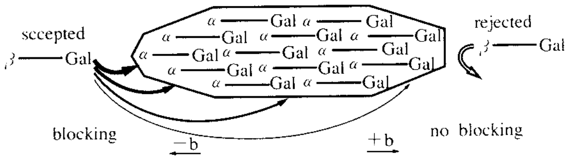

Fig. 14f

Fig. 14d₁

Fig. 14d₂

Fig. 14a Projection of crystal structure of monoclinic lactose crystals, down to the c axis of the α-lactose hydrate lattice. The O atoms are shown as larger and the C atoms as smaller circles ; H atoms are omitted. GLU = glucose part ; GAL = galactose part of lactose molecule. W = water ; ······ = screw axis ; a sin β = 0.7470nm.

Fig. 14b Crystal graph of lactose obtained after reducing lactose molecules to contres of gravity. Overall bonds are p, q, r, s, t, u, v.

Fig. 14c Constructed hypothetical crystal based on the criterion : rate of growth of a face (hkl) is inversely proportional to the Ising temperature θ.

Fig. 14d Observed tomahawk lactose crystals seen from different angles. Crystals seen enlarged about 25 times.

Fig. 14e Schematic drawing of observed lactose crystal.

Fig. 14f Where "wrong" β lactose molecules are absorbed blocking occurs. Where they are rejected no blocking occurs.

In **Fig. 14 a**, a projection is presented seen in the direction of the shortest b axis. The sugar-lactose molecules consist of a lactose and galactose moiety. Taking closest neighbouring hydrogen bonds, the complex sugar-lactose molecules are reduced to centres of gravity. In **Fig. 14 b**, the crystal graph is presented. This looks like a pseudo-body-centred structure. In **Fig. 14 c**, a crystal growth form is presented based on the principle that the rate of growth of faces parallel to connected nets is inversely proportional to $(\theta^c)^{-1}$. This predicted morphology is in absolute conflict with the observed morphology (**Fig. 14**$\mathbf{d_{1\sim2}}$**, e**), and the schematized habit (**Fig. 14 e**), which is also called "tomahawk habit". The reason is that due to a meta-rotation equilibrium in the solution, 80% of the lactose molecules have a "wrong" glucose part. The lactose part in solution and crystal has the same configuration. In **Fig. 14 f**, a scheme is given of the reason for the anormal tomahawk morphology. On the left hand side, wrong molecules enter and block the growth. On the right hand side, these blocking molecules cannot enter and do not block the growth. In **Figs. 14** $\mathbf{d_{1\sim2}}$**, e, f**, the dramatic blocking effect is demonstrated. The $(0\bar{1}0)$ face does not grow at all. Adjacent faces grow very slowly.

Using a systematic-logical recipe to describe the blocking effect on different crystallograhic faces, it was possible to explain the deviation from the ideal morphology in a satisfactory way (see refs[22,23]). This drastic change in morphology is an example of how specific tailor-made additives can change the ideal morphology in a systematic and drastic way. This is an example of an unplanned naturally-induced tailor-made additive. Pioneer work on man-made tailor-made additives giving planned changes in morphology has been carried out by Dr. Ziva Berkovitch-Yellin. (See reference 2)

6. Conclusions

From the examples given above it can be concluded that an integrated Hartman-Perdok roughening temperature theory based on Ising models, where the whole interface is partioned into equal cells which can have two properties, namely either solid or fluid, leads to relevant results for a wide variety of totally different crystal structures. Most important is the interpretation of observed roughening transition and kinetic roughening phenomena. Specific subtle interactions between solvent or additives with a special orientation {hkl} may change the crystal habit drastically. Crystals growing above the roughening temperature or which are kinetically roughened will soon show dentritic or cellular growth. Crystals growing below the roughening temperature are not kinetically roughened-up and have a much higher resistance against instabilities.

The author wants to thank Mrs. J. Kogelman and Mrs. D.D. van der Weij for typing the manuscript, and Mr. J.W.M. van Kessel for preparing the drawings.

References

1) P. Bennema, X.Y. Liu, K. Lewtas, R.D. Tack, J.J.M. Rijpkema and K.J. Roberts: Morphology of Orthorhombic Odd Alkanes, J. Crystal Growth, **121** (1992)679
2) G.M. van Rosmalen and P. Bennema: Characterization of Additive Performance on Crystallization: Habit Modification, J. Crystal Growth, **99** (1990), 1053-1060
3) K.A. Jackson: Mechanism of Crystal Growth in Liquid Metals and Solidification, Am.Soc. for Metals, Cleveland, (1958), 174-180
4) P. Bennema and J.P. van der Eerden: Crystal Graphs, Connected Nets, Roughening Transition and Morphology of Crystals, Morphology of Crystals, Part A, Ed. by I. Sunagawa Terra Scientific Publ. Comp. Tokyo, D. Reidel Publ. Company Dordrecht, 1987 (ISBN 90-277-2507-1), 1-75
5) P. Bennema: Morphology of Crystals: Integration of Principles of Thermodynamics Statistical Mechanism and Crystallography, Sir Charles Frank, An Eightieth Birthday Tribute, Edited by R.S. Chambers et al., Adam Hilger, Bristol, 1991, 46-78
6) P. Bennema: Morphology of Crystals Based on Crystallography, Statistical Mechanism and Thermodynamics: Applications to Si and Ga, Kinetics of Ordering and Growth at Surfaces, Ed. Max Lagally, NATO ASI, Series B, Plenum Press, New York-London, 1989, vol. **239**, 415-435
7) Henry Eyring, Douglas Henderson, Betsy Jones Stover and Edward M. Eyring: Statis-

tical Mechanics and Dynamics, John Wiley & Sons, Inc., New York-London-Sydney, second print 1966, chapter 10

8) P. Bennema: Growth and Morphology of Crystals: Integration of Theories of Roughening and Hartman Perdok Theory, to be published in Handbook of Crystal Growth to be edited by D. Hurle and published by Elsevier in 1993

9) R.H. Fowler: Statistical Mechanism, Cambridge University Press., Second Edition (1936), reprinted 1966, Chapter 13, completely recast by E.A. Guggenheim

10) D.E. Temkin: Molecular Roughness of the Crystal-Melt Boundary, Crystallization Processes, Consultants Bureau, New York, (1966), 15-22

11) G.H. Gilmer and P. Bennema: Simulation of Crystal Growth with Surface Diffusion, J.Appl. Phys., **43**(1972), 1347-1360

12) S.W.H. de Haan, V.J.A. Meeuwsen, B.P. Veltman, P. Bennema, C. van Leeuwen and G.H. Gilmer: Simulation of Crystal Growth with a Special-Purpose Computer, J.Crystal Growth, **24**(1974), 491-494

13) W.K. Burton, N. Cabrera and F.C. Frank: The Growth of Crystals and the Equilibrium Structure of their Surfaces, Phil. Trans. Roy. Soc., A 243 (1951), 299=358

14) Ilya Prigogine: From Being to Becoming. Time and complexity in the Physical Sciences, W.H. Freeman and Company, San Fransisco, 1980, ISBN 0-7167-1107-9

15) C. van Leeuwen and P. Bennema: unpublished

16) P. Hartman: Modern PBC Theory in Morphology of Crystals, Ed. I. Sunagawa, Morphology of Crystals, Part A, Terra Scientific Publ. Company, Tokyo and D. Reidel Publishing Comp., Dordrecht 1987, 269-319, (see also ref. 4))

17) L. Onsager: Crystal Statistics I, A Two-Dimensional Model for an Order-Disorder Transition, Phys.Rev., **65** (1977), 117-149

18) J.J.M. Rijpkema, H.J.F. Knops, P. Bennema and J.P. van der Eerden: Determination of the Ising Critical Temperature of F Slices with an Application to Garnet, J. Crystal Growth, **61**(1983), 295-306

19) M.A. Verheijen, H. Meekes, G. Meijer, E. Raas and P. Bennema: Growth and Morphology of C_{60} Crystals, Chem. Physical Lett., **191**(1992), 339-344

20) L.A.M.J. Jetten, H.J. Human, P. Bennema and J.P. van der Eerden: On the Observation of the Roughening Transition of Organic Crystals Growing from Solution, J. Crystal Growth, **68**(1984), 503-516

21) Xiang Yang Lui, P. Bennema and J.P. van der Eerden: Rough-Flat-Rough Transition of Crystal Surfaces, Nature 356, April (1992), 778-780

22) R.A. Visser and P. Bennema: Interpretation of the Morphology of β-Lactose Hydrate, Neth. Milk Dairy J., **37**(1983), 109-137

23) R.A. Visser: Crystal Growth Kinetics of Alpha-Lactose Hydrate, Thesis, University of Nijmegen, 1983

Review

Hydrodynamics and Heat Transfer to Vertically Flowing Gas-Solids Suspensions†

Yuri Molodtsof*
Département de Génie Chimique
Université de Technologie de Compiegne

Abstract

Vertically flowing gas-solids suspensions have been investigated both theoretically and experimentally. The theoretical approach suggested the possibility of self-similar flow patterns for the particles at low solids concentration. The experiments carried out on two different installations with four different solids confirmed the existence of a so-called similar profiles regime bounded at dilute-phase flow conditions. At a constant gas velocity, a sudden transition occurs for a critical solids concentration. Beyond this limit particle concentration increases faster with increasing solids rate. These similarity properties have been eventually extended to the temperature profiles, which allowed the derivation of a general wall-to-suspension heat transfer equation containing two shape factors summarizing the flow hydrodynamics. This equation proved to be in excellent agreement with experimental results. Moreover, beyond the flow regime transition, i.e. in dense-phase flow, the same equation applies with modified shape factors.

1. Introduction

Gas-solids suspensions flow vertically in many industrial processes, ranging from pneumatic transport to fluidized bed reactors, including risers in the petroleum industry, transport reactors and circulating fluidized beds. Consequently, a considerable amount of work has been devoted to the problem. Muzyka[15], recently presented a comprehensive review of these earlier works concerned with either hydrodynamics or heat transfer. The first generation of papers was mainly concerned with pneumatic transport and, therefore, directed toward the prediction of overall pressure drop and average slip between the phases. In this connection, Hariu and Molstad[4], suggested considering the overall pressure drop under fully developed flow conditions as the sum of three contributions: gas friction, gravity, and wall-particle interaction. Moreover, they suggested accounting for the latter using a particle friction factor. The concept was widely used for a while but failed in predicting a curious experimental observation: the so-called negative drag[15] which occurs under certain operating conditions.

In the 1960s, gas-solids suspensions were considered as possible coolant media for nuclear reactors. During this period, theoretical attempts as well as experimental studies were aimed at predicting the variation of the wall-to-suspension heat transfer coefficient with solids loading. Empirical approaches resulted in a number of correlations predicting contradictory trends of variation as shown, e.g., by Maeda et al.[5]. Moreover, theoretical attempts failed in explaining these discrepancies. With the development of circulating fluidized bed reactors, a renewed interest appeared in the literature for heat transfer, especially in connection with applications to coal combustion reactors from which great amounts of heat should be removed. Besides this, as far as modelling for the prediction of reaction efficiency became an actual concern, numerous papers have been published on the distribution of the phases throughout the riser. Those dealing with the radial profiles of either particle concentration or both-phases velocites have been reviewed in a recent paper[11].

---

* B.P. 649, F - 60206 Compiègne, FRANCE

† Recieved June 10, 1992

The results discussed hereafter are mainly those obtained as part of a long-term program of the Suspensions and Powder Technology Group of the Compiègne University of Technology. One part of this program was operated in collaboration with the University of Western Ontario (Canada). The research program concerned the investigation of the overall and local characteristics of the hydrodynamics of vertically flowing gas-solids suspensions. In addition, particular attention was paid to the wall-to-suspension heat transfer problem. Experimental investigations were carried out on two different installations with their specific characteristics and measuring facilities. They were intimately combined with a general and rigorous theoretical approach in order to obtain general properties of vertical gas-solids flow.

2. Theoretical Approach

2.1. General Equations

A general theoretical framework allowing a rigorous mathematical description of multiphase mixtures, termed *probabilistic Eulerian description*, has been developed[9,10]. According to this approach, the presence and all physical quantities (i.e. immediate Eulerian variables) of each phase are random variables governed by laws of probability determined by the overall boundary conditions imposed to the flow. A given phase p in the mixture is then characterized by a phase presence probability α_p and probabilistic mean Eulerian variables of the phases are defined as the expected value of the random immediate Eulerian variable under consideration. The general probabilistic multiphase flow equations are written in terms of these "phase mean variables" which are shown[9] to be identifiable with measurable quantities in the flow.

The probabilistic approach to general equations is well adapted to the analysis of the flow structure since these are local equations written in terms of local variables defined so as not to be dependent on the existence of an appropriate spatial or temporal averaging domain. Besides, among rigorously derived general flow equations, they are the only ones to account for the specifics of gas-solids suspensions, particularly addressing the interactions between particles[15]. In the analysis below, all particle phases are treated as the overall "solids" phase. The conditions under which this is valid (i.e. when all the particles have the same physical properties such as density, regardless of their size or shape) were studied by Molodtsof and Muzyka[10].

For any phase p in the mixture, a continuity equation is derived:

$$\frac{\partial}{\partial t}(\rho_p\alpha_p)+\frac{\partial}{\partial x_j}(\rho_p\alpha_p V_j^p)=0 \qquad (1)$$

where ρ_p denotes the phase p density and V_j^p are the components of the phase mean velocity. The momentum equation of the overall "solids" phase, when projected on the Ox_i axis, takes the following form

$$\frac{\partial}{\partial t}(\rho_s\alpha_s V_i)+\frac{\partial}{\partial x_j}[\rho_s\alpha_s(V_i V_j+\beta_{ij})]=$$
$$=\rho_s\alpha_s g_i+F_i+\frac{\partial}{\partial x_j}(\alpha_s\sigma_{ij})+\frac{\partial}{\partial x_j}(s_{ij}) \qquad (2)$$

where β_{ij} denotes the components of the velocity cofluctuation tensor, gi stands for the components of the acceleration of gravity, and F_i accounts for the gas-solids interaction force. Two stress tensors acting within the particles appear in this equation: σ_{ij} accounts for the stresses linked by the fluid; while s_{ij} is the probabilistic mean of intermittent stresses due to interparticle and/or wall-particle collisions. The momentum equation for the fluid is

$$\frac{\partial}{\partial t}(\rho_f\alpha_f U_i)+\frac{\partial}{\partial x_j}[\rho_f\alpha_f(U_i U_j+B_{ij})]=$$
$$=\rho_f\alpha_f g_i-F_1-\frac{\partial}{\partial x_i}(\alpha_f p)+\frac{\partial}{\partial x_j}(\alpha_f\tau_{ij}) \qquad (3)$$

where U_i and B_{ij} denote, respectively, the components of gas velocity and the velocity cofluctuation tensor, p stands for the pressure, and τ_{ij} represents the components of viscous stresses acting within the fluid. In Equations (2) and (3), the LHS represents the inertial terms, while all the external forces acting on the phase are regrouped on the RHS.

An additional equation relates gas and solids presence probabilities:

$$\alpha_s+\alpha_f=1 \qquad (4)$$

These equations cannot be solved in general, since there is an obvious closure problem associated with them.

2.2. Fully developed vertical upflow of a suspension

When a single-phase fluid flows at a constant rate in a straight pipe, the longitudinal pressure profile becomes linear beyond a certain distance downstream from the entrance; this situation corresponds to the establishment of flow patterns which are identical in each cross-section of the pipe, and is called *fully developed flow*. As reported by numerous authors[e.g. references 15,13,8 and 3] a similar situation is observed for suspension flows under similar conditions.

A rigorous definition based on the probabilistic Eulerian description has been given[9] for the fully developed flow of a gas-solids suspension. It follows from this definition that variables such α_s, α_f, V_i, U_i, β_{ij} and B_{ij} are independent of the axial coordinate (denoted x) throughout the fully developed flow region. Subsequently, the stress tensors s_{ij} and τ_{ij} are also x-independent. In addition, if the suspension flows vertically in a pipe of *circular cross-section*, the radial velocity components V_r and U_r identically vanish in the fully developed flow region. Finally, in the absence of initial swirl, tangential velocity components V_θ and U_θ are identically zero throughout the flow.

The main general property of a fully developed suspension flow is that the longitudinal pressure gradient is independent of axial as well as transversal coordinates. This is a convenient property allowing an easy experimental identification of fully developed flow regions. Moreover, it has been shown[9] that:

$$-\frac{\partial p}{\partial x}=\frac{\partial}{\partial x}(\sigma_{xx})=\text{const.} \qquad (5)$$

Under fully developed flow conditions, Equations (2) and (3) simplify considerably. Adding through the axial projections of these momentum equations of both phases, combining with Equations (4) and (5), and integrating over a cross-section yields the following equation expressing the pressure gradient in a circular pipe (the vertical axis Ox is directed upwards):

$$-\frac{\partial p}{\partial x}=-\frac{2}{R}(\tau_{rx})_w+[\rho_s c+\rho_f(1-c)]g-\frac{2}{R}(s_{rx})_w \qquad (6)$$

where R denotes the pipe radius and subscript w indicates that shearing stresses are evaluated at the wall; c is the cross-sectional average of α_s defined by:

$$c=\frac{1}{\pi R^2}\int_0^R 2\pi r\alpha_s dr \qquad (7)$$

c is therefore identified to the average volumetric concentration of particles over a cross-section.

Equation (6) confirms a result suggested by Hariu and Molstad[4], according to which the pressure drop in a fully developed suspension flow is the sum of three contributions: the first term accounts for the wall friction of the gas, the second term represents the average weight of suspension per unit volume, while the third term corresponds to the contribution of wall-particle interactions.

The general conceptual framework of our probabilistic Eulerian description allows a partial modelling of the third term. As noted above, the s_{ij} tensor, the shearing component of which appears in Equation (6), is due to interparticle and wall-particle collisions. As the term is evaluated at the wall where particle presence is reduced to points[10], the third term in Equation (6) is only due to wall-particle collisions. When an individual particle experiences a collision with the wall its loss of axial momentum is proportional to its actual axial momentum[9,14], provided that the restitution coefficients applied to the normal and tangential velocity components remain constant. (This latter assumption has at least a statistical validity.) On the other hand, the collision frequency of a class of particles over a unit surface of wall is proportional to the local phase presence probability of the species. On the average, the wall shear stress due to wall-particle collisions can, therefore, be written in the form:

$$(s_{rx})_w=-K(\rho_s\alpha_s V_x)_{vw} \qquad (8)$$

where the vw subscript means that the quantity is evaluated at the vicinity of the wall. The dimensional coefficient K depends upon the statistical distribution of transverse particle velocities in the wall region and is also a function of the thickness of the wall region from which, under the effect of their random radial velocities, the particles fly in the transverse direction to reach the wall and collide with it. According to Equation (8), the third term in Equation (6) is proportional to the mass flux of particles in the wall layer. It therefore allows a possible explanation for the "negative drag" problem: this effect could be due to a downflow of solids along the wall. Indeed, in this case, $(s_{rx})_w$ becomes negative. The occurrence of this phenomena will be clearly illustrated by the experimental results presented below.

2.3. Similar profiles regime

If the flowrate of solids injected into the gas stream is progressively decreased to zero while the gas rate (or gas superficial velocity U) is maintained constant, the suspension flow tends toward a single-phase flow. This has been called *reference flow*[9], since most of the authors compared their experimental results (pressure drop, gas velocity profiles, heat transfer coefficient, etc.) obtained with the suspension to those obtained with the gas alone flowing in the same installation with the same superficial velocity. When obtained as described above, the reference flow is, therefore, the limiting case of a suspension in which solids concentration vanishes throughout the pipe. Consequently, fluid phase variables in the suspension such as U_i, B_{ij}, τ_{ij}.... should tend toward their values (noted with a 0 superscript) U_i^0, B^0_{ji}, τ^0_{ji} in the reference flow as $c \to 0$, while all the terms in the solids phase equations tend toward zero. In addition, when c decreases to zero, $\alpha_s \to 0$ throughout the pipe according to Equation (7), subsequently, $\alpha_f \to 1$ according to Equation (4). A reference flow variable such as e.g. U_i^0, is thus the limiting value of both U_i and α_f U_i as $c \to 0$. By denoting ψ_f as any one of the fluid phase variables and ψ_f^0 its limiting value, the following MacLaurin series development can, therefore, be used:

$$\alpha_f \psi_f = \psi_f^0 + c\psi_f^1 + O(c^2)$$

In this equation, c ψ_f^1 is the first order term and $O(c^2)$ represents the second and higher order terms of the power series development in terms of the average concentration c.

When MacLaurin series developments analogous to (9) are substituted for the fluid phase variables appearing in the axial momentum equation of the fluid in the suspension, zeroth order terms (reference flow variables) drop and one obtains an equation relating first and higher order terms[9]. Neglecting $O(c^2)$ as $c \to 0$, a linear equation in terms of α_s and c is obtained. It therefore follows from this latter equation that $\alpha_s(r)$ is proportional to c throughout the cross-section of the pipe. An analogous approach is also applied to the solids momentum equation. (The details of the calculations can be found in references 9 and 11.) Finally, the following forms of solids concentration and velocity profiles appear as possible solutions to the equations of a fully developed suspension flow as $c \to 0$.

$$\alpha_s(r;c;U) = cf(r;U) \tag{10}$$

$$V_x(r;c;U) = V_x(r;U) \tag{11}$$

Equations (10) and (11) define a particular flow structure called *similar profiles regime*. Indeed, it can easily be seen that at a constant gas superficial velocity, solids velocity $V_x(r)$ and reduced concentration $\alpha_s(r)/c$ profiles remain unchanged as the solids rate or average concentration is increased. This flow regime is expected to occur as $c \to 0$, i.e. under dilute-phase flow conditions. In other words, similar profiles could be the *characteristic flow structure of dilute suspension flows*.

Because of the closure problem evoked above, it is not possible at the present stage of our knowledge to completely solve the general equations of the gas-solids system even under fully developed flow conditions. The *uniqueness* of these asymptotic solutions cannot, therefore, be shown, nor is it possible to determine explicit expressions of the functions f(r;U) and $V_x(r;U)$ which remain *unknowns*. These two tasks should therefore be performed experimentally. As they indeed are, among the objectives of the experimental work presented below. Finally, neither the upper limit of applicability of the similar solutions, nor the properties of the flow structure in the denser regime which would succeed to the similar profiles cannot - for the moment - be derived from the theory summarized above.

The possible existence of similar solutions allows the derivation of an explicit expression directly comparable to experimental measurements for the pressure drop. The first term in the RHS of Equation[6] which accounts for the wall friction of the gas *in the suspension flow* cannot be directly measured. However, an asymptotic expression of this term can be obtained in the similar profiles regime using for $\alpha_f \tau_{rx}$ a MacLaurin series development of the form defined by Equation (9):

$$\alpha_f \tau_{rx} = \tau^0_{rx} + c\tau^1_{rx} + O(c^2) \qquad (12)$$

Substituting for this expression evaluated at the wall in Equation (6) combined with Equation (8), subtracting the pressure gradient of the reference flow, and finally, neglecting the second order term $O(c^2)$ leads to the following equation defining the "additional pressure drop" (i.e. the change in pressure drop due to the solids) for a fully developed vertical upflow of a gas-solids suspension

$$-\frac{\partial p^1}{\partial x} = -\frac{\partial p}{\partial x} + \frac{\partial p^0}{\partial x} =$$

$$= c[-\frac{2}{R}(\tau^1_{rx})_w + (\rho_s - \rho_f)g] + \frac{2K}{R}(\rho_s \alpha_s V_x)_{vw} \qquad (13)$$

It should be noted that in the similar profiles regime, according to Equations (10) and (11), the last term in the RHS of Equation (13) is also proportional to c. Consequently, the additional pressure drop will be, at a constant gas superficial velocity, strictly proportional to the average solids concentration c.

Another relationship which can be deduced from the similar profiles is the one between the solids rate W_s and the average concentration:

$$W_s = \int_0^R 2\pi r \rho_s \alpha_s V_x dr =$$

$$= \rho_s c \int_0^R 2\pi r f(r;U) V_x(r;U) dr \qquad (14)$$

Therefore, in the similar profiles regime, the solids mass flowrate W_s is also strictly proportional to the average concentration c at a constant superficial gas velocity U. As a consequence, the average solids velocity V defined by:

$$V = \frac{W_s}{\rho_s c \pi R^2} \qquad (15)$$

depends only on U for a given gas-solids system flowing in a given pipe. Moreover, a local slip — or relative — velocity can be defined for the solids:

$$V_{rel}(r) = U_x(r) - V_x(r) \qquad (16)$$

By combining Equations (4), (7), (10), (11) and (15) together with a MacLaurin series development for U_x, and by applying the asymptotic simplifications according to which c^n is negligible compared to c^{n-1}, the following expression can be found for the average solids velocity

$$\pi R^2 V = \int_0^R 2\pi r f(r) U^0_x(r) - \int_0^R 2\pi r f(r) V_{rel}(r) dr \qquad (17)$$

When — in an experimental installation — W_s and c are simultaneously and independently measured, it is possible to find the relationship between V and U for the gas-solids system under consideration flowing in that particular pipe. The analysis of this relationship with the help of Equation (17) can yield some qualitative information about the reduced concentration profile f(r;U). Indeed, since the velocity field of the reference flow $U^0_x(r)$ is that of a - generally turbulent - single-phase flow, it is essentially proportional to U. Therefore,

(a) if f(r) is independent of U (or only slightly dependent on U within a limited range), the first integral in the RHS of Equation (17) can be written as $\pi R^2 C_0 U$ where C_0 is a dimensionless constant. Moreover,

(b) if the concentration profile is essentially uniform throughout the cross-section, in other words, if $f(r) \equiv 1$, the constant C_0 will take on the value of 1. On the other hand, if condition (a) is satisfied and, in addition,

(c) if Vrel(r) is also independent of the superficial gas velocity, the second integral in the RHS of Equation (17) can be written as $\pi R^2 C_1$, where C_1 is a constant equivalent to a velocity. Finally, if condition (b) holds and if, in addition,

(d) $V_{rel}(r)$ is uniform over the cross-section and equal e.g. to the average terminal velocity Vt of the particles, one would have $C_1 = V_t$.

It should be noted, however, that *none of the conditions (a) to (d) listed above are rigorously necessary conditions*, and that conclusions deduced from particular values taken on by C_0 and C_1 cannot therefore be considered as unquestionably evidenced. Nevertheless, the above argument gives an interesting sketch for interpretation since *it allows the deduction of* *presumably valid properties, especially concerning the solids concentration profiles, from overall measurements.*

2.4. Thermally fully developed flow

For the analysis of heat transfer in gas-solids suspensions, specific energy equations are derived for each phase using the probabilistic Eulerian description of multiphase mixtures[9]. When radiation is negligible and temperature differences in the installation moderate, the energy equation of the solids phase takes the following form

$$\frac{\partial}{\partial t}(\rho_s C_s \alpha_s T_s) + \frac{\partial}{\partial x_i}[\rho_s C_s \alpha_s (T_s V_i + \varepsilon_i^s)] =$$
$$= \frac{\partial}{\partial x_i}[\lambda_s \frac{\partial}{\partial x_i}(\alpha_s T_s) - \lambda_s T_I \frac{\partial \alpha_s}{\partial x_i}] + Q_{fs} \qquad (18)$$

where T_s stands for the local solids temperature, C_s for the specific heat capacity of the particles, and λ_s for the thermal conductivity of the particles; ε_i^s denotes the components of the temperature-velocity cofluctuation vector, and T_I represents the "interfacial mean temperature"[9,10] which expresses in fact, the continuity of immediate Eulerian temperature fields at the interface. Finally, Q_{fs} accounts for the heat transferred from the fluid to the solids per unit time and unit volume of suspension. An analogous equation is derived for the fluid:

$$\frac{\partial}{\partial t}(\rho_f C_f \alpha_f T_f) + \frac{\partial}{\partial x_i}[\rho_f C_f \alpha_f (T_f U_i + \varepsilon_i^f)] =$$
$$= \frac{\partial}{\partial x_i}[\lambda_f \frac{\partial}{\partial x_i}(\alpha_f T_f) - \lambda_f T_I \frac{\partial \alpha_f}{\partial x_i}] - Q_{fs} \qquad (19)$$

Equations (18) and (19) illustrate the great complexity of heat transfer mechanisms in a gas-solids suspension. Apart from the well known convective transport (first term within square brackets in the LHS), diffusional transport (second term) due to the random motion of the phases combines with transfer by conduction through the phases (first term within square brackets in the RHS). Besides this, the two equations are coupled through two variables T_I and Q_{fs} which account respectively for temperature and heat flux jump conditions at the interface.

A *thermally fully developed flow* can be defined in the case of the rectilinear pipe flow of a suspension, provided that the two following conditions are simultaneously satisfied[9,12]:

(i) the suspension flow is dynamically fully developed;

(ii) the heat flux provided to the suspension by the wall φ_w is uniform throughout the wall.

As a consequence, the radial temperature profiles of either the solids, the fluid or the interface are independent of the axial coordinate x and the axial gradients of both T_s, T_f and T_I are identical and equal to the gradient of the wall temperature $T_w(x)$. Finally, the latter is related to φ_w through the heat balance equation :

$$2\pi R \varphi_w = (W_s C_s + W_f C_f)\frac{dT_w}{dx} \qquad (20)$$

A "mixed mean temperature" can be defined either for the gas, the solids or the mixture. The latter is generally used when representing heat transfer to gas-solids suspensions[15]. The difference between local wall temperature and the mixture's mixed mean temperature T_{mM} is defined by the following equation

$$(W_s C_s + W_f C_f)(T_w - T_{mM}) =$$
$$= \int_0^R 2\pi r[\rho_s C_s \alpha_s (T_w - T_s) + \rho_f C_f \alpha_f (T_w - T_f)]dr \quad (21)$$

The temperature difference $\Delta T_m^{'} = (T_w - T_{mM})$ is used as the reference temperature difference for the definition of a heat transfer coefficient for the gas-solids mixture :

$$h_m = \frac{\varphi_w}{\Delta T_m} \qquad (22)$$

2.5. Similar profiles regime and wall-to-suspension heat transfer coefficient

An analysis of the asymptotic behaviour of the temperature fields in the suspension analogous to that presented in § 2.3 can be achieved in the range of the similar profiles regime. In order to match the requirements of limiting values reached continuously, the temperature field of the reference flow must be defined as that of the reference flow heated under the same thermal boundary conditions as the suspension, i.e. the same inlet temperature and *the same wall heat flux* φ_w. The heat transfer coefficient h_0 of the reference flow is then defined as :

$$h_0 = \frac{\varphi_w}{\Delta T_f^0} \qquad (23)$$

where the reference temperature difference $\Delta T_f^0 = [T_w^0(x) - T_{fM}^0(x)]$ is defined by the limiting form of Equation (21) as $c \to 0$.

Denoting $\theta_p(r) = T_w(x) - T_p(x,r)$, the radial temperature profiles for either the fluid (p=f), the solids (p=s) or the interface (p=I), the following asymptotic forms are obtained as $c \to 0$. (The details of the mathematical argument can be found in references 9, 15 and 12.)

$$\alpha_f \theta_f = \theta_f^0(r;U) + \frac{c\theta_f^1(r;U)}{1+\Gamma} + O(c^2) \qquad (24)$$

$$\alpha_s \theta_s = \frac{c\theta_f^1(r;U)}{1+\Gamma} + O(c^2) \qquad (25)$$

$$\theta_I = \frac{\theta_I^0(r;U)}{1+\Gamma} + O(c^2) \qquad (26)$$

where Γ is defined by the ratio:

$$\Gamma = \frac{W_s C_s}{W_f C_f} \qquad (27)$$

It is noteworthy that the asymptotic form of $\alpha_f \theta_f$ differs from that predicted by Equation (9) for hydrodynamic variables by a factor $(1+\Gamma)$. In fact, this scaling factor appears in Equations (24) to (26) because the heat capacity per unit volume of the flow increases by a factor $(1+\Gamma)$ when the solids are loaded into the gas stream.

The self-similar temperature profiles defined by Equations (24) and (25) can be used together with Equations (21) to (23) to calculate the variation of the heat transfer coefficient with solids loading. One obtains the following form

$$\frac{h_m}{h_0} = \frac{(1+\Gamma)^2}{1+a\Gamma+b\Gamma^2} \qquad (28)$$

where a and b are compound shape factors combining cross-sectional integrals of the reduced concentration, velocity and temperatures profiles of the phases as characterizing the similar profiles. As a consequence, for a given gas-solids system flowing in a given pipe, a and b are functions of only one variable: the superficial gas velocity U which determines the hydrodynamics of the suspension flow.

Dependent upon the values taken on by a and b, six different trends of variation of hm with the solids loading ratio W_s/W_f can be predicted[12]. At least three of them have already been observed by previous authors. In other words, Equation (28) predicts all the apparently contradictory trends of variation summarized by Maeda et al.[5], and which were not yet explained.

3. Experimental

3.1. Experimental installations

Experiments have been carried out on two different installations. Both contain a vertical column with an overall height exceeding 10 m. The first installation is a pneumatic transport line which has a small diameter (20 mm ID) in order to enhance wall effects such as they can be accurately measured and compared to the predictions of Equation (13). It is equipped with complete instrumentation for gas and solids flowrates, axial pressure gradient and average solids concentration measurements. Besides this, the test section can be replaced by a heating section in order to permit measurement of heat transfer coefficients. The second installation is a circulating fluidized bed column of 144 mm ID equipped with a non-isokinetic sampling probe which allows determination of radial particle mass flux profiles in the fully developed flow section.

In the pneumatic transport installation **Fig. 1**, the solids are injected into the gas stream by means of a fluidized bed feeder. The base of the transport line enters the bed and is submerged in the fluidized solids. Small holes drilled around the circumference of the submerged section allow the solids to flow from the bed into the line at a rate finely controlled by varying either the pressure above the bed or the bed height. At the outlet of the line, the suspension flows through a disengaging chamber where most of particles are recovered, followed by a cyclone for final cleaning. Recovered solids are recycled into the fluidized bed feeder by means of a standpipe. Gas flowrate is measured by a rotameter placed at the outlet of the cyclone, while the solids flowrate is determined by collecting the recycled solids over measured time intervals. The stainless steel transport line is divided into 3 sections: a 4.5 m acceleration zone, a 4.2 m test section, and a 2.5 m disengaging area. Two pneumatically activated slide valves are placed at the top and bottom of the test section. The simultaneous closing of these valves allows the mean solids concentration in

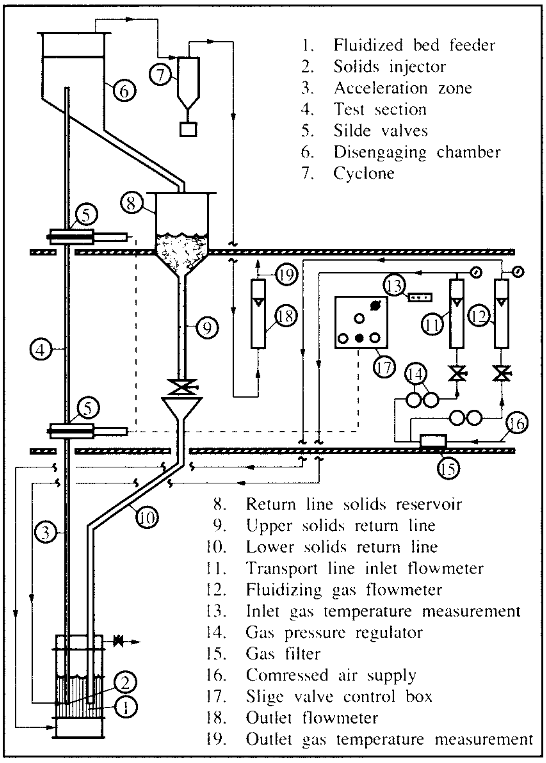

Fig. 1 Pneumatic transport installation (20 mm ID).

the test section to be measured. Finally, 21 wall pressure taps connected to water manometers allow accurate determination of the axial distribution of pressure along the transport line.

For heat transfer measurements, a heating section consisting of a thin-walled (0.5 mm), 20 mm ID stainless steel pipe specially drawn to ensure even wall thickness was inserted between the slide valves. Copper flanges are silver-soldered at each end of the pipe and the pipe is heated by applying a DC supply between the flanges. Heat input into the system is determined by measuring the voltage across the pipe and the current in the circuit. Wall surface temperatures are measured using platinium resistance thermometers placed at intervals of 250 mm along the pipe length. The heat transfer section is insulated with fiber-glass insulation to minimize radial losses. Axial losses by conduction along the wall pipe are minimized by the low thickness of the pipe wall. Overall, the losses are less than 10% of the heat input, and the system supplies an essentially uniform heat flux to the suspension. Additional details concerning the installation and operating procedure can be found in Muzyka15).

The second installation **Fig. 2**, is a circulating fluidized bed consisting of a riser column, a particle collection system and a solids return line. The 0.144 m ID plexiglass riser is equipped with 16 wall pressure taps connected to water manometers. The particle collection system combines in series a disengaging chamber, two cyclone stages, and a bag filter for final cleaning when fine particles are used. The particles collected by the disengaging chamber and the cyclones flow by gravity into a weighing hopper standing on three force transducers, and then into the buffer hopper through a pneumatically closing valve. The latter feeds by gravity a nonmechanical L-valve system by means of which the solids are re-injected into the riser, at the throat of a Venturi nozzle. The circulating solids rate is finely controlled by the aeration rate supplied at the elbow of the L-valve. This solids rate is determined by closing the outlet

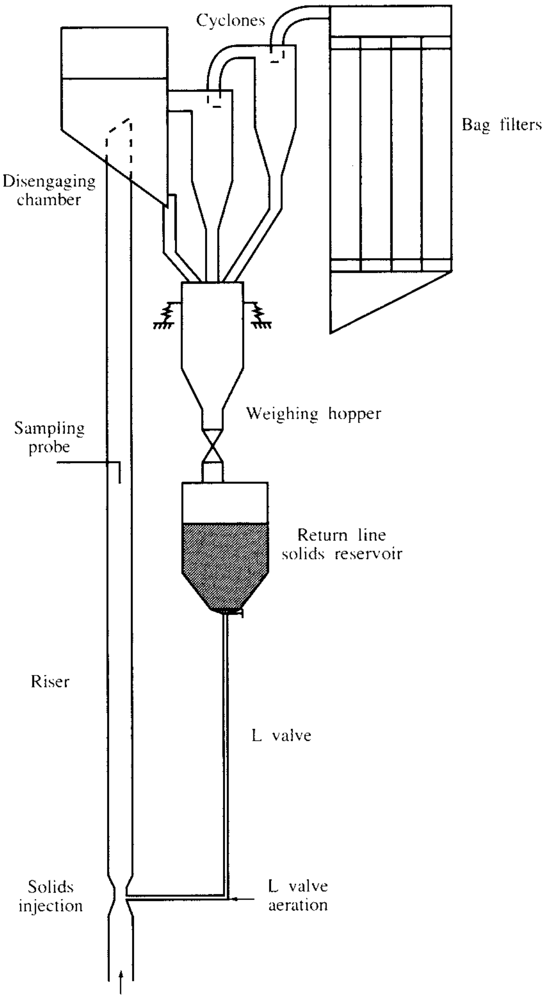

Fig. 2 Schematic diagram of the circulating fluidized bed installation (144 mm ID).

pneumatic valve of the weighing hopper and monitoring the increase in weight indicated by the force transducers over time intervals of about one minute. The carrying gas rate is measured by means of an orifice plate located upstream from the Venturi nozzle. L-valve aeration rate is determined by a rotameter. Additional details can be found in Monceaux[13].

Particle mass flux profiles are determined by means of a non-isokinetic sampling probe developed by Azzi[1], and shown schematically in **Fig. 3**. It consists of a steel tube (4 mm ID ; 6 mm OD) bent at 90° and connected to a suction circuit which has two identical branches in parallel, each equipped with a particle collecting box, and both connected to the same vacuum pump. The pump is operated continuously in order to allow steady state sampling conditions and the indrawn suspension flows either through the first branch of the circuit or is diverted toward the second branch over measured time intervals for particle mass flux measurements. The axis of the tapered nose of the probe is maintained vertical, and can be turned by 180° in order to collect the downflowing particle flux especially in the wall region. The probe is located at 4 m above the solids injection section, and sampling is therefore always performed in the fully developed flow region. The radial position of the probe tip can be varied at will in order to scan a diameter of the column for determining the radial profile of particle mass fluxes. The technique is called "non-isokinetic" sampling, since Azzi showed that measured particle fluxes remain essentially constant when suction velocity is varied within a range of at least xxx 1.5 m/s around the superficial gas velocity in the riser.

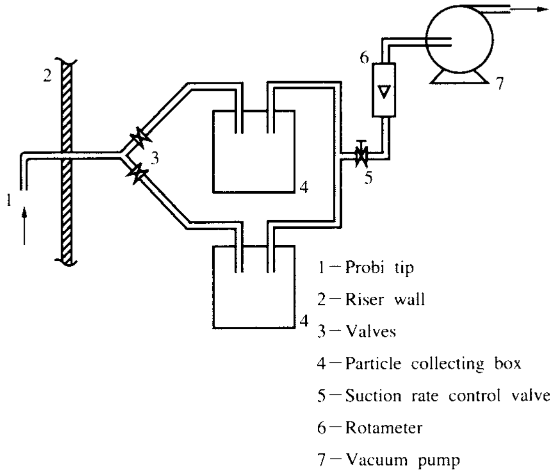

Fig. 3 Schematic diagram of the non-isokinetic sampling system.

3.2. Hydrodynamics of dilute-phase flow

The overall hydrodynamic properties of dilute suspension flows have been studied using both installations. In all cases[15,13,8,3], a fully developed flow region with its characteristic linear-axial pressure profile has been found at distances downstream from the solids feed section which do not exceed 3 m.

Pressure drop

Muzyka[15], investigated the relationship between pressure drop and average solids concentration under fully developed flow conditions for three different solids. A typical set of data obtained in these experiments carried out in the 20 mm pneumatic transport installation is shown in **Fig. 4**, where axial pressure gradients (at three different gas velocities) are plotted against correponding average solids concentrations of sand particles ($\rho_s = 2630$ kg/m^3) with a Sauter mean diameter of 172 μm. As predicted by Equation (13), at constant superficial gas velocity straight lines are obtained, the intercepts of which are equal to the pressure drops of their respective reference flows (i.e. the flow of the gas alone with the same superficial velocity U). The linear trend of variation of the "additional" pressure drop with average solids concentration c seen in **Fig. 4** suggests that the

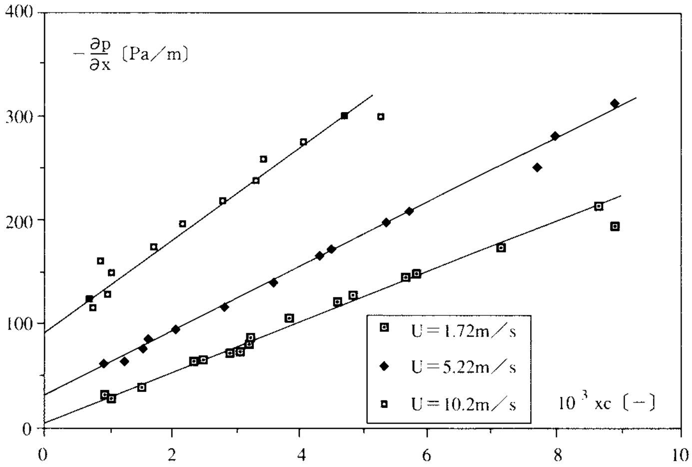

Fig. 4 Pressure drop as a function of average solids concentration at different superficial gas velocities for 172 μm sand particles, as per Muzyka [15] .

similar profiles regime assumption is valid since, in this case, the last term in Equation (13) becomes also proportional to c as predicted by Equations (10) and (11).

The trend of variation of the slopes of the straight lines with U is shown in **Fig. 5** for the same particles. As can be seen, the slope of the lines increases with U but is lower than $(\rho_s - \rho_f)g$ at low superficial gas velocity (approx. $U < 2.3$ m/s). This illustrates the so-called negative drag effect. According to Equation (13), it should be attributed to either gas or particle wall friction terms. If the observed negative drag was due predominantly to the change in the viscous shear stress at the wall, to match the data obtained e.g. for $U = 1.72$ m/s, $(\tau^1_{rx})_w$ should amount as high as about -350 times $(\tau^0_{rx})_w$, or in other words, for an average solids concentration of $c = 0.01$, the actual gas velocity in the wall region should be equal to about -2.5 times its value in the reference flow. Obviously, such a situation is highly unlikely. Therefore, it should be considered that the negative drag as well as the difference between the slope of the additional pressure drop curve and $(\rho_s - \rho_f)g$ is predominantly due to the last term in Equation (13). Moreover, particle mass flux profiles reported by Azzi which will be discussed below confirm this interpretation. Indeed, particle fluxes measured near the wall increase with U and negative fluxes exist at low gas superficial velocity. Therefore, these observations confirm that Equation (13) is a sound basis for the interpretation of the pressure drop of dilute vertical gas-solids suspensions under fully developed flow conditions.

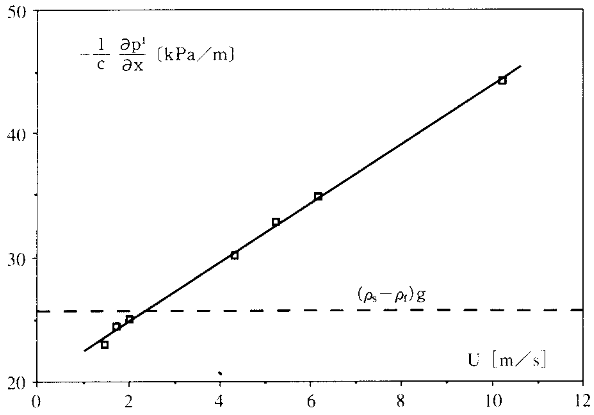

Fig. 5 Variation of the slopes of additional pressure drop curves with superficial gas velocity for 172 μm sand particles, as per Muzyka [15] ; the dashed line represents the gravity term.

Most of the authors dealing with vertical gas-solids have more or less intuitively considered that in large diameter risers, the unit pressure drop divided by $(\rho_s - \rho_f)g$ is approximately equal to the average solids concentration c. The validity of this approximation can be analysed on the basis of Equation (13). Indeed, the contribution of gas wall-shear stress to pressure drop decreases as 1/R and can be considered as negligible compared to solids hold-up in large diameter columns. Moreover, Equation (13) similarly suggests that the contribution of the third term (wall - particle interaction) will also become negligible as pipe radius is increased. This latter argument, however, considers implicitly that the compound $K(\rho_s \alpha_s V_x)_w / c$ retains its order of magnitude at a given gas velocity in large and small diameter risers. This requires, e.g., that the dimensionless profiles defined by Equations (10) and (11), re-written as functions of the reduced radial distance r/R, become independent of pipe radius. To our knowledge, such a property has not yet been reported based on experimental evidence. Besides, if Muzyka's data are considered for scaling-up calculations, it should be recalled that the solids velocity profiles, and especially the values taken on by V_x at the wall for a given gas-solids system, depend also on the geometrical (roughness) and physical properties of the wall[11], since wall-particle collisions define a boundary condition for V_x at the wall.

Muzyka's findings have been confirmed by the experimental results of Mok[8] and Bentahar[3]. The conclusions of the above discussion can, therefore, be generalized and summarized as follows. The pressure drop of a vertical, dilute phase, fully developed flow of a gas-solids suspension is the sum of three contributions: gas wall friction, gravity, wall-particle interactions. The first term is essentially equal to the pressure drop of the gas alone flowing in the same pipe with the same superficial velocity (reference flow); the gravity term accounts for the average apparent weight of the particles per unit volume of pipe; and wall-particle interactions are proportional to the axial solids mass flux in the wall layer. As a result, the "additional" pressure drop is proportional to average solids concentration at constant gas superficial velocity. The difference between additional pressure drop and solids hold-up is essentially due to the wall-particle interaction term from which "negative drag" results when a downflow of solids exists in the wall layer.

Similar profiles

As noted in § 2.3, similar profiles defined by Equations (10) and (11) are possible asymptotic solutions to general equations. The effective existence of a similar profiles regime under dilute-phase fully developed flow conditions has been experimentally shown by Azzi[1]. His experiments were carried out using cracking catalyst particles ($\rho_s = 900$ kg/m^3) with a Sauter mean diameter of 60μm in the circulating fluidized bed installation. The radial profiles of net axial particle mass fluxes were determined using the non-isokinetic sampling probe described above. (The net flux is the difference between upflowing and downflowing fluxes.) A typical set of data obtained by varying solids concentration at three different levels of superficial gas velocity is plotted in **Fig. 6** in dimensionless form. As can be clearly seen from **Fig. 6**, the radial profiles of particle mass fluxes divided by their cross-sectional averages are independent of solids loading at a constant gas velocity. This is, therefore, in complete agreement with the predictions of Equations (10) and (11).

These similar mass flux profiles deform when gas velocity is increased. A downward directed net particle flow in the wall region is clearly observed at low gas velocity as evoked above in the negative-drag discussion. Moreover, particle fluxes in the vicinity of the wall increase as superficial gas velocity increases. Finally, it should be noted that with the gas-solids system under consideration, similar profiles exist up to volumetric solids concentrations as high as 0.04 or slightly more. This observation gives a first indication of the range of applicability of asymptotic similar solutions and suggests that several industrial installations are operated in the similar profiles regime. All dimensionless similar mass flux profiles determined in this case intersect at a radial distance corresponding approximately to 50% of the cross-sectional area of the riser. Besides this, Azzi attempted to correlate his results within a unique equation. He found that a correlation of the form:

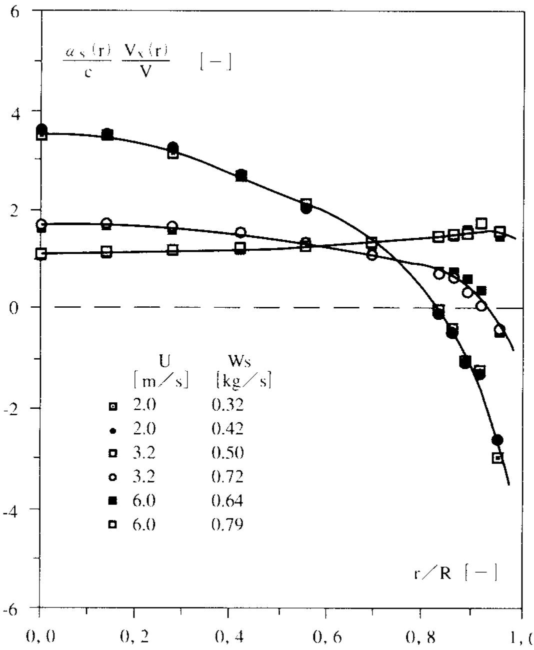

Fig. 6 Reduced solids mass flux profiles for 60 μm cracking catalyst particles, as per Azzi [1].

$$\frac{\alpha_s V_x}{cV} = B(r) - \frac{A(r)}{U} \tag{29}$$

accounts very well for the effect of gas velocity in the range 2m/s < U < 6m/s. A(r) and B(r) are quadratic functions of radial distance r; but he failed in finding a unique expression valid throughout the cross-section for each of these functions. In fact, on each side of the intersection point, the numerical coefficients of these functions assume essentially different values. However, the ratio A(r)/B(r) can be considered in all these cases as being essentially constant and equal to 4.3 m/s. This observation suggests that for this particular value of the superficial gas velocity, the mass flux profiles are essentially uniform over a cross-section. Indeed, it can be seen from his detailed results[1], that the concavity of radial mass flux profiles changes when increasing superficial velocities pass through this value of 4.3 m/s.

Average solids velocity and in-line particle size distribution

Analysing the trend of variation of the solids rate W_s and average particle concentration c, Muzyka[15] found — at constant superficial gas velocity — a strict proportionality between these two measured variables as predicted by Equation (14). Later experiments by Mok[8] and

Bentahar[3] confirmed this observation in dilute-phase flow.

Equation (14), which derives from the similar profiles hypothesis, proves therefore to be in excellent agreement with all experimental data obtained in this program. Besides this, the properties of suspension pressure drop discussed above have been found to be in agreement with the predictions of Equation (13) which also derives from the similar profiles. Finally, the particle flow structure determined by Azzi corresponds exactly to the pattern predicted by Equations (10) and (11). These complementary observations have been made in two different installations using three different solids: 63 μm glass beads, 60 μm cracking catalyst, and coarser sand, the latter with four different particle size distributions. *It can, therefore, be reasonably concluded that the characteristic flow structure of vertical gas-solids suspensions, under fully developed dilute-phase flow conditions, is that of the similar profiles regime.*

Several particular properties of mass flux profiles have been deduced from Azzi's experiments. Some of these properties are in agreement with the observations deduced from the analysis of pressure drop data. Additional indications can be found in average solids velocity results.

Indeed, from the plots of W_s vs c, the average solids velocity V at a constant superficial gas velocity U can be deduced. The trend of variation of V is plotted in **Fig. 7** as a function of U as per Muzyka[15] ; the data were obtained with two different size distributions of sand. As can be seen, the relationship can be written in the form :

$$V = C_0 U - C_1 \qquad (30)$$

where C_0 and C_1 are constants independent of gas velocity. The same form of functional dependence of V on U has been found for glass beads[15], as well as for other particle size distributions of sand by Mok[8] and Bentahar[3]. Moreover, Monceaux[18], found also constant coefficients C_0 and C_1 for cracking catalyst particles in the circulating fluidized bed installation. It should be noted, however, that in this latter case, c was not measured directly but deduced from additional pressure drop measurements acoording to the assumptions discussed above at the end of the pressure drop section.

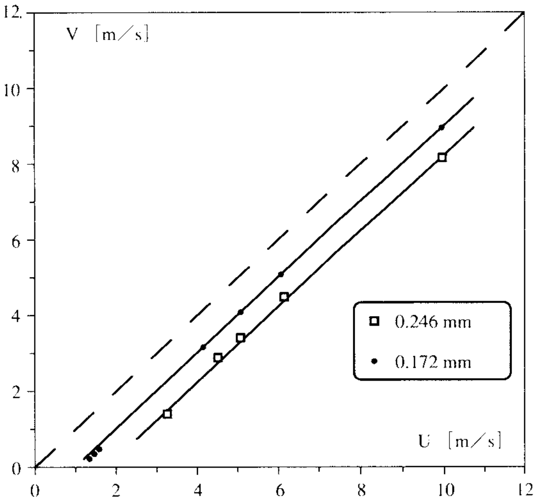

Fig. 7 Variation of average solids velocity with superficial gas velocity for sand with two different particle size distributions as per Muzyka [15] .

A constant C_0 found by all these authors suggests, according to the analysis based on assumption (a) developed in § 2.3, *that solids concentration profiles are essentially independent of U*, at least in the range of gas velocities investigated in these works (i.e., 2 m/s to 10 m/s). Moreover, in all experiments carried out on the pneumatic transport installation (20 mm ID), C_0 has been found equal to 1 as can be seen in **Fig. 7**. This particular value of C_0 therefore suggests that according to condition (b) in § 2.3, particle concentration profiles are also essentially uniform over a cross-section. For 60 μm cracking catalyst particles in the 144 mm ID circulating fluidized bed column, Monceaux found $C_0 = 0.617$. This value is too different from 1 for the difference to be attributable to systematic errors in the indirect determination of c. An essentially uniform radial profile of particle concentration does not seem to be considered as a possibly general property in similar profiles regime. Besides, it should be noted in this connection that $f(r) \equiv 1$ is mathematically impossible since α_s and its radial derivative should vanish at the wall[9,10]. Finally, C_1 has always been found very close to the average particle terminal velocity in the 20 mm ID line, while the value reported by Monceaux is an order of magnitude greater than the corresponding V_t. In any case, as noted in § 2.3, additional experimental information — if not experimental evidence — is required to generalize the properties pointed out in this paragraph.

Muzyka also examined the size distribution of the particles trapped between the slide valves (i. e. the hold-up). He showed that the Sauter mean diameter of these particles remainsconstant as solids loading is increased at a constant superficial gas velocity[15]. Average diameter decreases, however, with increasing U, suggesting a higher hold-up of the coarse fraction at low gas velocity. Specific behaviours of fines and coarse fractions have been particularly investigated by Mok[8], who found that the average slip velocity of each fraction was essentially equal to its terminal velocity in the similar profiles regime. Finally, Azzi did not find any significant difference in the particle size distributions of the solids mass flux samples obtained at different radial positions.

3.2. Transition to denser flow and regime diagram

The existence of a sharp transition from the similar profiles regime to a denser flow has been initially reported by Monceaux[13]. This transition has been pointed out in a plot of the additional pressure drop measured in the 144 mm ID circulating fluidized bed installation against the solids rate, at constant levels of gas superficial velocity as seen in **Fig.** 8. For low solids loading, additional pressure drop and W_s are strictly proportional as predicted in the similar profiles regime. When W_s is further increased, the trend of variation of the pressure drop exhibits a sudden change for a critical solids rate W_s^*. Beyond this value, the rate of change of the pressure drop with W_s is higher than in the similar profiles regime.

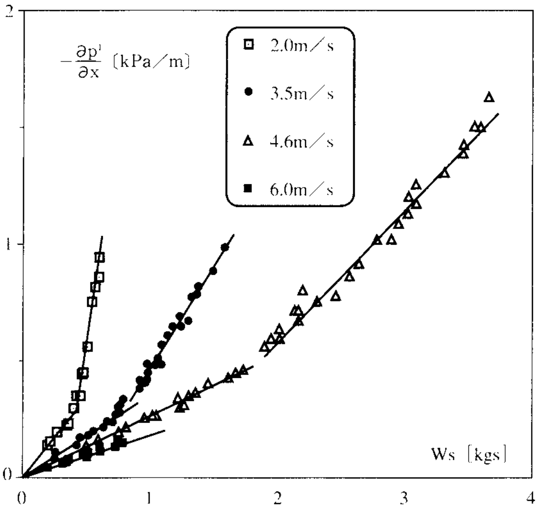

Fig. 8 Trend of variation of additional pressure drop with solids rate at different superficial gas velocities in dilute and dense-phase flow, as per Monceaux [13].

Azzi[1], determined particle mass flux profiles below and beyond this critical rate W_s^*. As can be seen in **Fig. 9** where a typical set of data is reported, particle mass flux profiles are no longer self-similar beyond W_s^*. The change in the slopes of the straight lines in **Fig.** 8 corresponds, therefore, to a change in the flow structure, i.e. to a regime transition. This transition occurs for critical solids rates increasing with the gas velocity as can be clearly seen in **Fig.** 8. The critical values c* of solids concentration can also be estimated from **Fig.** 8. In the case under consideration, they range between 4% and 5%, slightly depending upon gas velocity.

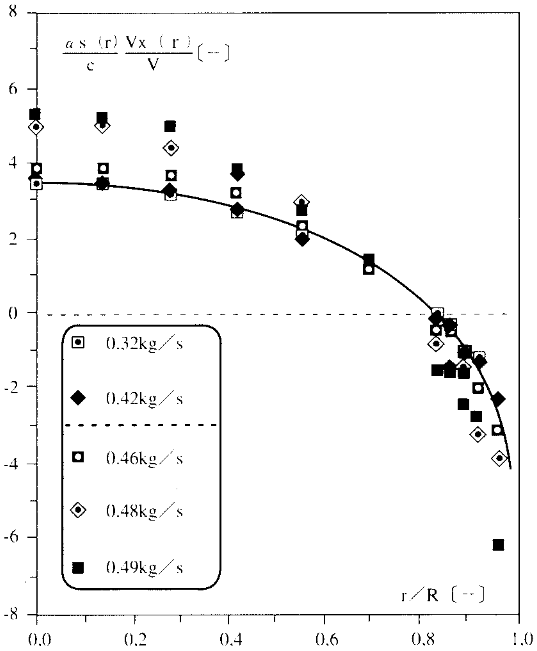

Fig. 9 Deformation of the reduced particle mass flux profiles in dense-phase flow with increasing solids loading at a superficial gas velocity of 2 m/s, as per Azzi [1]. (Solid line : similar profiles regime).

Mok[8], investigated the occurrence of a similar transition for sand particles in the 20 mm ID line. He found that transition can be seen either in additional pressure drop vs W_s, additional pressure drop vs c, or W_s vs c plots, in all cases with a sudden change in the linear relationship followed by a new linear trend of variation. These results have been confirmed by those of Bentahar[3], as can be seen in **Fig. 10** where the trend of variation of overall pressure drop with c at a constant superficial velocity of 4.10 m/s is shown for 0.2 mm average diameter sand particles. A sudden change in the slope occurs at a critical concentration $c^* \approx 0.01$. Beyond this point, the trend of variation remains essentially linear but the slope of the straight line is lower than its value for the similar profiles regime. Since at this level of concentration, the pressure drop of the gas alone is negligible compared to solids hold-up, the change in the slope should be attributed to the wall-particle interaction term according to Equation (6), which has a general applicability regardless of the flow structure. The experimental pressure drops in dense-phase flow are, then, consistent with the predictions of Equation (8), which derives from our wall-particle collisions model summarized in § 2.2. Indeed, Azzi found an essentially linear trend of variation with average concentration for the particle mass fluxes in the wall region beyond transition. Moreover, at low gas velocity, this trend of variation is a decrease as observed in **Fig. 10** analyzed in conjunction with Equations (6) and (8). At high gas velocities (e.g. 10 m/s), Mok found a greater slope in the denser regime than in dilute phase flow. This observation is also in agreement with the shape of particle flux profiles determined by Azzi. In other words, Equation (6) combined with Equation (8) remains valid beyond the transition to denser flow for the description of pressure drop variations.

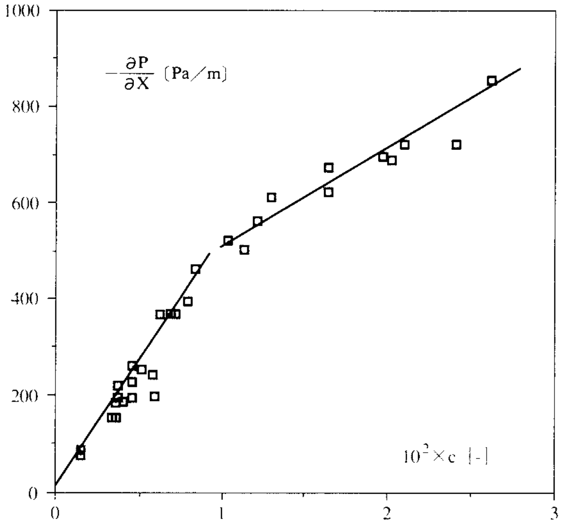

Fig. 10 Variation of suspension pressure drop with average concentration in dilute and dense-phase flow at a superficial gas velocity of 4.1 m/s, as per Bentahar [3]

This dense-phase flow, which occurs at a constant superficial gas velocity when the solids concentration (and/or solids rate) is increased beyond a critical value, is characterized by particle mass flux profiles which deform with increasing concentration. This deformation is at least due to that of particle velocity profiles (there is a lack of information concerning the behaviour of concentration profiles), since in Azzi's results, net particle fluxes which are positive at intermediate radial positions in the similar profiles regime become negative in denser flow conditions as can be seen in **Fig. 9**. As a result, average solids velocity V becomes a decreasing function of c[8,13]. Average slip velocities either for fines or coarse particles are, moreover, higher than their terminal velocities[8,6,7]. The numerical values of either solids rate or average concentration at which transition from the similar profiles regime to dense-phase flow occurs depend both on the gas-solids system, on pipe diameter, and presumably on the properties of the wall. A regime diagram such as the one shown in **Fig. 8** should therefore be considered as the characteristic diagram of a gas-solids system flowing in a given installation. Besides this, Mok and co-workers[8,6,7], reported a second transition occurring at solids volumetric concentrations of about 5% to 6% with air suspensions of 210 μm sand particles flowing in the 20μm ID pneumatic transport line.

3.3. Wall-to-suspension heat transfer

Wall-to-suspension heat transfer coefficients under thermally fully developed flow conditions have been measured by Muzyka in dilute-phase flow, and later by Bentahar[3] for dilute and dense-phase flow. Muzyka's heat transfer results are in excellent agreement with Equation (28). Moreover, previously published heat transfer data are also consistent with this equation. These observations therefore confirm that in the similar profiles regime, the trends of variation with solids concentration, of the local temperatures of the phases are described by

Equations (24) and (25). As a result, Equation (28) is a powerful tool for the analysis of heat transfer especially for circulating fluidized bed applications. It should be recalled, however, that for a-priori prediction purposes, coefficients a and b cannot yet be computed at the present stage of our knowledge. Muzyka[15], found that a and b depend only slightly on gas velocity in the range 4.6 m/s to 10.2 m/s.

Equation (28) has been also confirmed by Bentahar and coworkers[3,2], as can be seen in **Fig. 11** where the variations of the heat transfer coefficient are presented using a new variable Y defined as :

$$Y=\frac{1}{\Gamma}\left[\frac{(1+\Gamma)^2}{(h_m/h_0)}-1\right] \tag{31}$$

If the heat transfer coefficient ratio is governed by Equation (28), the plot of Y against Γ would result in a straight line, the intercept of which would be equal to a and the slope to b. As can be clearly seen in **Fig. 11**, this prediction is confirmed by experimental results. Moreover, a sudden change in the slope of the straight line which occurs for a critical value Γ* is observed in this figure. Beyond this limit a new linear relationship is manifest. For all different superficial gas velocities investigated in her work, Bentahar found an excellent correspondence between Γ* and the critical value of the solids rate W_s* at which transition from the similar profiles regime to denser flow occurs. The change in the slope of the straight line in **Fig. 11** corresponds, therefore, to the effect of flow structure change on heat transfer.

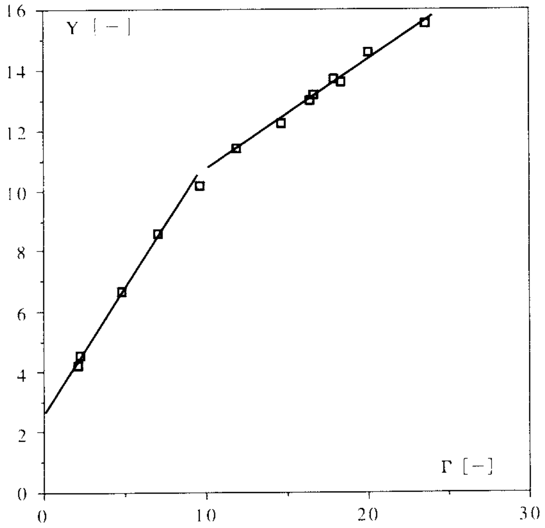

Fig. 11 Variation of wall-to-suspension heat tranrfer characteristics with solids loading in dilute and dense-phase flow at a superficial gas velocity of 7.7 m/s, as par Bentahar [3]

Surprisingly enough, the trend of variation of Y with Γ remains linear beyond transition in all cases. In other words, Equation (28) remains valid in dense-phase flow since a and b assume again, beyond transition, constant numerical values which are different, however, from their respective values in the similar profiles regime. This observation suggests that in dense-phase flow at least some of the reduced concentration, velocity and temperature profiles retain their properties of independence of average concentration. At the present stage of our knowledge the analysis cannot be developed further, however, because of the lack of information concerning the functional relationships between the profiles and average concentration in dense-phase flow.

4. Concluding Remarks

In this program, the hydrodynamics and heat transfer properties of vertical fully developed flow of gas-solids suspensions have been investigated both theoretically and experimentally. The theoretical approach based on the general probabilistic multiphase flow equations proved to be a powerful tool for the analysis of suspension flows. Experiments carried out using two different installations and several different solids confirmed all theoretical predictions and provided most of the required data, as well as additional information to complete the analysis.

The correspondence between the dilute-phase flow of vertical suspensions and the theoretically defined similar profiles regime has been clearly established. Several general properties of either overall hydrodynamics or local flow structure has been pointed out as well as variable properties depending upon the characteristics of the installation. The dependence laws of temperature fields on solids concentration has been suggested from which a general equation describing the trend of variation of the wall-to-suspension heat transfer coefficient with solids loading has been derived.

A sudden transition to dense-phase flow when solids concentration passes beyond a specific critical value has been observed in all cases. Beyond this transition, at least some of the similarity properties of the flow structure no longer hold true. The general heat transfer equation still applies, however, with modified coefficients.

Presently, the program is still in progress, especially in connection with circulating fluidized bed reactor applications. It is primarily concerned with the flow structure of dense-phase flow and the specific conditions under which transition to dense-phase flow occurs. A general law describing mass flux profiles in both regimes is sought for the purpose of scaling-up calculations. The characteristics of the acceleration region are also investigated as well as their connections with those of the fully developed flow region. The behaviour of mixtures of particles differing by density in vertical flow is an additional concern. Finally, the characteristics of suspension flows in inclined pipes and their connections with those of vertical flow will soon be published.

Nomenclature

a : Dimensionless shape factor defined in Eq. (28) [−]
b : Dimensionless shape factor defined in Eq. (28) [−]
B_{ij} : Velocity cofluctuations tensor for the fluid [m^2/s^2]
c : Volumetric solids concentration averaged over a cross-section [−]
C : Heat capacity [J/kgK]
C_0 : Constant in Eq. (30) [−]
C_1 : Constant in Eq. (30) [m/s]
$f(r)$: Reduced solids concentration profile [−]
F : Fluid-solids interaction force [N/m^3]
g : Acceleration of gravity [m/s^2]
h : Heat transfer coefficient [W/m^2K]
K : Constant defined in Eq.(8) [m/s]
$O(c^2)$: Second order terms in a series development
p : Pressure [Pa]
Q_{fs} : Heat rate transferred from the fluid to the solids [W/m^3]
r : Radial coordinate [m]
R : Pipe radius [m]
s_{ij} : Intergranular stress tensor [Pa]
t : Time [s]
T : Temperature [K]
Ui : Gas velocity components [m/s]
U : Superficial gas velocity [m/s]
V_i : Solids velocity components [m/s]
V_t : Terminal velocity of the solids [m/s]
V : Average solids velocity [m/s]
W : Mass flowrate [kg/s]
x : Axial coordinate [m]
x_i, x_j : Cartesian coordinates (tensor notation) [m]
Y : Heat transfer function defined in Eq. (31) [−]

Greek symbols

α : Phase presence probability [−]
β_{ij} : Velocity cofluctuations tensor for the solids [m^2/s^2]
Γ : Ratio defined in Eq. (27) [−]
ε_i : Velocity-temperature cofluctuations vector [mK/s]
φ : Unit heat flux [W/m^2]
λ : Heat conductivity [W/mK]
θ : Radial temperature profile [K]
ρ : Density [kg/m^3]
σ_{ij} : Stress tensor acting within the solids phase [Pa]
τ_{ij} : Viscous stress tensor [Pa]

Subscripts and superscripts

f : Fluid phase
i, j : Tensor notation
I : Interface
m : Mixture (Gas+solids)
M : Mixed mean (temperature)
p : Phase p
r : Radial projection
rel : Relative or slip (velocity)
s : Solids phase
vw : In the vicinity of the wall
w : At the wall
0 : Zeroth order terms in series developments (Reference flow)
1 : First order terms in series developments
$*$: Critical conditions (transition)

References

1) Azzi, M.: Etude des profils de flux de par-

ticules dans l'écoulement vertical établi d'une suspension gaz-solides, Thèse de Doctorat, Université de Technologie de Compiègne, Compiègne (1986)

2) Bentahar, F., Molodtsof, Y., Large, J.F., Alia, K.: Heat Transfer to Vertically Flowing Dilute and Dense-Phase Gas-Solids Suspensions, A.I.Ch.E. Symp. Series No 276, **86** (1990), 10-15

3) Bentahar, F.: Ecoulement vertical d'une suspension dense: Hydrodynamique et transfert thermique suspension-paroi, Thèse de Doctorat d'Etat, Université des Sciences et de la Technologie d'Alger / U.T.C., Algiers (1992)

4) Hariu, O.H., Molstad, M.C.: Pressure Drop in Vertical Transport of Solids by Gases, Ind. Eng. Chem., **41** (1949) 6, 1148-1160

5) Maeda, M., Saigusa, T., Ikai, S.: Study of Heat Transfer to Gas-Solids Suspension — Part 1: Influence of Free Turbulence on Heat Transfer, Bull. J.S.M.E., **19** (1976) 137, 1317-1325

6) Mok, S.L.K., Molodtsof, Y., Large, J.F., Bergougnou, M.A.: Hydrodynamic Characteristics of Dilute and Dense-Phase Flows in Vertical Pneumatic Transport, Proc. 37 th Canadian Conf. Chem. Eng., Montréal, (1987)

7) Mok, S.L.K., Molodtsof, Y., Large, J.F., Bergougnou, M.A.: Characterization of Dilute and Dense-Phase Vertical Upflow Gas-Solid Transport Based on Average Concentration and Velocity Data, Canadian J. Chem. Eng., **67** (1989), 10-16

8) Mok, S.L.K.: The Study of Hydrodynamic Characteristics of Vertical Upflow Gas-Solids Suspension in Dilute and Dense-Phase Regimes, Ph. D. Thesis, University of Western Ontario, London, Canada (1991)

9) Molodtsof, Y.: Equations Générales Probabilistes des Ecoulements Polyphasiques et applications aux mélanges gaz-solides, Thèse de Doctorat d'Etat, Université de Technologie de Compiègne, Compiègne (1985)

10) Molodtsof, Y., Muzyka, D.W.: General Probabilistic Multiphase Equations for Analysing Gas-Solids Mixtures, Int. J. Eng. Fluid Mech., **2** (1989) 1, 1-24

11) Molodtsof, Y., Muzyka, D.W.: A Similar Profile Regime in the Vertical Fully Developed Flow of Gas-Solids Suspensions, Int. J. Multiphase Flow, **17** (1991) 5, 573-583

12) Molodtsof, Y., Muzyka, D.W.: Wall-to-Suspension Heat Transfer in the Similar Profiles Regime, Int. J. Heat Mass Transfer, **35** (1992) 10, 2665-2673

13) Monceaux, L.: Etude des régimes d'écoulement dans un lit circulant, Thèse de Docteur-Ingénieur, Université de Technologie de Compiègne / E.N.S.P.M., Compiègne (1985)

14) Muzyka, D.W., Molodtsof, Y., Large, J.F., Bergougnou, M.A.: Application of Probabilistic Multiphase Flow Equations to Dilute-Phase Pneumatic Transport, Proc. 33 rd Canadian Conf. Chem. Eng., Toronto (1983)

15) Muzyka, D.W.: The Use of Probabilistic Multiphase Flow Equations in the Study of the Hydrodynamics and Heat Transfer in Gas-Solids Suspensions, Ph. D. Thesis, University of Western Ontario, London, Canada (1985)

Review

Environmental Effects on Friction and Wear of Ceramics †

Shinya Sasaki
*Mechanical Engineering Laboratory**

Abstract

It is well known that the characteristics of friction and wear of ceramics are extremely sensitive to the environment. It is possible to divide the mechanism of the environmental effects into three major steps : The formation of the adsorbed layers, the change of the surface properties and the formation of tribochemical reaction products. Under actual sliding conditions, the influence of tribochemical reaction plays an effective role. An attempt have been made to use this effect to activate an excellent lubrication. This work deals with the relationships between the environment and the tribological characteristics of ceramics.

1. Introduction

Friction and wear of solids are caused by phenomena which occur on material surfaces. Thus, friction and wear characteristics depend highly on the physical and chemical properties of the surfaces. One of the most important factors used for defining the properties of surfaces is the environmental effect which results in a thin surface layer. It is well known that the mechanical strength of ceramic materials is likely to be strongly affected by the surrounding atmosphere[1]. In particular, their tribological properties are extremely sensitive to the environment. Many factors influence the usual phenomena of friction and wear simultaneously, so it is difficult to observe the environmental factor alone. Therefore, the first important step in the study of the tribology of ceramics is to single out those factors from among many factors that contribute to the environmental effect which exert a strong influence on the friction and wear characteristics and to elucidate the mechanisms of their action. If it were possible to start from this premise and construct lubricating systems which make use of the environmental effect and use this feedback of the tribology of materials as a guide for planning the development of ceramic materials, it would definitely be possible to design new sliding systems possessing properties required for applications under different environmental conditions.

2. Mechanisms of environmental effect

The elucidation of environmental effect mechanisms is much easier if the effects are classified into three major steps depending on the environmental action, as shown in **Table 1.**

Table 1 Mechanism of environmental effect on friction and wear of ceramics

1	Formation of adsorption layers
2	Change of mechanical properties by adsorption
2-1	Chemo-mechanical effect
2-2	Stress corrosion cracking
3	Tribochemical reaction

2.1 Formation of adsorption layers

The adhesion theory[2] concerning the mechanism of friction between solids proposed by Bowden-Tabor is based on experimental results obtained by studying friction phenomena, mainly between metal surfaces in friction. However, this adhesion theory can also be applied to NaCl crystals and to numerous types of hard and brittle materials as was proven by King and Tabor in 1954[3]. At present[4], the adhesion theory is applicable to friction between ceramic materials[5], excluding the controversy[6] concerning the anisotropy of friction observed in single crystalline materials. According to the adhesion theory, the shearing stress at the junction between two solids within

---

* Namiki 1-2, Tsukuba-shi, Ibaragi 305, JAPAN
TEL. 0298-58-7196

† Received July 15th 1992

the region of an actual contact decreases with an increase in the adsorbed molecular layer. The formation of the adsorbed layer results in a wear reduction through the reduction of the friction coefficient.

2.2 Change of mechanical properties of surfaces with adsorption

Molecules adsorbed from the environment cause a change in the surface properties of solids. At present the following two main factors are related to this process.

2.2.1 Chemo-mechanical effect

The mechanical strength of a solid surface is affected by the adsorption of extraneous molecules from the surface. The changes in the strength depend highly on the type and molecular weight of the molecules adsorbed. Rehbinder et. al.[7] explained that these phenomena were due to the fact that the rupture stress of the solids is related to the surface energy γ by the equation[8,9]:

$$\sigma=\left[E\frac{\gamma+P}{C}\right]^{1/2} \qquad (1)$$

where

σ: Rupture stress of ideal brittle material containing micro-cracks

E: Young's modulus

P: Surface plastic work

C: Depth of micro-crack on the surface

In brittle materials such as ceramics $\gamma >> P$. Since it is believed that other variables are not affected by the environment, is lowered with a reduction in r. The relationship between the surface energy and the strength was established for quartz glass[10] as shown in **Fig. 1**. Numerous data proving this relationship were also reported[11].

On the other hand, Westwood et al. performed a series of studies on the mechanical strength of crystals and glass in various liquid surroundings. They proposed the WGL (Westwood, Goldheim, Lye) hypothesis[12,13], which states that the surface potential and distribution of mobile charge carriers in the near-surface region change with chemisorption of molecules. These changes, it is suggested, affects the ease with which kinks are generated on, and move along, near-surface dislocations in crystals, and hence affect line-defect mobility. For ionic solids, changes in the electron occupancy of near-surface point defects will also influence their interactions with dislocations, and this too will affect dislocation mobility and crystal hardness. **Figure 2** illustrates one of the results obtained in the experiments performed by Westwood et al. where the relationship between the hardness and the zeta potential[14] of alumina single crystals in a water solution of sodium hydroxide and nalcohol with a number Nc of carbon atoms in a molecule can be verified. In both solutions the maximal hardness is observed when the zeta potential is equal to 0. This correlation between the zeta potential and the mechanical properties was also observed in soda glass and MgO[15]. Numerous reports indicating indefinite results based on the WGL hypothesis have been published as well[16].

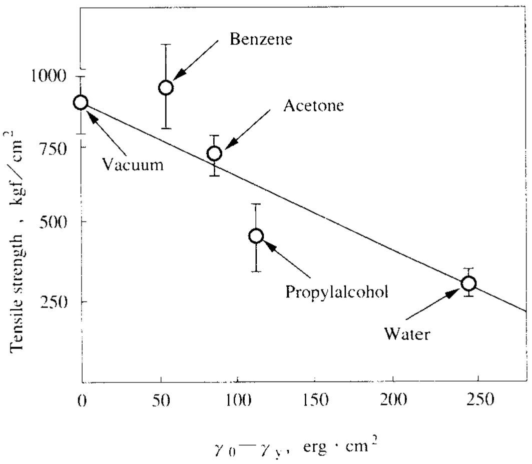

Fig. 1 Tensile strength and drop in amount of quartz glass in various atmosphere.

It is possible to say that we are now at a stage where the existence of chemo-mechanical effects[17] is being confirmed, but a comprehensive insight into their mechanisms has not yet been reached. However, if the chemo-mechanical effect is accepted as an environmental effect on friction and wear behavior of ceramics, then such mechanisms as the reduction of the friction coefficient by a lowering of the yield stress in the subsurface layers and the restricting effect on the rupture by wear due to the avoidance of local stress concentrations are possible.

2.2.2 Stress corrosion cracking

This phenomenon appears following adsorption of polar molecules to solid surfaces. However, it is different from the chemo-mechanical effect[18]. In some types of ceramics, it is known that the crack growth speed at the surface of a material under stress is accelerated by adsorption of polar molecules such as water and anmonia[19,20,21]. This phenomenon is called stress corrosion cracking. It is attributed to the fact that the chemical reaction at the crack tip accelerates under the influence of the applied stress. Since stress corrosion cracking has an influence deep beneath the surface compared with the chemo-mechanical effect, it is likely to cause destructive wear. **Figure 3** shows a model of stress corrosion cracking of partially stabilized zirconia.

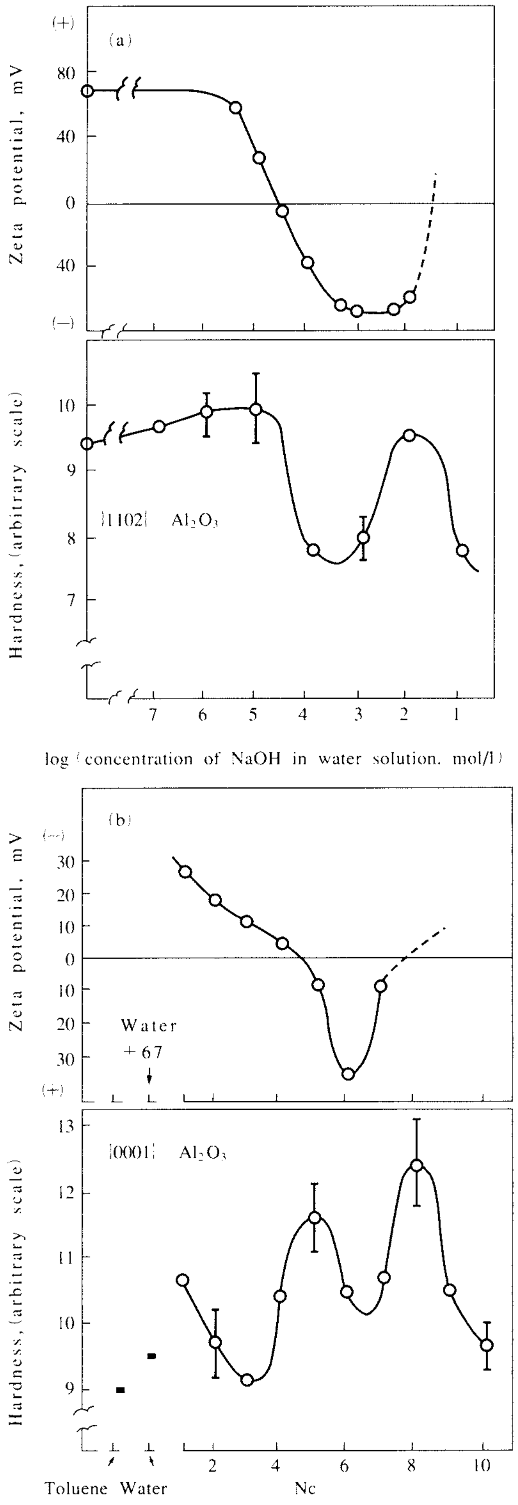

Fig. 2 Relationship between hardness and zeta potential of Al_2O_3
(a)in water sodium hydroxide
(b)in n-alcohol

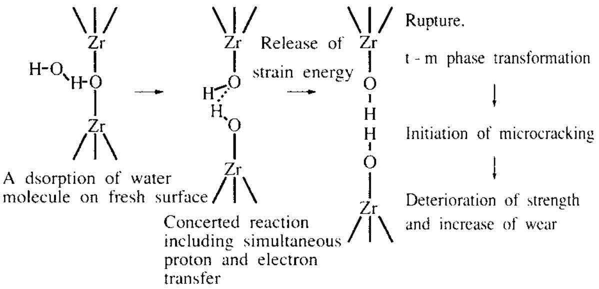

Fig. 3 A model of stress corrosion cracking

2.3 Tribochemical reaction

At the sliding surface, the peculiar chemical reaction which is caused by friction is generically called a tribochemical reaction[22]. When subjected to the mechanical action of friction, surfaces are activated by the exposure of fresh surfaces which are free from any adsorbed molecules or by a change in the crystalline structure (lattice defects, dislocation, amorphous state)[23]. During friction, sites of specific reactions are initiated by high temperature, high pressure and high shear stress. The occurrence of secondary or tertiary physical and chemical phenomena, such as exoelectron (Kramer electron) radiation[24], triboelectrification[25], triboluminescence[26] and tribo-plasma generation[27] promote peculiar chemical reactions. Reactions between adsorbed molecules, reactions between adsorbed molecules and surface molecules, or reactions between atoms of solids through adsorbed molecules result in the formation of a layer of a third material which differs from the initial materials on the sliding surfaces. This tribochemical reaction is believed to promote lubrication trough the formation of reaction products at the sliding surface which reduce friction and wear in ceramics. However, removal of these reaction products leads to a slight increase in wear.

3. Friction and wear characteristics and tribochemistry

We will now attempt to establish the relationships between the actual friction and wear characteristics taking into account tribochemistry. Friction and wear in ceramics from the view point of tribochemistry were analyzed by Fischer and Tomizawa[28] who reported their studies on the friction characteristics of silicon nitride and silicon carbide in water. **Figure 4** shows a typical example of friction and wear behavior of ceramics being lubricated with pure water[29]. The friction coefficients of silicon nitride and silicon carbide have very small values even under low sliding velocity conditions, and are comparable with that of hydrodynamic lubrication. In addition, the specific wear rate of these materials decreases with an increase in sliding velocity. These phenomena of friction reduction in water are explained by the formation and the dissolution of silicon hydrates as a result of tribochemical reactions and by the simultaneous synergistic effect of the smoothing of the sliding surfaces. The form of wear in which the wear proceeds with a gradual dissolution due to tribochemical reactions is called tribochemical wear. This wear mechanism was established by Tomlinson[30] 60 years ago; it was called "atomic wear"[31].

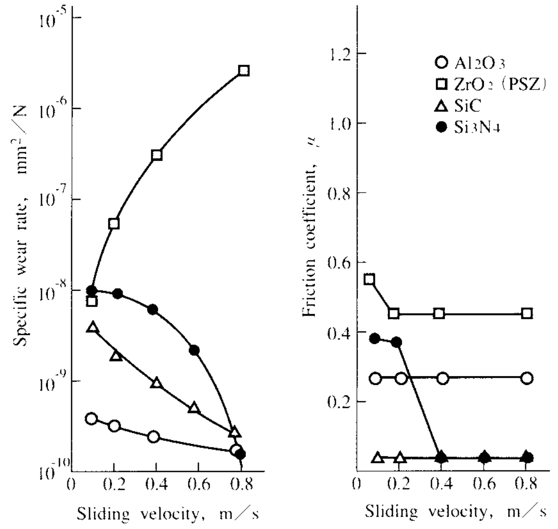

Fig. 4 Friction and wear of behavior of ceramics in water.

Figure 5 shows the effect of humidity on the friction and wear properties[29]. Under such dry conditions, especially in low humidities, the distractive wear dominates the wear properties. The friction coefficient decreases with an increase in relative humidity for all ceramics, but the wear rates shows no such definite tendency. For example, while the wear rates of alumina and silicon carbide decrease as the relative humidity increases, the highest wear rate of partially stabilized zirconia appears at 20% relative humidity. In the case of silicon nitride, the lowest wear rate is obtained at 50% relative humidity. The increase in humidity restrains the distractive wear, but it accelerates the tribochemical reaction of silicon nitride with water, resulting in the formation of reaction products, silicon hydrates.

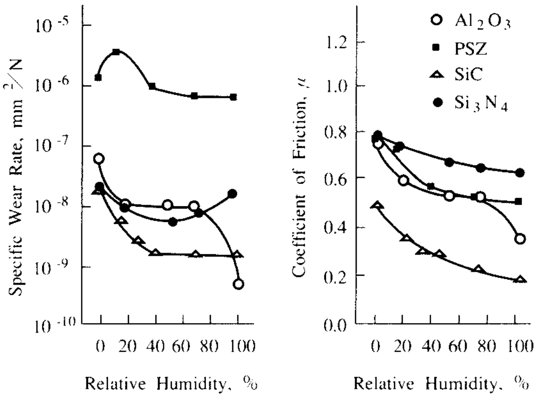

Fig. 5 Friction and wear behavior as a function of relative humidity in air : load 10N, velocity $0.4 m/s^{-1}$, total wear distance 1256m.

Figure 6 shows the influence of an organic compound atmosphere on the friction and wear behavior of alumina. Both friction and wear in these organic compounds are very low as compared to those in nitrogen. In hexane and benzene, the formation of reaction products similar to friction polymers can be observed on the sliding surfaces as shown in **Fig. 7**. These reaction products are highly viscous grease-like substances, and have lubricating effects[32]. Such lubricating effect of the reaction products can also be observed for alumina being lubricated with a water solution of fatty acid sodiums[33] as shown in **Fig. 8**. The friction and wear of oil

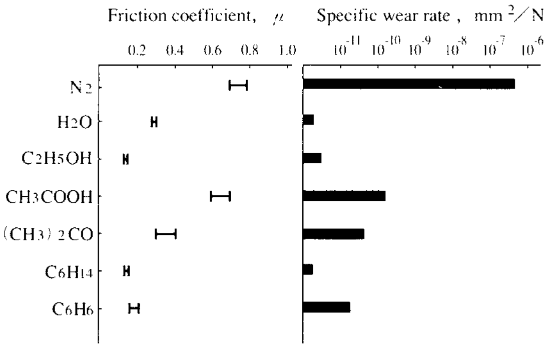

Fig. 6 Influence of organic compounds on friction and wear of Al_2O_3 : load 10N, sliding velocity 0.4m/s, total sliding distance 1256m.

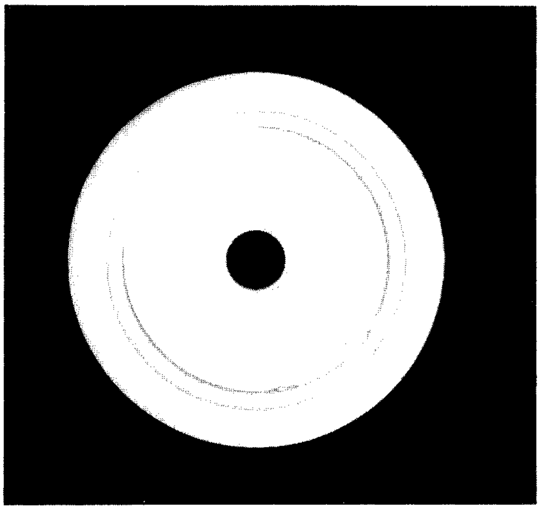

Fig. 7 Example of friction polymer like reaction product on alumina disk surface in atmosphere of benzene vapor.

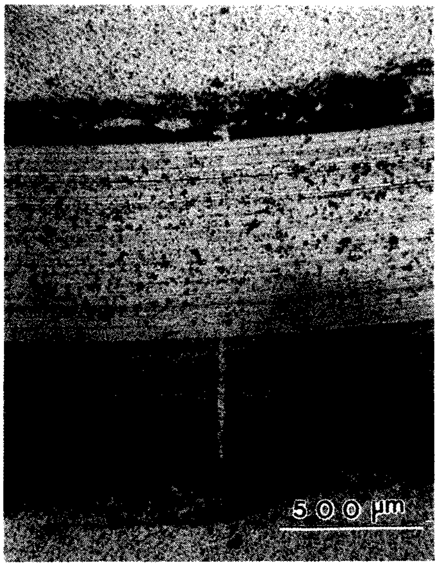

Fig. 8 Optical micrograph of Al_2O_3 in water with lauric acid sodium.

-lubricated ceramics are likely to be strongly affected by the formation of reaction products which result from tribochemical reactions that contribute to the lubrication effect of a particular introduced additive[34]. Studies on the formation of friction polymers by Hermance and Egan[35] were first published more than 30 years ago[36], but mechanisms of their formation still remain unclear in many aspects.

When the surfaces of different materials are mated, a reaction through the surrounding atmosphere between them occurs. For example, when sliding alumina and iron surfaces, the formation of a spinel-type solid solution occurs between the iron oxide and alumina. This is attributed to the process of wear[37]. The characteristics of friction and wear for silicon nitride and alumina in water are shown in **Fig. 9**[38]. On

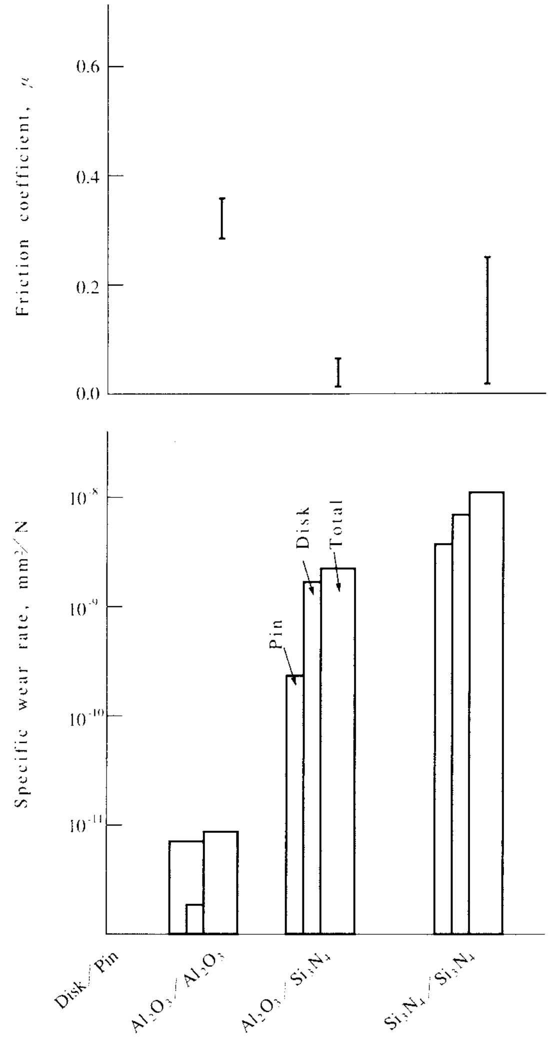

Fig. 9 Friction and wear characteristics in water when mating silicon nitride and alumina : Pin-on disk, load 50N, sliding velocity 0.4m/s, total sliding distance 1256m.

the other hand, when the wear process proceeds with the dissolution resulting from the reaction between silicon nitride and alumina, the distractive wear of silicon nitride is restrained. In this case the friction characteristics are significantly improved. The improvement of the lubrication characteristics using the reactions between mated surfaces of different materials is one of the important methods for future tribo-systems.

Figure 10 shows the wear characteristics of alumina particles dispersed zirconia and partially stabilized zirconia (PSZ) in water[39]. This composite material was developed to improve the mechanical properties of PSZ; it raised the stress level required for the martensitic transformation of tetragonal phase to a monoclinic phase and restrained the stress corrosion cracking. The wear rates of both PSZ (ZYM, ZYH) increase with the sliding velocity. On the other hand, the specific wear rate of the composite materials (ZYS) decreases slightly with sliding velocities of over 0.2 m/s, and is found to be less than 1/10 that of ZYM and ZYH. A larger superiority in the wear characteristics of ZYS is obtained in organic liquids as shown in **Fig. 11**. Such an excellent tribological property is believed to be strongly related to the chemical activity of alumina, in addition to an improvement in the mechanical strength.

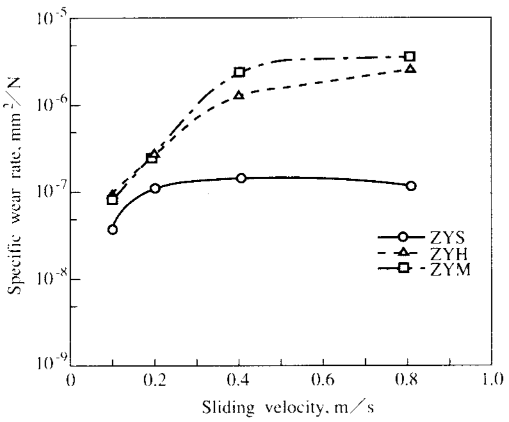

Fig. 10 Wear characteristics of alumina particles disoersed zirconia and PSZ in water : load 50N, total sliding distance 1256m.
ZYM : normal sintered PSZ
ZYH : HIP treated PSZ
ZYS : alumina particles dispersed zirconia

4. Conclusion

Efficient applications of tribochemical reactions in lubricating processes require a quantitative estimation of the reactions at specific stages and the possibility of controlling them. One of the methods to achieve this objective is to clarify the tribochemical reactions that are necessary, giving a deeper insight into the tribochemical activation and development of materials while taking their tribology into account. Therefore, fundamental approaches to the tribochemical reactions will be more and more important with the sophistication of analytical equipments.

References

1) S. W. Freiman : Ceramic bull., **67**, 2 (1988) 392.
2) F. P. Bowden and D. Tabor : "The friction and Lubrication of Solids". Oxford (1954).
3) R. F. King and D. Tabor : Proc. of Roy. Soc.

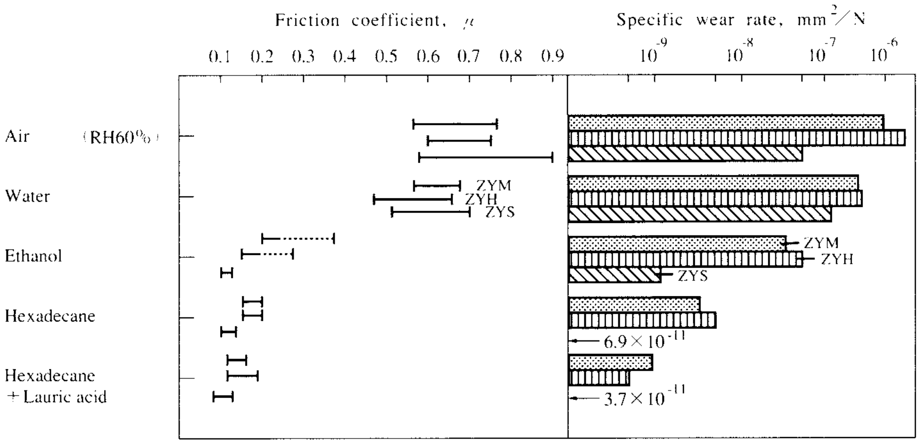

Fig. 11 Friction and wear characteristics in each environments : load 50N, sliding velocity 0.2m/s, total sliding distance 1256m.

(London), A223 (1954) 225.
4) F. P. Bowden and C. A. Brooks : Proc. Roy. Soc. (London), A227 (1966) 244.
5) T. Sasada : KIKAI-NO- KENNKYUU, **40**, 1 (1988) 138.*
6) Y. Enomoto : KIKAI-NOKENNKYUU, **37**, 1 (1985) 31 & **37**, 2 (1985) 280.*
7) P. A. Rehbinder : Proc. 6th Phys. Conf. State Press, Moscow (1928) 29.
8) T. Kubo : "MUKIBUTU-NOMECHANO-CHEMISTRY", SOUGOU - GIJYUTU - SYUPPAN (1987) 37.*
9) E. Orowan : Weld. Res. (London), Suppl., (1955) 157.
10) M. L. Hammond, S. F. Ravitz : J. Amer. Soc., 46 (1965) 329.
11) D. Hardie, N, J, Petch : Proc. Br. Ceram. Soc., 46 (1963) 329.
12) A. R. C. Westwood, D. L. Goldheim and R. G. Lye : Phil. Mag., 16 (1967) 505.
13) Idem, ibid. 17 (1968) 951.
14) A. R. C. Westwood, N. H. Macmillan and R. S. Kalyoncu : J. Ameri. Ceram. Soc., **26**, 5 (1973) 697.
15) N. H. Macmillan, R. D. Huntington and A. R. C. Westwood : J. Mater. Sci., 9 (1974) 697.
16) S. M. Wiederhorn and D. E. Roberts : Wear, 32 (1975) 51.
17) P. A. Rehbinder :Nature, **159**, 6 (1947) 866.
18) J. T. Czernuszka and T. F. Page : J. Mater. Sci., 22 (1987) 3917.
19) T. A. Michalaske and S. W. Freiman : J. Ameri. Ceram. Soc., **66**,4 (1983) 284.
20) S. M. Wiederhorn, E. R. Fuller Jr & R. Thomson : Metal Science, 14 (1980) 450.
21) A. R. C. Westwood and R. S. Kalyoncu : J. Ameri. Ceram. Soc., **56**, 5 (1973) 258.
22) G. Heinike : "Tribochemistry", Charlhanser Verlag Munchen Wien, (1984).
23) K. Tamai : HYOUMENN, **24**, 4 (1986) 189.*
24) J. Kramer : "Der metallishe Zustand", Gottingen, Vandenhoeck & Ruprechet (1950).
25) S. Sasaki : ASME Wear of Materals, H0631A (1991) 327.
26) A. J. Walton : Advances in Physics, **26**, 6 (1977) 87.
27) P. A. Thissen : Ber II Inter. Pulvermetallurgie Tagung, Eisenach (1961) 23.
28) T. E. Fischer and Tomizawa : Wear, (1985) 21.
29) S. Sasaki : Tribologist, **33**, 8 (1988) 620. *
30) G. A. Tomlinson : Phil. Mag., 7 (1929) 905.
31) K. Inoue : Tribologist, **12**, 2 (1967) 40.*
32) S. Sasaki : Wear, 134. (1989) 185.
33) S. Sasaki : Proc. Japan Congress on Material Reasearch (1990) 205.
34) K. Hata : JAST Tribology Forum '90 Texts (1990) 79.*
35) H. W. Hermance and T. F. Egan : Bell System Tech J. 37 (1958) 739.
36) S. W. Chakin : Wear, 10 (1967) 49.
37) N. Yasunaga, A. Ohara and N. Tarumi : Reports of ETL (1977) 779.*
38) S. Sasaki : Tribologist, **36**, 7 (1991) 7.
39) S. Sasaki : Bulletin of Mechanical Engineering Laboratory, No. 58 (1992) 94.

* in Japanese

Review

Microencapsulation : The Creation of Synthetic Fine Particles with Specified Properties †

B. H. Kaye
*Physics Dep. of Laurention University**

1. Introduction

The aim of microencapsulation is to create synthetic powders or fineparticle suspensions with required properties[1)6–]. Thus, in powder mixing technology a liquid component of the mixture can be transformed into a free flowing powder, which reduces the technical problems of creating a mixture with other powdered ingredients, and can be the basis of a strategy for preventing segregation in the assembled powder mixture.

For example, consider the formulation of a powder mixture in which one ingredient is a finely powdered toxic drug of relatively high density and another ingredient is a small amount of liquid which is compatible with the drug fineparticles. The drug fineparticles can be suspended in the liquid, and then the slurry spray dried to form a powder the grains of which can be regarded as heterogeneous microcapsules. One can adjust the size and the density of these microcapsules by adding hollow bubbles of a soluble cellulosic based material so that the overall density of the microcapsules and their size is comparable to an excipient powder with which the drug has to be mixed in the tabletting process. By adjusting the density of the microcapsules one eliminates the density driven segregation of the powder components in an ultimate mixture and by bulking them out with a bubble ingredient one is able to make it difficult for the heterogeneous microcapsules to migrate under the influence of vibration within the mixture.

Microencapsulation is one of those industrially important technologies in which successful solutions to technical problems tend to become closely guarded commercial secrets. For this reason the literature on the performance of microencapsulated products is sparse. For example, it has recently been announced that the artificial sweetener Aspartame (NutraSweet) has been successfully incorporated into microcapsules to enable the artificial sweetener to survive the heat of baking in products such as cakes. It is highly unlikely that the technical details of the process will be made available in the scientific literature to the company's competitors.

The mainstay of the development of microencapsulation in industry are several companies that will create microcapsules on a custom basis. (A selection of these companies is listed in references 7 through 11.) In such a situation the purchaser of the microcapsules acquires the specialty knowledge of the creator of the capsules and appropriate secrecy contracts keep the information from emerging into the technical literature. One of the aims of this review is to direct the reader to sources of information on development possibilities for the evolution of microencapsulated products. The second aim of the review is to present an overview in the way in which microencapsulation technology promises to revolutionize various branches of applied science, and through such an overview to stimulate the reader to seek out innovative developments of new techniques for solving technical problems.

For some time scientists and technologists have been employing microencapsulation techniques without a clear understanding of the fact that the process they were using involved microencapsulation. Thus, in the mixing of powders, sometimes the practice of adding a very fine powder to a very coarse powder has been very successful despite, having considered the physical process of mixing the powders, the expectation that the fines would segregate through the assembled mixture as soon as the mixing process ceased. In such cases the finer powder is actually electrostatically coating the

---

* Sudbury, Ontario, CANADA
† Received Oct. 10, 1992

coarser fineparticles to produce a heterogeneous microencapsulated system. Again in the pharmaceutical industry, flow agents are used to promote the movement of cohesive powders. The mechanisms employed by such flow agents (or glidants, as they are sometimes called) are not fully understood but, in the case of silica flow agents, the flow agent appears to coat the individual grains of the primary powder, increasing the friction between the grains and preventing packing. A different type of glidant added to pharmaceutical powders is powdered magnesium stearate. This powder appears to promote flow by de-dusting the powder as it creates heterogeneous microcapsules of agglomerated fines held together by the waxy stearate compound, a phenomenon described in the powder industry as spontaneous balling of the powder[12-].

It is difficult to draw a sharp boundary between what should be considered as a microcapsule or as a coated tablet. Thus in the pharmaceutical industry one system for contolled release involves the packing of a capsule with millimeter sized encapsulated ingredients which have different coating thicknesses to create different dissolution rates in the stomach, thus releasing the drug over a period of time. Each different thickness of coated microcapsule contributes the drug to the body's circulation system at a different time interval. On the other hand a large coated tablet designed to protect drugs which can be destroyed by stomach fluids is not, strictly speaking, a microencapsulated system. However, the two systems, the micropills in a controlled release system and the large coated tablets, use the same technology.

Before proceeding to a discussion of some of the basic processes for microcapsulation it is necessary to summarize and develop some terminology.

In **Figure 1** some of the vocabulary used in the description of microcapsules is illustrated with schematic drawings. The simplest form of microcapsule is known as a coherent, homogeneous element, simple microcapsule : in short form, a simple microcapsule shown in **Figure 1(a)**. This is the type of microcapsule used to encapsulate a fuel such as kerosene with a thin gelatin wall so that the kerosene represents 99% of the volume of the microcapsule. Such capsules can then be pressed into bricks to make odorless stable bricks of fuel which can be transported over great distances safely and without having to carry containers. The basic simple microcapsule can be increased in complexity by adding more coherent layers to the original simple microcapsule. Thus in an agricultural application multiple layer simple microcapsules of the type shown in **Figure 1(b)** have been broadcast in one traverse of the field. The multiple layer capsule delivers an early season herbicide first, followed by the application of a fertilizer as the capsule continues to erode under the effect of weather. Finally a late season herbicide can be released from the remnants of the capsule to facilitate the harvesting of the crop.

In a heterogeneous simple microencapsulation, such as that shown in **Figure 1(c)**, a microcapsule containing dispersed smaller droplets or fineparticles can be prepared at any level of complexity of dispersed material within the microcapsule. Obviously one can make composite microcapsules which have a heterogeneously structured core with a coherent coating about the outside. Toner beads (dry ink) used in xerography are actually microcapsules containing dispersed carbon black although more recent attempts to improve the performance of toner have looked at the possibility of coating carbon directly onto the outside of a resin fineparticle. More recent techniques of encapsulation have used heterogeneous coatings in which a sparse quantity of discrete coating material is placed around a core fineparticle as shown in **Figure 1(d)**. The bonding between such coating fineparticles and the core can either be permanent or temporary. The heterogeneous type coating is the system used in the Mechanofusion and Hybridization techniques to be described in a latar Section Workers in this area of microencapsulation use the specialized vocabulary indicated in **Figure 1(d)**.

Another type of encapsulation uses a liquid to bond together smaller fineparticles to create heterogeneous crumbs. This technology, a form of heterogeneous microencapsulation, has been the subject of an extensive scientific literature in which granulated crumbs are sometimes fired to make the bonding permanent. The use of liquid to agglomerate fineparticles to form

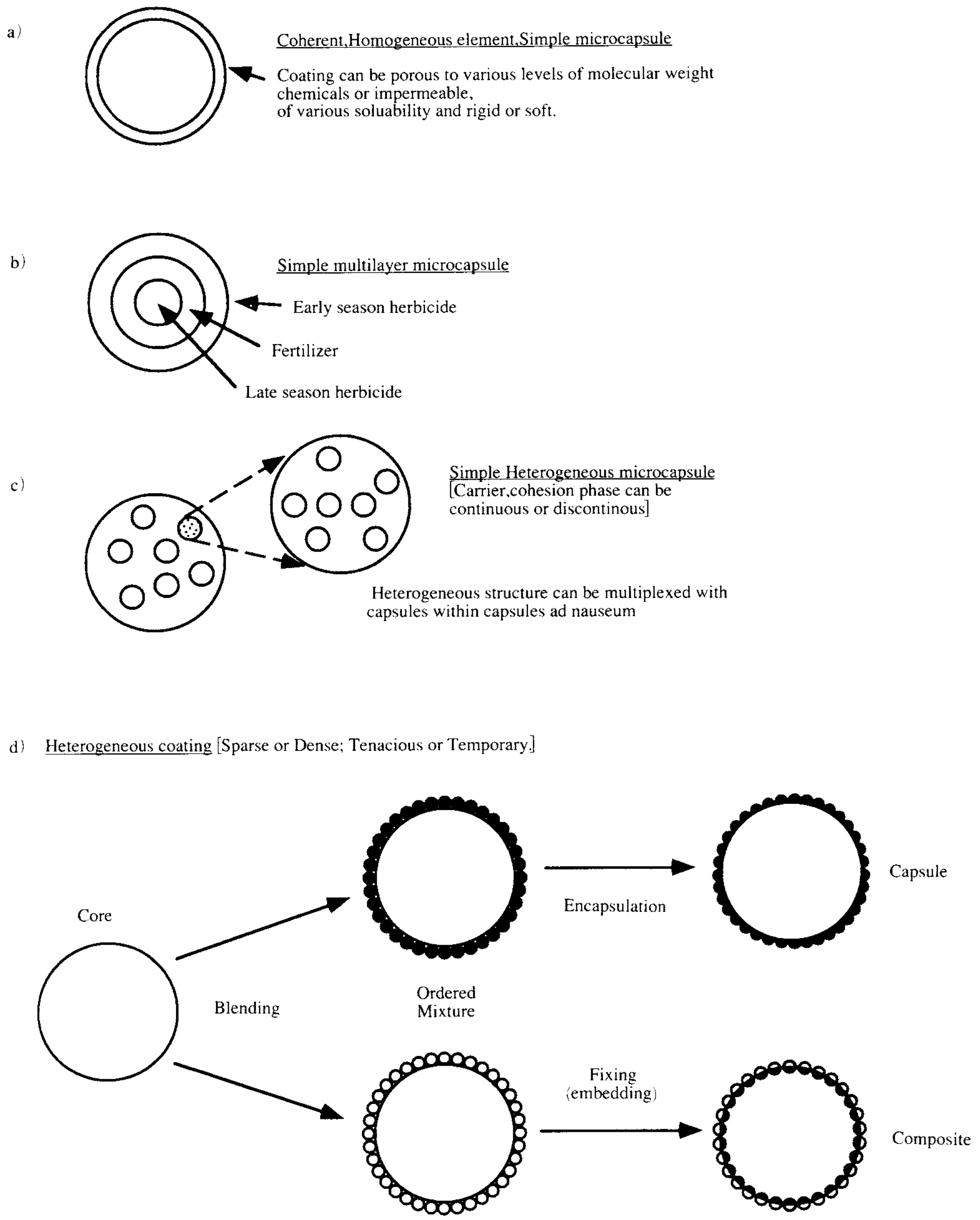

Fig. 1 The structure of a microcapsule can have various levels of complexity (and shape).

crumbs will not be considered further in this review. An excellent recent dicussion of this agglomeration technology is to be found in reference 13.

Technologies For Producing Microcapsules

In one review of the technology used to create microcapsules it is estimated that there are up to 25 different ways described in the scientific literature for making micro-capsules[6–]. In this review we will concentrate on a few of the major methods which should acquaint the reader with the basic concepts of the technology and introduce the methodologies available.

The Wurster Process. One of the most widely used methods of microencapsulation was developed by Wurster at the University of Wisconsin in Madison[1–]. The patents for this process are now vested in a corporation known as The Coating Place Inc.[7–] The Wurster technique for creating microcapsules is essentially a spouted fluidized bed system in which the moving fineparticles are coated with the appropriate material. The basic equipment used in the process is illustrated in **Figure 2**. The powder grains to be coated are air fluidized. As they move up through the center of the fluidized bed they are sprayed with the coating material. At the top of the central cylinder the coated fineparticles fall back down the outside to recirculate for a second coating to be applied. One of the advantages of this procedure is that coatings of any given thickness can be built up on the powder grains by repeated circulation of the material. If one attempts to use this technique with very fine powders the most difficult part of the process is to fluidize the powder grains. The circulating action of the fluidized bed also results in each increment of the coating being dried in the downward portion of the circulation trajectory. One has to be cautious with some materials to avoid explosions since a dry circulating system can build up an electrostatic charge, and there is a danger of explosion in some situations. Other manufacturers use similar air circulation systems in fluidized bed equipment. Thus the two systems of **Figure 3(a) and (b)** are described in the trade literature of the Glatt corporation[8-].

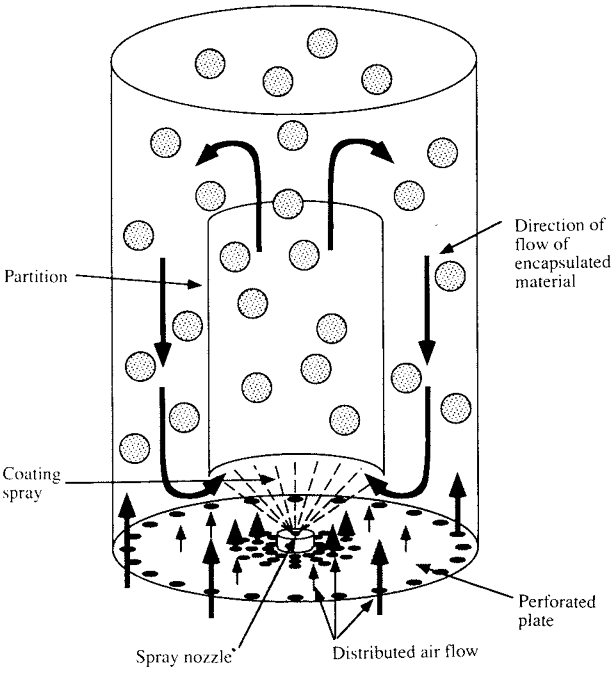

Fig. 2 In the Wurster technique for creating microcapsules the powder to be coated is fluidized in a circulating spouted bed and the coating sprayed onto the suspended powder grains[7-].

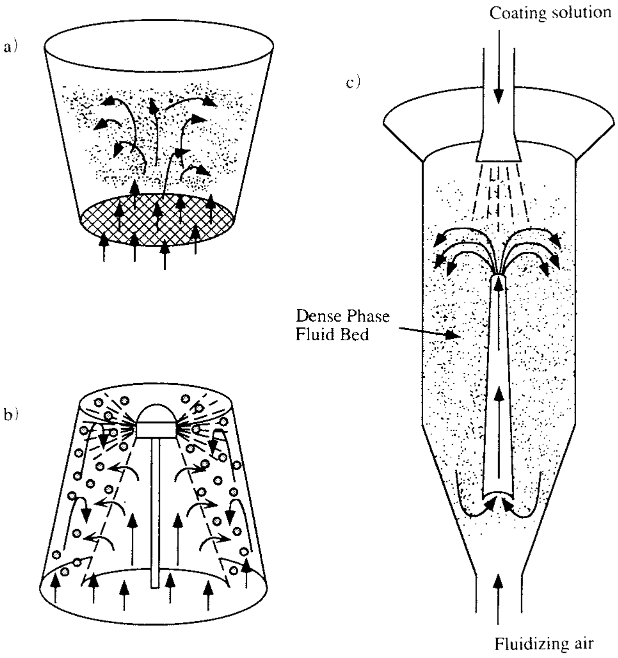

Fig. 3 Variations in the configuration of air fluidized - spray coating have been discovered by other manufacturers of microencapsulation equipment.

Microencapsulation System Developed by the South West Research Institute. The basic system developed at the South West Research Institute for creating microcapsules is shown in **Figure 4**[2-]. The core material is fed to a spinning disc at the center of the equipment. Core droplets, or grains of the powder to be encapsulated, are thrown off of the disc towards an outer cylinder containing many small holes around the periphery of the disc. The coating material is fed to this outer disc in liquid form so that it coats the holes in the cylinder with a thin film of the coating material. The core droplets or fineparticles pass through this film, which is constantly renewed, they are coated and then fall out into the outer container where they can be hardened by physical or chemical methods.

Electrostatic Coating Techniques. Several techniques for mixing core and coating fineparticles which have been given opposite electrostatic charges to attract them to each other have been developed. In this section we will describe the basic system developed by Leiberman and co-workers at the Illinois Institute of Technology Research Institute (IITRI) Chicago[14-]. The

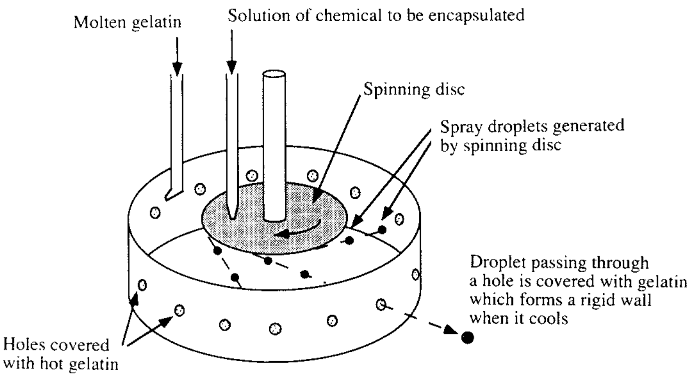

Fig. 4 In the SWRI technique for creating microcapsules a spinning disc is used to fling droplets, or fineparticles, through a film coating material[2-].

system used by Lieberman and co-workers is illustrated in **Figure 5**. In this technique the core material can be either solid or liquid. The usual choice of coating is a liquid for ease in subsequent handling of encapsulated fineparticles. Typical coating materials used by Lieberman and co-workers include a wax that solidifies on cooling, a dissolved polymer resin that forms a skin upon the evaporation of a solvent, a polymeric skin formed by interfacial action between a component in the core material, and a component in the coating material and liquid coatings that solidify upon exposure to a suitable gas phase. The two components to be turned into a microencapsulated system are fed into a reaction chamber which can be heated. The aerosol fineparticles are given an ionic charge of the appropriate sign using sub-corona discharge systems. To achieve sufficient encapsulation the system must be designed to achieve a high rate of collision between the two types of aerosol in a turbulent supportive air or gas system. If there is any danger of explosion appropriate supportive gas systems such as nitrogen must be used. In this process one must choose the coating substance so that it will wet, i.e. spread out on, the core material and cover it completely. If the core is also liquid the coating must have a lower surface tension otherwise the desired encapsulation will not be achieved. In **Figure 6** an encapsulated sodium chloride crystal system coated by this procedure is shown.

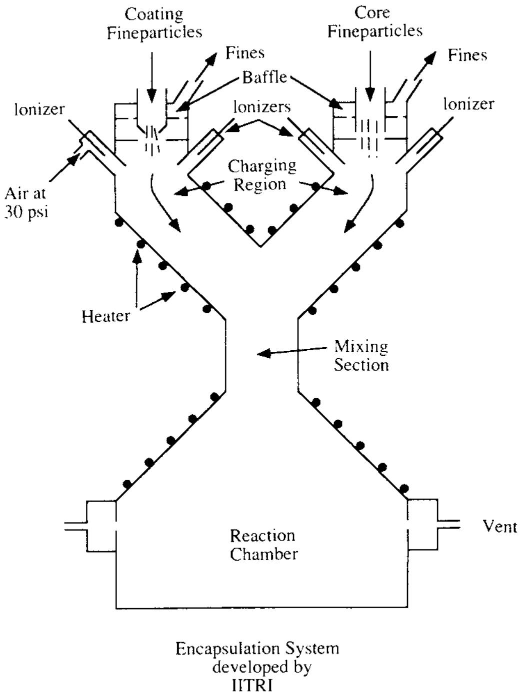

Fig. 5 In electrostatic, aerosol based, microencapsulation technologies the ingredients are attracted to each other by electrostatic forces in a reaction chamber.

Coacervation Technique for Producing Microcapsules. The process known as coacervation was developed by colloid chemists Kruyt and colleagues in the 1930's and remained a technology without an application until it was further developed by scientists at the National Cash Register company to create microcapsules for use in carbonless copy paper[1,2-]. (See discussion later in this review of applications of microcapsules in business systems.) The basic technique is illustrated in **Figure 7**. The core material to be encapsulated is placed in an immiscible liquid to form liquid droplets. The coating material is also suspended in the liquid medium or actually dissolved in this support material. To induce the process known as coacervation the temperature, pH or other environmental conditions are changed in such a way that the wall material comes out of solution and aggregates around a core droplet to form continuous encapsulating walls. Then in the final stage of the process these capsules are hardened.

An alternative technique for creating microcapsules out of the suspension of coacervated droplets is to spray dry the resulting slurry to create heterogeneously encapsulated composite microcapsules. A third avenue for creating microcapsules with coacervated suspensions is to add another ingredient that gels the support

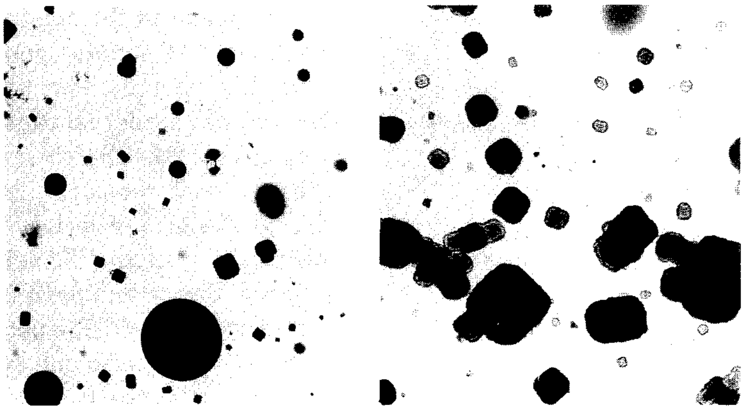
Unencapsulated Encapsulated

Fig. 6 Electronmicrographs of sodium chloride crystals, magnified 30,000 times, with and without carboxymethylcellulose encapsulation using the electrostaticly charged aerosol system.

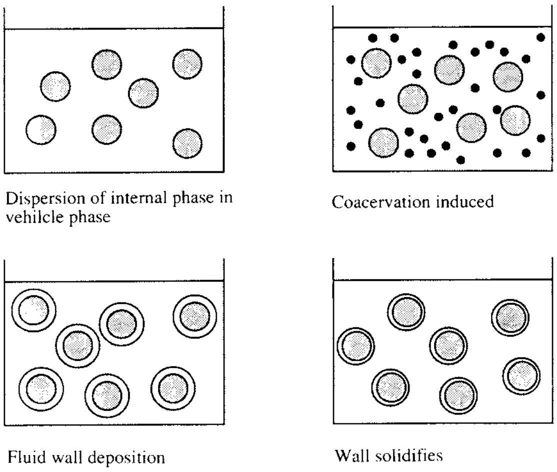

Fig. 7 The coacervation process starts with an emulsion of two immiscible liquids and then a wall is formed around the droplets by changing the physical and chemical properties of the supporting liquid.

liquid to create a solid form which can then be crumbled to create composite microcapsules. Another way of forming the walls around the droplets suspended in the supporting liquid is to use a monomer dissolved in the support liquid which can then be directly polymerized onto the droplet suspended in the liquid. The volume of the core material in the finished microcapsule can be varied anywhere from 20% to 99% of the volume of the microcapsule. By controlling the wall formation process the wall can either be made solid or porous to any required level.

Dry Powder Encapsulation Technology. The most recently developed system for creating microcapsules involves the mixing of two dry powders under high shear conditions so that one powder coats the other. Usually in this technique there has to be a considerable size difference in the two or more ingredients so that the encapsulated material adheres to the larger component of the mixture and the subsequent high shear treatment of the composite system embeds the encapsulating material into the core fineparticles. Note that in some discussions of this type of technology the core material is described as the host material and the encapsulating material is referred to as the guest fineparticles. In this discussion we prefer the term core and coating powders to differentiate between the two main members of the sytem. Dry encapsulation techniques using high shear conditions appear to have been simultaneously developed by two companies: Hosokawa Micron International Inc.,[15–] and the Nara Machine Company Ltd.[16–]. The system developed by Hosokawa is known by the name Mechanofusion whereas that developed by Nara is known as Hybridization. In the technical literature available at the time that this review was written the initial developments of the Mechanofusion system appear to be mainly in the material science and ceramic industry whereas the studies carried out using the Nara Machine process had found applications in the pharmaceutical industry[19)23–]. Since the two systems are very similar we will confine our discussion in this review to the Hosokawa Micron system of Mechanofusion. The basic equipment for this instrument is shown in **Figure** 8. As illustrated in **Figure** 8, in the Mechanofusion process a mixture of the two powders to be processed is compressed and sheared by a rotating cylindrical chamber which traps the mixture between the wall of the chamber and the head of a fixed element inside it. As mentioned earlier, in this process one often uses coating powders of a very small size with core fineparticles being considerably larger as illustrated for the powders shown in **Figure 9**. Titanium dioxide is an expensive white pigment which does not flow readily when placed in a powder mixture. By coating the titanium dioxide onto a carrier (core) fineparticle maximum use is made of the expensive pigment which when spread out on the core of the resin generates maximum scattering power for the weight of the powder used. At the same time the microencapsulated powder flows much more readily than either of the constituent ingredients. It is not immediately obvious whether this change in flow properties comes from the fact that the stress of the microencapsulation process actually changes the oxide state of the titanium dioxide or whether the core plus microencapsulated powder constitutes an electrically charged system with desirable surface characteristics[15–].

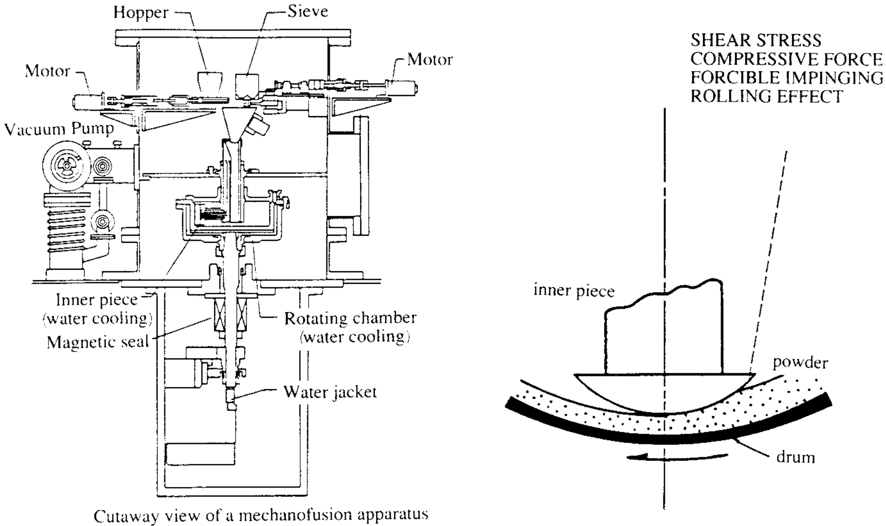

Cutaway view of a mechanofusion apparatus that works under a variety of processing atmospheres

Fig. 8 In the mechanofusion process a rotating cylinder stresses and shears the powders to be processed in the annular gap around the periphery of the milling chamber and the head of a fixed element inside.

Industrial use of Microencapsulated Material

Microencapsulated Technology In Business Administration Systems. The first widespread use of microencapsulated products was the development of carbonless copy paper by the National Cash Register (NCR) company in 1954[1–]. The elimination of layers of carbon paper for making multiple copies of documents greatly facilitated the operation of computer printer systems and simplified completion of forms in triplicate etc. as required by many commercial and government operations. The layer of carbon paper between two ordinary pieces of paper was eliminated by coating the underside of the top paper with microcapsules of ink which in their microencapsulated state were transparent; then the lower paper which was to receive the copy was coated with special clay fineparticles. In the early development of this type of paper it was common practice to include two initially colorless dyes, one of which gave an instant pattern of writing on the lower paper as the capsules were ruptured, and

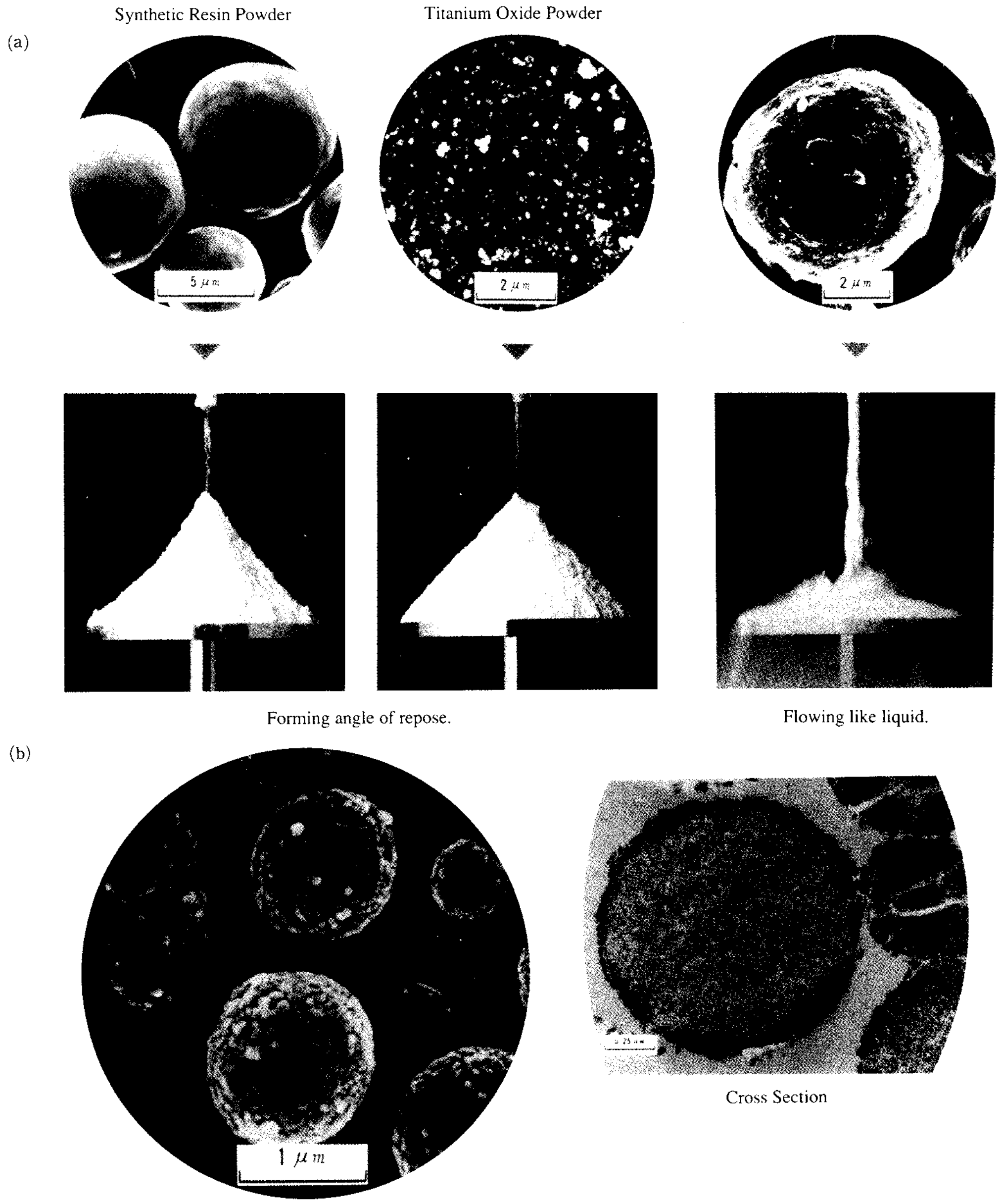

Fig. 9 Mechanofusion can create synthetic powders with desirable properties.

(a) Desired flow properties can be built into microcapsules produced by the mechanofusion process.
(b) Superfine TiO_2 on a silica carrier (core) fineparticle.

another dye which gave a more permanent color to the writing after a short time.

The size of the microcapsules of ink has to be controlled closely since if the microcapsules are too small they will disperse into the matrix of cellulose fibers that constitutes the structure of the paper. On the other hand, if the microcapsules are too large, when they rupture they will spread out too far and form a poor quality boundary to the print lines of the copy[24-].

To prevent premature release of ink onto the lower copy paper the manufacturers of carbonless copy paper place starch granules between the two sheets of paper. These granules hold the copies apart until the rupturing starts by the application of pressure.

The Post-it note stickers manufactured by 3M Company also make use of microencapsulation technology. The sticky part of such Post-it notes contains microencapsulated glue made from urea-formaldehyde which rupture under finger pressure. The spheres are between 15 and 40 microns in diameter. Each time the note paper is pressed a few more spheres rupture to release a fresh film of glue. If one writes extensively with a ball point pen over the glue area of the Post-it note, one can sometimes create too strong a bond between the note intended to be removed and the lower piece of paper, resulting in damage to the lower document. This is because one has ruptured too many microspheres to make the material easily detachable[25-].

Medical Applications of Encapsulated Materials.

One of the major uses of encapsulated material in the medical profession is to give a slow controlled release of medication to the patient. Another use of encapsulation is to hide the nasty taste of some medication. Particularly with children, there is often resistance by the patient to the swallowing of a foul tasting medication. If encapsulated in something like gelatin, the medication can be given as a spoonful of dry powder in a glass of water and swallowed without any taste sensation being felt by the patient. In the same way, medication for animals can be made up as a dry free-flowing tasteless powder and mixed with feedstuff.

Some liquid crystal compounds appear to have different colors as their temperature changes. Encapsulated liquid crystals can be used to take the temperature of a patient. In the simplest device which is available commercially, the letters N and F are printed in two different forms of encapsulated liquid crystals on a thin strip of plastic. This strip of plastic is then placed against the forehead of the patient. The liquid crystals are so chosen that if the person has a normal temperature, the letter N appears a strong blue. If, however, the person has a fever, the F shows as a bright green. The plastic strip can be used many times and is obviously easier to use than a thermometer made of mercury in glass.

Often in diseases of the circulation, doctors would like to know the distribution of body temperatures on the surface of the skin. This is not easy to determine with a traditional thermometer. However, if the skin is painted black and microencapsulated liquid crystals are sprayed onto the black surface, colored patterns made on the skin enable the doctor to see the temperature distribution of the skin. This can be then matched with deficiencies in the blood circulation of the patient. Tumors growing in the breast or other surface locations of the body are warmer than the surrounding tissue because of the concentration of blood in the growing tumor. For this reason, encapsulated liquid crystals are a useful diagnostic device for the early detection of breast cancer. Again, the surface of the skin could be sprayed black and then coated with encapsulated liquid crystals. The presence of a tumor would be indicated by a bright green spot in the patterns of the liquid crystal color contours[26-].

A special type of pressure sensitive microcapsule, similar to those used in the carbonless copy paper, has been developed for use in rehabilitating leprosy patients. Patients who have suffered from a severe bout of leprosy lose the sense of feeling in their extremities. They have often lost fingers or toes so that they need to be taught new ways of doing simple tasks. Because of the lack of feeling in their extremities, they frequently apply excessive pressure in doing simple manual operations. This pressure is sufficient to damage the the tissue to the point where further amputations are often necessary. In the same way, patients wearing special shoes designed to fit around their deformities may be subject to unfelt severe pressures which can further damage their remnant limbs. Special gloves or socks are provided with pressure sensitive capsules which release dyes when crushed. By studying the pattern of dye release, a patient can become aware of the areas of his hand or foot being subjected to dangerous pressures. This technique was developed at the U.S. Public Health Hospital at Carville, Louisiana[4-].

The medical profession and the pharmaceutical industry have recognized for a long time that placing a drug into the general body circulation (described as systemic treatment) is inefficient. In recent years, there has been a big increase in efforts to develop targeted delivery of drugs. In targeted delivery, one delivers the drug to where it is needed without exposing the rest of the body to the therapeutic substance. For example, the Alza Corporation has developed an alternative system for administering hormone contraceptive preparations without taking the pill. The technique they use is a form of encapsulation. To prevent pregnancy, the material is encapsulated into a strip of plastic. A relatively massive capsule can be prepared using microcapsules pressed into a block to create a porous body out of which the chemical can dissolve slowly. The strip of loaded plastic is positioned in the uterus on a cross bar. Experiments have shown that a year's protection against pregnancy can be achieved with the equivalent of one day's dose given in the form of pills. Not only is a much smaller amount of material required for this targeted delivery system, but also patients do not have to remind themselves of the need to take a pill according to a schedule. Furthermore, it is well known that the orally taken contraceptive pill has caused problems for some women with respect to blood clots. By delivering the contraceptive substance directly to the uterus, the problems associated with side effects in the bloodstream are avoided[27-].

Another target delivery system developed by the Alza Corporation is used in the treatment of glaucoma. The medication is again dispersed throughout a plastic strip in such a way that it can dissolve out of the strip into the eye. This little plastic strip can be placed under the eyelid. It delivers a steady dosage of the necessary chemical over a period of up to two weeks. For elderly patients, this is much easier than having to administer eye drops. Furthermore, the steady delivery of the dose is better than the surges of medication associated with separate administration of eyedrops on an intermittent schedule. The strip of plastic is so designed that after it has given up its medication, it becomes stiff and pops out of the eye. Experiments with a similar target delivery system for treating river blindness, which is very widespread in Africa, have been encouraging. If such a treatment could be developed, it would allow a field worker to place a single strip in the eye of many patients, giving two weeks course of medication. This is usually sufficient to clear up the infection of river blindness.

Another novel delivery system for use with pharmaceutical chemicals developed by the Alza corporation is a new system for giving travel sickness medication to people. The medication is again encapsulated in a strip of plastic so that it will dissolve slowly over a period. The plastic is mounted in the center of an adhesive strip, similar to a band-aid. To avail oneself of the medication, one affixes the strip to one's skin, in the same way that one applies a band-aid. The chemical then dissolves in the sweat of the surface of the body and moves through the skin into the body system. Travel sickness protection can be obtained in this way with a low dosage over long periods. This type of travel sickness medication has been used by astronauts in the United States Space Program.

The Greek word for fat is LIPO. This has given us several technical terms such as "lipid" which is defined as "any organic compound insoluble in water but soluble in a fat". Lipids, as a group of compounds, includes such substances as oils, fats, and steroids. The Greek word SOMA means "body". By emulsifying a drug with a fatty substance, one can obtain a compound droplet which is a form of microcapsule and is described as a "liposome". When injected into the human body, a liposome appears to be a normal fat droplet. Therefore, if we can load a liposome with a toxic drug which would normally damage body cells, the fat capsule is harmless until it reaches the parts of the body which deal with the particular fatty substance used to create the liposome, or until the capsule is broken up by special procedures. Liposomes must be small enough to travel through the bloodstream without causing obstructions to the blood flow[28)31-].

Experimental work with liposomes to inject steroid drugs near to the place where they are required have shown that these oily droplets can be 50 to 100 times more effective than the straightforward injection of the steroid. For example, medical research workers at Cambridge, England have shown that liposome formulations of steroids injected into the joints of arthritic rabbits were effective at one-hundreth of the dose normally required to reduce swelling and temperature. It is believed that cell bodies in the joint which cause arthritis are the very cells which are intended by the body to clean up the fluid around the joints. It is a disturbance of this function that causes the inflammation of the joint. When these scavenger cells are presented with fat droplets in the fluid, they immediately attack them and absorb them so that the steroid preparation is delivered directly to those cells which need to be treated to reduce inflammation of the joint. The first human tests on injecting liposome forms of steroid drugs into arthritic joints were very promising.

One of the reasons why insulin must be injected rather than taken via the mouth is that the stomach chemicals destroy insulin. Professor Brenda Ryman of the Charing Cross Hospital in Great Britain has shown that diabetes can be treated effectively by giving insulin in liposome form through the mouth. The liposomes protect the insulin molecule from breakdown during its passage through the gut and ultimate absorption into the bloodstream.

Many people in South and Central America and in India, Pakistan, and parts of Africa suffer from a parasite which causes a disease known as "Leishmaniasis". It is estimated that 100 million people suffer from the disease. The most commonly fatal form of this disease involves colonization of the liver, spleen, and bone marrow by the parasites. Toxic antimony based drugs are used to kill the parasites. However, the traditional treatment with the drug damages healthy parts of the body as well as the diseased parts. If these drugs are injected as liposomes into the veins, the blood circulation takes the fat capsules to the cleaning cells of the organs infected by the parasites. Field trials with liposome injections of antimony-based drugs into mice have been very successful, and initial work with humans is beginning. Drug delivery by liposome capsule appears also to offer better treatment for malaria, bilharzia (a disease affecting millions of people in underdeveloped countries) sleeping sickness, and leprosy.

Anti-cancer drugs often severely damage living cells and the amount that can be given to destroy the cancer is limited by the amount that normal cells can tolerate. Thus, treatment becomes a delicate balance between killing the cancer cells and not killing more of the normal tissues of the body than can be repaired by the human body. For specific cancers, such as cancers of the liver and the kidneys, liposome delivery of the anti-cancer drugs also appears to be very promising.

Thus, research work has been carried out at Northwick Park Hospital, Great Britain, into the delivery of the anti-cancer drug "actinomycin", by liposome injection. Tests show that healthy tissues were largely protected from the actinomycin by the liposomes which were selectively absorbed up to 50 times more rapidly by kidney tumors than by the surrounding tissue. This selective absorption appears to come from a combination of factors. First of all, the cancer cells seem able to absorb fatty compounds more quickly than similar tissues around them. Secondly, the rich supply of blood vessels which usually surrounds tumors brings a high concentration of the injected liposomes directly to the tumor cells. Thirdly, the liposomes appear to be broken down faster by tumor cells than by ordinary body cells.

A leader in the area of liposome drug delivery is Dr. Gregoriadis who is experimenting with techniques for attaching certain chemicals to the outside of the liposome bodies so that they go directly to the cancer tumor with even higher efficiency of delivery being achieved[29-]. Other workers are exploiting the fact that liposomes can be sprayed directly into the lung so that they may prove very effective in treating lung cancer.

Drs. Weinstein and Magin of the U.S. National Cancer Institute, along with Dr. Yatvin of the University of Wisconsin, have developed a technique for releasing the drug from the liposome to the part of the body where it is required. In their experiments, a rat was injected with liposome drug formulations. At a particular part of the body where the drug was required, they raised the temperature of the body to 107 degrees Fahrenheit using infrared radiation. This temperature is just below that which causes damage to healthy cells but enough to melt the oily body of the liposomes to release the drug. This type of release mechanism is known as hyperthermia and appears to be another promising cancer treatment technique.

Yet another technique for carrying the liposomes to the immediate area where they are required has been described by workers at the Northwestern University Medical School in Chicago[32-]. They packaged the anti-cancer drug, "adriamycin", into microspheres of the protein albumin, which was also loaded with very small fineparticles of magnetite. These drug delivery microcapsules could then focus at the tumor in the body by using a magnetic field. By using the magnetic focussing of encapsulated drugs in the bloodstream, these workers were able to produce useful therapy effect with one hundredth of the previous dosage used for treatment, and without damage to the immediate tissues en route to the tumor.

Preliminary work is under way to look at the possibility of using orally administered liposomes containing drug neutralizing companions to treat drug overdoses and that are being used to assist kidney machines in clearing poisons form the bloodstream. The use of fat encapsulated drugs is a rapidly growing area of research. Part of the success of future therapies will depend upon the ability of the scientist to create droplets of a given size and loaded in a given manner with different types of drugs.

One of the main problems arising in the body when kidneys do not function properly is the build-up of a chemical known as 'urea' in the bowels. Li has suggested that one way to remove urea from the patient's intestines is to take orally a mixture of two types of liquid membrane capsules. One type of capsules would contain an organic acid and the other would contain an enzyme to give off ammonia and carbon dioxide. These gases would move out of the capsule back into the gut. The carbon dioxide can be readily eliminated through the lung but the ammonia would diffuse into the acid-containing droplets and convert them into an ammonium compound. The constitution of the wall of the droplets would be designed so that the ammonium could not get out of the capsule which would be eliminated from the body by normal bowel processes. The dose which would have to be taken by the patient would look just like a spoonful of liquid since the little encapsulated drops would not be visible and could not be tasted by the patient. The simple mixture we have discussed would be an aid to a kidney machine but more complex systems are being investigated as possible replacements for kidney dialysis machines. (Complex application of liquid membrane encapsulated enzymes in medical practice have recently been described by Li.)

A complete description of the use of microencapsulated pharmaceuticals is beyond the scope of this discussion but the interested reader will find the technical publications full of interesting ideas[40)54–].

Agricultural Uses of Microcapsules.

When fighting insect pests, scientists are trying to use natural enemies which they rear in captivity and release in the fields infested with the pest. The larvae of such friendly insects have to be fed. A useful application of encapsulation technology has been the manufacture of synthetic insect eggs which are microcapsules containing edible nutritious centres of the same size as the natural food of the larvae. The provision of such synthetic insect eggs removes the necessity of rearing another set of insects to provide food for the "friendly" insect to be used in pest control.

Any chemical susbstance emitted by an animal, fish, or insect as an odor which influences the behaviour of another member of the same species is described as a "pheromone". Pheromones are now being used by scientists to attack insect pests. By isolating the odor which attracts male insects to the female, they are able to dope an insect killing device with the necessary perfume which attracts males to their doom. Pheromone chemicals are expensive and if they are simply dabbed onto the lure, they evaporate quickly. If, however, the pheromone is encapsulated in a porous microcapsule, the lure can be coated with the microcapsules and the odor will be given off for a period of weeks at a sufficient concentration to still attract the insects. Such pheromone microcapsules are being used to combat the gypsy moth and the spruce budworm. Pheromone-based strategies against insects have the advantage that the insects cannot develop defense mechanisms against them without interfering with their own reproduction program. Furthermore, the effectiveness of such procedures can be evaluated directly since the insects killed are brought into a central location. If the costs of the procedure can be lowered, such devices will probably be much more effective than indiscriminate spraying of large areas of forests. Again, unlike sprays, the pheromones are very specific against one type of insect and do not damage other friendly insects which are required for the normal functioning of a forest.

Encapsulated food, with the capsules being about one hundred microns in diameter, forms a useful food for small fish being reared in fish farms. The usual food for such fish is chopped up material which, if the fish do not eat immediately, can cause pollution through rotting in the water. The encapsulated food, however, stays good until eaten and simulates the type of food eaten by the fish in their natural circumstances.

Experiments have been conducted with encapsulated pesticide for use against flies in cattle droppings. The encapsulated pesticide is fed to the cattle with their normal food. It is tasteless to the animal and passes through the digestive system to be released in the droppings, where it is most effective against the fly larvae which would breed in the droppings. Although such an application is still too expensive for general use, it has special applications in areas such as zoos, where there is a great need to protect the public from the swarms of flies that would breed on the dung from animals such as hippopotami, elephants, and other animals.

Experiments have been conducted by scientists at the United States Department of Agriculture to increase the percentage of unsaturated fat in milk. This was achieved by encapsulating a vegetable oil in the substance, "casein". These microcapsules were placed in the grain ration given to cows. This increased the unsaturated fat content in their milk to a substantial degree. The same scientists conducted experiments in which calves were fed milk produced by cows that had been previously fed with the encapsulated oil. Examination of the tissue of the calves showed an increase in the unsaturated fat present in the meat. Thus, microencapsulation of unsaturated oils could improve the quality of meat intended for human consumption. However, many tests would have to be performed before such meat was made available for retail sale.

The Pennwalt Corporation has developed encapsulated pesticides for use against different kinds of pests. Their process makes use of capsules with nylon-type porous walls. The trade name Penncap-M is an encapsulated form of the pesticide 'methyl parathion'. They have found that this material is just as effective against the pests as the unencapsulated product but five times safer for the worker who must use material. In fact, the protection given to the worker by the capsule wall is sufficient for the material to be taken out of the dangerous category, and cans of the encapsulated pesticide do not need to be laballed with the skull and crossbones. When performing a test on a field of sweet corn, scientists found that they could reduce the amount of pesticide used to one quarter of a pound per acre, two to four times less than the amount used in the normal spraying treatment. Furthermore, in other tests, it was found that the encapsulated product controlled insects from five to seven days in the field, whereas the unencapsulated product was only effective for one to two days. Thus, not only is the amount required per spraying smaller, but also in crops requiring several treatments, the number of sprayings can be reduced thus saving energy and pesticide[33].

The Pennwalt Corporation has also carried out tests using encapsulated synthetic pyrethrins to combat cricket infestation. The microcapsules were still giving 100% kill of crickets 56 days after an application, whereas the normal spray of the same material had a kill of 85% after one day and 54% after four days. Another insecticide marketed by Pennwalt, which is non-toxic enough to be used by homeowners, persists only one day in the field. Greenhouse tests on an experimental microencapsulated formulation of the same material was still giving 100% kill of cockroaches after 12 weeks. Anyone who has tried to kill white flies by repeated daily sprayings over several weeks can appreciate the potential benefit of this approach.

An unexpected difficulty in the use of encapsulated pesticides was encountered in the United States, when it was found that some pesticide capsules had been made so like pollen grains that bees had no means of knowing which fineparticles were pollen and which were pesticide. As a result, the pesticide capsules were collected and taken to the hive and stored as food. Later ingestion of the capsules caused high mortalities in the bee colonies. From this example, it is obvious that one must make sure that the microcapsules do not look like pollen to insects in our fields[34].

Starch xanthate capsules, manufactured by the process developed by Shasha and coworkers, have proven to be very useful in combatting weeds. The herbicide to be used is encapsulated in the starch matrix and then placed on the field at the time of planting the seeds. The capsule does not release its chemical until the time when the weather conditions are suitable for seed germination, and so it can be spread well in advance of the time it is required to control the weeds. Furthermore, it is possible to develop double encapsulated material, in which the prime capsule is given a second coating of starch xanthate. These double encapsulated materials take longer to release their material so they can be applied at the same time as the original capsules, but release a secondary dose of material later in the growing season. It is conceivable that by using different forms of capsules, one could have weed control and fertilizer material encapsulated so that they are released into the field at the appropriate times and the necessity for going over the field several times would be removed.

Nematodes are tiny thread-like parasitic worms that can cause problems for plants and animals. Plant parasitic nematodes are estimated to cause four billion dollars damage to U.S. agricultural products annually. To kill nematodes, one must treat the soil and this usually requires massive doses of the material in order to achieve a significant effect on the parasites. However, recent experiments with starch xanthate encapsulated pesticide have been very encouraging, in that when used in greenhouse tests, small doses were found to be effective for longer periods against the parasite[35)37)].

Applications of Encapsulation Technology in the Food Industry

Perhaps the best known application of encapsulation technology in food science is the fact that encapsulated flavors retain their odour and taste much longer than free flavoring agents placed in such things as gelatin desserts and chewing gum. Much play in advertising has stressed the fact that "flavor buds" (ie. microcapsules) in the gelatin or the chewing gum give you longer lasting flavour. Another interesting application of encapsulated material is in the making and storing of frozen bread dough. In the traditional process for making bread, the bubbles for aerating the dough are made by the fermentation of yeast. The same effect can be achieved by using baking powder which when in contact with an acid, generates bubbles of carbon dioxide. Thus, many recipes call for sodium bicarbonate and tartaric acid to be placed in the mixture. In frozen dough, one does not want these bubbles to be generated until one is ready to cook the product. Therefore, the sodium bicarbonate and tartaric acid are encapsulated with a wall material that does not dissolve in the water of the frozen dough until the material is thawed out and heated.

Salt interferes with the action of yeast and in the domestic situation, one compensates for this by adding extra yeast to the mixture. In the mass baking of bread in large scale bakeries, this is not a satisfactory solution and a recent innovation using encapsulated salt promises to solve this problem. In this situation, the salt is coated with a wall which does not break down until the temperature of the baking bread or food product is reached. Such salt is known in the food industry as "enrobed" salt.

Vitamin C is not very stable on the shelf or in the cooking process. However, encapsulated vitamin C has a much improved shelf life. The wall substance can be designed to protect vitamin C even at normal baking temperatures so that the vitamin C is not degraded in a baked product and is still available for nutritional purposes. (Note : Even such well known compounds as aspirin tend to degenerate on the shelf, and encapsulation of aspirin increases the shelf life.) In the food industry, many of the capsule walls are made from specially treated oil which transform to a wax-like, edible, substance in the treatment process.

Iron deficiency is still a major problem among many groups in the United States. The treatment of the public bread supply with iron material to combat this problem is made difficult by the instability of some iron compounds during the baking process. Recently the development of encapsulated ferrous sulphate, which is readily available to the body, promises to overcome this problem[38−].

Convenience foods flavored with citrus-type flavourings have a limited shelf life because of the incompatibility of the acid flavours with the other ingredients. This problem has largely been overcome by the use of encapsulated citrus flavors which do not come into contact with the other ingredients until a paste or other mixture is made[39−].

Miscellaneous Applications of Microencapsulation Technology.

Some types of modern adhesives require the mixing of two components referred to as the resin and the hardener. These two chemicals then interact to form the strong adhesive. It is not always convenient to make the mixture when carrying out the joining together of two components. It is now possible to make the two glue ingedients into microcapsules and coat the surfaces to be joined with dry capsules. These are brought together under pressure so that the capsules rupture and mix with each other. The wall of the capsule can be quite thin and its presence does not weaken the final joint.

Encapsulated glue is particularly useful in carrying out underwater repairs on boats or on structural systems such as oil rigs standing on the sea bed. For such applications, encapsulated specialist adhesives have been developed which set rock hard within 30 seconds of the rupturing of the microcapsules[2-]. When rivets are used to join two pieces of metal together, they are often coated with an anti-corrosion liquid. Again, the coating of each rivet as it is put into position is not always easy. A microencapsulated anti-corrosion fluid has been developed, which enables one to coat the rivets before they are handled. The act of driving the rivet into the hole ruptures the capsules releasing just the right amount of anti-corrosion fluid in the place where it is needed on the internal walls of the riveted joint.

In the home laundry, it is useful to use both a bleach in the early stages of the washing process followed by the addition of a whitening agent. The whitening agents in the powder are the little blue crystals. When they are coated on to the fabric, they absorb ultraviolet light, invisible to the eye, and give out extra light in the range of visible light. This make the fabric look brighter than white! Unfortunately, many brighteners are incompatible with bleaches. In the normal wash process, the bleach is used up in two to four minutes. If one encapsulated bleach and put it into a washing powder along with encapsulated brighteners, one could arrange for the bleach capsules to rupture as soon as water was added to the mixture but arrange for the capsules of brightener to be released five minutes after the wash process began. In this way, the whole system becomes one dry powder without the necessity to use separate bleach bottles. Ultimately, it would also be possible to develop washing powders in which softener was released from a third set of microcapsules, twenty to thirty minutes after the process began.

The removal of oil and fat stains from clothing often requires the use of an oil solvent which may be either toxic or inflammable. To store a bottle of such substance with subsequent overuse of the material forms a domestic hazard. A new product has been evolved in which a piece of disposable cleaning cloth is coated with encapsulated cleaning material. When a spot has to be removed from a fabric, the act of rubbing the spot with the coated disposable cleaning cloth ruptures the capsule to release a sufficient amount of fluid for the cleaning process. One could sell such a product in a package of ten cleaning tissues so that one could use them one at a time. It has been shown that encapsulated solvents can be stored for several years without the loss of significant amounts of solvent through the capsule wall, so that such a cleaning product would have a long shelf life (or purse life) and would be safe until needed.

In the design of rocket fuel, it is sometimes useful to include water in the fuel as a temperature moderator and also as a source of hydrogen and oxygen. To use the water as a liquid in the formulation of rocket fuel causes many problems. Encapsulated water, however, can be mixed with the other ingredients of the rocket fuel and pressed together to form a solid fuel combustion chamber. However, it is not easy to add water to gasoline in a uniform manner. Encapsulated water, however could be made of an appropriate size so that is remained in suspension in the fuel tank. The encapsulated water could assist in combustion by acting as extra hydrogen and oxygen fuel and also explosively disrupting in the heat of the combustion chamber to give a more finely divided spray of gasoline which would further improve the combustion process. Such an additive would increase the efficiency of the engine and reduce pollution. Many waxes would prove suitable as an encapsulation wall. Perhaps tomorrow's motorists will buy fuel with added encapsulated water for better mileage.

In our discussion of medical applications of encapsulated products, it was mentioned that one can determine skin temperature by spraying encapsulated liquid crystals onto the skin. The same technique can be used to measure the temperature of moving mechanical parts. For example, liquid crystals have been sprayed onto the outside of a wheel drum of a car and the temperature rise, caused by the braking action, appeared as colored contours on the drum[1-].

Anyone who consistently reads upscale "women's magazines" such as Vogue or Mademoiselle must have noticed the proliferation of perfume ads employing microencapsulation technology. A trace of perfume is held inside a spot of weak adhesive until the opening of the pages causes the microcapsules to burst and release the scent. This phenomenon has led creative marketers to add microencapsulated fragrances to printing inks (such as chocolate to brown ink, used to depict chocolate in newspaper advertising) in a continuing effort to diversify a product's appeal to the reader's senses.

Dry Microencapsulation In Advanced Materials

Ceramicists have demonstrated that one can make novel compounds out of metal and ceramic material (cermets) by dry mixing the ingredients followed by pressure treatment. Thus in **Figure 10** a novel material which contains a conducting path of a metal network formed by the collapsed coatings of metal coated ceramic material is shown. Such networks can give materials with desired conductive properties as well as tailor-made strength structure[17,18-].

This example is only meant to show the possibilities inherent in applying microencapsulation technology to composite powders of metal, ceramic and/or polymer constituents. A review of such applications is beyond the scope of this article.

Acknowledgements

The author wishes to thank the many people who provided information on encapsulated products and their use.

References

1) A. C. Watson, "Microencapsulation", Science Journal, February 1970.
2) H. W. Mattson, "Miniature Capsules", International Science and Technology, April 1965, pp. 66-76
3) W. Sliwka, "Microencapsulation", Agnew Chemical International Edition, Vol. 14, No. 8, 1975, pp. 539-551.
4) J. T. Goodwin, and G. R. Somerville, "Microencapsulation by Physical Methods", Chemical Technology, Vol. 4, October 1974, pp. 623-626.

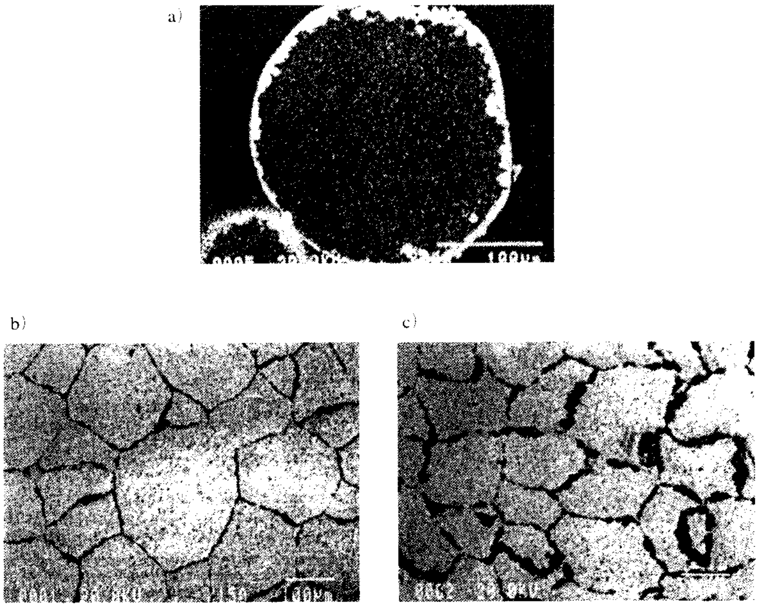

Fig. 10 Mechanofusion can create microcapsules of material which can be compressed to create composite materials of desirable structure.

(a) X-ray micrograph (Ni, $K\alpha$) of the microcapsule after 4500 s treating at 11.7 rps.

(b) and (c) Nickel network formed along the interface between contiguous encapsulated fineparticles after hot pressing, (b) $1\mu m$ nickel coated onto alloy particles, (c) $0.02\mu m$ nickel coated onto alloy particles[19-].

5) J. R. Nixon, "Microencapsulation", review in New Scientist 10 June 1976, p. 595.
6) "New Life For Microcapsules", news story in Chemical Engineering October 1st, 1984, page 22-25.
7) Coating Place Inc., Box 248 Verona, WI 53593. Application literature describing many uses of microencapsulated products are available from this corporation.
8) Glatt Air Techniques Inc., 520 livingston Street, Norwood, New Jersey, U.S.A., 07648.
9) Djinnii Industries Incorporated, 153E. Hellena Street, Dayton Ohio. 45404. This company undertakes the development of custom microencapsulation systems and has issued a series of application sheets describing various applications of the new technology.
10) Custom Microencapsulation is undertaken by the R.T. Dodge Company 55 West Park Rd, Dayton, Ohio, U.S.A., 45459.
11) Encapsulation Systems Incorporated, P.O. Box 350 Darby Pennsylvania 90213 U.S.A.
12) This aspect of mixing technology is discussed in detail in the forthcoming book, "Powder Mixing" by B. H. Kaye, Chapman Hall, 1993.
13) W. Pietsch, "Size Enlargement by Agglomeration", John Wiley and Sons, 1991.
14) The electrostatic encapsulation technique was developed by the fineparticle section of the IIT Research Institute, 10 West 35th Street, Chicago, Illinois, U.S.A.
15) Technical literature from the Hosokawa Micron Corporation, No. 9, 1-chome, Shoudai Tajika,
Hirakata-shi, Osaka 573 Japan.
16) Nara Machine Company Limited 5-7-2 Chome Ionan - Jima, Ohta-Ku, Japan, process is handled by the Beepex Corporation in North America.
17) K Tanno, "Current Status Of The Mechanofusion Process for Producing Composite Particles", KONA No. 8, 1990 Page 74-82.
18) M. Satoh, K. Higashi, K. Miyanami, S. Tanimura, K. Tsuji, H. Inada, K. Kojima., "Application of Powder Coating Method To Dispersions of Fine Nickel Powders Into Silver Nickle Alloy Matrix", Powder Technology 70 (1992) 71-76
19) T. Ishizaka, H. Hirotaka, I. Kenichi, K. Norio, Y. Kouichi, K. Masumi, "Complexation of Aspirin with Potato Starch and Improvement of Dissolution Rate by Dry Mixing", Chem. Pharm. Bull, 36(7), 1988, Pgs. 2562-2569.
20) T. Ishizaka, H. Hirotaka, K. Yuji, O. Kenji, K. Toshio, K. Masumi, "Preparation of Drug-Diluent Hybrid Powders by Dry Processing", J. Pharm. Pharmacol, 1989, 41, Pgs. 361-368
21) M. Koishi, T. Ishizaka, T. Nakajima, "Preparation and Surface Properties of Encapsulated Powder Pharmaceuticals", Appl. Biochem. Biotechnol., Vol. 10, 1984, Pg. 259-262.
22) M. Koishi, H. Hirotaka, I. Takafumi, M. Takashi, K. Toshio, K. Kenji, "Dry Impact Blending Preparation and Properties of Encapsulated Powder Nylon 12", Chimicaoggi - luglio-agosto, 1987, Pgs. 43-45.
23) M. Koishi, I. Takafumi, "Mechanochemical Encapsulation Process by Dry Blending", Controlled Release Systems : Fabrication Technology, Volume 1, Edited by Dean S.T. Hsieh, Chapter 6 in CRC Press, Inc. 1988.
24) G. Baxter, "Microencapsulation Technology and Modern Business Forms", Tappi, Vol. 60, No. 5, May 1977, pp. 84-86.
25) See news item "The Tatoo with a Fruity Scent" New Scientist 28, February 1985.
26) O. S. Celawry, H. S. Celawry and J. F. Holland, "The Use of Liquid Crystals for Thermographic Measurement of Skin Temperature in Man", Molecular Crystals, Vol. 1, 1966, pp. 495-501.
27) Literature on these devices is available from The Alza Corporation, Pagemill Road, Palo Alto, California, U.S.A.
28) D. Lasic, "Liposomes", American Scientist Volume 8, January/February 1992 page 20-31
29) D. Lasic, "Liposomes From Physics To Applications", Elsiver Science Publishing Company, 1992.
30) Liposome Technology Incorporated, 1050 Hamilton Crt, Menlow Park, CA 94025.
31) E. Mayhew, G. Nikolopolus, and A. Sicilino, "An Advanced Technique for the Manufacture of Liposomes", R & D Magazine December 1985, Page 36-41

32) S. W. May and N. N. Li, "Liquid Membrane Encapsulated Membranes", published in Bio-Medical Applications of Immobilized Enzymes and Proteins, Thiomas Ming Swi Chang editor, Vol. 1, Plenum Press, 1977, pp. 171-190.
33) Information on the Pennwalt encapsulation process is available from The Pennwalt Corporation, 900 1st Avenue, King of Prussia, Pennsylvania, U.S.A., 19406
34) R. J. Barkerm, Y. Lehner and Z. Kunzmann, Fur Naturforschung, Vol. 34C, p 153. See also "Small is not Beautiful for Bees", news story, New Scientist, 5 April 1979.
35) B. S. Shasha, "Methods for Testing and Factors Affecting the Rate of Release of Encapsulated Products prepared via Starch Xanthate", presented at the Fifth International Symposium on Controlled Release of Bioactive Materials, National Bureau of Standards, Gaithersburg, Maryland, U.S.A., 14-16 August, 1978.
36) W. Doane, B. S. Shasha and C. R. Russel, "Encapsulation of Pesticides within a Starch Matrix", A.C.S. Symposium Series No. 53, 1977, pp. 74-83.
37) J. Feldmesser and B. S. Shasha, "Evaluations of Controlled Release DBCP-Starch Xanthide Granules in Laboratory and Greenhouse Soil Tests", report issued by the U.S. Department of Agriculture, Beltsville Agricultural Research Centre, West Beltsville, Maryland, U.S.A., 20705.
38) "Uses for Microencapsulation in Food Additives", Cereal Science Today, Vol. 17, No. 4, April 1972.
39) Many applications of encapsulated products in the food industry have been developed by The Balchem Corporation, P.O. Box 175, Slate Hill, New York, U.S.A., 10973.
40) J. Newell, "Emulsified Drugs Find Their Targets", Spectrum, No. 156, 1978, pp. 6-7, Published by the Central Office of Information, London, England.
41) J. Schmeck, "Anti-Cancer Missiles", news story in the Globe and Mail, Science section, Monday, 21 May, 1979.
42) K. Widder, G. Fouret and A. Senyei, Journal of Pharmaceutical Sciences, Vol. 68, p. 79.
43) M. H. Gutch, "Microcapsules and Other Capsules Advances to 1975", Noyes Data Corporation, Parkridge New Jersey, 1979.
44) H. P. Merkel, P. Speiser, "Preparation and in vitro evaluation of cellulose acetate phthalate coacervate microcapsules", J. Pharm. Sci., Vol. 62, 1973, Pg. 1444.
45) A. Nakagawa, T. Ishizaka, K. Yano, M. Koishi, "Encapsulation of Granules by dry blending method and drug release", J. Pharm. Dny., Vol. 7, 1984, Pg. s31.
46) A. Nakagawa, I. Takafumi, Y. Koichi, K. Masumi, "Granule Surface Modification by Dry Mixing and Applications to Sustained Release Preparations", Material Technology, Volume 2, No. 10, 1984.
47) T. Nakajima, T. Ishizaka, M. Koishi, "Coating of Drugs By Powder-Powder Blending Method", J. Pharm. Dyn., Vol. 7., 1984, Pg. s-21.
48) J. N. Staniforth, J. E. Rees, "Electrostatic Charge Interactions in Ordered Powder Mixes", J. Pharm. Pharmacol., Vol. 34, 1982, Pg. 69.
49) J. N. Staniforth, J. E. Rees, "Powder Mixing by Triboelectrification" Powder Technology, Vol. 30, 1981, Pg. 255.
50) W. J. Theil, L. T. Ngugen, "Fluidized Bed Film Coating of an Ordered Powder Mixture to Produce Microencapsulated Ordered Units", J. Pharm. Pharmacol., Vol 36, 1984, Pg. 145.
51) W. J. Thiel, L. T. Nguyen, F. J. Sberna, "Content Uniformity of Microdose Tablets (dosage 1 ug-10mg) Produced by Fluid Bed Granulation of Interactive Mixtures", Ibid. Vol. 38, 1986, Pgs. 335-343.
52) W. J. Thiel, L. T. Nguyen, P. L. Stephenson, "Fluidized bed granulation of an ordered powder mixture reduces the potential for ordered unit segregation", Powder Technology, Vol. 34, 1983, Pg. 75.
53) H. Toida, T. Ishizaka, M. Koishi, "Preparation of Vinyl Face Masks Containing Titanium Dioxide Modified Nylon 12 Powder", Cosmetics and Toiletries, 94(12), 1979, Pgs. 33-37.
54) K. Ukita, K. Minoru, H. Hirotaka, K. Masumi, "Characterization of Powder-Coated Microsponge Prepared by Dry Impact Blending Method", Chem. Pharm, Bull. 37(12) 1989, Pgs. 3367-3371.

Pore Size Distribution of Cast, Compressed and Lightly Sintered Alumina with Preliminary Mechanical Treatments †

Katsuhiro Kobayashi and Mamoru Senna
Faculty of Science and Technology,
*Keio University**
Claus Bernhardt and Thomas Zschoge
*KAI e.V., WIP Gruppe Feinstkornherstellung***

Abstract

Effects of various mechanical pre-treatments and grinding aids on the pore structure of cast green compacts with and without post-compression, and lightly sintered body of alpha alumina were studied. Alumina powders were mechanically activated by a vibration mill, using grinding balls made of polyamide-coated steel (PS) and sintered Si_3N_4 *(SN). Milled products were redispersed by subsequent wet grinding with and without an additive, dextran. PS balls brought about compacts and sintered bodies denser than those treated by SN balls. Wet-grinding and redispersion by a centrifugal ball mill with dextran resulted in by far a better dispersion and hence denser compacts. Dextran lead to the smaller average pore, but broader pore size distribution. The preferential importance of state of dispersion in the green compacts over the mechanical activation was revealed in the present system.*

1. Introduction

Higher sinterability is always desirable for ceramic fabrication. Mechanical activation is expected to have positive effects for these purposes. As a matter of fact, attempts were made to lower the sintering temperature and density or strengthen the sintered products [1-5]. It is often recognized, on the other hand, that the formation of agglomerates during mechanical treatment brings about negative results [6]. Existence of agglomerates is quite serious when they cannot be destroyed during subsequent molding process, since they cause the inhomogeneity of the structure [7]. Consequently, it is required to have active and yet well dispersed, homogeneous fine powders as starting materials for sintering.

High activity for sintering and good dispersibility cannot always be fulfilled simultaneously. Wet grinding, for example, is suitable for better dispersion but not always for mechanical activation. An idea of mechanical activation in air and subsequent redispersion in a wet process seems, therefore, to be worth trying. When the agglomerates were disintegrated during molding, then their existence is not particularly harmful [6]. It is therefore also important to compare the results obtained by different molding methods.

The condition of mechanical activation plays also an important role for the quality of ground product [8]. Apart from the choice of grinding machine and its operating condition, the choice of the grinding media affects the properties of the products significantly, as well [9]. The aspect is particularly important with the advent of high quality grinding media such as polymer coated or those made by non-oxide, tough ceramics.

The present study deals with such techniques of mechanical activation and redispersion. Pore size distribution of cast and compressed compacts as well as the lightly sintered body was examined as a typical characteristic of the pretreated alumina, since it is sensitive to the structure and homogeneity of the products and hence suitable for the present evaluation.

---

* 3-14-1 Hiyoshi, Kohoku-ku Yokohama 223 JAPAN
TEL. 045-563-1141

** Cheminitzer Straße 40, D-0-9200 Freiberg, FRG
TEL.+49-3731-70221

† Received September 9th, 1991

2. Experimental

Materials and mechanical pre-treatments : For the experiments alumina type CTB7 (Alcoa) was used as starting material. Its granulometric properties released by the manufacturer are : specific surface area 0.6 - 0.9 m^2 g^{-1} and the median particle size (d_{50}) ca. 3 μm.

The dry mechanical activation was carried out in a special vibration mill developed by the former Forschungsinstitut für Aufbereitung (FIA), Freiberg, with the amplitude as high as 7 mm. After grinding for 4h in air, the samples were either taken from the mill or mixed with water and subjected to redispersion for 2 to 10 min in the same mill. After drying, the samples were dispersed in a pin-mill, Contraplex (63C, Alpine), with its peripheral velocity 200 ms^{-1}. Another dispersion technique was carried out by using dextran as a dispersion aid. 0.5 g of dextran (Dextran 40, Meito) was added to 10 g alumina and ground for 3 h in air with a planetary mill (Fritsch). A 300 cm^3 alumina vessel and 14 pieces of 21 mm balls of the same material were used for that purpose. The conditions for grinding and redispersing are summarized in **Table 1**.

Table 1. Pre-treating condition

Notation	Grinding[a)]	Redispersion[b)]
Z0D	none	none
Z0D	none	with alumina ball with dextran
Z68	silicon nitride	none
Z68B	silicon nitride	with alumina ball
Z71	silicon nitride	RD 2min (disintegr.)
Z61	polyamide	none
Z61D	polyamide	with alumina ball with dextran
Z64	polyamide	none
Z67	polyamide	RD 10min (disintegr.)

a) for 7h, b) for 3h

Molding and firing of powders : Powdery materials were dispersed into a liquid medium comprising 25 vol% ethylene glycol and 75 vol% water, containing 0.01N-NH_4Cl as a supporting electrolyte, to give a slurry of 10 vol%. The pH of the suspension was adjusted at 8.5±0.05. The material was then cast into a cylindrical vessel with a perforated bottom and filtrated under reduced pressure of 600 torr gauge to obtain a disc-shaped cake. The filtered cake was subsequently dried at 50°C for 4 days in open air.

Some of the cast compacts were post-compressed uniaxially in a cylindrical mold at 78MPa. The dried cake and post-compressed tablets were then fired at 1450°C for 0.5 h in air.

Characterization of the materials : Granulometry was carried out mainly by using a centrifugal sedimentation method (CAPA500, Horiba). The pore size distribution was determined by a mercury porosimeter (Carlo Elba 2000).

Results and discussion

Powder characteristics : The median Stokes diameter, d_{50}, of particles is shown in **Table 2.** The difference in d_{50}, the median particle size, scattered in a relatively narrow range between 3.7 - 2.6 μm, in spite of different main- and post-grinding conditions. The BET specific surface area was measured for some representative samples. It increased by 50 - 60% after redispersing treatment.

The scanning electron micrographs show that the primary particles of mechanically activated alumina was in the submicron regime, as shown in **Fig. 1**.

Table 2. Characteristics of powders

Sample	BET surface area (m^2g^{-1})	Median particle size (μm)	Percent smaller than 10μm (%)
Z0	0.6-0.9*	3*	
Z0D		2.7	
Z68	1.8	2.8	91.0
Z68B		2.6	91.0
Z71	2.9	2.7	93.2
Z61	1.7	3.6	85.5
Z61D		2.8	
Z64	2.4	3.7	96.0
Z67	2.6	3.6	97.0

*Guaranteed by Alcoa

Density of the compacts : As shown in **Table 3**, the relative density of the green compacts was around 45% for the samples ground by SN and PS balls when they were cast formed. The change in the green density was only a little in spite of the different methods of redispersion. The use of dextran brought about an extraordi-

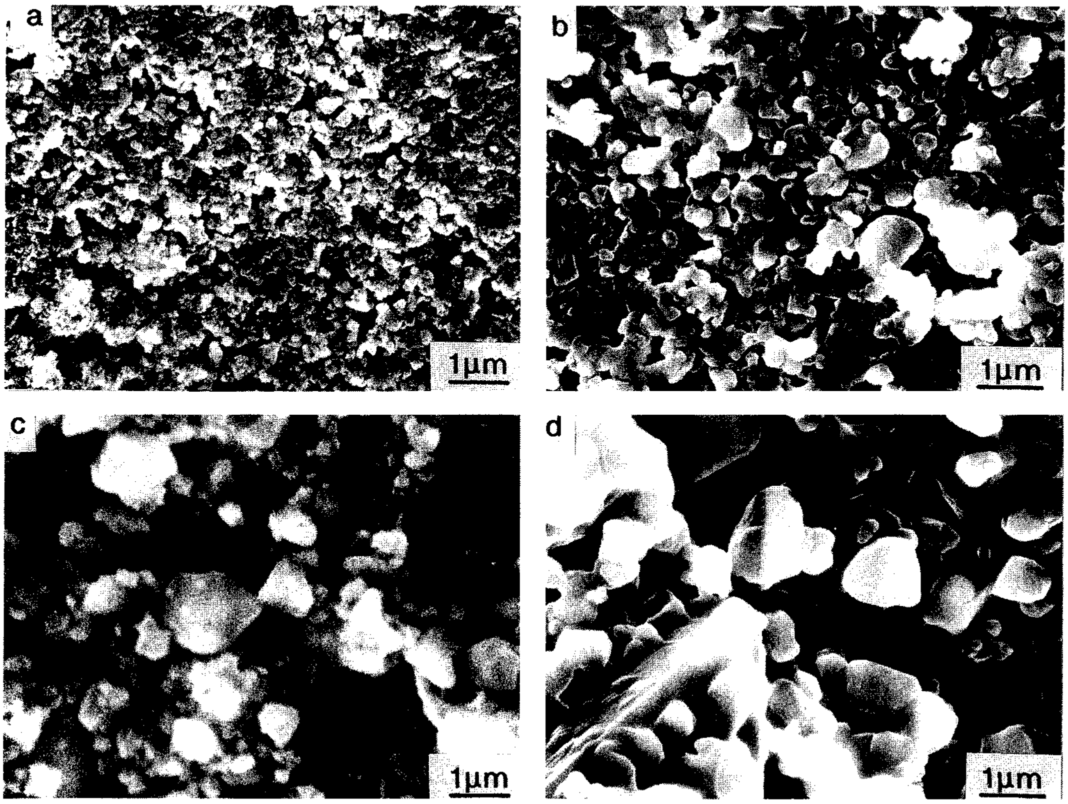

Fig. 1 Scanning electron micrographs of the compacts.
(a) Sample : ZOD-green compact
(b) Sample : ZOD-sintered body
(C) Sample : Z61D-green compact
(d) Sample : Z61D-sintered body

Table 3. Characteristics of green compacts and fired bodies (casted)

Sample	Relative density		Median pore diameter		Schrinkage	Pore growth
	Green	Sinter	Green	Sinter		
	(%)		(nm)		(%)	(%)
Z0	—	42.8	—	758	—	—
Z0D	60.0	62.1	127	226	3.5	78.0
Z68	47.2	51.0	368	389	8.1	5.7
Z68B	43.1	47.9	368	551	11.1	49.7
Z71	47.5	46.1	253	538	0	112.6
Z61	44.7	54.7	572	659	22.4	15.2
Z61D	56.8	64.0	176	472	12.7	168.2
Z64	47.5	58.1	475	603	22.3	26.9
Z67	46.4	57.4	510	601	23.7	17.8

Table 4. Characteristics of green compacts and fired bodies (post-compressed)

Sample	Relative density		Median pore diameter		Schrinkage	Pore growth
	Green	Sinter	Green	Sinter		
	(%)		(nm)		(%)	(%)
Z68B	55.1	58.5	240	249	6.2	3.7
Z71	52.4	56.5	259	317	7.8	22.4
Z61	61.2	67.6	248	378	10.5	52.4
Z64	60.4	67.1	245	359	11.0	46.5
Z67	59.6	66.4	251	345	11.4	37.5

narily high green density, which will be discussed later.

For the compressed materials, the green density increased up to 61% as shown in **Table 4**. The increase in the green density with respect to the cast green compacts was slightly more remarkable for the samples ground by PS balls than by SN balls. Mechanical compression was more effective for densification on the samples ground with polyamide coated steel balls (SP).

In spite of similar or even lower densities, the sintered density of the cast bodies obtained from the powders ground by PS balls resulted in a significantly higher density as compared with those ground by SN balls. In the case of post-compressed bodies, the difference between those ground by PS and SN balls was even larger. The difference in the shrinkage, on the other hand, was smaller between PS and SN balls in the case of the post-compressed bodies. It is therefore concluded that the superiority of the grinding with SP balls over SN balls is attributed to the higher densification ability of the pretreated powder on casting and post-compression.

The difference in the densification after post-compression is attributed to the difference in the change in the state of the agglomerates formed during dry grinding.

Pore size distribution : The results of porosimetry are also summarized in **Tables 3** and **4**, as well as **Figs. 2** and **3**. The median pore size of the cast green compacts decreased significantly by post-compression. For the cast bodies, those preliminarily ground with polyamide-coated balls was much larger than those ground by SN balls. For the post-compressed compacts, no significant difference in the median pore diameter was observed between PS-ball treated and SN-ball treated powders. The larger change for the samples ground with SP would thus mean that the larger and more brittle agglomerates were formed, compared with those ground by SN balls.

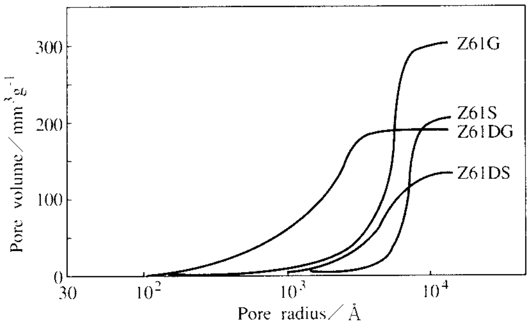

Fig. 2 Cumulative pore size distribution curves for cast compacts.
G : green compact, S : sintered body

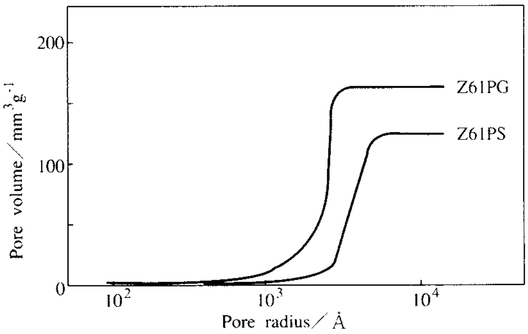

Fig. 3 Cumulative pore size distribution curves for cast and post-compressed compacts of sample Z61.
G : green compact, S : sintered body

It is also to be noted that the pore size distribution is broader in the compacts of powders ground by SN balls than those ground with PS balls. The median pore size and the breadth of the pore size distribution decreased on firing.

From the foregoing it is clear that the post-compression at 78MPa brought about the significant break down of the agglomerates formed during dry grinding. Similar disintegration was obviously not achieved by the mechanical redispersion of these agglomerates by using wet vibration mill.

The median pore size of the samples treated with dextran was much smaller than any other samples. This is a clear indication, that the dextran used during grinding brought about a very good dispersion state, which could not be alternatively achieved even through a post-compression.

The sintered body of the samples activated by polyamide balls showed particularly narrow pore size distribution, but very large median pore size. In contrast, the average pore size of those ground with dextran showed pores much smaller than any other samples, but a little broader pore size distribution.

The grain growth of alumina in the present study is not expected to be attributed mainly to the mechanical activation. The degree of amorphization, determined from the X-ray diffraction intensity was at most 30% for Z64. For all the other samples, the degree of amorphization was much smaller.

Addition of dextran : One of the most remarkable results obtained by using dextran is the green density increase of the sample Z0. Dextran was chosen as an additive from our experience with its use as a dispersing aids for Nb_2O_5 [10] . In spite of the seemingly mild wet grinding, the particle size decreased down to 2.7 μm, the relative density of the cast body was the highest of all, i.e., 60.0% and the median pore size was by far the smallest, i.e., between 130 and 180 nm. The shrinkage of the compacts of Z0D and Z61D, i.e., the powder specimen obtained by using dextran, was particularly small. Therefore, the high sintered density reflects straightforwardly the high green density and small pore size. It is also to be noted that the pore growth was very large and the pore size distribution became wider on heating.

When the dextran brings about a mere homogeneous size reduction and good dispersion, the pore size distribution after sintering would not significantly be widened. It is therefore assumed that some kind of inhomogeneity might have been existed after grinding with dextran. Nevertheless, it is evident that dextran serves as a particularly good dispersing aid of alumina. The abundant -OH group imparted by dextran brought about a rich hydration layer which made the state of agglomeration in aqueous media much softer to give a well compacted cast body, which, in turn, made the volume diffusion easier. More detailed mechanism of dextran absorption is yet to be elucidated.

4 Conclusion

Mechanical activation has been shown in the literature to be effective for the promotion of sintering. The present experimental results showed, that, in addition to this, the formation of agglomerates and their resistance against deagglomeration played a serious negative role on the densification of green compacts as well as sintered bodies.

The relatively small mechanochemical effects in the present study are considered to be attributed to the insufficient mechanical stress, for one thing, due to the low density of the grinding balls like Si_3N_4, and to the reduced impact in the case of plastic coated steel balls.

For the purpose of deagglomeration, subsequent wet grinding (post-grinding) and post - compression of the green compact were carried out. In spite of similar granulometric properties of the products of post-grinding, the addition of surfactants like dextran was revealed to be quite effective for the purpose of obtaining high green and sintered densities.

Post-compression brought about denser compacts with smaller pores for all the powders. It was not possible, however, to reach the level of the products obtained by using dextran.

References

1) D. Lewis and M.W. Lindrey, J. Am. Ceram. Soc., **49** (1966) 49.

2) B. Hoffmann, Silikattech., **23** (1972) 224.

3) K. Steier and W. Fuerstenau, Chim.-Ing. Tech., **48** (1976) 569.

4) G. Werner, Freibergerg. Forsch. -H., A779 (1987) 127.

5) M. Kume and M. Senna, Funtai oyobi Funmatsuyakin, **33** (1986) 344.

6) J.W. Halloran, in J.A. Mangels (Ed.) Advances in Ceramics, vol. 9, Am. Ceram. Soc., Ohio 1984, p.67

7) T. Iwamoto and M. Senna, Funtaikogaku Kaishi, **12** (1984) 774.

8) C. Bernhardt and H. Heegn, in "Proceedings of the International Symposium on Powder Technology" (Ed. G. Jimbo) Kyoto, 1981, p. 442.

9) K. Tanaka, K. Minai, K. Wakino and I. Kamii, Zairyou, **35** (1986) 54.

10) T. Ikeya, Y. Hiratsuka and M. Senna, to be published.

Applications of X-Ray Computed Tomography in Particulate Systems †

C. L. Lin, J. D. Miller, and A. Cortes
*Comminution Center, University of Utah**

Abstract

X-ray computed tomography (CT) is an ideal technique for investigating the internal structure of multiphase materials in a noninvasive and nondestructive manner. CT technology used in conjunction with specialized algorithms and advanced computer facilities can be used to provide quantitative information in addition to being an ideal medium for scientific visualization. This paper reviews some advanced reconstruction algorithms and examines two cases in which CT has been successfully used : (1) coal washability analysis and (2) density gradient determination in an air-sparged hydrocyclone (ASH) flotation.

Introduction

X-ray computed tomography (CT) technique had its origin in the medical services[1-] and is now being applied to non-medical and industrial applications[2-]. CT techniques have an inherent advantage in providing very detailed images of the internal structures of opaque materials in a nondestructive manner. Nevertheless, most of the industrial applications of CT are qualitative in nature, probably a carry over from its use in the medical field. It should be noted that CT images contain enough information to allow for the quantitative description of the object being analyzed.

This paper is divided into two major sections, the first section covers the theoretical aspects of tomography and the numerical algorithms necessary for image reconstruction. The second section deals with some examples of quantitative X-ray CT applications in particulate processing.

Fundamental Principles

Basic Theory

The relationship between the initial intensity of an X-ray beam as it leaves the source and the final intensity of the same beam after it has passed through a section of the target material can be described by the following equation.

$$I_f = I_i \exp\left[-\int_{Ray} \mu(x,y)\,ds\right] \qquad (1)$$

where :

I_i = initial intensity of the X-ray beam
I_f = final intensity of the X-ray beam
μ = linear attenuation coefficient.

Figure 1 illustrates the above mentioned equation.

An important assumption that was made implicitly in Equation 1 is that the X-ray beam

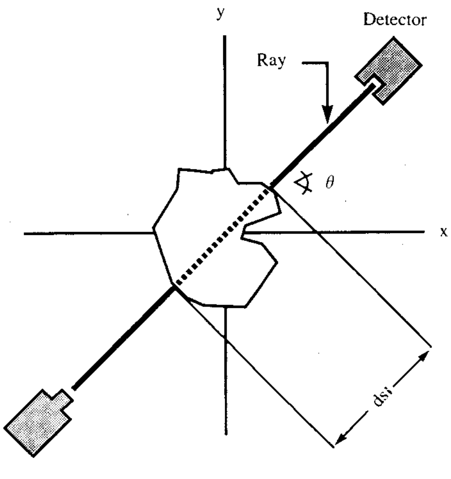

Fig. 1 A diagram showing an X-ray beam as it emanates from the source, passes through the sample, and finally is collected at the detector.

---

* 306, WBB Salt Lake City. Utah 84112, USA

† Received July 1992.

intensity is monochromatic in nature. This is not strictly true. Rearranging Equation 1 in the following manner,

$$ln\left[\frac{I_i}{I_f}\right]=\int_{Ray}\mu(x,y)ds \qquad (2)$$

shows that the left-hand side of Equation 2 is a measured quantity. This value can be obtained from the CT machine. The right-hand side of Equation 2 represents the ray integral of the X-ray beam that passed through the sample. If Ray is defined as follows :

$$x\cos\theta-y\sin\theta=Ray \qquad (3)$$

then the line integral can be written in the following manner.

$$P_\theta(Ray)=\int_{Ray}f(x,y)ds \qquad (4)$$

where :

$P_\theta(Ray)$=is the projection of the X-ray beam that passes through the sample.

Notice that the right-hand side of Equation 4 is essentially the same as the right-hand side of Equation 2. The unknown function *f(x,y)* simply takes the place of the linear attenuation coefficient $\mu(x,y)$. By using the definition of the Dirac delta function, Equation 4 can be reformulated as :

$$P_\theta(Ray)=\int_{-\infty}^{\infty}\int_{-\infty}^{\infty}f(x,y)\delta(x\cos\theta-y\sin\theta-Ray)dxdy \qquad (5)$$

Equation 5 is known as the Radon transform of the function *f(x,y)*. If we pass a series of line integrals through the unknown function *f(x,y)* at a fixed angle θ, we obtain what is called a projection *P(θ)*. This is shown in **Figure 2**.

P(θ) can be obtained by using an assemblage of sources and detectors and translating them at predefined intervals until they cover the entirety of the sample being scanned. In order to correlate the projection *P(θ)* to a reconstructed X-ray CT image, we need to use the properties of Fourier transforms[3-]. Although a very simplified and conceptual approach will be presented here, a more rigorous mathematical treatment can be found in standard texts[4,5-]. Furthermore, the treatment here will be confined to the case of parallel-beam geometry. Other geometries are treated in the references cited.

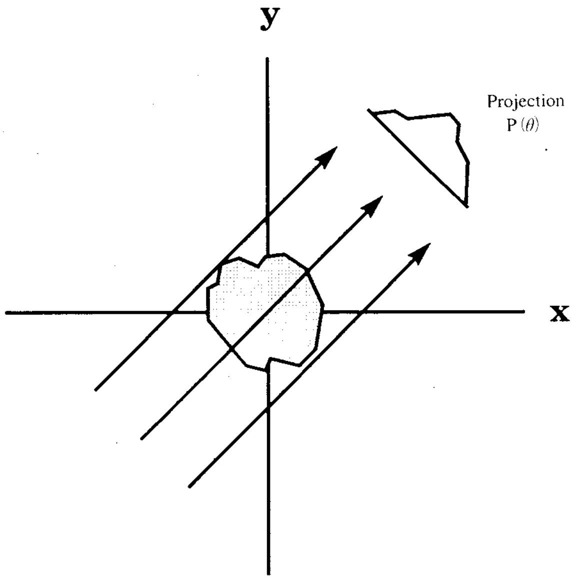

Fig. 2 An illustration showing several rays traversing through the sample at a fixed angle. The data from the series of rays are called a projection P(θ).

If a 2-D Fourier transform is performed on a function *f(x,y)*, Equation 6 would be the result.

$$F(u,v)=\int_{-\infty}^{\infty}\int_{-\infty}^{\infty}f(x,y)e^{-j2\pi(ux+vy)}dxdy \qquad (6)$$

This is illustrated in **Figure 3**. The shaded circle in **Figure 3** is the two-dimensional Fourier transform of the function *f(x,y)*. The transformed coordinates are designated as u and v.

Similarly, if a 1-D Fourier transform is performed on the projection data *P(θ)*, Equation 7 would result.

$$S_\theta(\omega)=\int_{-\infty}^{\infty}P(\theta,t)e^{-j2\pi\omega t}dt \qquad (7)$$

To relate the 1-D Fourier transform of the projection of an unknown function *f(x,y)* to the 2-D Fourier transform of the same unknown function, we make use of the Fourier Slice Theorem[5-]. As an illustration, for the angle of measurement $\theta=0$, Equation 6 reduces to

$$F(u,v)|_{\theta=0}=\int_{-\infty}^{\infty}P(0,x)e^{-2\pi(ux)}dx \qquad (8)$$

The right-hand side of Equation 8 is just Equation 7 measured at $\theta=0$. To help in visualizing the relationship of Equation 7 to Equation 8, refer to **Figure 4**. **Figure 4** shows that if a 1-D Fourier transform is performed on projection *P(θ)*, the result would correspond to the data points in the line at an angle θ in the transformed coordinate axes u and v. The u and v coordinate system represents the 2-D Fourier transform of the unknown function $f(x, y)$. This is the same coordinate system shown in **Figure 3**.

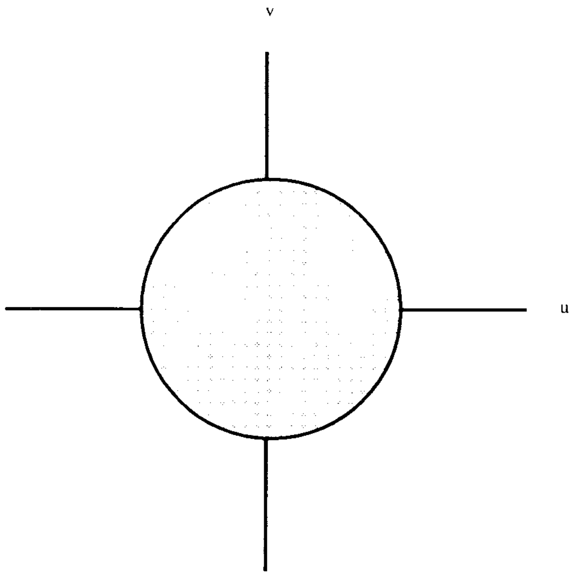

Fig. 3 An illustration showing the function f(x,y) after it undergoes a 2-D Fourier transform operation. The transformed coordinate system is designated by variables u and v.

By extension of logic, it can be concluded that, to construct a 2-D Fourier transform of an unknown function, one has to collect projection data at different angles, perform a 1-D Fourier transform on the projection data and finally plot the data on the u and v coordinate system. Once the 2-D Fourier map is completed, it is a simple matter of performing a 2-D inverse Fourier transform to reconstruct the image.

The above discussion provides a mathematical basis for the relationship between the projected data and the image reconstruction which is the foundation of CT technology. In practice, however, the above procedure is not followed. The reasons for deviating from the theoretical approach are twofold: 1) algorithm stability and 2) computational efficiency. **Figure 5** shows a block diagram for one of the procedures used to obtain an image from CT projection data. The first step is to collect the projection data from the CT machine. The next step is to perform a convolution between the projection data and a suitable filter. The filtered projection is then back-projected to obtain the reconstructed image. Additional image-processing techniques such as thresholding can be applied to obtain more pleasing images.

Back-projection is a discrete operation that mimics the operation of the CT machine but is done in the reverse manner. **Figure 6** shows a simplified illustration of the projection and back-projection operations. The upper part of **Figure 6** shows a sample conveniently subdivided into nine parts. The apparent density of each part is shown. If a ray is passed through the sample at an angle of 0 degrees, as shown by the broad gray-shaded line, it will report that the apparent density of the cross section that

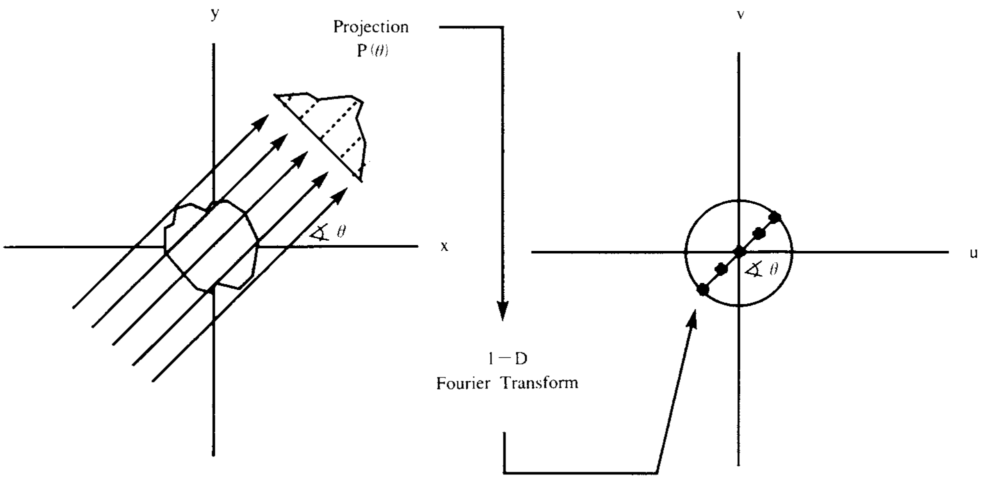

Fig. 4 A drawing showing how the 1-D Fourier transform of the projection P(θ) can be mapped into the 2-D domain of the transformed coordinate system.

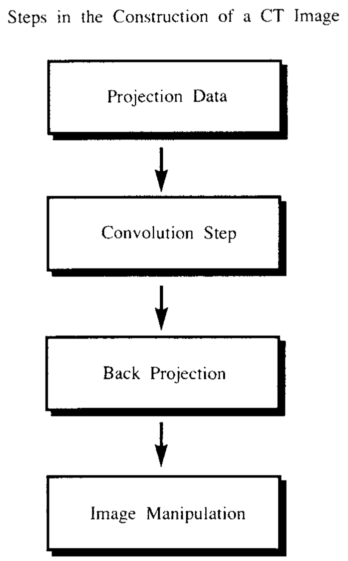

Fig. 5 A block diagram showing the steps necessary in the construction of an image obtained from a CT scanner.

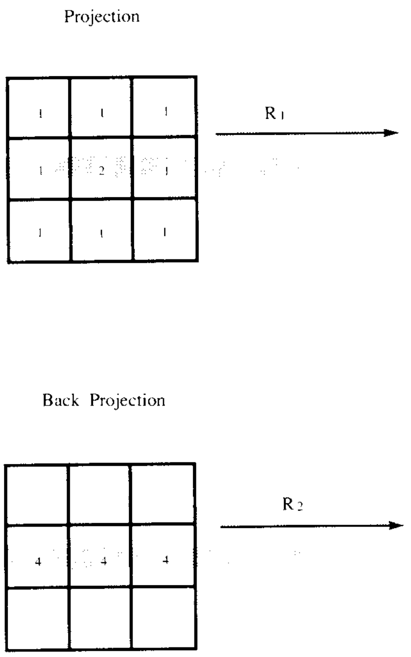

Fig. 6 An illustration showing how the projection operation determines the apparent density of the material that an X-ray beam traverses. The lower drawing shows how the back-projection operation places the calculated density in the synthetic grid designed to represent the sample being scanned.

has been traversed is 4. The value 4 represents the projected density through the middle of the sample at an angle 0 given by ray R_1. During the back-projection operation, R_2 traverses a grid designed to represent the sample being scanned and places the value 4 on all the blocks it intersects. The geometric characteristics of R_2 (location and angle) are precisely the same as R_1. At first glance, it appears that the results of the reproduction operation are very different from the values of the original sample. However, if the projection and back-projection operations are performed using a large number of angles and if the final back-projected image is normalized by the number of angles used, the reconstructed image approximates the original sample.

Advanced Reconstruction Algorithm

In order to obtain more accurate reconstruction of tomographic images, a new algorithm is being developed[6-]. This algorithm draws from the strength of the filtered back-projection methods but is iterative in nature. This approach allows for the inclusion of *a priori* information into the solution. A block diagram of the unit operations involved in the algorithm is shown in **Figure 7**. The basic steps in the new algorithm are as follows :

1. Obtain the projection data (sinograms) from the CT machine.
2. Convolve the projections with a suitable filter.
3. Perform the back-projection.
4. Normalize the resulting image.
5. Use a synthetic projector to create a new set of projection data from the reconstructed image.
6. Compare the new set of projection data with the original data from step 1.
7. Generate a set of error vectors.
8. Back-project the generated error vectors to form an error image.
9. Combine the error image with the original image to create a corrected image. If satisfied terminate the iteration, otherwise go back to step 5.

The unit operations enclosed in the dashed-lined block represent the steps normally present in a conventional CT reconstruction. All other unit operations shown represent enhancements that are introduced by the new algorithm.

The effectiveness of the new algorithm was

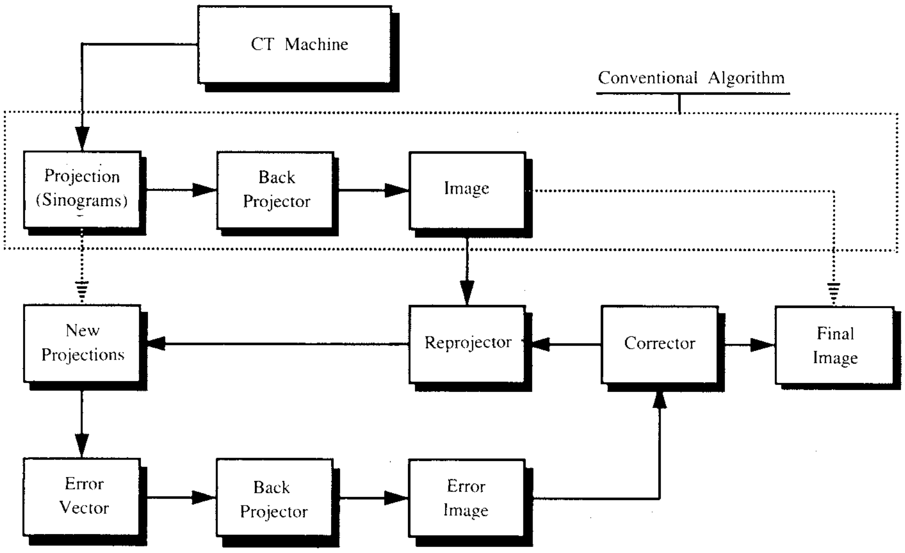

Fig. 7 A block diagram showing the various operations of the advanced algorithm. The operations enclosed in the dotted rectangle represent operations that are present in the conventional CT reconstruction algorithm.

tested by performing a numerical simulation. The simulation pattern consisted of three concentric squares. This test pattern is shown in **Figure** 8. The outermost square has a density of 4.0 g/cc, the middle square has a density of 2.0 g/cc and the innermost square has a density of 8.0 g/cc. The test pattern was chosen so that streaks emanating from the high-density square could be easily seen. The simulation was done using a 256 × 256 computational grid. All calculations were performed using a Stardent 3040 graphics workstation.

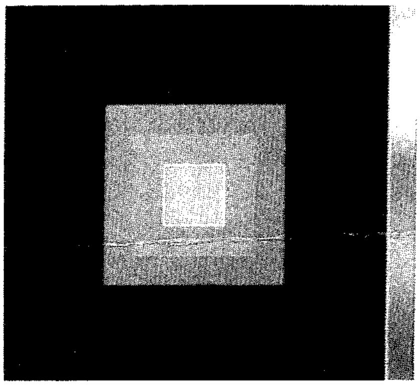

Fig. 8 The image used to test the applicability of the advanced reconstruction algorithm.

In order to quantify the overall reconstruction quality, a criterion called image error was defined. This represents the "distance" of the reconstructed image from the known original test pattern. The definition is given below.

$$\textit{Image Error} = \sqrt{\frac{(\textit{original image} - \textit{reconstructed image})^2}{\textit{original image}^2}} \qquad (9)$$

where,

original image = *the density values of the test pattern*

reconstructed image = *the density values of the reconstructed image.*

Table 1 presents the image errors calculated from a conventional filtered back-projection algorithm and from the new algorithm. The number of iterations used was 3. The results show that the new algorithm was able to reduce the reconstruction error by a factor of 2.

Table 1 Comparison of image errors obtained from the conventional filtered back-projection method and from the new algorithm after 3 iterations

	Conventional	New Algorithm
Image Error	0.0791	0.0328

Particulate Processing Applications

Coal Washability

Coal quality is determined, to a large extent, by both its calorific value and its associated mineral-matter content. The mineral-matter impurities not only decrease the heating value of steam coal but are also responsible for maintenance and pollution problems during subsequent combustion. The mineral-matter dispersion gives rise to a continual variation in particle density best described by the washability curve. A coal-washability curve is important to the process engineer because it shows the limits of any physical separation of mineral matter from coal. Thus, the washability curve provides information on the expected quality of the clean coal product.

The conventional method for determining the washability curve is based on the series of sink-float separations using heavy liquids[7-]. The steps that are necessary for this operation are as follows:

1. The coal sample is first sized into different size intervals, from 38 mm down to 0.1 mm.
2. For each size class, a suitable amount of sample is taken.
3. Then, dense liquid separations are performed for each size class-a series of binary fractionation based on density.
4. From the weight and analysis of each density fraction in step 3, the coal-washability curve for each size class is created.

In the case of X-ray CT-based washability calculation[8-], the third step of the conventional approach is replaced by a series of steps based on CT scanning of the sample and 3-D reconstruction. Thus, in similar fashion, the steps needed in constructing a washability curve are as follows:

1. The coal sample is first sized into different size intervals, from 38 mm down to 0.1 mm.
2. For each size class, a suitable amount of sample is taken.
3. Density fractionation by CT analysis.
    a. Each sample is loaded into a separated cylindrical container, placed in the CT scanner and properly aligned.
    b. CT measurements (sequential scans) are taken as the container passes through the scanner in predetermined scan spacings.
    c. Computer analysis is performed on the scan data to determine the 2-D density data.
    d. The 2-D CT images (density data) are then used to reconstruct the particles in 3-D.
    e. The particles are isolated and the mass and volume of each particle is calculated.
4. From the weight and density calculations in step 3, the coal-washability curve for each size class is created.

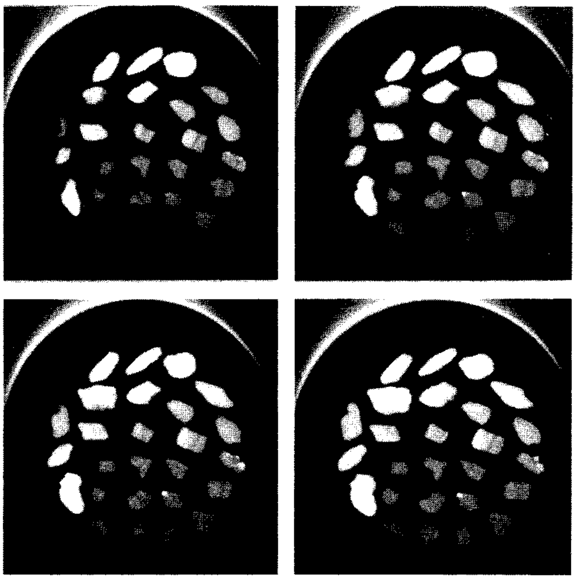

Fig. 9 Sequential 2-D X-ray CT scans of a coal sample. The grey-shaded bar at the right-hand side of the photograph represents the density scale in terms of CT number.

Figure 9 shows the sequential 2-D X-ray CT scan of the coal sample. The scale bar (CT number) located at the right-hand side of the figure indicates the relative density of the material. **Figure 10** shows the washability curve for the coal sample as obtained by both the conventional sink-float analysis and CT-based method. From these results, it is evident that coal-washability curves derived from the CT-based technique are in good agreement with the results obtained by the conventional sink-float analysis.

Air-Sparged Hydrocyclone (ASH) Flotation

The air-sparged hydrocyclone (ASH) is distinguished by its high-specific capacity for fine particle flotation in a centrifugal field. To elaborate, it is now evident that the ASH has a specific capacity of at least 100 times that of

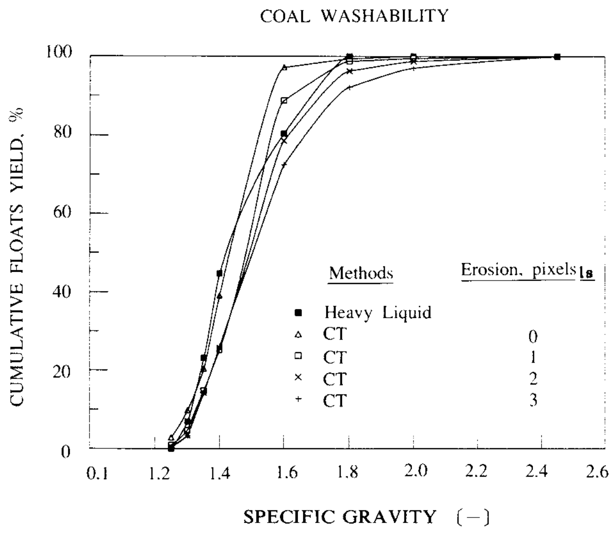

Fig. 10 A comparison of the coal-washability curve constructed using CT techniques with the coal-washability curve obtained by the traditional sink-float method.

conventional flotation equipment. The air-sparged hydrocyclone has shown promising potential for the flotation of copper porphyry ore, low-grade placer gold, auriferous pyrite ores, and various industrial minerals. Another promising application has been found to be the use of ASH for fine coal flotation. This has been demonstrated for a number of U.S. and Canadian coals. Also, attention has been given to applications of air-sparged hydrocyclone flotation technology outside of the mineral industry, including the pulp and paper industry and the food industry. The most significant development, however, is the construction of a 20-million dollar waste-paper recycling plant which will use ASH technology for the de-inking flotation.

A schematic diagram of the air-sparged hydrocylone is shown in **Figure 11**. The main features of the air-sparged hydrocylone (ASH) are a porous tube through which air is sparged and a tangential flow of the particle suspension orthogonal to the airflow. The suspension passes downward through the separator in swirl flow and a counter-current flow of the froth phase moves upward and towards the center of the device. Hydrophilic particles are thrown against the porous tube wall by the centrifugal field and are discharged at the bottom as tailings. Hydrophobic particles encounter the air bubbles which are sparged radially through the porous wall. Particle/bubble attachment occurs, and the hydrophobic parti-

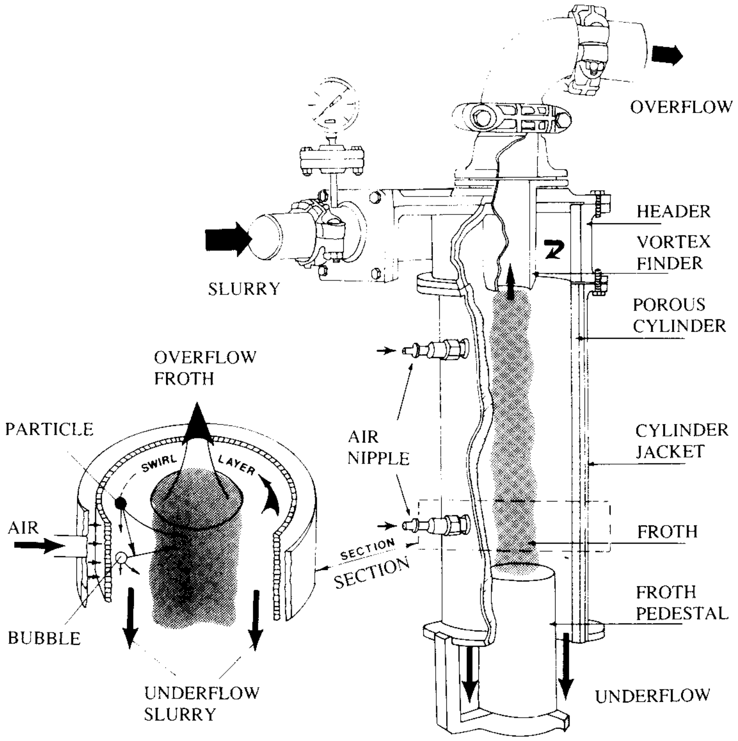

Fig. 11 A perspective drawing of the air-sparged hydrocyclone (ASH).

cles are transported into the froth phase which exits axially at the top of the cyclone through a vortex finder[9,10,11].

In order to gain a better understanding of how different particles are distributed inside the air-sparged hydrocyclone, CT scans have been performed on an operating ASH unit. **Figure 12** shows an example of the CT data obtained for a suspension of hydrophilic limestone particles (20% solids) flowing at 20 gpm with the air-flow rate of 200 slpm. In **Figure 12** the time-averaged density is plotted versus the position along a straight line for a particular cross-sectional scan of the ASH. By analyzing the scan sections made at different sections of the ASH, information regarding the density profile (time averaged) can be obtained. This information is being used to understand the fundamentals of the complex multiphase flow, optimize the operating conditions and thus improve the separation efficiency.

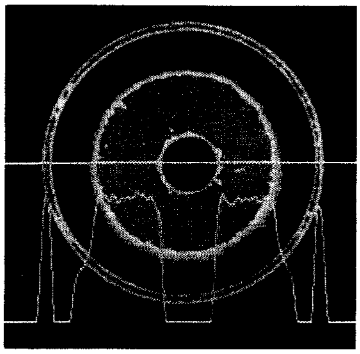

Fig. 12 ASH CT images with the reconstructed density of the segregated multiphase flow plotted with respect to radial position in the ASH at a particular elevation.

Conclusion

This paper demonstrates the effective use of CT technology in engineering applications, more specifically, to particulate systems. By using suitable algorithms, an alternative method of constructing the coal-washability curve has been developed. Furthermore, the time-averaged density profiles obtained from CT scans of an operating air-sparged hydrocyclone (ASH) have proved to be invaluable in helping to optimize the operating variables. Although the early results have been quite successful, much work needs to be done in the following areas : 1) advanced CT algorithms, 2) 3-D computer graphics, and 3) particle isolation algorithms.

Acknowledgement

The research has been supported by the Department of Interior's Mineral Institute program administered by the Bureau of Mines through the Generic Mineral Technology Center for Comminution under Grant No. G1105149. In addition, financial support from NSF Grant No. CTS 9000406 and DOE Grant No. DE FG22 90PCP0311 is gratefully acknowledged.

References

1) Herman, G. T. : Image Reconstruction from Projections : the Fundamentals of Computerized Tomography, Academic Press, New York (1980).
2) Banholzer, W. F. et al. : *Ind. Eng. Chem. Res.*, **Vol. 26**, pp. 763-767 (1987).
3) Boas, M. L. : Mathematical Methods in the Physical Sciences, John Wiley and Sons, New York (1983).
4) Rosenfeld, A. and Kak, A. C. : Digital Picture Processing, Second Edition, Academic Press, **Vol. 1** (1982).
5) Kak, A. C. and Slaney, M. : Principles of Computerized Tomographic Imaging, IEEE Press, New York (1988).
6) Cortes, A. B., Lin, C. L. and Miller, J. D. : Review of Progress in Nondestructive Evaluation, D. O. Thompson and D. E. Chimenti, Eds. **Vol. 10A**, Plenum Press, New York (1991).
7) Weiss, N. L. (Ed.) : SME Mineral Processing Handbook, AIME/SME, New York (1985).
8) Lin, C. L. et al. : *Coal Preparation*, **Vol. 9**, pp. 107-119 (1991).
9) Miller, J. D. et al. : XVI International Mineral Processing Congress, Stockholm, Sweden, E. Forssberg, Ed., Elsevier, Part A (1988).
10) Ye, Y. et al. : Proceedings International Column Flotation Symposium, AIME/SME, Phoenix, Chapter 34, pp. 305-313 (1988).
11) Miller, J. D. and Ye, Y. : Mineral Processing and Extractive Metallurgy Review, J. Laskowski, Ed., **Vol. 5**, pp. 307-329, Gordon and Breach, New York (1989).

Computer Simulation of Flow Processes in Fluidized Bed Reactors †

Björn H. Hjertager
*Telemark Institute of Technology (SiT)**
Arild Samuelsberg
*Telemark Technological R&D Centre**

Abstract

The paper outlines and exemplifies a multi-dimensional multi-phase Computational Fluid Dynamics (CFD) model for the various processes that occur in fluidized bed reactors. The model is based on the Eulerian description of the two phases: gas and particles. This means that separate conservation equations are set up for these phases. Calculations are shown for some examples that include flow patterns in circulating beds.

1. Introduction

1.1 The problem

Many different processes influence the total performance characteristics of fluidized bed reactors. Among these are the gas/particle flow and distribution, chemical reactions, and heat transfer. All these processes occur simultaneously and are intimately coupled to each other. The performance of the reactor is strongly dependent on the interactions between these processes and the geometrical design of the reactor. Because of the complexities of such problems, there are no analytical methods available that can describe in detail what is occurring inside a fluidized bed reactor. In each new reactor it is very often the geometrical details that will determine the performance of the final design of the reactor. Until recently the design of fluidized bed reactors has therefore been based on experimental work done on a laboratory and pilot-plant scale, and on extrapolation of these data to full scale by the application of various empirical scaling techniques.

These design techniques may be very expensive, and give insufficient and inaccurate information about the performance. New computer techniques for fluid flow processes have now made it possible to develop new design methods based on mathematical modelling of the basic processes that occur in the actual geometrical model of the reactor. To apply these methods, the basic conservation equations of flow, chemical reactions, and heat transfer as well as the coupling between them and the coupling between the two phases, must be solved for a multi-dimensional calculation domain.

1.2 Previous work

Gidaspow[1], has reviewed the CFD models that had evolved up until about 1985. The models at that time had demonstrated the capability to simulate some of the crucial characteristics such as bubble formation and development in bubbling fluidized beds. The models assumed a two-phase gas-particle flow with given apparent viscosities in the gas and in the particle phases. Shih et al.[2], introduced a model that takes account of the multi-sized particle problem and showed application to a sedimentation problem. The work of Tsuo and Gidaspow[3], showed that the model was able to calculate the flow patterns in circulating fluidized beds. This model had to assume an apparent viscosity for the particle phase to be able to predict the experimentally observed phenomena. The works of Ding and Gidaspow[4], and Ma and Ahmadi[5], propose to couple the apparent viscosities in the two phases by introducing turbulence models for each of the phases. A comprehensive model for two-phase flow, heat transfer and chemical reactions in a fluidized bed gasifier has been presented by Gidaspow et al.[6].

1.3 Objectives of paper

The present paper will present a two-phase

---

* TMIH, Kjolnes N-3900 Porsgrunn, NORWAY
† Received April 15, 1992.

multi-dimensional model for the processes that occur in fluidized beds for catalytic chemical reactions. The model will be verified against experimental data for isothermal flow fields in various systems.

2. Governing Equations

2.1 Fluid dynamics model

The governing equations are deduced based on the Eulerian concept. This means that the phases share the space and interact with each other. All equations are such that all volume fractions may take values between zero and one.

Based on the works of Ding and Gidaspow[4], and Ma and Ahmadi[5], the following flow model for gas particle flow may be formulated using the following dependent variables: α_g, α_p, $U_{j,g}$, $U_{j,p}$, k_g, k_p, ε_g, ε_p and p. Here the variables have the index g for the gas phase and index p for the particle phase. The variables are volume fractions, velocity components, turbulent kinetic energy, dissipation of turbulent kinetic energy and the pressure. Conservation equations written in Cartesian tensor notation may be formulated as:

Mass balances:

Gas:

$$\frac{\partial}{\partial t}(\rho\alpha)_g+\frac{\partial}{\partial x_i}(\rho\alpha U_i)_g=O \qquad (1)$$

Particles:

$$\frac{\partial}{\partial t}(\rho\alpha)_p+\frac{\partial}{\partial x_i}(\rho\alpha U_i)_p=O \qquad (2)$$

These equations are valid for catalytic reactions with no mass transfer between the phases.

Momentum balances:

Gas:

$$\frac{\partial}{\partial t}(\rho\alpha U_j)_g+\frac{\partial}{\partial x_i}(\rho\alpha U_iU_j)_g=$$
$$-\alpha_g\frac{\partial p}{\partial x_j}+\frac{\partial}{\partial x_i}\tau_{ijg}+C_{pg}(U_{jp}-U_{jg})+(\rho\alpha)_g g_j \qquad (3)$$

Particles:

$$\frac{\partial}{\partial t}(\rho\alpha U_j)_p+\frac{\partial}{\partial x_i}(\rho\alpha U_iU_j)_p=$$
$$-\alpha_p\frac{\partial p}{\partial x_j}+\frac{\partial}{\partial x_i}\tau_{ijp}+C_{pg}(U_{jg}-U_{jp})+(\rho\alpha)_p g_j+G(\alpha_g)\frac{\partial\alpha_g}{\partial x_j} \qquad (4)$$

Friction between the phases:

$$C_{pg}=150\frac{\alpha_p^2\mu_{lamg}}{\alpha_g(d_p\Phi_s)^2}+1.75\frac{\rho_g\alpha_p|\vec{V}_g-\vec{V}_p|}{d_p\Phi_s} \quad \text{when } \alpha_g<0.8$$
$$C_{pg}=\frac{3}{4}C_d\frac{\alpha_g\cdot\alpha_p\rho_g|\vec{V}_g-\vec{V}_p|}{d_p\Phi_s}\alpha_g^{-2.65} \quad \text{when } \alpha_g\geq 0.8 \qquad (5)$$

Where Φ_s is the form factor of the particles.

$$C_d=\frac{24}{Re_p}\left[1+0.15\cdot Re_p^{0.687}\right] \quad for\ Re_p<1000$$
$$C_d=0.44 \quad for\ Re_p>1000$$
$$Re_p=\frac{\alpha_g\rho_g|\vec{V}_g-\vec{V}_p|d_p}{\mu_{lam,g}} \qquad (6)$$

Shear stresses are related to the gradients of velocity components and a turbulent viscosity as:

Gas:

$$\tau_{ij,g}=\mu_{t,g}\left[\left(\frac{\partial U_{j,g}}{\partial x_i}+\frac{\partial U_{i,g}}{\partial x_j}\right)-\frac{2}{3}\delta_{ij}\frac{\partial U_{k,g}}{\partial x_k}\right]$$
$$where\ \mu_{t,g}=\mu_{lam,g}+C_\mu\alpha_g\rho_g\frac{k_g^2}{\epsilon_g};\ C_\mu=0.06 \qquad (7)$$

Particles:

$$\tau_{ij,p}=\mu_{t,p}\left[\left(\frac{\partial U_{j,p}}{\partial x_i}+\frac{\partial U_{i,p}}{\partial x_j}\right)-\frac{2}{3}\delta_{ij}\frac{\partial U_{k,p}}{\partial x_k}\right] \qquad (8)$$
$$where\ \mu_{t,p}=C_{\mu,p}\alpha_p\rho_p d_p k_p^{\frac{1}{2}}$$

$$C_{\mu,p}=0.0853[(g_o\alpha_p)^{-1}+3.2+12.182\alpha_p g_o]$$
$$with$$
$$g_o=\frac{1+2.5\alpha_p+4.5904\alpha_p^2+4.515439\alpha_p^3}{\left[1-\left(\frac{\alpha_p}{\alpha_{p,m}}\right)\right]^{0.678021}} \qquad (9)$$

Where $\alpha_{p,m}$ is the maximum solid volume fraction for a randomly packed bed. $\alpha_{p,m}$ is taken to be 0.65.

Solid stress is given by:

$$G(\alpha_g)=\frac{\partial\tau}{\partial\alpha_g}$$
$$G(\alpha_g)=G_o e^{-20(\alpha_g-0.62)} \qquad (10)$$
$$where\ G(\alpha_g)=G_o=1.0\ when\ \alpha_g=0.62$$

Turbulent kinetic energy:

Gas:

$$\frac{\partial}{\partial t}(\rho\alpha k)_g+\frac{\partial}{\partial x_i}(\rho\alpha U_i k)_g=$$
$$\frac{\partial}{\partial x_i}\left[\Gamma_{k,g}\frac{\partial k_g}{\partial x_i}\right]+\tau_{ij,g}\frac{\partial U_{j,g}}{\partial x_i}+2\cdot C_{pg}(k_p-c\cdot k_g) \tag{11}$$
$$-(\rho\alpha)_g\epsilon_g$$

Particles:

$$\frac{\partial}{\partial t}(\rho\alpha k)_p+\frac{\partial}{\partial x_i}(\rho\alpha U_i k)_p=$$
$$\frac{\partial}{\partial x_i}\left[\Gamma_{k,p}\frac{\partial k_p}{\partial x_i}\right]+\tau_{ij,p}\frac{\partial U_{j,p}}{\partial x_i}+2\cdot C_{pg}(c\cdot k_g-k_p) \tag{12}$$
$$-(\rho\alpha)_p\epsilon_p$$

Here, the effective transport coefficients are related to the turbulent viscosities as:

$$\Gamma_{k,g}=\mu_{t,g}\ \ og\ \ \Gamma_{k,p}=\mu_{t,p} \tag{13}$$

Dissipation of turbulent kinetic energy:
Gas:

$$\frac{\partial}{\partial t}(\rho\alpha\epsilon)_g+\frac{\partial}{\partial x_i}(\rho\alpha U_i\epsilon)_g=$$
$$\frac{\partial}{\partial x_i}\left[\Gamma_{\epsilon g}\frac{\partial \epsilon_g}{\partial x_i}\right]+C_{\epsilon 1,g}\cdot\left(\frac{\epsilon}{k}\right)_g\left[\tau_{ij,g}\frac{\partial U_{j,g}}{\partial x_i}+2\cdot C_{pg}(k_p-c\cdot k_g)\right]$$
$$-C_{\epsilon 2,g}\left(\frac{\epsilon}{k}\right)_g(\rho\alpha)_g\epsilon_g \tag{14}$$

Particles:
The dissipation in the particle phase is given by an algebraic equation as:

$$\epsilon_p=3.9\frac{\alpha_p g_o(1-r^2)}{d_p}\cdot k_p^{\frac{3}{2}} \tag{15}$$

where r is the restitution.

Here, the effective transport coefficient is related to the turbulent viscosity as:

$$\Gamma_{\epsilon,g}=\frac{\mu_{t,g}}{1.3} \tag{16}$$

and

$$c=\frac{1}{1+\dfrac{(\rho\alpha)_p}{C_{pg}T_L}}\ \ where\ T_L=\frac{0.165k_g}{\epsilon_g} \tag{17}$$

2.2 Heat transfer model

The heat transfer is taken account of by solving the two energy equations for the two phases where heat is generated by the exothermic (homogeneous) gas phase chemical reactions and then transported between the phases. These equations are:

Gas:

$$\frac{\partial}{\partial t}(\rho\alpha h)_g+\frac{\partial}{\partial x_i}(\rho\alpha U_i h)_g=$$
$$\frac{\partial}{\partial x_i}\left[\Gamma_{h,g}\frac{\partial h_g}{\partial x_i}\right]+h_{vpg}(T_p-T_g)+\sum_{k=1}^{k=nreac}\Delta H_k\cdot r_k \tag{18}$$

Particles:

$$\frac{\partial}{\partial t}(\rho\alpha h)_p+\frac{\partial}{\partial x_i}(\rho\alpha U_i h)_p=\frac{\partial}{\partial x_i}\left[\Gamma_{h,p}\frac{\partial h_p}{\partial x_i}\right]+h_{vpg}(T_g-T_p) \tag{19}$$

Here, the effective transport coefficients are related to the turbulent viscosities as:

$$\Gamma_{h,g}=\frac{\kappa_{lam,g}}{c_{lam,g}}+\frac{\mu_{t,g}}{0.7}\ ;\ \Gamma_{h,p}=\frac{\mu_{t,p}}{0.7} \tag{20}$$

where $\kappa_{lam,g}$ is the laminar conductivity of the gas and $c_{p,g}$ is the specific heat of the gas.

The volumetric heat transfer coefficient h_{vpg} is calculated as:

The basis for calculating the volumetric heat transfer coefficient is based on correlations of the Nusselt number N_p in the various flow regimes characterized by the Reynolds number and volume fraction of gas according to:

$$\begin{array}{l}
If\ \ \alpha_g\ \le\ 0.8\\
N_p=2+0.106\cdot Re\cdot S_p\ \ Re\le 200\\
N_p=0.123\left(\dfrac{4\cdot Re}{d_p}\right)^{0.83}\cdot S_p^{0.17}\ \ 2000\ge Re>200\\
N_p=0.61\cdot Re^{0.67}\cdot S_p\ \ Re>2000\\
If\ \ \alpha_g>0.8\\
N_p=(2+0.16\cdot Re^{0.67})\cdot S_p\ \ Re\le 200\\
N_p=8.2\cdot Re^{0.6}\cdot S_p\ \ 1000\ge Re>200\\
N_p=1.06\cdot Re^{0.457}\cdot S_p\ \ Re>1000\\
where\\
Re=\dfrac{\rho_g d_p(|\vec{V}_g-\vec{V}_p|)}{\mu_{lam,g}}\\
S_p=\dfrac{\alpha_p\cdot 6}{d_p}\\
N_p=\dfrac{h_{vpg}\cdot d_p}{\kappa_{lam,g}}
\end{array} \tag{21}$$

2.3 Chemical reaction model

Since chemical reactions are only taking place in the gas phase, only species conservation for this phase is needed. These are:

Gas:

$$\frac{\partial}{\partial t}(\rho\alpha Y_j)_g+\frac{\partial}{\partial x_i}(\rho\alpha U_i Y_j)_g=\frac{\partial}{\partial x_i}\left[\Gamma_{Yj,g}\frac{\partial Y_{j,g}}{\partial x_i}\right]$$

$$=\frac{\partial}{\partial x_i}\left[\Gamma_{Yj,g}\frac{\partial Y_{j,g}}{\partial x_i}\right]+\alpha_g r_j+\alpha_p\rho_p r_{j,c} \qquad (22)$$

Here, r_j is the net bulk gas-phase reaction rate for component j, and $r_{j,c}$ is the gas phase reaction occurring on the surface of the catalyst particle for component j. The effective gas-phase transport coefficient is calculated as:

$$\Gamma_{Yj,g}=D_{Yj,g}+\frac{\mu_{t,g}}{0.7} \qquad (23)$$

$D_{Yj,g}$ is the molecular diffusivity of the gas-phase component with mass fraction $Y_{j,g}$.

3. Solution Procedure

Solution of the set of partial differential equations given above is performed by finite-domain methods. The calculation method is taken from the work of Spalding[7]. The calculation domain is divided into a finite number of main grid points where pressure, densities, void fractions, turbulent quantities, enthalpies and mass fractions of the chemical species are stored. The velocity components are, on the other hand, stored at grid points located midway between the main grid nodes. The relevant conservation equations are integrated over control volumes surrounding the relevant grid points in space and over a time interval. This integration is performed using upwind differencing in space and implicit differencing in time. The result of this is a set of non-linear algebraic equations which are solved by the application of the well known Tri-Diagonal Matrix Algorithm (TDMA) used along the various coordinate directions. For the void fraction and velocity equations, a point iteration method is used. Special care has been taken to solve the coupling of the momentum equations with the continuity equations. For this we use the so-called IPSA procedure proposed by Spalding[7]. The Partial Elimination Algorithm (PEA)[7], is used to de-couple the drag force between the phases in the momentum equations.

4. Simulations

Parts of the model given above are compared against two isothermal non-reacting gas-particle flow situations. In the present paper, focus has been directed towards calculating the flow fields and particle distributions and comparing the predictions with data from literature and data generated in our own laboratory using Laser-Doppler Anemometry (LDA). The first case is related to a core annulus type flow in an 11-m-high, 0.305-m diameter tube of Bader et al[8], and the second is related to our own laboratory setup of a 1-m-high, 0.03-m diameter circulating fluidized bed.

CASE 1: Large-scale tube of Bader et al[8]

The particles used in this study had a diameter of 76 μm, a density of 1714 kg/m^3 and a sphericity of 1.0. The tube was initially empty and the flow was started at the inlet with flow velocities of 0.228 m/s for the particles and 3.7 m/s for the gas. The particle volume fraction at the inlet was fixed at 0.25. The calculation was performed using a Cartesian description with 76 grid points along the height and 30 grid points across the diameter. It took about 14 seconds to fill the the empty tube. **Fig. 1** gives an overview of the results of stream lines for gas, particles and distribution of volume fraction of particles at 16 seconds after start-up. Please note that the contours are expanded in the transverse direction to improve visualisation of the details. It was generally found that the flow did not reach a true steady state situation, but had a cyclic behaviour. The general trend was that the gas and particle flow had an upward flow in the centre of the tube and a downward flow along the wall. Bader et al[8], had measured profiles across the tube diameter of both volume fraction of gas (porosity) and particle velocity. **Fig. 2** and **Fig. 3** show comparisons between measured and predicted profiles at a height of 9.1 m from the inlet. The predicted profiles were determined by averaging over 5 seconds. **Fig. 2** shows that the porosity is well predicted, whereas the particle velocity profile in **Fig. 3** shows some discrepancies between

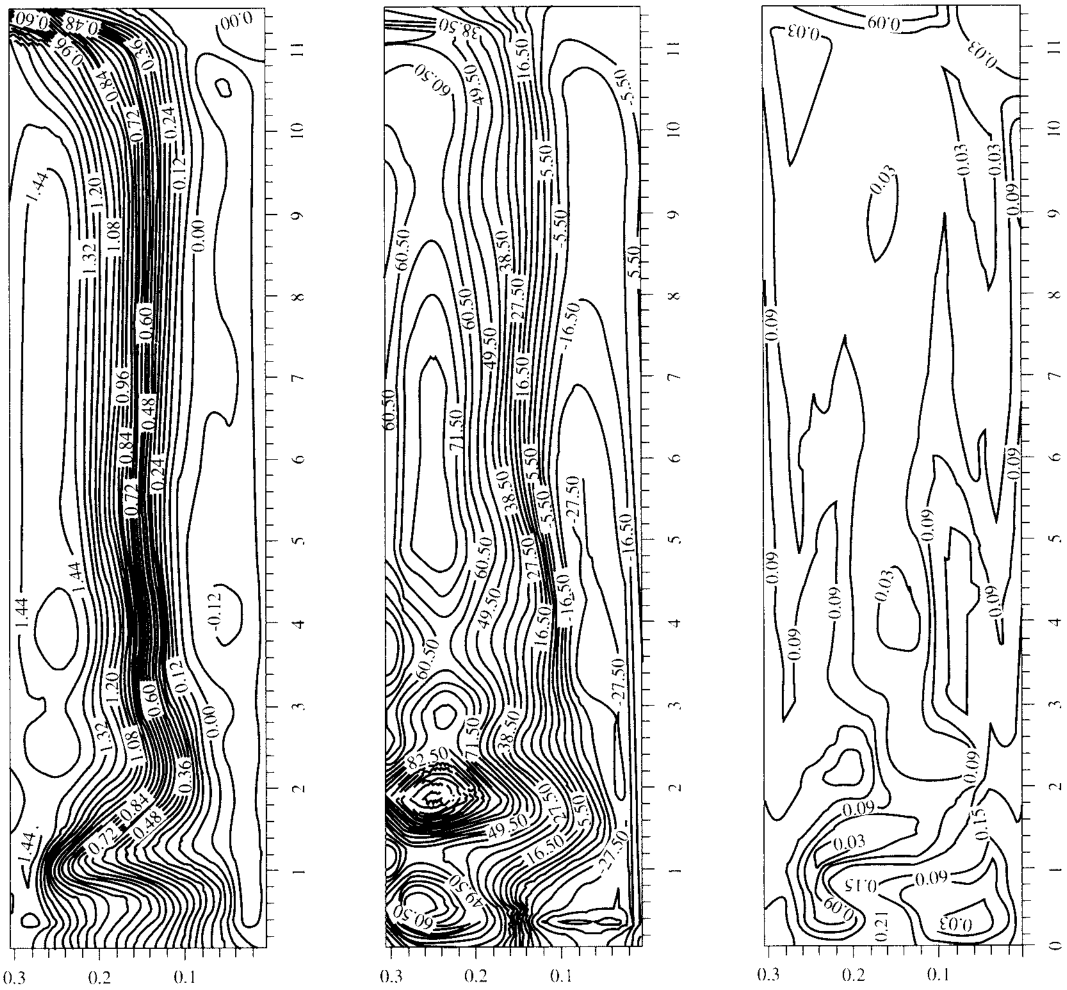

Fig. 1 Contours of stream lines of gas and particles and volume fraction of particles.

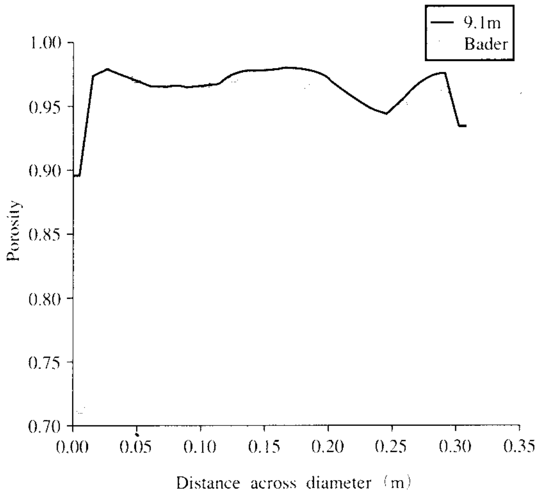

Fig. 2 Measured and predicted profiles of gas volume fraction (porosity) as a function of distance across the tube diameter at 9.1 m from the inlet.

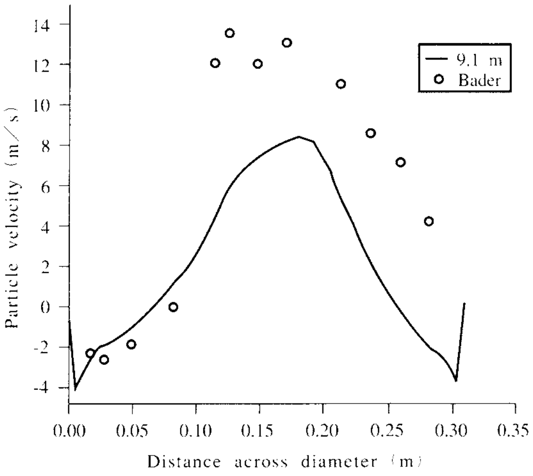

Fig. 3 Measured and predicted profiles of particle velocity as a function of distance across the tube diameter at 9.1 m from the inlet.

experiments and predictions. The general trend seems, however to be well predicted, namely upward flow in the centre and downward flow along the wall.

CASE 2: Laboratory-scale circulating fluidized bed

The vertical particle flow velocity in the lab.-scale fluidized bed reactor was determined by a laser Doppler anemometer delivered by Dantec. This system made it possible to measure both positive and negative particle velocities. Velocity profiles across the tube diameter were measured at three different heights above the distributor plate. The average particle diameter was about 55 μm and the density was 1600 kg/m^3. The particles that were transported from the reactor were separated in a cyclone and directed back into the fluidized bed just above the distributor plate. The gas superficial velocity was 1.7 m/s.

The calculation was performed using a Cartesian description. The calculation domain included both the vertical tube and the separator and return tube. 102 grid points were used in the axial direction and 26 points were used in the radial direction.

Fig. 4 shows the predicted contours of volume fraction of particles, particle and gas streamlines. The figure shows that the gas and particles are flowing upwards in the centre of the tube and have regions with negative velocities. The figure also shows a significant slip between the gas and particle flow. This is especially seen in the separation section of the flow system. **Fig. 5** shows a comparison between the measured and predicted profiles of the vertical particle velocity at three different heights above the distributor plate. It is seen that the overall agreement is good, i.e. the flow is upward in the centre of the tube and is directed downwards along the wall. However, the negative velocity is overpredicted.

Discussion

The comparisons between measurements and predictions in the two cases given above are reasonable. However, more work is needed to improve the model. This is particularly so for the turbulence model that determines the effective viscosity for the two phases. It must also be mentioned that the simulations were performed with a Cartesian geometry description, whereas the geometry is axisymmetric. Calculations

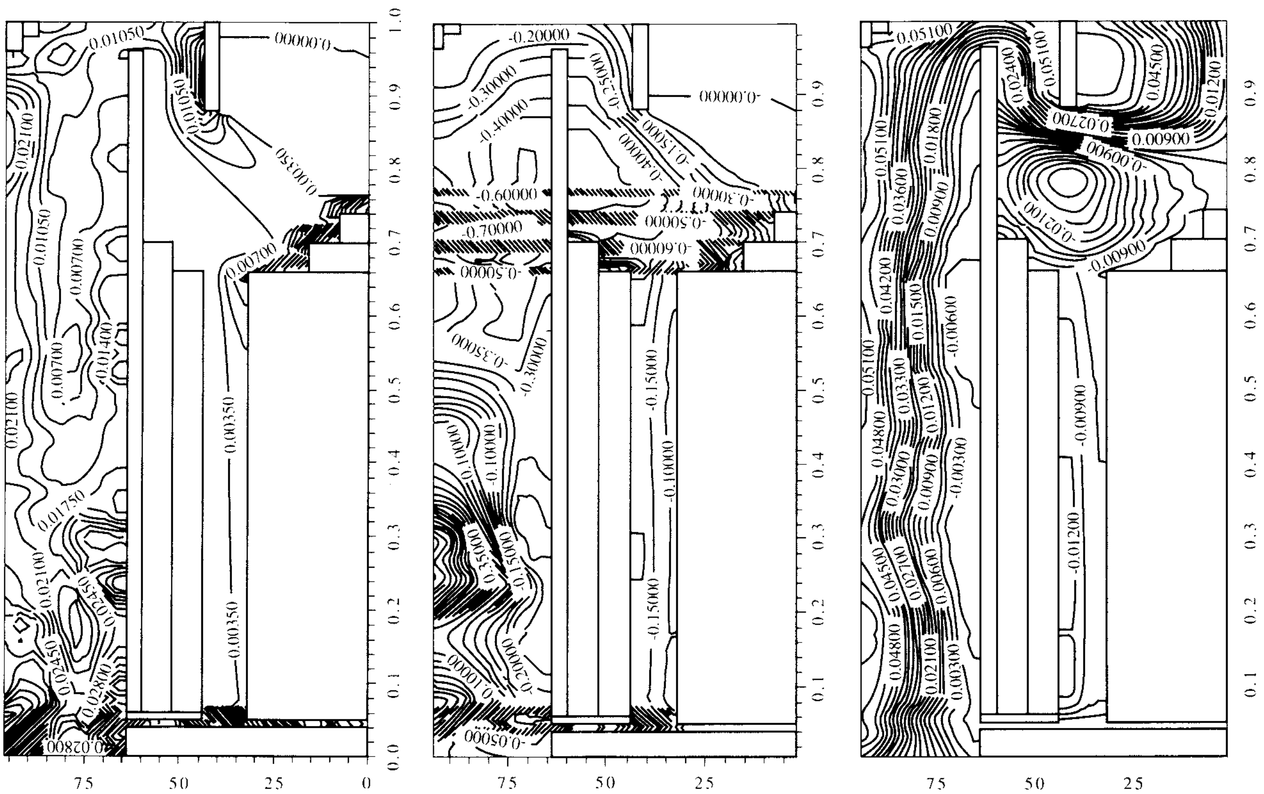

Fig. 4 Contours of volume fraction of particles, stream lines of particles and gas.

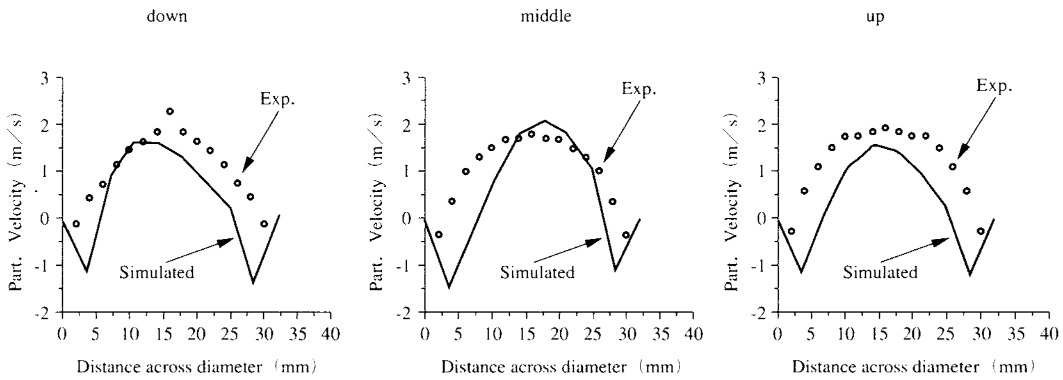

Fig. 5 Measured and predicted profiles of particle velocity as a function of distance across the tube diameter at three heights from the distributor plate.

should therefore also be performed using an axisymmetric geometry description.

5. Concluding Remarks

A comprehensive multi-dimensional CFD model for gas/particle flow, heat transfer and chemical reactions in fluidized bed reactors has been proposed. The model is incorporated in a 2D computer code and some initial verification simulations of isothermal flows have been carried out. The predictions give reasonable agreement with data from literature and our own experimental data. However, more model development is still needed especially with regard to turbulence modeling. In addition to this, the model needs to be tested against experimental data where chemical reaction and heat transfer is included.

6. Acknowledgements

The present work is financially supported by Norsk Hydro a.s. and the Royal Norwegian Council for Scientific and Industrial Research (NTNF). The authors are grateful to the following MSc students that have contributed to the work: E. Lode, H. Aadland and J. Stokke.

7. Nomenclature

c : constant
$c_{p,g}$: specific heat for gas
C_{pg} : gas - particle friction coefficient
C_d : drag coeficient
$C_{\varepsilon 1}, C_{\varepsilon 2}, C_{\mu}$: constants in turbulence model
d_p : particle diameter
D : molecular gas diffusivity
g_j : j-direction component of gravity acceleration
g_o : radial distribution function
G : solid stress modulus
h_g, h_p : gas and particle enthalpy
h_{vpg} : volumetric heat transfer coefficient
ΔH_k : heat of reaction for reaction no. k
k_g, k_p : kinetic energy of turbulence in gas and particle phase
N_p : Nusselt number
p : pressure
$r_j, r_{j,c}$: gas phase reaction rate in the bulk phase and on the surface of the particles
r : restitution factor
Re_p : Reynolds number
S_p : specific surface area of particles
t : time
T_g, T_p : gas and particle temperature
T_L : Lagrangian time scale of turbulence
$U_{j,g}, U_{j,p}$: j-component of velocity for gas and particles
$\vec{V}_g, \vec{V}_p$: velocity vector for gas and particles
x_i : coordinate direction in i-direction
$Y_{j,g}$: mass fraction of component j in the gas phase

Greek

α_g, α_p gas and particle volume fraction
$\Gamma_{\phi,g}, \Gamma_{\Phi,p}$ effective turbulent transport coefficient for scalar variable Φ for the gas and particle phase
δ_{ij} Kroenecker delta
$\varepsilon_g, \varepsilon_p$ dissipation of kinetic energy of turbulence
$\varkappa$ molecular thermal conductivity
$\mu_{t,g}, \mu_{t,p}$ turbulent viscosity of gas and particles
ρ_g, ρ_p density of gas and particles
$\tau_{ij,g}, \tau_{ij,p}$ stress tensor in gas and particle phases
Φ_s form factor of particles

Subscripts

g : gas phase
lam : laminar
p : particle phase
t : turbulent

References

1) Gidaspow, D.: Hydrodynamics of fluidization and heat transfer, Super-computer modelling, Appl. Mech. Rev., Vol **39**, 1(1986), 1-23
2) Shih, Y.T., Gidaspow, D., and Wasan, D.T.: Hydrodynamics of sedimentation of multi-sized particles, Powder Technology, Vol. **50**, (1987), 201-215
3) Tsuo, Y.P and Gidaspow, D.: Computations of flow-patterns in circulating fluidized beds, AIChE Journal, Vol. **36**, (1990), 885-896
4) Ding, J. and Gidaspow, D.: A bubbling fluidization model using kinetic theory of granular flow, AIChE Journal, Vol. **36**, (1990), 523-538
5) Ma, D. and Ahmadi, G. : A thermodynamical formulation for dispersed multi-phase turbulent flows - Part II: Simple shear flows for dense mixtures, Int. J. Multi-phase Flows, Vol. **16**, (1990), 342-351
6) Gidaspow, D., Ettehadieh, B., and Bouillard, J.: Hydrodynamics of fluidization: Bubbles and gas compositions in the U-gas process, AIChE Symposium Series No. 241, Vol. **80**, (1985), 57-64
7) Spalding, D.B.: Computer simulation of two-phase flows with special reference to nuclear reactor systems, Computational techniques in heat transfer, Ed.: R.W. Lewis, K. Morgan, J.A. Johnson and W.R. Smith, Pineridge Press, 1985, 1-44
8) Bader, R., Findlay, J., and Knowlton, T.M.: Gas/solid flow patterns in a 30.5-cm-diameter circulating fluidized bed, 2nd Int. circulating fluidized bed conference, March 14-18, Compiegne, France, 1988.

Slot Flow Metering: Fundamental Investigations, Pilot-Scale Tests and Industrial Prototype.†

B.J. Harris and J.F. Davidson
*Department of Chemical Engineering, University of Cambridge****
C.E. Davies
*Department of Scientific and Industrial Research***

Abstract

A new technique for measuring the flow of granular materials continuously is described. Slot Flow Metering utilizes the flow from vertical slots to determine flow rate. A Slot Flow Meter (SFM) consists of a hopper with one or more vertical slots in its sides supported by a means for weighing the hopper's contents, eg. a load cell. Solids flow rate can be correlated against the apparent weight of solids in the hopper.

Recent experimental and theoretical work on the flow of granular materials from vertical slots is reviewed and a simple in-situ calibration technique is described. This is tested against direct calibration (bucket and stop-watch) with a pilot-scale unit located in an experimental circulating fluidized bed. The industrial prototype, installed in a Urea plant, is described.

1. Introduction

Flow measurement is routine and commonplace in most chemical processes. There are a wide variety of technologies for measuring gas and liquid flows but very few for measuring solid (granular) flows. Only two techniques have found acceptance in the process industries: impact flow meters (Jimbo and Watanabe (1985)) and Coriolis mass flow meters (Jost (1987)); both methods have disadvantages. Impact flow meters, although suitable for measuring a wide range of materials, require careful empirical calibration which can be difficult (Burkell et al (1988)). Coriolis flow meters are potentially more useful as they are insensitive to the physical properties of the solids and give a true measure of mass flow rate; but the technique suffers from the disadvantage of requiring moving parts in contact with the flowing solids.

Slot flow metering is a recently developed method for measuring the dense-phase flow rate of granular materials and is analogous to liquid flow measurement using weirs. In its simplest form, a Slot Flow Meter (SFM) consists of a chamber or hopper with one or more vertical slots in its sides. Solids are fed into the hopper from the top, and flow out through the vertical slots. Out-flow area is proportional to the height of the slots occupied by out- flowing solids: for a given solids flow rate there is an equilibrium height at which the feed rate equals the out-flow. The basis of the technique is to correlate solids flow rate with height of solids in the hopper. This height is termed the active slot height, h, and for a solid of constant bulk density, it is uniquely related to the mass of solids in the meter. This mass can be determined by weighing, provided (i) the slots are sufficiently narrow to give adequate hold up, and (ii) the impact force of the impinging inlet solids stream from above is negligible. Thus the solids flow rate can be correlated with the apparent mass of solids in the hopper. It is necessary that all particles should pass through the meter, leading to two design requirements as follows: (i) the slot width must be sufficiently greater than the maximum particle diameter; (ii) the hopper design must be such that no particle — eg. a large one — becomes permanently lodged in the hopper.

Slot Flow Meters can be of a variety of forms. An example of a prototype unit is illustrated in **Fig. 1**. This design has been used for small-scale tests and scaled-up to pilot scale for use in an experimental Circulating Fluidized Bed (CFB), see **Fig. 6**, where the solids circulation rate is measured. The cone located in the

---

* Pembroke Street, Cambridge, CB2 3RA, U.K.
** PO-Box 31-310, Lower Hutt, NEW ZEALAND.

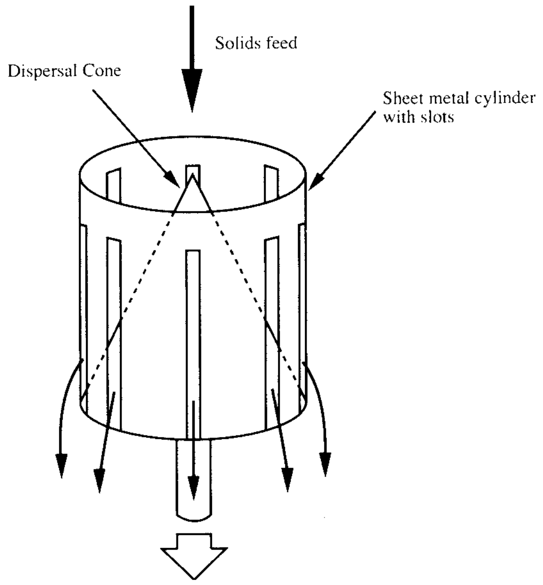

Fig. 1 Prototype Slot Flow Meter

centre of the hopper serves two purposes: to disperse the entering solids and to improve the draining characteristics; without the cone there would be a central stagnant region. Many other variations are possible: the slots need not be rectangular, and different geometries and hopper shapes are possible. Patent applications have been made for the general concept of Slot Flow Metering.

The purpose of this paper is three-fold:
(i) to review recent experimental and theoretical investigations of the nature of flow from vertical slots, beginning with fundamental studies of flow through single slots and moving on to tests on a prototype SFM;

(ii) to report and confirm the validity of a dynamic, in-situ calibration technique using a pilot-scale unit in an experimental Circulating Fluidized Bed; and

(iii) to describe the prototype industrial SFM which has been installed in a Urea plant.

2. Developmental Work

2.1 The relationship between flow rate and SFM geometry

Several practical and theoretical investigations into flow of granular materials through vertical slots have been undertaken. Davies and Foye (1991) investigated flow from both open slots (slots where the solids level is less than the full slot height) and closed slots (whose full height is occupied by the flowing solids). They quantified the effect of slot width (<70mm) and height (<400mm), on the flow of casein and rape seed, using a rectangular vessel 165mm x 155mm with a single slot. Their results were well correlated by:

$$\dot{m}=K_e(W-w)(L-l)\left[\frac{2(W-w)(L-l)}{(W-w)+(L-l)}\right]^{1/2} \qquad (1)$$

Here, $\dot{m}$ is the mass flow rate of solids from a slot of height L and width W; l and w are corrections to L and W, respectively, and are believed to be related to the average particle size. K_e is an empirical constant. Davies and Foye (1991) concluded that K_e is a function of bulk density and other undefined particle properties.

For a long, narrow, open slot ($L>>l$,$L>>W$, and $L=h$, where h is the active slot height), thus equation (1) reduces to:

$$\dot{m}=\sqrt{2}K_e(W-w)^{3/2}h \qquad (2)$$

This equation is clearly analogous to the well-known Beverloo equation (Beverloo et al. (1961)) for the vertical flow of granular material, of mean diameter d_p, through a circular orifice of diameter D_o, viz.:

$$\dot{m}=0.58\rho g^{1/2}(D_o-1.4d_p)^{5/2} \qquad (3)$$

Here, g is the acceleration of gravity, and ρ the particle bulk density. If the analogy holds, it is plausible that the slot width reduction, w, is related to average particle diameter: $w=kd_p$. Davies and Foye (1991), and more recently Davies et al. (1992), investigated this dependence. Experimental values for K_e and k, denoted K_e* and k* are reproduced in **Table 1**, as are the results of Harris et al (1992).

Harris et al. (1992), developed theory from first principles to give the dependence of the flow constant, K_e of equation (2), on particle properties. They found:

$$\dot{m}=Cg^{1/2}\rho(W-kd_p)^{3/2}h \qquad (4)$$

where

$$C=\left[\frac{1}{2\alpha}\frac{K+1}{K-2}\sin\phi\right]^{1/2} \qquad (5)$$

Here, K is the ratio of major to minor principal

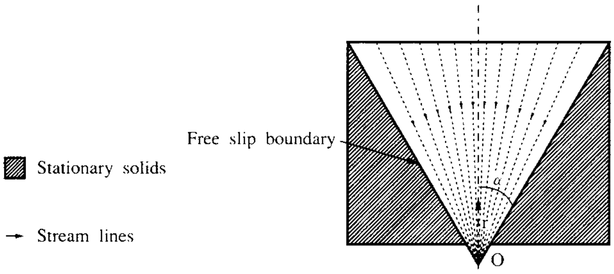

(a) View on arrow N

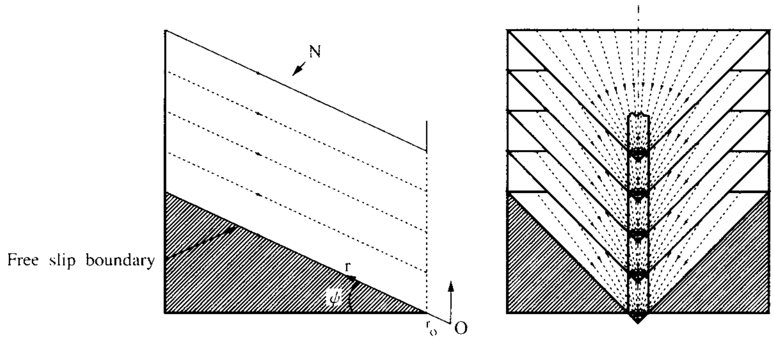

(b) Side elevation (c) Front elevation

Fig. 2 Slot flow geometry for flow analysis (Harris et al. (1992)).

stresses and α and ψ are angles defined in **Fig. 2**.

Harris et al. (1992), used a cylindrical multi-slot flow meter (**Fig. 1**), 0.1m diameter and 0.1m high, with eight variable width slots (maximum 4mm) to investigate the effect of slot width and particle size (155, 233 and 518 μm mean diameter sand). Their results were regressed against equation (4) and are reproduced in **Fig. 3**, where $g^{1/3}\,d_p{}^{-1}(\dot{m}/\rho h)^{2/3}$ is plotted against W/d_p. Here, the slope equals $C^{2/3}$ and the intercept, $C^{2/3}k$. The best fit values (solid line), each denoted by an asterisk, are $C^*=0.43$ and $k^*=0.12$. Confidence limits (95%) are also shown (dashed lines). The fit is reasonable although there is some scatter. The value obtained for the slot width reduction constant k^*, is significantly less than those of Davies et al. (1992) and Davies and Foye (1991), see table 1. This discrepancy may be due to the small scale of the apparatus, and its multi-slot design: also, the catchment areas of adjacent slots are not independent.

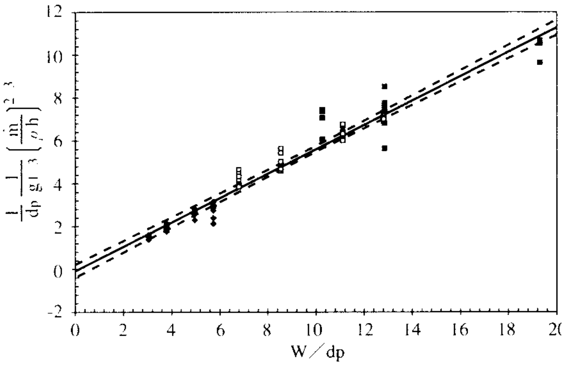

Fig. 3 Regression of measured $\dot{m}$, Wand d_p against equation (4) for all data, Harris et al. (1992). Solid line : best fit ; dashed line : 95% confidence intervals. Particle size (μm) : ■ 155 ; □ 233 ; ◆ 518.

The flow constant C^* measured by Harris et al. (1992) is compared to values obtained by Davies et al. (1992) and Davies and Foye (1991) in **Table 1**. Note that= $K_e^*=pg^{1/2}C^*/2^{1/2}$. The validity of equation (5) has not been experimentally verified as systematic measurements of α and ψ have not been made, although Harris et al. (1992) estimated C using values of $\alpha=30°$, $\psi=30°$ and $K=3$ for sand and casein. Equation (5) was found to over-estimate the flow constant C, and a discharge coefficient, C_d, of order 0.3 was incorporated into equation (4) to account for the discrepancy.

The theoretical developments described above are concerned only with out-flow whose mean velocity shows no variation with height. Davies and Harris (1992) subdivided flow through vertical slots into two regimes: fluidized and unfluidized. In the former, with a controlled flow of fluidizing air, the solids flow like an inviscid liquid and slot out-flow is proportional to $Wh^{3/2}$. With unfluidized flow, slot out-flow is proportional to $W^{3/2}h$. Davies and Harris (1992) inferred from their observations that some Geldart Group A particles behaved as though they were fluidized or partly fluidized as they flowed through the SFM, even though there was no fluidizing air other than that entrained with the incoming solids. They also found that the flow of 'fluidizable' particles (Geldart Group A or B) through vertical slots could be transformed from unfluidized to fluidized by forced aeration of the particles within the SFM: the maximum flow capacity of an SFM of given volume can be increased by fluidization using forced aeration.

2.2 Dynamic response of a SFM

Davies and Harris (1992) investigated the dynamic response of a single Slot Flow Meter with capacity for internal fluidization (**Fig. 4**).

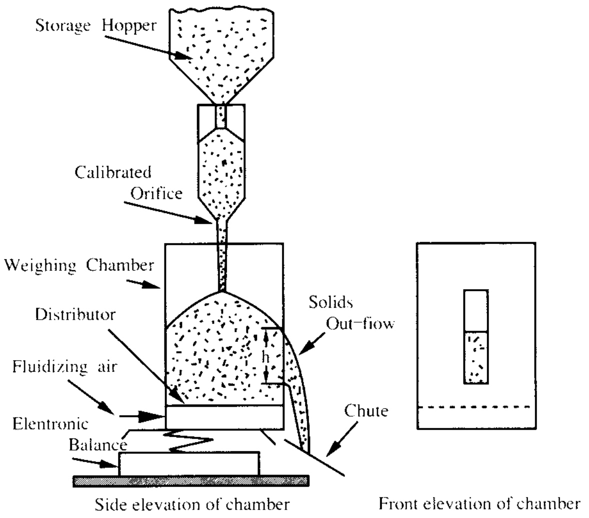

Fig. 4 Single-Slot Flow Meter of Davies and Harris (1992) with capacity for fluidization.

They applied step changes to the solids flow to confirm the validity of the above-mentioned relationships for fluidized and unfluidized flow. For unfluidized slot flow they found that for a step change from zero flow to $\dot{m}$, the response of the SFM is given by:

$$t/\tau = \ln\left[\frac{1}{1-\eta}\right] \qquad (6)$$

where $\tau = M_\infty/\dot{m}$ and $= \eta/\ h/h_\infty$; τ is the mean residence time; M_∞ and h_∞ are respectively the steady state values of the mass of solids in the hopper and the height to which they rise. When the material in the SFM is fluidized, the response is given by:

$$t/\tau = \frac{2}{3}\left[\frac{1}{2}\ln\left[\frac{1-\eta^{3/2}}{(1-\eta^{1/2})^3}\right] + \sqrt{3}\tan^{-1}\left[\frac{-\sqrt{3}\,\eta^{1/2}}{\eta^{1/2}+2}\right]\right] \qquad (7)$$

Experimental results are compared with predictions for both fluidized and unfluidized flow for sand in **Fig. 5**, where t/τ is plotted against M/M_∞. It is assumed that $\eta = M/M_\infty = h/h_\infty$; this is true when the following conditions are satisfied: (i) the shape of the solids surface is invariant with height, (ii) the container has vertical sides and (iii), the bulk density of the flowing material is constant.

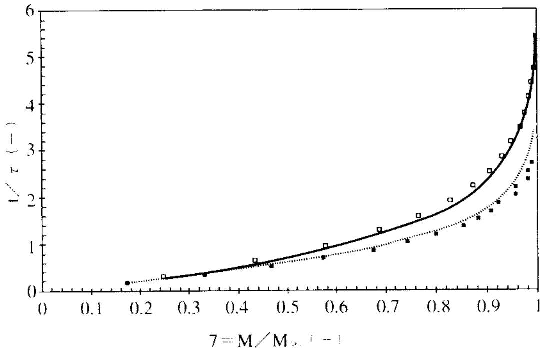

Fig. 5 Transient behaviour of single slot flow meter : response to step change in flow, Davies and Harris (1992).

□ sand unfluidized, ■ sand fluidized, ——equation 6, ······equation 7.

3. Dynamic Calibration

Regular calibration of any flow meter is important. However, where this requires removal of the measuring element, or calibration is difficult or hazardous, it is often neglected. Slot Flow Meters possess a unique characteristic, identified by Davies et al. (1992): on-line, in-situ calibration is possible. The technique is based on the dynamic response of the SFM to cessation of flow: the inlet flow is stopped at time $t=0$ and the mass, M, of solids in the load cell is subsequently measured as a function of time, M(t); dM/dt gives the mass flow rate corresponding to M(t), provided the momentum of the entering particles is negligible.

This technique has been tested on a pilot-scale SFM installed in an experimental Circulating Fluidized Bed (Harris and Davidson

(1992)). The experimental rig is shown in **Fig. 6**. Here, a 0.2m diameter by 0.2m high SFM with eight 10mm x 180mm open slots, of the same geometry illustrated in **Fig. 1**, is used to measure the external solids circulation rate of Fluid Cracking Catalyst (FCC) ($\rho=850$ kgm^{-3}, $d_p=71$ μm). The FCC discharges through a central hole which pierces the distributor plate and plenum chamber of a conventional low-velocity bubbling fluidized bed (the slow bed in **Fig. 6**), and flows into the SFM. Flow rate is adjusted using a slide valve with variable orifice diameters. The discharge from the SFM flows under gravity, via a double manifold, to the CFB riser.

The dynamic response of the 0.2 m diameter SFM to cessation of flow is shown in **Fig. 7**. The curve is approximately exponential and has been regressed as such. For short times there is some scatter, but the fit is reasonable ($R^2=0.97$) and adequate for this analysis. The fitted curve ($M=1.06\ e^{-1.45t}$) is differentiated to give $dM/dt=1.53\ e^{-1.45t}$, the discharge rate from the hopper. dM/dt is plotted against M in **Fig. 8** as are the data from the direct (bucket and stop-watch) calibration. Agreement between the two calibration methods is excellent. Calibration at higher flows was not possible due to limited bucket volume.

Harris et al. (1992) considered the general case of the dynamic response of an SFM with

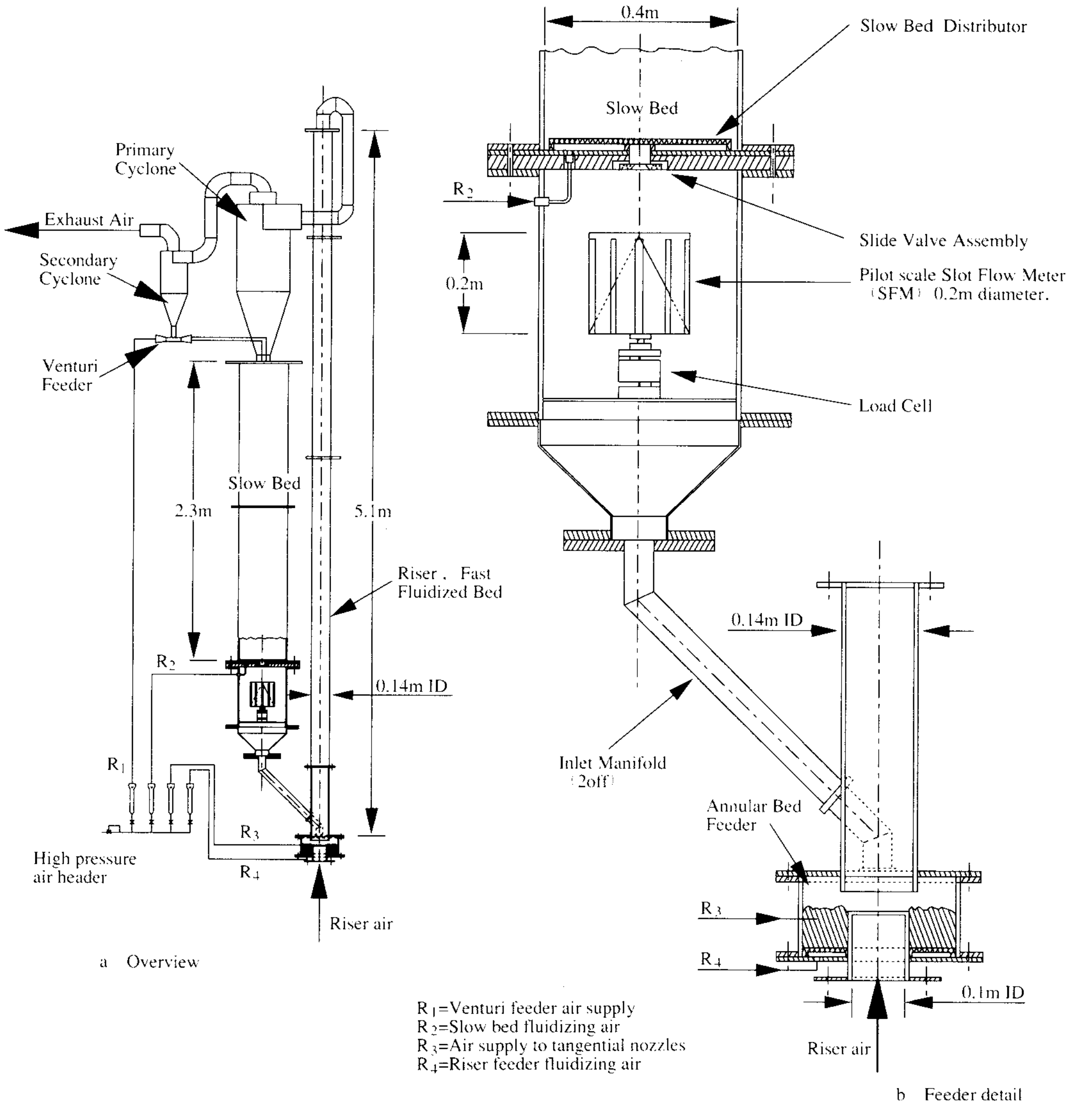

Fig. 6 Experimental Circulating Fluidized Bed (CFB) with 0.2m diameter pilot scale SFM installed (Harris and Davidson (1992)).

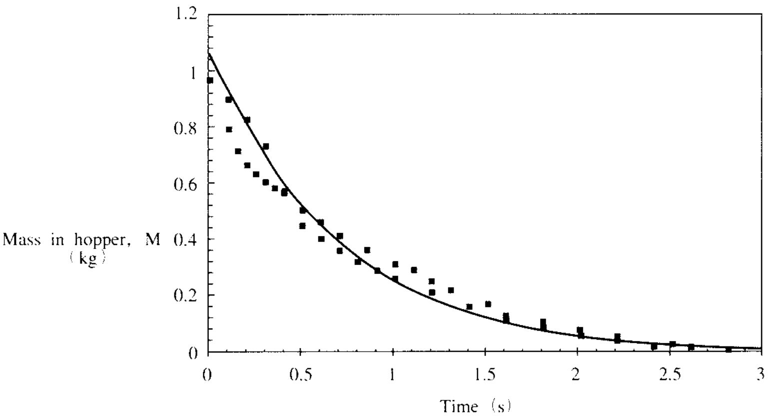

Fig. 7 Dynamic response of 0.2m diameter 'pilot-scale' SMF to cessation of flow, with FCC, 71 μm mean diameter, Harris et al. (1992).

no internal cone and with particles which show linear variation of out-flow with height (unfluidized). They found that the time variation of solids mass in a hopper of constant cross-sectional area A, with n slots, for cessation of flow at t=0 is given by:

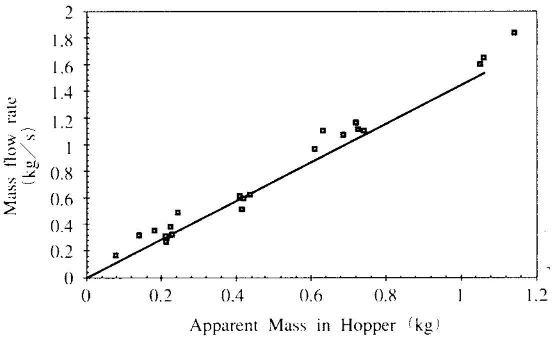

Fig. 8 Calibration curve for 0.2m diameter SFM with FCC : comparison of dynamic (solid line, dM/dt against M) and bucket and watch (□) techniques, Harris et al. (1992).

$$M=\rho A h_i \exp\left[-\frac{nC_g^{1/2}W^{3/2}}{A}t\right] \tag{8}$$

Here, h_i is the initial active height of solids in the hopper. The mass flow rate from the slots is therefore:

$$\frac{dM}{dt}=-\rho h_i nCg^{1/2}W^{3/2}\exp\left[-\frac{nCg^{1/2}W^{3/2}}{A}t\right] \tag{9}$$

It follows from equations (8) and (9) that $-(dM/dt)/M=nCg^{1/2}W^{3/2}/A$, which is linear with respect to the mass of solids in the hopper and independent of bulk density: an SFM in this situation acts as a mass flow meter, giving the mass flow rate without the need to measure the solids density.

Similar analysis can be performed for slot out-flow which is non-linear with respect to height. Here the out-flow of solids, through n slots, in a vessel of constant cross-section, is $\dot{m}=nC_f h^{n_f}$, $n_f \neq 1$. Note for a material which flows as a Newtonian liquid $C_f=(2/3)C_d\rho(2g)^{1/2}W$ and $n_f=3/2$, see Davies and Harris (1992). The mass of solids in the SFM as a function of time is:

$$M=h_i\rho A\left[1-\frac{(1-n_f)nC_f}{h_i^{1-n_f}\rho A}t\right]^{1/(1-n_f)} \tag{10}$$

differentiation gives the out-flow:

$$\frac{dM}{dt}=h_i^{n_f}nC_f\left[1-\frac{(1-n_f)nC_f}{h_i^{1-n_f}\rho A}t\right]^{n_f/(1-n_f)} \tag{11}$$

The variation of out-flow with mass of solids in the hopper for a fluidized ($n_f=3/2$) solid is:

$$\frac{dM}{dt}=\frac{n(2/3)C_d(2g)^{1/2}W}{\rho^{1/2}A^{3/2}}M^{3/2} \tag{12}$$

This is clearly a function of bulk density. In general, an SFM of constant cross-section cannot be considered a mass flow meter when the out-flow is non-linear with respect to height.

Non-linear variation of out-flow with height for FCC was observed by Harris et al. (1992). They interpreted the calibration data from the pilot-scale SFM by estimating the active slot height (calculated from the geometry of the SFM and the mass of solids) and found non-linear out-flow behaviour, which at the highest flow rates measured, approached that expected for a fluidized solid. Despite this, the response for this unit was well described by an exponential decay, as expected for an unfluidized solid with no internal cone. From this observation, it appears that the internal cone counteracts the non-linear variation of outflow with height. Indeed, it is possible to demonstrate that this is the case by considering the equations which describe (i) the mass of solids in the SFM as a function of height, and (ii) the variation of out-flow with height. The mass of solids in the hopper is given by:

$$M=\rho\pi\left[r_h^2 h-\frac{1}{3}r_h^2 h_o+\frac{1}{3}(h_o-h)^3\tan^2\theta\right] \qquad (13)$$

Here r_h is the hopper radius, h_o the height of the hopper, and θ is the half angle of the cone. The mass flow rate of fluidized solids through n slots (Davies and Harris (1992)) is:

$$\dot{m}=n(2/3)C_d(2g)^{1/2}\rho W h^{3/2} \qquad (14)$$

The discharge coefficient, C_d, is assumed equal to 0.3. These two equations, which are parametric in h, are plotted in **Fig. 9** for a number of different solids densities, as are the 'bucket and stop-watch' calibration data for the 0.2m diameter SFM with FCC. At high flow rates, the calibration curve is approximately linear, which agrees with the observations of Harris et al. (1992). It is also apparent that the SFM is relatively insensitive to the bulk density of the material: the SFM, with a conical insert and fluidized solids flow, has pseudo mass-flow-metering characteristics.

4. Industrial Prototype

A full description of the industrial prototype is given by Davies et al. (1992): only a synopsis is given here. The industrial prototype (**Fig. 10**), which is installed in a Urea plant, was designed to measure flows of the order of 26 tonnes per hour with peak flows of at least 35 tonnes per hour. It differs significantly from the prototype and the pilot-scale units described in the previous sections. The principal differences are the absence of the internal cone and the different solids dispersal method. The unit is made free-draining using a conical base with a central drain hole; the flow through this drain is only a small proportion of the total flow. Also incorporated into this unit is a device for measuring continuously the bulk density of the flowing solids (readers are referred to the original paper, Davies et al. (1992), for a description): again only a small fraction of the total flow is fed to the density measuring device. The inclusion of the density device within the SFM was necessitated by space constraints.

Solids enter the dispersal chamber via an inclined chute and flow through 'T-shaped' slots to the cylindrical weighing chamber. This

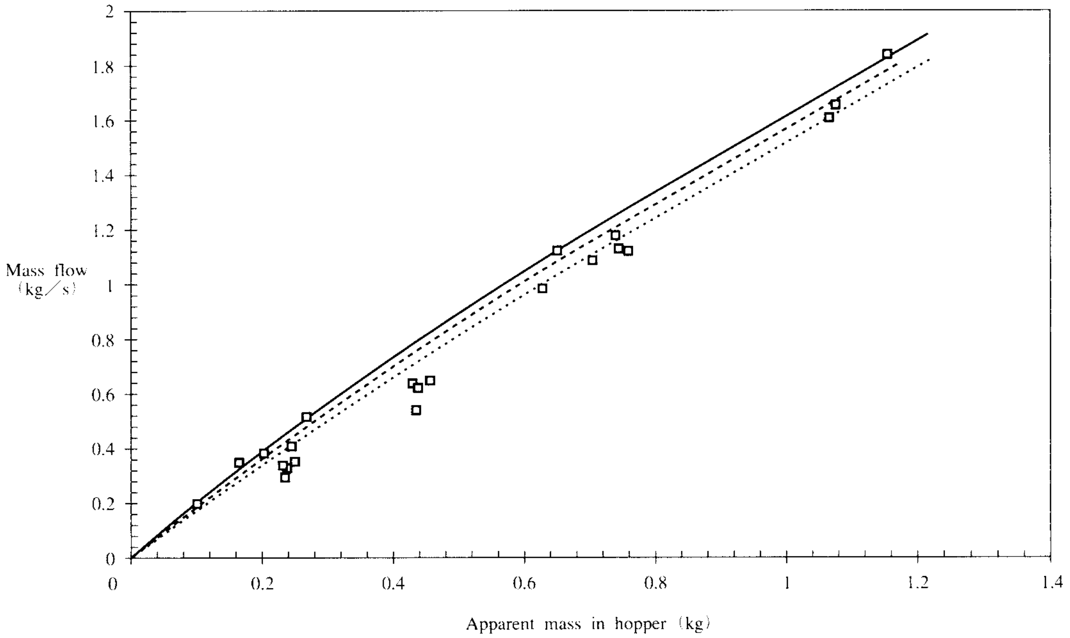

Fig. 9 Comparison of theoretical calibration for pilot scale SFM with fluidized particles (equations (13) & (14)) against experimental data (□), with bulk density as parameter.——1050kgm^{-3}, ---- 850kgm^{-3}, ••••• 650kgm^{-3}.

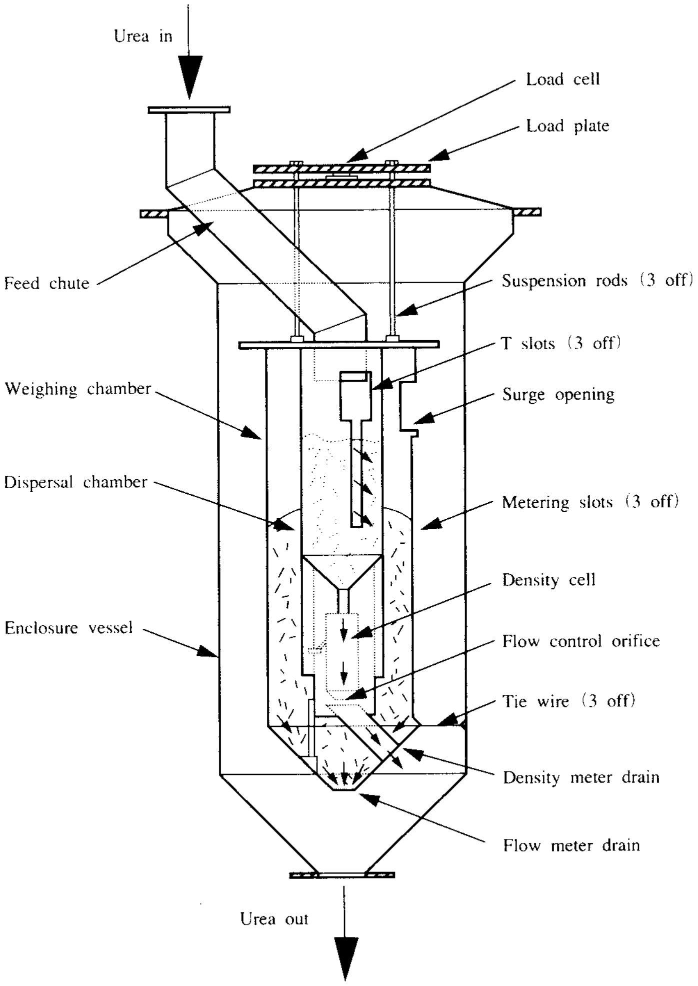

Fig. 10 Industrial SFM prototype : Flow and density measurement of Urea (Davies et al. (1992)).

has three equi-spaced replaceable metering slots in its sides which are offset from the dispersal slots. The entire unit (dispersal and weighing chamber) is supported from above by three rods which are attached to a load cell via a connecting plate. The SFM is kept horizontally stable by three tie wires aligned so that they apply no vertical force. Rectangular surge openings are located above the top of the metering slots.

The response of the unit to cessation of flow is complicated by the internal geometry (density meter and drain hole), and this must be kept in mind when examining the response curve. An example is presented in **Fig. 11**.

5. Conclusions

1. Slot Flow Metering has been demonstrated from prototype, through pilot scale, to the first industrial instrument, which is installed in a Urea plant.

2. Slot Flow Meters are based on very simple technology: the flow of a granular material from a vertical slot. There are no moving parts:

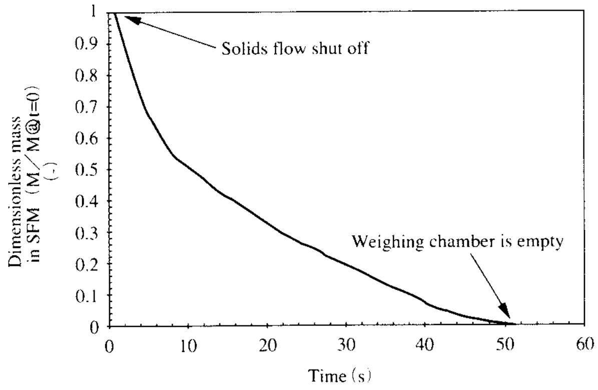

Fig. 11 Response of industrial prototype SFM to cessation of flow, Davies et al. (1992).

they are ideally suited to dusty environments.

3. Empirical theory has been developed. The out-flow from a vertical slot for unfluidized flow is given by:

$$\dot{m} = Cg^{1/2}\rho(W-kd_p)^{3/2}h$$

Theory developed from first principles gives the dependence of the dimensionless constant C on the flow properties of the granular solid.

4. On-line calibration is possible. This is accomplished by observing the dynamic response of the meter to cessation of flow. The resulting response curve is differentiated with respect to time to give the flow rate corresponding to the mass of solids in the hopper.

5. In some cases (unfluidized flow from an SFM of uniform cross-section), an SFM will behave as a mass flow meter, ie. its characteristics are independent of solids density.

Nomenclature

A : cross-sectional area of SFM [m^2]
C : theoretical flow constant [$-$]
C^* : experimental flow constant [$-$]
C_d : discharge coefficient [$-$]
C_f : non-linear flow constant
d_p : average particle diameter [m]
D_o : orifice diameter [m]
g : acceleration of gravity [ms^{-2}]
h : active height of solids [m]
h_∞ : active height of solids at steady state [m]
h_i : initial height of solids in hopper [m]
h_o : height of SFM [m]
k : slot width reduction constant [$-$]
k^* : experimental slot width reduction constant [$-$]
K : $(1+\sin\phi)/(1-\sin\phi)$ [$-$]
K_e : empirical flow constant [kg m$^{-5/2}$ s^{-1}]
K_e^* : experimental flow constant [kg m$^{-5/2}$ s^{-1}]
L : closed slot length [m]
l : slot length reduction [m]
M : apparent mass of solids in hopper [kg]
M_∞ : apparent mass of solids in hopper at steady state [kg]
$\dot{m}$: slot mass flow rate [kg s^{-1}]
n : number of slots [$-$]
n_f : non-linear flow height exponent [$-$]
r_h : radius of cylindrical SFM [m]
R^2 : coefficient of determination [$-$]
t : time [s]
W : slot width [m]
w : slot width reduction [m]
α : flowing wedge half angle
θ : half angle of internal cone
η : dimensionless height ratio, h/h_∞ [$-$]
ρ : bulk density [kg m^{-3}]
ϕ : angle of internal friction
ψ : angle of slip plane to horizontal
τ : mean residence time [s]

References

Beverloo, W.A., H.A. Leniger, J. van de Velde, 1961, 'The flow of granular solids through orifices' Chem. Eng. Sci., 15, 260

Burkell, J.J., J.R. Grace, J. Zhao, C.J. Lim, 1988, 'Measurements ofsolids circulation rates in circulating fluidized beds' in Circulating Fluidized Bed Technology II, eds. P. Basu, J.F. Large, Pergamon Press, 501

Davies C.E., J. Foye, 1991, 'Flow of granular material through vertical slots' Trans. I. Chem. E. , 69(A), 369

Davies C.E., J. Grey, M. Webb, D. Nicholls, 1992, 'Instrumentation for monitoring the flow of particulate solids in transport system', submitted for publication: 4th International Conference on Bulk Material Storage Handling and Transportation, 6- 8th July, Australia

Davies C.E., B.J. Harris, 1992, 'A device for measuringsolids flow rates: characteristics, and application in a circulating fluidized bed' in Fluidization VII, Engineering Foundation, New York, 741.

Harris B.J., C.E. Davies, J.F. Davidson,1992, submitted for publication

Harris B.J., J.F. Davidson, 1992 'Velocity profiles, gas and solids, in fast fluidized beds' in Fluidization VII, Engineering Foundation, New York, 219.

Jimbo, G., K Watanabe, 1985, 'Instumentation for monitoring the flow of particulate solids in transport system' Proc. Reliable Flow of Particulate Solids, Bergen, Norway, August.

Jost G, 1987, 'New mass flowmeter on Coriolis principle' Chem. Plants and Processing, December.

Channel Flow †

T. P. Meloy and M. C. Williams
*Particle Analysis Conter. Univ. of West Virginia**
P. Bevilacqua and G. Ferrara
*Univ. of Trieste***

1. Introduction

In the story of the Greek Argonauts, there is an anecdote about Jason and his "golden fleece." Somebody stole a golden fleece. Many think Jason's golden fleece was his warm coat, perhaps a coat with magical properties. The authors' interpretation of this anecdote differs. They interpret the golden fleece as a mature fleece used in the placer mining of gold. From the Black Sea Turks, Jason stole a fortune and the technology of recovering fine gold particles. Early Greek industrial espionage.

For recovering gold, early Greek miners used sheepskins as riffles to sluice gold ores (Aravidis, 1979; Axiotis, ; Koromila, 1991). Fine gold particles accumulated in the fleece of the sheepskin. To recover the gold, they burnt the mature sheepskin. Therefore "the golden fleece" is a mature sheepskin laden with gold.

Because of their high density, fine golden particles settle to the bottom of a flowing stream. If there are riffles such as the sheepskin's fleece, the dense fine particles settle through the hairs till they rest on the skin itself. Once the gold particles settled to the skin, the miners have no simple way to remove them. Thus, burning the fleece recovers the gold.

Particle flow in a channel such as a sluice box or a vibratory feeder has, to the authors' knowledge never been modeled. See **Figure 1**. This paper models such flow. Used for the modeling was the spreadsheet, Quattro Pro.

Modern sluice boxes no longer use sheepskins as the source of riffles. Now used are : block riffles, longitudinal riffles or orthogonal riffles. As the name implies, block riffles are fingers or blocks in the floor of the flow channel - like the hairs in the sheepskin. These blocks impede flow. They afford a region in which dense small particles may settle.

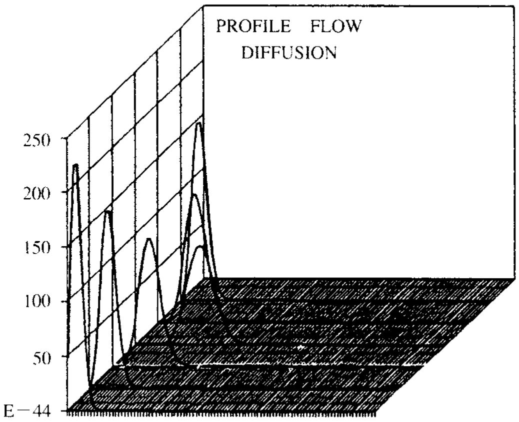

Fig. 1a Distributed flow after 300 seconds.

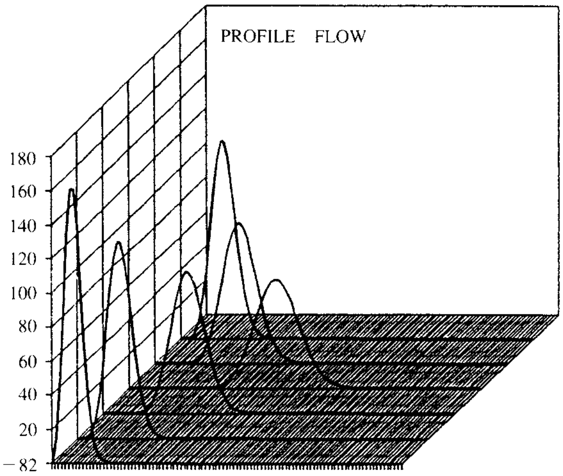

Fig. 1b Distributed flow after 600 seconds.

Longitudinal and orthogonal riffles are strips of material attached to the floor of the sluice way to selectively impede, particle flow. Longitudinal riffles run parallel to the direction of water flow. Orthogonal riffles run perpendicular to the flow. Because riffles selectively slow the rate that some types of particles move down a sluice, there is a discriminating build up of small dense particles in the sluice. This selective build up of particles on the sluice permits the recovery of small dense particles in sluices.

Particles of different physical properties move at different rates down the sluice way.

---

* Morgantown, West Virginia 26506, USA
** Italy
† Received September, 1992

Large light particles move rapidly. Riffles have little influence on light particles. Small dense particles move slowly. These dense particles, affected by the riffles, become trapped behind riffles, rest in a region of low water velocity or may be buried below larger lighter particles.

2. Literature

Though sluicing of metalliferous ores was known and used by the Greeks (Conophagos, 1980), only a few works can be found on its modelling. Most of the models developed for sluice ways, shaking tables, also for spirals and other flowing or thin-film separation devices, are of the "black box" or curve fitting models, i.e., models that describe separation performance through partition curves (Tucker et al., 1991; Pearl et al., 1991; King et al., 1992). These types of models may be useful for predicting specific industrial results on a given sluice, when the size-density frequency distribution of the feed ore is known.

In contrast, few attempts have been made to develop phenomenological models of sluice ways or sluices with riffles. These physically based models extrapolate well. They are better for understanding the physical process of separation. Thus for improving separation equipment and operating conditions, phenomenological models are superior. These models are better for research, design, operations and control processes.

Much of the credit for the mathematical study of thin-film concentration goes to Gaudin (1939), whose treatise is still used in more recent books (Kelly and Spottiswood, 1982; Burt, 1984; Wills, 1985). Recently Ferrara and Preti (1991), developed a new kinetic-probabilistic approach for studying the movement of minerals in thin films of water. Their approach describes the basic phenomena of separation of different minerals along the direction of flow in a thin film of water.

Recent studies on two-dimensional networks done by Meloy and Williams (1990), used a finite element analysis approach in a spreadsheet. This new approach may be used for modelling sluicing as a two-dimensional array of cells. In this simplest of sluice way models, Meloy assumes that the probability of a particle moving to the right or down is independent of the particle's position in the sluice way or the loading of a given cell with particles. This is a pure linear model of a sluice way.

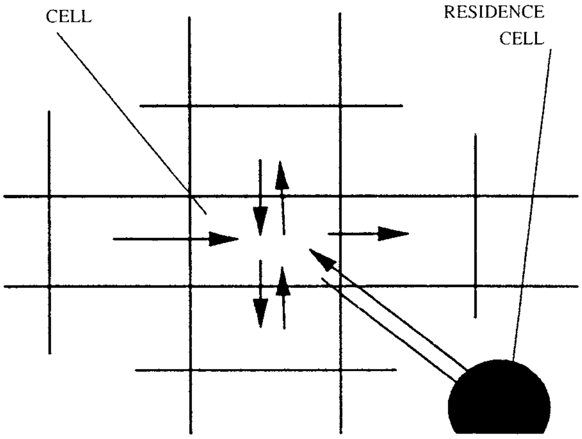

Fig. 2 The material balance in a single cell of the table. Note residual cell.

3. Model

This paper dynamically models a sluice way with riffle as a rectangular array of cells seven cells wide and one hundred cells long. See **Figure 2a**. Feed enters the sluice-way through the left hand feed cells and exits the sluice from the exit cells at the end of the sluice.

On a sluice, one defines a unit of time as one second. During a unit of time, particles move either to the **right, lower or upper** adjacent cell. In this model, particles do not move left (back) or diagonally.

In this paper, up and down on the sluice-way are defined in terms of the three dimensional graphs. In **Figure 1**, up is the most distant curve or position from the ear or bottom edge of the graph. Down is the bottom or near edge of the graph. In the conventional terms right is toward the end or exit of the sluice. In the model used, there is a particle residence time for each type of particle in a given cell. Within a unit of time, some particles in a given cell at the start of that unit of time, leave that cell (for adjacent cells) during that period. See **Figure 2**. The remainder of material plus that entering the cell remains in the cell for that unit of time. At steady state, a given cell's content would not vary with time. However, the sluice ways were not tested at steady state.

All tests used mono-characteristic particle sets, In a mono-characteristic particle set, all particles have identical physical properties. So these particles have the same probability of moving to the right, up or down during each unit of time. While industrial mineral feeds to a sluice way have a broad range of particle characteristics, the use of mono-characteristic particles yields more useful experimental information. For example, it is easier to see and quantify the separation with different riffle shape using mono-characteristic particles.

3.1 Computational procedure.

Using a Quattro Pro spreadsheet to simulate the sluice-way, one establishes a seven column by one hundred row cell array. The sluice way is seven cells wide and one hundred cells long. Two of the seven cells in a column are edge cells. These edge cells behave differently from interior cells. Feed enters the cells in the first row. Material moves through the rows of cells in the sluice way and exits from the one hundredth row of cells.

On the sluice's interior surface, each cell receives material from the adjacent cell to the left and the adjacent cells above and below. There are three exceptions to this rule : 1) cells along the top edge of the sluice that only receive material from the adjacent cells to the left and below; 2) cells along the bottom edge receive material from the adjacent cells left and above; 3) the row feed cell(s) that receives material only from the feed source.

By symmetry, on the sluice's interior surface, each cell donates material to the adjacent cell to the right and the adjacent cells above and below. There are two exceptions to this rule : 1) cells along the top edge of the sluice that only donate material to the adjacent cells to the right and below; 2) cells along the bottom edge donate material to the adjacent cells right and above.

The following sluice tests were perfomed.

1. Simple profile flow.
2. Simple flat profile flow.
3. Simple flat profile flow with diffusion.
4. Simple profile flow with diffusion.
5. Simple flat profile flow with high diffusion.
6. Simple flat profile flow with bias & diffusion.
7. Simple flat profile flow with high bias.

Sluices are not simple surfaces in which a particle enters and then is selected to exit the sluice at the other end after taking one hundred steps down the sluice. They are complex unit operations in which an individual particle takes hundreds to perhaps thousands of steps before exiting the sluice's end. During each step the particle moves either down, up or to the right.

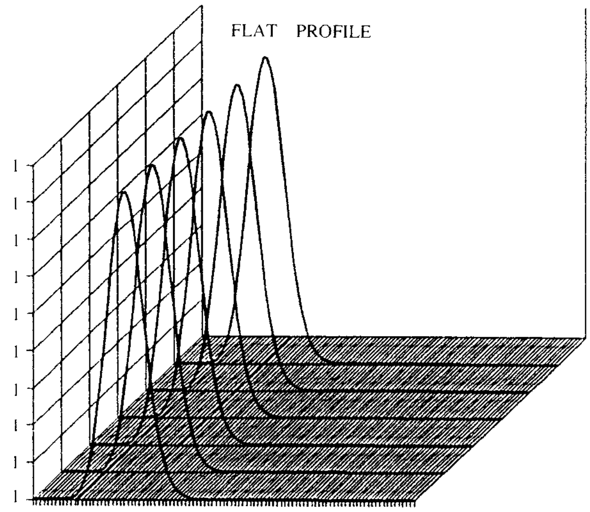

Fig. 3 Frequency spectra of impulsive force.

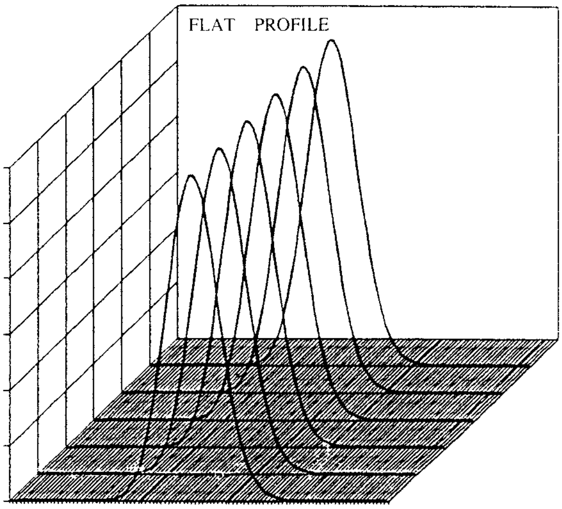

Fig. 3b Flat profile flow after 1200 seconds.

4. Results

Excepting **Figure 2**, all results are presented in the three dimensional graphs shown in **Figure 1 through Figure 7**. The type of analysis done in this paper, generates huge amounts of data. For clarity, the large amount of information gathered in this study, requires a compact form of data presentation.

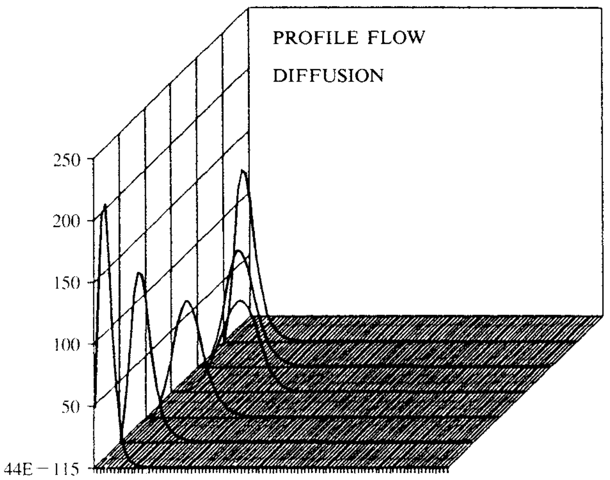

Fig. 4a Flat profile flow with diffusion after 600 seconds.

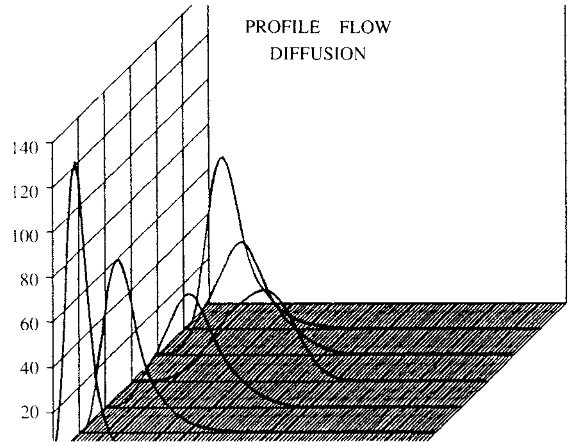

Fig. 4b Profile flow with low diffusion after 1200 secpnds. See Figure 1.

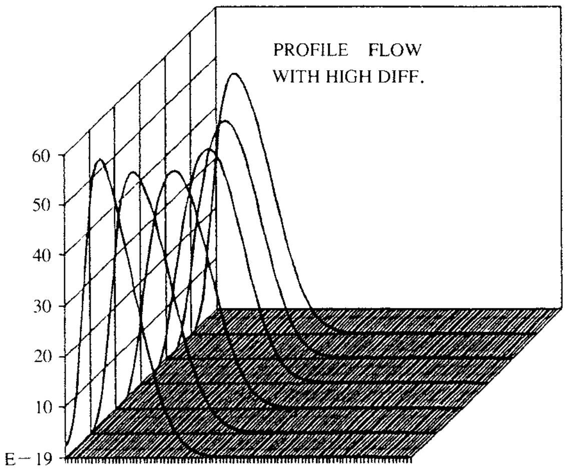

Fig. 5a Profile flow with high diffusion after 600 seconds.

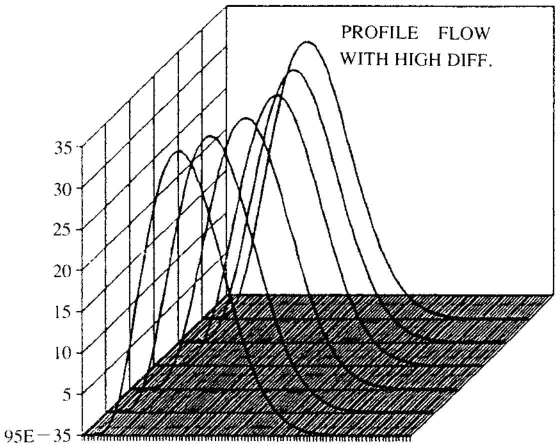

Fig. 5 Profile flow with high diffusion after 1,200 seconds.

Each above referenced graph contains six curves. Each curve is a plot of the material in a given cell in one of the seven rows (channels) of cells in the sluice way. Because Quattro Pro limits the number of curves that may be plotted on one graph to six, only six of the seven channels is plotted.

In **Figure 1**, as in all of the three dimensional graphs, the bottom curve is the bottom edge channel of the sluice way. The channels are in their natural order. The curve, forth from the bottom, is the middle channel of the sluice way. On the graph, the missing channel is the upper edge channel.

Figure 1 presents profile flow without either bias or diffusion. This graph represents independent flow in each channel. No interaction between channels exists. There is no inter-channel particle exchange.

Material in the middle channel, number four, is the of the sluice-way. This middle channel has a Ti value of 0.07. In the two flanking channels, three and five, Ti values are 0.04. For the next pair of channels, two and six, Ti values are 0.02. The bottom edge channel has a Ti value of 0.01.

In contrast to **Figure 1, Figure 3** presents flat profile flow. All seven streams have a Ti value of 0.04. As before, there is no interaction between channels. There is no inter-channel particle exchange.

Figure 4 presents profile flow with a small amount of diffusion. Define the diffusion up and down respectively as Tu and Td. Tu and Td are set equal to 0.001. As will be seen more clearly in the next figure, diffusion slows the movement of particles down the channel. Diffusion also broadens the width of a given channel line - as may be seen in **Figure 4**. Compare **Figures 1 and 4**.

Note in **Figure 5** the influence of high diffusion between adjacent channels. High diffusion profile flow appears like flat profile flow. Movement rate down the fastest channel has decreased significantly. In contrast, flow in the boundary channel, number 1, has increased. Moreover, the widths of the curves in a given channel have increased front to back distance.

To the flat profile shown in **Figure 3**, bias has been introduced. Bias means the particles move preferentially to a given edge. Thus bias may be used to simulate the presence of a magnetic or electrostatic accelerational field. Bias is achieved by making Tu Td. Note that the particles move preferential to the upper channel, number six.

Figure 6 has the same high diffusion profile flow as **Figure 5**, besides the bias. Again note the effect of diffusion is to slow the movement of particles in the faster channels and to widen the curves.

Figure 7 shows the effect of pure high bias on flat flow. Adjacent channels rob near channels of material. Most material resides in the high channels. A Franz magnetic separator has this type of biasing.

5. Discussion

This section contains a discussion of the : a) results, b) model used, c) methods used and d) implications of the results. Unquestionably, the results show the importance of sluice diffusion and bias. Using a user friendly spreadsheetmakes solving and understanding the results intuitive and simple. Using the finite element analysis model in the spreadsheet presents no problems. Clearly the results imply that shaking sluice design can be modeled.

5.1 Results

Three flow variables examined in this model of a sluice-way : type of flow profile, diffusion and bias. **Figures 1 and 3 through 7** show the results.

Two type of flow profiles : were used flat and parabolic. The data shows nothing remarkable about either flow when free of bias or diffusion.

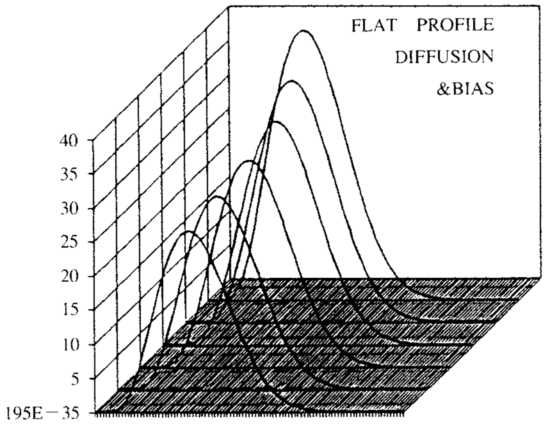

Fig. 6a Flat profile, high diffusion & bias. Time 300, 900 seconds.

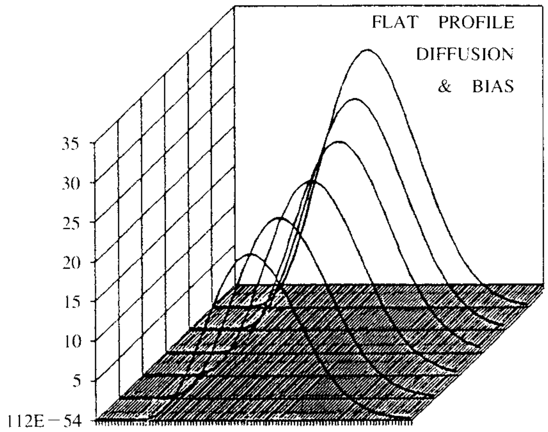

Fig. 6 Flat profile, high diffusion and high bias. Time of run 300 seconds.

Once diffusion becomes a factor, parabolic flow profiles alter significantly. Faster streams of particles move more slowly. Slower streams move more rapidly. The peakedness or stream width broadens with increasing diffusion. The bullet shaped parabolic profile flatten looking more like a flat profile flow.

Diffusion changes the flow profile of the particle streams, not the flowing water stream. When a lead particle in the fastest stream enters the adjacent stream, it extends the extent of the adjacent stream and decrease the height of the leading edge of the fastest stream. A particle from the back of a slower stream moving into the faster stream, broadens the faster stream. Simultaneously, by moving from the back of the slower stream, the particle makes the slower stream move more rapidly. Diffusion is the great leveler.

Turbulence probably causes most of the diffusion or lateral movement of particles in a sluice-way. Brownian motion of particles in a sluice-way is negligible. Depending on the sluice design, flow splitting causes some diffusion. Thus diffusion is a combination of factors.

Bias is unbalanced diffusion. More particles move in one direction than another. Thus an outside or edge channel receives most of the particles. **Figure 7** shows the profound effect of high bias toward the upper edge. When mixed with other materials, they have either no bias or a bias in the opposite direction, one can make a sharp separation. As is true of the Franz isodynamic separator, one can have two sets of particles effected by bias in opposite directions - magnetic and gravitational.

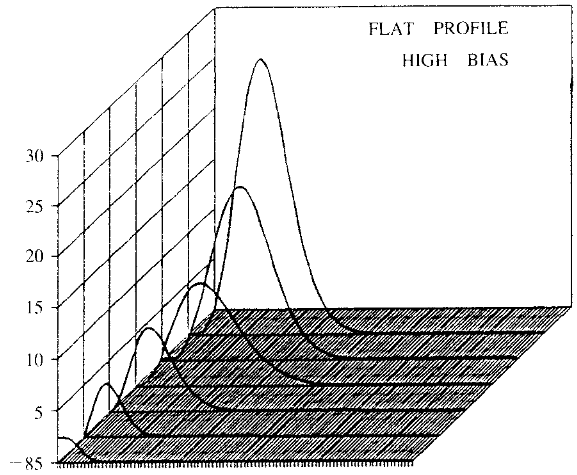

Fig. 7a Flat profile and high bias after 300 seconds.

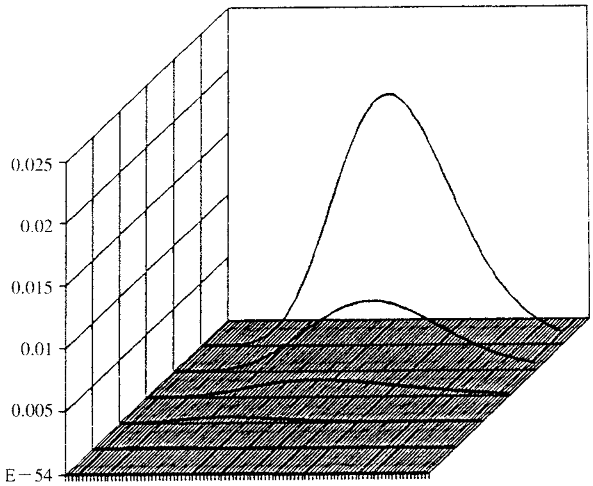

Fig. 7b Effects of high bias after 1200 seconds.

5.2 Model Used

The model may be divided into two parts. The single cascadograph model proposed by Meloy et al. (1985) and the finite width sluice shape model, proposed in this paper. The former model discussed in the cited paper will not be reviewed here. However the finite width sluice model is new and is discussed below.

This latter model assumes that there is no short circuiting of material.

Specifically, this simplest of models assumes that a particle can move down the sluice one step at a time. Modeling both multiple steps and short circuiting, would not be difficult.

Also, this simple model assumed a particle behaves the same way on each part of the sluice. One might call this the "homogeneous surface" sluice model. A non homogeneous sluice model would be tedious but not difficult to develop.

The authors feel that modeling with one layer of fluid is too simple a model for true understanding and thus predicting the behavior of particles in a sluice way. Recommended is a five layer thick flow pattern. The seven channels width model is acceptable. With the added depth of flow, one can model flow in the riffle area and flow above the riffles. Computational times would increase five fold, but computational times are short and thus irrelevant.

5.3 Procedure.

First, established in Quattro Pro, was a seven by one hundred array of sluice cells. Next, one computed the transitory flow of particles across the sluice surface. This computation lead to the mass of material on the sluice's surface for each cell. Then, using Quattro Pro graphics, one made a graph of the particles in each cell for a given processing time. These are the graphs used in this paper.

Error free models required multiple mass balances. One made mass balances of the feed and product. Achieved was an accuracy of one part in 10^{12}. Rounding errors during calculations caused this error.

Implication of Results

Unquestionably sluice riffles affects sluice performance. Using spreadsheets, sluices may be designed and performance checked. It is time to use modeling for the design of sluices for specific application.

Major shaking sluice design factors readily modeled are : a) sluice size, b) shape, c) riffle design and placement. Also, never done, modeling the design and method of sluice tuning for optimum separation and through-put is feasible.

How large an influence could this modeling of sluice design have on new commercial sluices? One would like to think that there would be an immediate major influence. Realistically, in a technology as ancient as sluicing, finding an *easy* major improvement is not feasible. Nevertheless, solid performance improvements can be expected. Finding or failing to find a major improvement is a lot faster and far less costly, using models than done experimentally. Money and time cost money.

6. Conclusions

Using a robust model of a particle movement in a sluice-way, satisfactory simulation results were obtained. Examined were flow profile, diffusion rates and bias. Diffusion, most of it due to turbulence, profoundly affects the rate and profile of particle movement. Recommended is changing the model to include five levels of flow. Specific conclusions are :

i) Riffled sluice-ways are easy to model in a spreadsheet.

ii) Such a model is a good tool for interpreting experimental results.

iii) Diffusion is a major factor governing the behavior of sluice-ways.

iv) Bias lateral movement is a form of unbalanced diffusion.

v) Develop a more sophisticated sluice way model for better understanding the particle behavior. This model should have five levels of flow. Other parameters are satisfactory.

vi) Said model is an excellent tool for teaching, lecturing and sales.

vii) Said model or its successor, is an excellent tool for sluice way design.

Bibliography

Aravidis A. J., 1979, *Mineral Wealth of Pontos,* Pontiaki Estia, pp 113-124

Axiotis, T., The first Argonautic Expidition in 3,500 BC, Smirniotakis, Athens.

Burt, R. O. Gravity concentration technology. Elsevier, Amsterdam, 1984.

Conophagos, C. E. Le Laurium antique et la technique Grecque de la production de l' argent. Ekdotike Hellados S. A., Athens, 1990

Ferrara, G. and Preti, U. A kinetic probabilistic approach to flowing-film concentration processes. Proc., XVII Int. Mineral Processing Cong., Dresden, 1991, pp. 21-30.

Gaudin, A. M. Principles of mineral dressing. McGraw-Hill, New York, 1939.

Kelly, E. G. and Spottiswood, D. J. Introduction to mineral processing. John Wiley & Sons, New York, 1982.

King, R. P., Juckes, A. H. and Stirling, P. A. A quantitative model for the prediction of fine coal cleaning in a spiral concentrator. Coal Preparation, Vol. 11, 1992, pp. 51-66.

Koromila, M., 1991, The Greeks in the Black Sea, Panorama Co., Athens.

Meloy, T. P. and Williams, M. C. Controlled particle sizing with two-dimensional networks. Proc., 5th European Symp. Particle Characterization, Nürnberg, Germany, 1992, pp. 561-571.

Pearl, M, Lewis, K. A. and Tucker, P. A mathematical model of the Duplex concentrator. Minerals Engineering, Vol. 4, No. 3/4, 1991, pp. 347-354.

Tucker, P., Lewis, K. A. and Wood, P. Computer optimization of a shaking table. Minerals Engineering, Vol. 4, No. 3/4, 1991, pp. 355-367.

Wills, B. A. Mineral processing technology. Pergamon Press, Oxford, 1985.

Preparation of Electrically Conductive Particles by Dry Coating and Evaluation of Fine Particle Dispersion †

Keijiro Terashita and Kei Miyanami
*Dept. of Chem. Eng., University of Osaka Prefecture**
Mikio Higashi
*Hirakata Factory, Mita Industrial Co., Ltd.***

Abstract

Electrically conductive composite particles were prepared by dry coating of various types of electrically conductive fine powders on insulator resin. The course of composite formation and the state of dispersion were investigated by scanning electron microscope (referred to as SEM observation), X-ray elementary analysis and electrical property characterization.

Combining SEM observation and electrical property characterization determined the course of composite formation. The state of fine particle dispersion of the surface of a single composite particle could be quantitatively evaluated by calculating the coefficient of variance for the fine particles on the basis of elemental analysis of composite particles. Experiments also revealed that composite particles with excellent electric conductivity can be obtained, provided that the state of fine particle dispersion and coating on the core particle is good.

1. Introduction

In recent years, R & D activities have been concentrated on particle design, new materials and functional composite materials. Functional composite materials are characterized by the derivation of new features which cannot be achieved by the starting material bulk powder alone by mixing, kneading, dispersing and otherwise treating several types of powders. Therefore, the function of a composite material often depends upon the state of dispersion of the materials involved.

As an efficient means of composite particle formation and functional composite material design, the mechanofusion system has drawn attention, and a number of reports have been presented.[1)–7)] This system may be characterized by the possibility of particle design based on the dry process rather than by its capability of fine powder processing. In other words, the aim of the mechanofusion system is to design composite particles with the desired function by fixing and coating fine particles on core particles by shearing, compression and tumbling actions in the absence of binders and other additives to obtain an ordered mixture.

In the previous papers[8),9)], we reported on composite forming studies with the aim of preparing composite particles with excellent electric conductivity by dry coating (dry process), in which various types of electrically conductive fine powders and various sets of coating apparatus operating conditions were tested. Data on the volume specific resistivity, SEM observation and X-ray elemental analysis of the obtained composite particles determined the course of composite formation and the relationship between the state of coating (composite formation) and electric conductivity. Also investigated was the composite formation for an improved flow of fine particles from the viewpoint of SEM observation and charge distribution as well as the basic mechanical prop-

---

* 1-1 Gakuen-cho, Sakai Osaka 593, JAPAN

** 1-chome Tsudakita-machi Hirakata Osaka 573-01 JAPAN

† Received Oct. 8, 1992

erties. However, quantitative evaluation of the state of dispersion (coating) in composite formation remains unsatisfactory.

In the present study, various types of electrically conductive fine powders were dry coated on insulator resin, in single layers or double layers, to form composite particles. To determine the course of composite formation, SEM observation and electrical property characterization were performed. Also, quantitative evaluation of the state of fine particle dispersion on the surface of composite particles was attempted by calculating the coefficient of variance for electrically conductive fine powders on the basis of elemental analysis of fine particles on composite particles. The function of composite particles was investigated from the viewpoint of their electrical properties and correlated to the state of fine particle dispersion and coating.

2. Apparatus and methods

The compressive mill (Angmill, mechanofusion system, Hosokawa Micron Corp.) shown in **Fig. 1** was used to perform dry coating for composite particle formation. Details of the apparatus are described elsewhere.[8),9)] The Angmill used has a casing of 150 mm in diameter and 40 mm in depth.

The powders used in the present study are listed in **Table 1.** Polymethyl methacrylate (PMMA), an insulator, was used as the core particle material. The electrically conductive fine particles used were Ag particles, Ni particles, Cu particles and Ag-coated TiO_2 (referred to as ATK50) particles.

The experimental conditions of composite formation were as follows: clearance between the inner piece and the casing inside wall was 3.4 mm, rotation rate N was 12.5 to 25 rps, and treatment time t was 600 to 3600 sec.

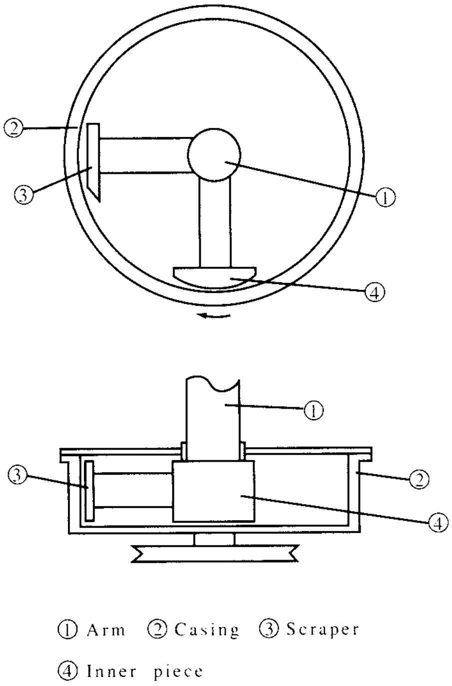

Fig. 1. Schematic of the Angmill used for dry coating experiments

Table 2 gives specific conditions of complex formation. Samples A1 through A3 were prepared by dry coating one type of electrically conductive fine particles on the surface of PMMA core particles. Samples B1 through B3 were prepared by coating Ni particles or ATK50 particles on A1 through A3 composite particles (core particles). B1 through B3 are thus three-component composite particles consisting of resin and two types of fine particles,

Table 1. Core particle and electrically conductive fine powder

Material		Mean particle size [μm]
Core particle	Polymethyl-methacrylate (PMMA)	50
Fine Powder	Cu Ni Ag coated with TiO_2 (ATK50)	2.5 0.02 0.5

Table 2. Composite particle formation operating conditions

Sample	Core Particle	Fine electric conductive powder	Addition rate [wt%]	Rotation rate [rps]	Treatment time [s]
A1	PMMA	Cu	10	25.0	3600
A2	PMMA	Ni	15	12.5	2700
A3	PWWA	ATK50	15	20.0	3600
B1	A1	Ni	15	12.5	2700
B2	A2	ATK50	15	20.0	3600
B3	A3	Ni	15	12.5	2700
C1	PMMA	Cu	10	25.0	2700
		Ni	15		
C2	PMMA	Ni	10	20.0	2700
		ATK50	15		

resulting from the coating of core particles with two layers of electrically conductive fine particles. The method of such double coating will be described later. Samples C1 and C2 are also three-component system, but they differ from B1 through B3 in that two types of fine particles have been simultaneously coated on the surface of core particles in a mill. In other words, the core particle is coated with a single layer of a mixture of two types of fine particles.

Dry coating of two layers of electrically conductive particles on core particles (composite particle formation) was achieved in the following manner: First, core particles and electrically conductive particles were loaded onto the mill casing, and the casing was tumbled to coat the first layer. After cooling in air, the single coated particles were further coated with electrically conductive fine particles.

As seen in **Table 2,** the rotation rate, coating treatment time t and fine particle feed rate varied depending on the type of electrically conductive particles charged. This is due to the fact that the conditions shown in **Table 2** were developed after dry coating experiments under various sets of conditions. This demonstrates the necessity for suitable conditions for composite particle formation for each powder system.

In the composite formation experiments, dry coating was conducted without premixing the resin and electrically conductive particles, with 70 g of core particles used.

3. Evaluation of composite particle formation

As regards the course of composite particle formation and the function of composite particles, it is critical to evaluate the state of dispersion of electrically conductive fine particles on the surface of composite particles after dry coating. In the present study, composite particle formation was evaluated with an emphasis on the state of fine particle dispersion on the surface of a single core particle (microscopic aspect) and powder bed (formed product) function (macroscopic aspect).

3.1 State of electrically conductive particle dispersion on a single particle

To numerically depict the state of dispersion of electrically conductive particles coated on the surface of a single core particle, elemental analysis (surface analysis) was conducted using an energy dispersive X-ray spectrometer (EDX). On the basis of the analytical data thus obtained, the state of electrically conductive fine particle dispersion was evaluated as schematized in **Fig. 2.** First, a single composite particle was subjected to surface analysis and photographed. Next, each photographic image was divided into 19 sections, and the luminance L for each section was determined using a color difference meter (CL-100, produced by MINOLTA Corporation). Although the luminance determination should cover the entire surface of the particle, the central portion of the particle surface was especially analyzed to eliminate the problem of strain. The measuring range in each section was a circle of 8 mm in diameter. On the surface analysis images, the presence of a metal element appears as a white dot, which represents an electrically

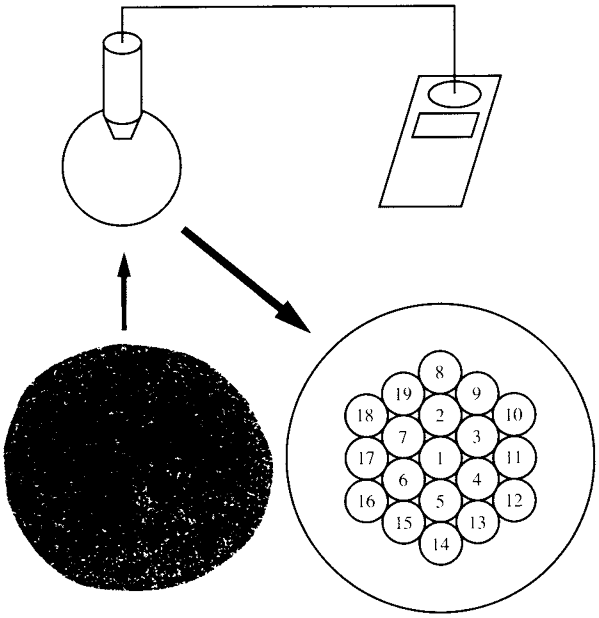

Fig. 2. Method of luminance determination

conductive fine particles, i.e., luminance is equivalent to the density of coated electrically conductive fine particles. Since the surface analysis images were obtained at x 860 magnification, the actual luminance measuring range was a circle of 9.3 μm in diameter in each section of the surface of composite particles. By calculating the standard deviation σ for luminance levels L1 through L19, the state of electrically conductive fine particle dispersion (coating) on the surface of a single core particle can be obtained. For the correction of the sensitivity difference between the target elements, the coefficient of variance CV was calculated for the evaluation of the state of dispersion as follows:

$$\mathrm{CV}(\%) = \frac{\sigma}{\bar{\mathrm{L}}} \qquad (1)$$

where $\bar{\mathrm{L}}$ is the mean of the luminance levels L1 through L19. The uniformity of electrically conductive particle dispersion on the surface of a core particle increases or the state of coating (composite particle formation) is better, as the coefficient of variance CV decreases. There is no previous study of quantitative expression of the state of fine particle dispersion on a single core particles, as far as the author knows.

3.2 Evaluation of the state of electrically conductive particle dispersion based on electrical properties

With respect to the resinmetal composite particles studied, the state of dispersion and coating of electrically conductive fine particles on the insulator resin core particle is believed to affect the electrical properties. The state of electrically conductive fine particle dispersion (coating) was correlated to the volume specific resistivity ρ, the reactance X and the dielectric loss tangent tan δ. Alternating current electrical properties were determined by the LCR method using an impedance analyzer (model 4192A, produced by Yokogawa-Hewlett Packard) with a pressure of 2.9 MPa exerted on a pair of three-terminal parallel plate electrodes energized with composite particles. The determination was made at a frequency f of 100 kHz for a parallel equivalent circuit of resistors, condensers and coils (**Fig. 3**). The method of determination is schematized in **Fig. 4.** This method gives dispersed measurements because it is difficult to average all samples with regard to thickness. Dispersion was corrected using the following equations (2) and (3):

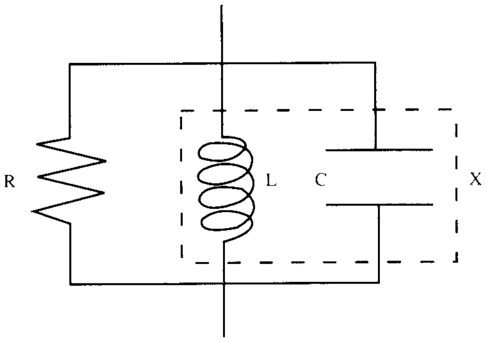

Fig. 3. Parallel equivalent circuit

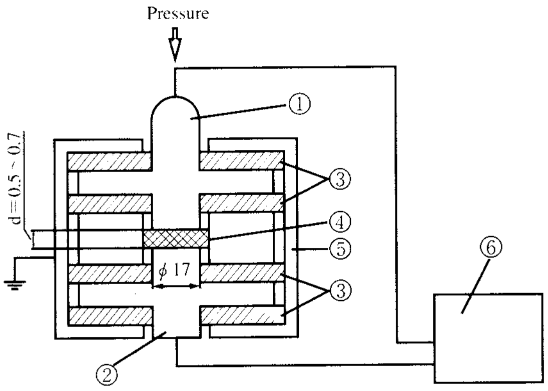

① Main electrode ② Opposite electrode
③ Insulatated supporter ④ Powder sample
⑤ Shield case ⑥ Impedance analyzer

Fig. 4. Method of electrical property characterization

$$\rho = R\left(\frac{s}{d}\right) \qquad (2)$$

$$X' = X\left(\frac{s}{d}\right) \qquad (3)$$

where ρ is the volume specific resistivity, R is the resistivity measurement, s is the sample cross sectional area, d is the sample thickness, X' is the corrected reactance value and X is the reactance measurement.

The dielectric loss tangent tan δ can be expressed as the ratio of the electrical resistance to the reactance using the following formula (4):

$$\tan\delta = \frac{X}{R} = \frac{X'}{\rho} \qquad (4)$$

4. Results and Discussion

4.1 Course of composite particle formation

Examples of SEM observations of particles obtained by dry coating treatment are shown in **Fig. 5.** A PMMA-Cu system was treated at a rotation rate of 25 rps. As seen in **Fig. 5,** fine particles of Cu adhered to the core particle in the form of scales at treatment times of 900 to 2700 sec. This may be associated with the compressive rolling of ductile Cu particles due to interparticle frictional force produced during the dry coating (composite particle formation) process. At a treatment time of 3600 sec, Cu particles were dispersed and coated on the entire surface of the core particle, in which Cu was present in a film form with indefinite borders between particles rather than with the scale form.

Fig. 6 (a) schematizes the course of composite particle formation found by SEM observation. It should be noted, however, that this model is not applicable to all the types of electrically conductive particles used in the study. The course of composite particle formation for other particle systems was examined.

Using Ni particles and ATK50 particles (fine particles), dry coating was conducted, and the course of composite particle formation was compared with Cu particles. **Fig. 7 (a)** shows that the PMMA-Ni system (A2) had Ni lumps of 2 to 10 μm thickness adhering to the surface of the core particle even when the coating treatment time t was changed from 900 sec to 2700 sec. Since the Ni particles used were spherical particles having an average particle size of 0.02 μm (see **Table 2**), the Ni lumps can be identified as aggregates rather than elongated particles. With respect to this system, it can be said that coating occurred at lower levels of rotation rate N and treatment time t (see **Table 2**) in comparison with the PMMA-Cu system. This suggests that the Ni particles are more likely to adhere to the core particle than Cu particles; Ni aggregates became coated on the surface of the core particle before they were thoroughly disintegrated in the initial stage of dry coating, as shown in the model of **Fig. 6 (b).**

In the PMMA-ATK50 system shown in **Fig. 7 (b)**, it was seen that ATK50 was coated on the entire surface of the core particle to form a composite particle. ATK50 exhibits no ductility because it is derived from Ag coating on the surface of TiO_2 particles. It can therefore be interpreted that ATK50 particles offer good coating on the core particle without considerable deformation. In this case, the state of fine particle (ATK50) dispersion was better than that in the PMMA-Ni system. The course of composite particle formation for the PMMA-Ni system is modelled as shown in **Fig. 6 (c).**

Next, the effect of core particle surface condi-

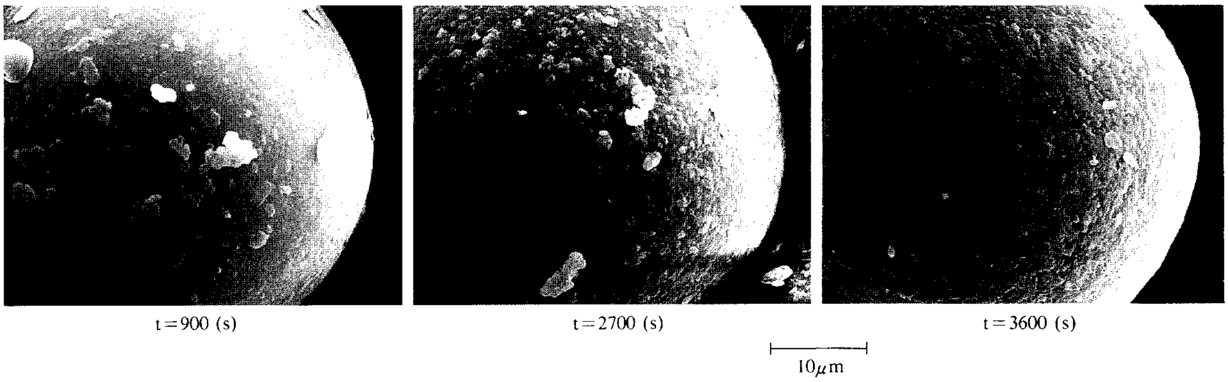

Fig. 5. Composite particle SEM observation (PMMA-Cu system (A1))

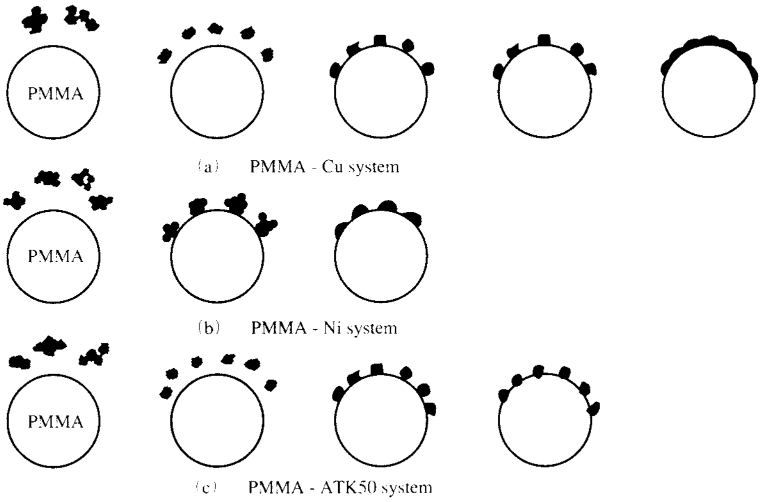

Fig. 6. Model of composite particle formation process

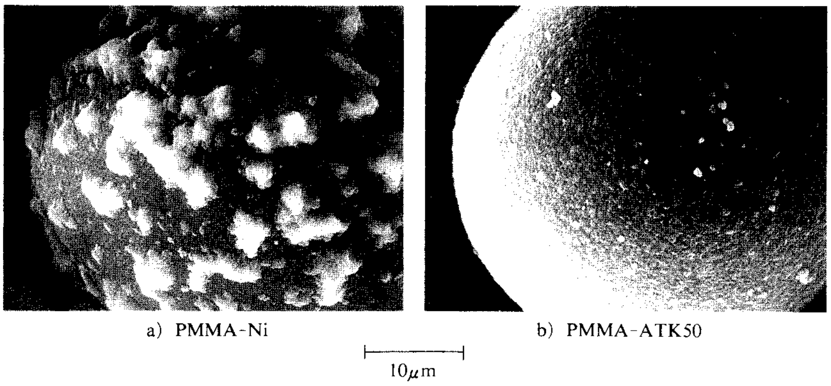

Fig. 7. Composite particle SEM observation

tion on the state of electrically conductive particle dispersion and coating was examined. Here, the use of Ni particles as coating particles (fine particles) is discussed. **Fig.** 8 shows an example of SEM observations on composite particles of the PMMA-Cu-Ni system (B1) or the PMMA-ATK50-Ni system (B3). In these systems, composite particles of the PMMA-Cu system (A1) or the PMMA-ATK50 system (A3), as core particles, were dry coated with Ni particles. As seen in **Fig.** 8, Ni in the PMMA-Cu-Ni system was coated as aggregates as in the PMMA-Ni

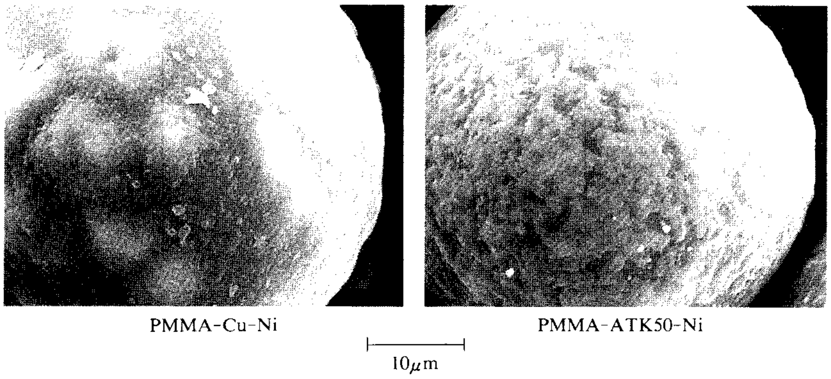

Fig. 8. Composite particle SEM observation (PMMA-Cu-Ni system (B1) or PMMA-ATK50-Ni system (B3))

system (**Fig. 7 (a)**). On the other hand, in the composite particles of the PMMA-ATK50-Ni system, Ni particles were coated in a film form. These findings suggest that Ni aggregates were coated after disintegration into primary particles when the core particle was coated with ATK50.

Although it has thus become possible to visualize the course of composite particle formation and the state of fine particle dispersion and coating, the state of fine particle dispersion cannot be quantified. Thus, quantitative evaluation of the state of electrically conductive particle (fine particle) dispersion on the surface of the core particle was attempted.

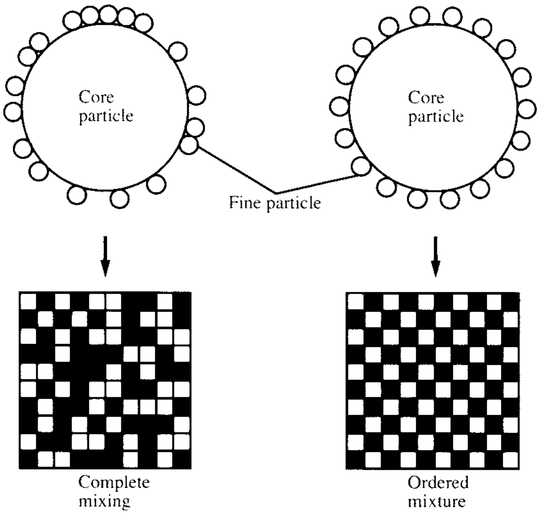

Fig. 9. Model of state of dispersion (mixing)

4.2 State of fine particle dispersion on the surface of a single particle

A model of the state of fine particle dispersion is given in **Fig. 9.** Conventionally, the state of mixing has often been evaluated on the basis of "complete mixing" or statistical homogeneity, and the target has been a group of particles (powder bed). However, in recent years, particle designing and composite particle formation have been actively investigated with an emphasis on "ordered mixture" or microscopic homogeneity. It is therefore essential to discuss "complete mixing" and "ordered mixture" from the viewpoint of a single particle. First, to examine the state of fine particle dispersion and coating on the surface of a core particle, elemental analysis (surface analysis) was performed using an energy dispersion X-ray spectrometer (EDX). Next, the state of fine particle dispersion was quantitatively evaluated by the method described in section 3.1, on the basis of the results shown in **Fig. 2.**

Table 3 gives the coefficients of variance CV for Cu, Ni and Ag on the surface of composite particles. These composite particles were obtained with the treatment times shown in **Table 2.** A low value of coefficient of variance means that fine particles have been uniformly dispersed (coated) on the surface of the core particle, i.e., an "ordered mixture" has been formed. As seen in **Table 3**, Ag-coated TiO_2 (ATK50) had the lowest value of coefficient of variance CV, indicating a good state of fine particle dispersion, which can be said to represent an "ordered mixture". With respect to the state of dispersion, ATK50 showed the best results followed by Ag and Cu particles, while Ni particles showed the worst results.

These findings suggest that when using Ag-coated TiO_2 particles, which are not liable to deform under shear, compression and other forces, composite particles with the most uniform dispersion of fine particles on the surface of the core particle are formed. This agrees with the SEM observation made in Section 4.1. It can be said that the use of the method described in Section 3.1. enables the evaluation of the state of fine particle dispersion on the sur-

Table 3. Coefficient of variance for target particle

Sample	Composite particle	First layer		Second layer	
		Target	Cv [-]	Target	Cv [-]
B1	PMMA-Cu-Ni	Cu	8.9	Ni	10.3
B2	PMMA-Ni-ATK50	Ni	11.4	ATK50	4.2
B3	PMMA-ATK50-Ni	ATK50	1.9	Ni	7.8
	PMMA-Cu-Ag	Cu	8.0	Ag	6.6

face of a single particle from the viewpoint of the "ordered mixture".

4.3 Relationship between the state of fine particle dispersion and coating and electrical properties

Since the resin-metal composite particles studied were prepared by dry coating of electrically conductive particles on the surface of insulator resin core particle, the coating state is apt to affect the electrical properties. Thus, the state of coating was discussed in view of the resistivity, reactance and dielectric loss tangent. **Fig. 10** shows the relationship between the alternating current electrical properties (volume specific resistivity tan ρ reactance X', dielectric loss tangent tan δ and treatment time t in composite particles of the PMMA-Cu system (A1). The volume specific resistivity ρ decreased with the treatment time. Since coating of the surface of the core particle by Cu particles proceeds according to the treatment time (see **Fig. 5**), electrically conductive paths are formed among particles, resulting in a decreased volume of specific resistivity and a good electric conductivity. As seen in **Fig. 10**, the reactance X' remained almost constant even when the treatment time the increased. Thus the dielectric loss tangent tan δ as calculated from equation (4), increased with the treatment time t. As regards these electrical characteristics, further investigation was made.

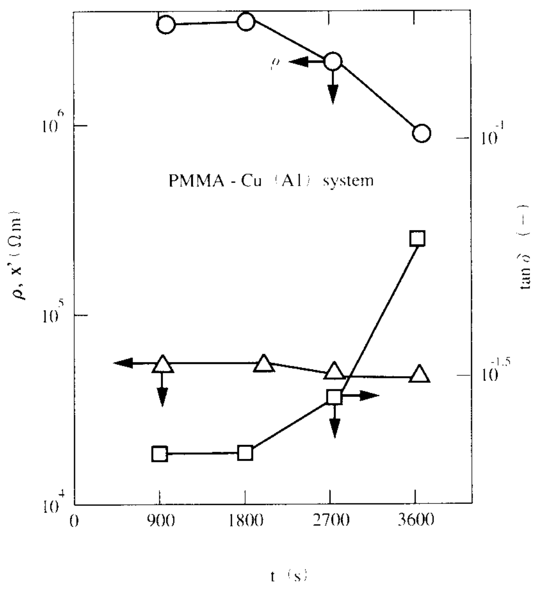

Fig. 10. Relationship between electrical properties and coating treatment time

First, the volume specific resistivity ρ was investigated on the basis of the R component of the parallel equivalent circuit of **Fig. 3.** If the resin core particle is the only factor for the determination, the resistance circuit can be represented by the resin's specific resistance RS, contact resistance RC and surface resistance RL, as shown in **Fig. 11 (a)**. RS and RC are negligible, as 1/RS and 1/RC go zero because the resin is usually an insulator, so that the surface resistance RL can be regarded as the resistance R of the entire circuit.

When the core particle resin and electrically conductive fine particles remain dispersed without composite particle formation, the electrically conductive (metal particles are present in the core particles; therefore, the electrical resistance is of a serial circuit of core particles and the metal (**Fig. 11 (b)**). The resistance of the system can be taken as being equivalent to that of the core particle (R = RL), since the resistance of the metal (electrically conductive particles) used is generally much lower than that of the core particle (resin).

When composite particles are prepared by accelerated dry coating, the metal particles coating of the surface of the core particle in an elongated form, as stated above. Therefore, the resulting composite particle system is characterized by surface contact (**Fig. 11 (c)).** In this case, in addition to the serial circuit of the resistance RL of the core particle and the resistance RM of the metal, the parallel circuit should be considered. As seen in **Fig. 11 (c)**, the surface resistance RL2 of the core particle forms a parallel circuit with the metal resistance RM in the area covered by electrically conductive particles. Since RM is much lower than RL, the resistance of the parallel circuit is equivalent to RM; this system forms a serial circuit of RL1 and RM. Because the RM of the serial circuit is negligible, the resistance R of the composite particle system can be expressed as the surface resistance RL of the core particle in the area not covered by electrically conductive particles. This means that the volume specific resistivity ρ decreases as the core particle surface area covered by Cu particles increases. This supports the finding that the volume specific resistivity ρ of the PMMA-Cu system (A1) decreased (electric conductivity

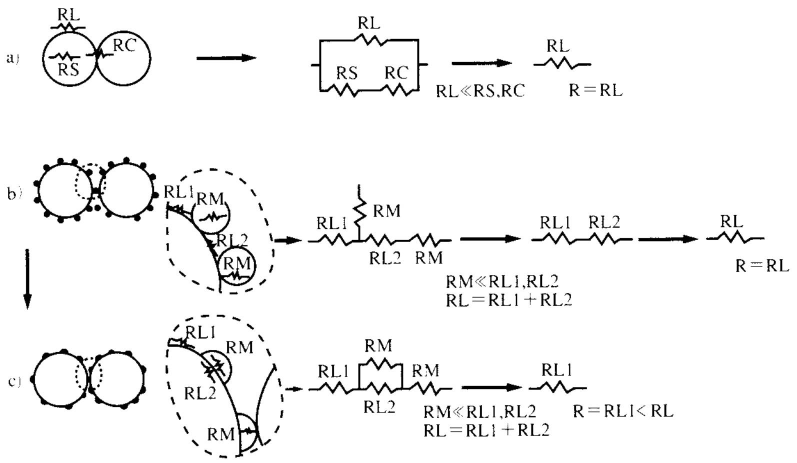

Fig. 11. Relationship between composite particle dispersion and coating state and electrical resistance circuit

increased) with the treatment time t.

Next, the reactance X' is discussed. In a circuit of reactance X', interparticle spaces, as well as the resin core particle and electrically conductive fine particles, should be considered. In this case, the system can be regarded as a system in which electrically conductive particles of inductance L are dispersed in two different media with different values of static capacity C. Therefore, the reactance of this system can be expressed in a circuit of the static capacity (condenser) of the core particle and the interparticle spaces and the inductance of electrically conductive particles. However, in the present experiment, the volume fraction of electrically conductive particles is about 1 to 5 vol%, as seen in **Table 2.** This level appears to have no significant effect on X'. **Fig. 12** shows the relationship between the reactance X' and the volume specific resistivity ρ of composite particles obtained in the present experiment. Unlike the volume specific resistivity, the reactance X' remains almost constant without any marked change, even when the type, feed rate and treatment time of electrically conductive particles were changed. The same applies to the results shown in **Fig. 10.** As seen in **Fig. 12,** it was the PMMA-ATK50-Ni (B1) system which had highly electrically conductive composite particles with a small value of volume specific resistivity ρ followed by particles of the PMMA-Ni-ATK50 (B2) system and of the PMMA-Cu-Ni (B3) system.

These findings demonstrate that the state of dispersion and coating of electrically conductive fine particles on the surface of the core particle can be evaluated in terms of the volume specific resistivity ρ rather than the reactance

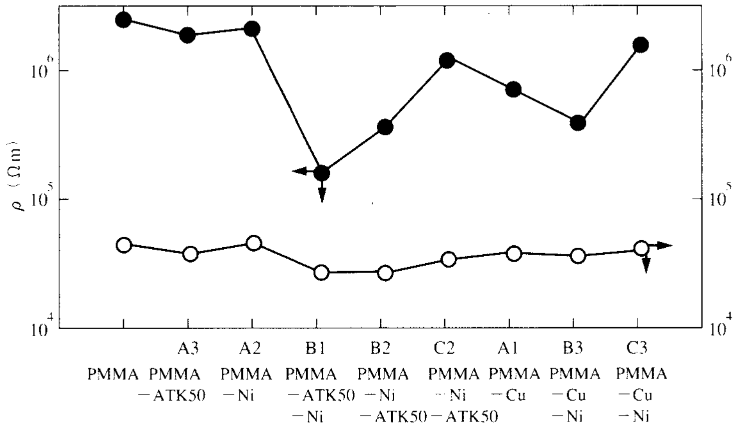

Fig. 12. Relationship between composite particle volume specific resistivity and reactance

X'. Also, when the reactance X' has a constant value as in composite particles prepared in the present experiment, the state of coating can be evaluated even on the basis of the dielectric loss tangent tan δ since the numerator of equation (4) is a constant so that equation (5) is obtained as follows:

$$\tan\delta = \frac{A}{\rho} \text{ (A is constant)} \qquad (5)$$

Equation (5) shows that dry coating accelerates as tan δ increases. There are some cases where the use of tan δ is advantageous. This is because tan δ can be expressed as the ratio of resistance R and reactance X' as in equation (4) so that it is unnecessary to determine the cross sectional area and thickness of the sample. Thus the dielectric loss tan δ was used as the basis for the evaluation of the state of dispersion and coating.

Composite particles were prepared with different treatment time t. The results are shown in **Fig. 13** as a function of dielectric loss tan δ and treatment time t. In the resin-ATK50 system, it appears that the model of Fig. 11 (b) is applicable, since ATK50 particles are fixed on the surface of the core particle without definite deformation, as described in the previous section. However, experimentation revealed that in all the systems examined, the dielectric loss tangent tan δ increases to some extent with the treatment time, i.e., the model of composite particle system shown in **Fig. 11** is applicable. When using ATK50 fine particles, some are embedded in the core particle[9], whereby the composite particle system model is formed. The tan δ of the composite particles B2 (PMMA-Ni-ATK50 system) can be said to be greater than that of the composite particles C2 (PMMA-Ni-ATK50 system). In other words, the former presents a better condition for coating. According to the SEM observation shown in **Fig. 8**, there is no clear difference between these two systems with respect to composite particle surface condition. However, the measurements of the dielectric loss tangent tan δ revealed that there is a clear difference in the state of coating between double coating (two types of fine particle subjected to dry coating one by one) and single coating (two types of fine particles are simultaneously treated as a mixture). This means that double coating offers better electrical properties.

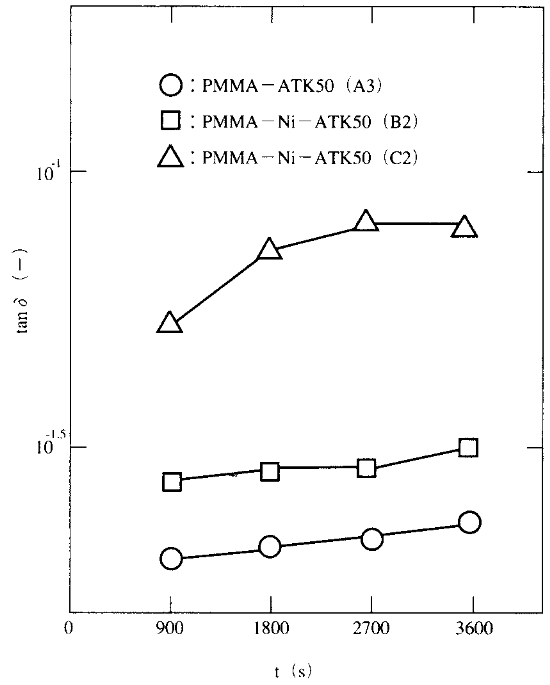

Fig. 13. Relationship between dielectric loss tangent and coating treatment time

Next, the use of fine Ni particles is discussed. **Fig. 14** shows measurements of tan δ of the PMMA-Ni system and other systems. Since the tan δ of the PMMA-Ni system remained almost constant even when the treatment time t was

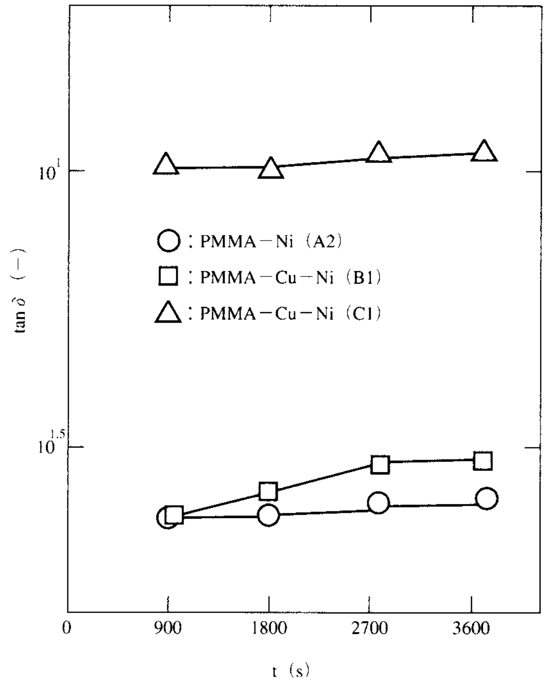

Fig. 14. Relationship between dielectric loss tangent and coating treatment time

changed from 900 to 2700 sec, the state of dispersion and coating appears to be constant. As seen in **Fig.** 8, the SEM observation of the PMMA-Ni system reveals that Ni was covered with aggregates at $t = 900$ sec, while the composite particle surface condition remains constant even at $t = 2700$ sec. It can therefore be speculated that dry coating can be completed at $t = 900$ sec. The same applies to composite particles of the PMMA-Cu-Ni system (B3). The $\tan\delta$ of the PMMA-Cu-Ni system, represented by the symbol C1, increased to some extent with the treatment time t, demonstrating a gradual progress of coating. These changes in $\tan\delta$ are similar to those found in the PMMA-Cu system rather than in the PMMA-Ni system, i.e., the course of composite particle formation of the PMMA-Cu-Ni system is strongly affected by Cu particles.

5. Conclusion

It has been demonstrated that electrically conductive composite particles can be obtained by dry coating electrically conductive fine powders on the surface of insulator particles. The course of composite particle formation, function etc. have been discussed on the basis of SEM observations, electrical properties and electrical resistance circuits. The method for evaluating the state of fine particle dispersion and coating on the surface of a single core particle has been investigated. The present findings can be summarized as follows:

1) The state of fine particle dispersion on the surface of a single composite particle can be evaluated by calculating the coefficient of variance of the target particle on the basis of data of the elemental analysis of fine particles on the composite particle. In other words, the state of dispersion can be quantitatively evaluated. The use of this evaluation method appears to ease the comprehension of the state of "ordered mixture" on the surface of a single particle.

2) The state of fine particle dispersion can be evaluated on the basis of the volume specific resistivity and dielectric loss tangent. The course of composite particle formation can be elucidated by measurements of these parameters and SEM observations. The state of dispersion and coating of electrically conductive fine particles improves as the volume of specific resistivity decreases or the dielectric loss tangent increases.

3) When using two types of electrically conductive particles to obtain composite particles with excellent electric conductivity, double coating (the two types are coated one by one) is better than single coating (the two types are simultaneously coated as mixture).

References

1) Alonso M., M. Sato and K. Miyanami: Powder Technol., **59**, 45 (1989)
2) Alonso M., M. Sato, K. Miyanami, K. Higashi and T. Ito: Powder Technol., **63**, 35 (1990)
3) Tanno K.: Funsai, No. 33, 81 (1989)
4) Naito M., M. Yoshikawa and T. Yotsuya: J. of the Japan Soc. of Powder and Powder Metallugy, **37**, 131 (1990)
5) Tanno K.: KONA, No. 8, 74 (1990)
6) Tanno K., T. Yokoyama and K. Urayama: J. of the Soc. of Powder Technol. Japan, **27**, 153 (1990)
7) Mizota K., S. Fujiwara and M. Senna: Mat. Sci, and Eng., **B10**, 139 (1991)
8) Terashita K., K. Umeda and K. Miyanami: J. of the Soc. of Powder Technol. Japan, **27**, 457 (1990)
9) Higashi M., K. Terashita and K. Miyanami: J. of the Soc. of Mat. Sci. Japan, **40**, 417 (1991).

Nomenclature

A = constant [−]
C = static capacity [F]
CV = coefficient of variance [%]
d = sample thickness [m]
f = frequency [Hz]
L = luminance levels [−]
$\bar{L}$ = mean of luminance levels [−]
N = rotation rate [rps]
s = sample cross sectional area $[\mathrm{m}^2]$
t = treatment time [s]
$\tan\delta$ = dielectric loss [−]
X = reactance measurement [Ω]
x' = corrected reactance value [Ωm]

σ = standard deviation for luminance levels [−]
ρ = volume specific resistivity [Ωm]

Simulation of Aggregate Packing and Analysis of Aggregating Process of Ultra-Fine Powder by Brownian Dynamic Method †

Hidehiro Kamiya and Genji Jimbo
*Dept. of Chem. Eng., Nagoya Univ.**

Abstract

Dense and uniform packing of ultra-fine powders, the primary particle size which ranges from 1 nm to 0.1 μm, is very difficult because of strong and sparse aggregation. In this paper, the aggregating process of ultra-fine powder is examined by Brownian dynamic methods, and the effects of interaction between the primary particles and the initial concentration on aggregate shape and size is analyzed quantitatively by Fractal dimension and Weibull's distribution function. Furthermore, the packing of aggregates, which are of various shapes and are composed of different numbers of particles, is investigated by computer simulation. The effect of the geometrical characteristics and size distribution of aggregates on the porosity and distribution of micropore diameters in a packed bed is analyzed. When many aggregates consist of hundreds of particles, the porosity exceeds 94%. The porous structure is obtained by bridging between several aggregates. The wide spaces in ultra-fine powder composed by bridging are confirmed experimentally by mercury porosimetry. The effect of shape and size distribution of aggregates on packed bed structures is remarkable in the case of weakly aggregated powder, which means that the number of constituent particles is below 10.

Introduction

Inorganic system ultra-fine powders of primary particle size 100 nm or less are expected to be of use as functional material powders or easy-to-sinter raw materials for structural ceramics, but problems may be involved in homogeneous dispersion or densification of packed beds and compacts since ultra-fine powders form strong and sparsely aggregated structures. With respect to the aggregating process of ultra-fine powders, an analysis using the diffusion model[3,11] has been carried out in the fields of aerosols, etc. On the other hand, with respect to the aggregate's shape and structure which affect the packed bed structure, simulations[12,13] in which particles are made to adhere one by one to a seed particle have been carried out. In particular, the Diffusion Limited Aggregation model[16] (DLA model), in which particles are allowed to move through a Brownian motion by pseudo-random numbers, is coupled with Fractal science and has been attracting the attention of researchers and the industry. Meakin[7] and Kolb et al.[5] almost at the same time carried out simulations by extending the DLA model and allowing all particles generated in a space to adhere and aggregate by pseudo Brownian motion and investigated the changes in aggregate structures by the Fractal dimension. In addition, Mountain et al.[9] eliminated the restrictions arising from the methods of Meakin[7] and Kolb et al.,[5] who advocated that particles move on the square lattice points, and carried out simulations representing a near actual Brownian motion, and called these methods Brownian Dynamics methods. The method advocated by Mountain et al.[9] is used for the analysis of the aggregation and destruction processes in the shear flow field[1] but since a large number of particles requires a very long calculating time, many of the studies primarily deal with few hundreds of

---

* Furou-cho, Chikusa-ku Nagoya 464-01, JAPAN
TEL. 052-781-5111

† This report was originally printed in *Kagaku Kougaku Ronbunshu*, **17**, 837-845 (1991) in Japanese, before being translated into English with the permission of the editorial committee of the Soc. Chemical Engineers, Japan.

particles. The methods advocated by Meakin,[7] Kolb,[5] etc. are believed to be effective when the number of particles is of the order of several thousands or more, but they have been adopted only for the analysis of particle growth[15] by sintering catalyst particles. No systematic investigation of the effects[4] of interaction between particles on the aggregate shape and structure has yet been undertaken. For the packing characteristics of powders, simulations in which rigid single ball are packed one by one[14] have been carried out, but investigations in which the relationship between aggregate structures and packed bed structures are studied using particles which cause aggregation, such as ultra-fine powders, have scarcely been reported.

In this paper, allowing the interactions between particles to be represented by adhesive probability and varying the initial concentration of the primary particles, clusters of various shapes and a wide range of distribution of the constituent particles have been formed by the Brownian Dynamics method which is similar to the techniques of Meakin,[7] Kolb,[5] etc. The effects of interaction between particles and of their concentration on the aggregation process as well as on the aggregate's shape and distribution of constituent particles were quantitatively analyzed using Fractal dimension and Weibull's distribution function. In addition, simulations of packing clusters obtained were carried out and an analysis of the relationship between the ultra-fine powder packed bed structures and aggregate structures was performed. Lastly, ultra-fine powder compacts were experimentally analyzed by mercury porosimetry and the adequacy of the simulation results was investigated with special emphasis placed on the distribution of micropore diameters.

1. Simulation and Experiment

1.1 Simulation of aggregation

Figure 1 (a) shows schematically the aggregation simulation method. The simulation was carried out in two-dimensions. The space was divided into square cells of side A and it was assumed that particles were generated and aggregated in the same manner in all cells.[16] The space for which the simulation was performed was one of these cells. It was assumed that particles were generated in this cell randomly and the particles (i) leaving the cell by pseudo-Brownian motion entered the cell in the opposite direction. This square cell was divided into square lattices, one side of each of which was equal to the particle diameter (d_P) to be generated and particles were assumed to be circles moving on lattice points. For the Brownian motion of primary particles, it was assumed that the particles moved by unit lattice in either one of the four directions, up, down, right, or left, according to one calculation loop using pseudo random numbers (R [0, 1]). On the other hand, it was assumed that the Velocity of Brownian motion decreased as the aggregate grew and the movement was restricted in accordance with the Einstein equation,[3,10] Eq. (1), in which the mean displacement of a particle per unit time ($\Delta x/t$) through the Brownian motion is proportional to the primary particle diameter (d_P) to the power -1/2.

$$\frac{\Delta\chi}{t} \propto \{D_B\}^{1/2} \propto d_P^{-1/2} \qquad (1)$$

The representative diameter of the aggregate (d_{Pag}) was considered to be the square of the mean distance from the center of gravity of the aggregate to each particle in Eq. (2) and the displacement was considered to be proportional to d_{Pag} to the power 1/2.

$$d_{pag} = 2R_g = 2\{\sum_{i=1}^{N}(\frac{r_i^2}{N})\}^{1/2} \qquad (2)$$

All particles composing the aggregate were assumed to move by unit lattice in either one of the four directions, up, down, right, or left, only when the relationship between pseudo random numbers newly generated and Eq. (3) was satisfied.

$$\frac{1}{(d_{pag})^{1/2}} > R[0, 1] \qquad (3)$$

where, D_B is the coefficient of diffusion, r_i is the displacement from the i-th particle to the center of gravity of the aggregate, and N is the number of constituent particles in each aggregate. Whenever other particles came above, below, right, or left of each particle through the pseudo Brownian motion and the generated pseudo random number was greater than the first assumed adhesive probability for the aggregation process (P_a), adhesion aggregation occurred and if it were small, the particles moved in a direction away from other particles in the next calculation loop. For calculation conditions, the magnitude of various repulsive forces between particles such as repulsion by electric double layers in the liquid were represented by the adhesive probability (P_a). The aggregates with various types of structures and distribution of constituent particles were prepared by varying the initial concentration of primary particles (n_0) and the adhesive probability. The target cell size (A) was fixed at 180 times the primary particle diameter.

1.2 Packing simulation

Figure 1 (b) outlines the packing simulation method of aggregates. The horizontal direction (x) of the plane being simulated was assumed to be an infinitely repeated width (B) in the same manner as in the aggregation simulation, and the vertical direction (y) was considered to extend infinitely upward with the origin fixed. Prior to packing aggregates, clusters of particles obtained through the aggregation simulation were ranked, and the aggregate of the rank closest to the product of the total number of aggregates by pseudo random number R [0, 1] was designated as being a generated aggregate particles. After rotating the selected aggregate through an angle of 2 πR [0, 1] about the center of gravity (x_{ag}, y_{ag}), it was moved laterally so that they y coordinate of the center of gravity did not come in contact with the packed particles (y_{max} + r_{max}) while the x coordinate remained at a distance equal to the product of the newly generated pseudo random number R [0, 1] and the cell width (B). Then, all particles forming the aggregate were allowed to settle per unit lattice. Whenever one of the aggregate constituent particles came into contact with the packed particles, the aggregate was allowed to adhere to the packed bed if the adhesive probability for the packing process (P_c) previously assumed was greater than the newly generated pseudo random number.

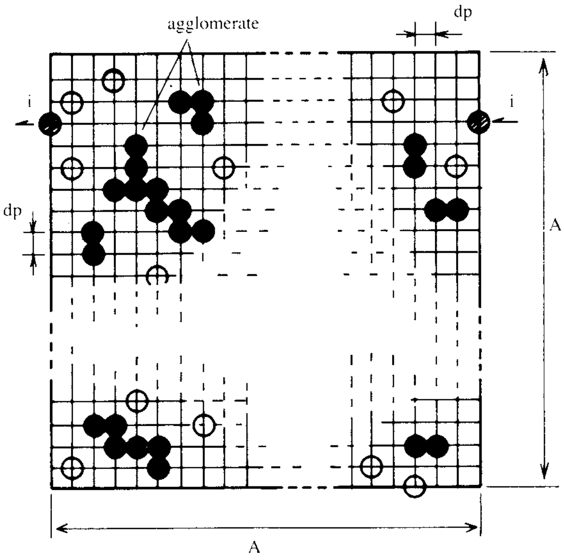

(a) Aggregation by Brownian dynamics method

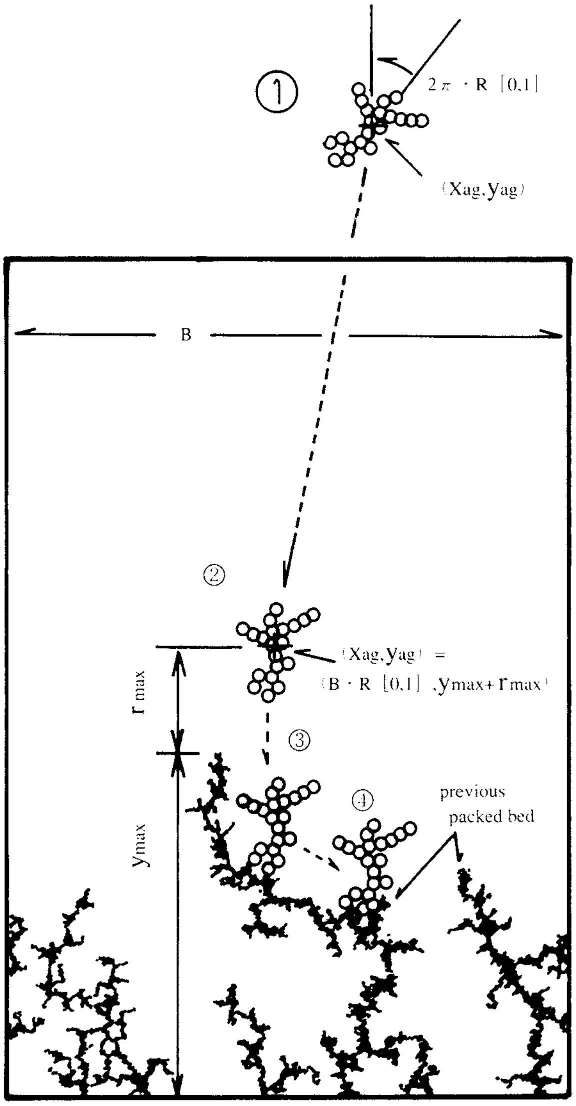

(b) Simulation of cluster or aggregate packing

Fig. 1 Schemes of simulated methods

Whenever the adhesive probability was high, more than several hundreds of aggregates were able to be linked even through one-point contact. For particles of several hundreds of nm in diameter, the adhesive force between particles may reach tens of thousands of times the dead weight of the particle,[10] and these conditions were assumed to exist actually.

When particles did not adhere and there was no particle of packed bed one lattice below all the aggregate composing particles, the aggregate was allowed to settle in one further lattice. Whenever any packed particle existed, the aggregate was allowed to move horizontally and settle at a position where there was no packed particle one lattice below while moving by one lattice either right or left by random numbers. Every time a particle settled, adhesion judgment was made, and when the generated random number became greater than the adhesive probability (P_c) or the aggregate entered the packed bed and was unable to move downward, the aggregate adhered to the packed bed. For simulation purposes, the adhesive probability of the packing process (P_c) was defined as being either 1 or 0. From the obtained packed bed, the porosity and micropore diameter distribution were determined.

1.3 Experiment by mercury porosimetry

As a comparison with the packing simulation results, the micropore diameter distribution was measured by mercury porosimetry (Micrometrics Inc., Poresizer 9310). **Table 1** shows powder samples used for the experiment. The micropore diameter distribution was measured at a maximum uniaxial pressure of 414 MPa by cutting out a small piece assuming that powder packed beds are filled into a 20-mm-diameter mold and formed under pressures ranging from 12 to 30 MPa.

2. Results and Discussion

2.1 Aggregation simulation results

Figure 2 shows one example of the results. In order to investigate the effect of the initial concentration of primary particles (n_0) defined by the ratio of the total area of generated circular particles to the area of square cells of side (A), in **Figures 2 (a)** and **(b)**, the adhesive probability (P_a) was fixed at 1.0 and the generated concentration was varied between 0.185 and 0.077, respectively. **Figures 2 (b)** – **(d)** show cases in which the initial concentration (n_0) was fixed at 0.077 and the adhesive probability (P_a) was varied between 1.0 and 0.005. The numerals in the figure ($\Delta x/d_P$) represent the ratio of the overall displacement of individual particles (Δx) to the diameter of the primary particle (d_P), which indicates the nondimensional elapsed time counted from the generation of the particle and corresponds to the number of calculation loops in the simulation of this report.

A comparison of **Figures 2 (a)** and **(b)** indicates that in the case of the higher the particle concentration ($n_0 = 0.185$), the faster is the aggregating speed, and the gel condition in which all particles are bonded is produced at $\Delta x/dp = 528$. The shape of the aggregate tends to become denser as the concentration increases. A comparison of **Figures 2 (b)** – **(d)** indicates that a lowering of the adhesive probability decreases the aggregating speed and at the same time, and the aggregate shape changes from a coarse structure with many branches to a mass. The primary particles or small aggregates with comparatively small numbers of constituent particles have a high probability of coming into contact at the tip end of large aggregates first through Brownian motion. Consequently, when the adhesive probability is high, the particle or aggregate is caught at the tip end of the large aggregate and cannot move deeper inside, whereas in the case of a low adhesive probability, the particles or aggregates do not adhere even when they are in the vicinity of the tip end and are allowed to move deeper inside,[8] where they may produce a mass structure.

In order to quantitatively determine the change of the aggregate's shape as a function of the conditions, an analysis by Fractal dimension (D) was carried out. **Figure 3 (a)** shows one example of the analysis results. This figure shows the relationship between the mean radium (R_g) of an aggregate found from Eq. (2) and the number of particles in a cluster or aggregate (N), with respect to every aggregate having 10 or more constituent particles (N) obtained through the aggregation process. The Fractal dimension (D) is given by the following equation.

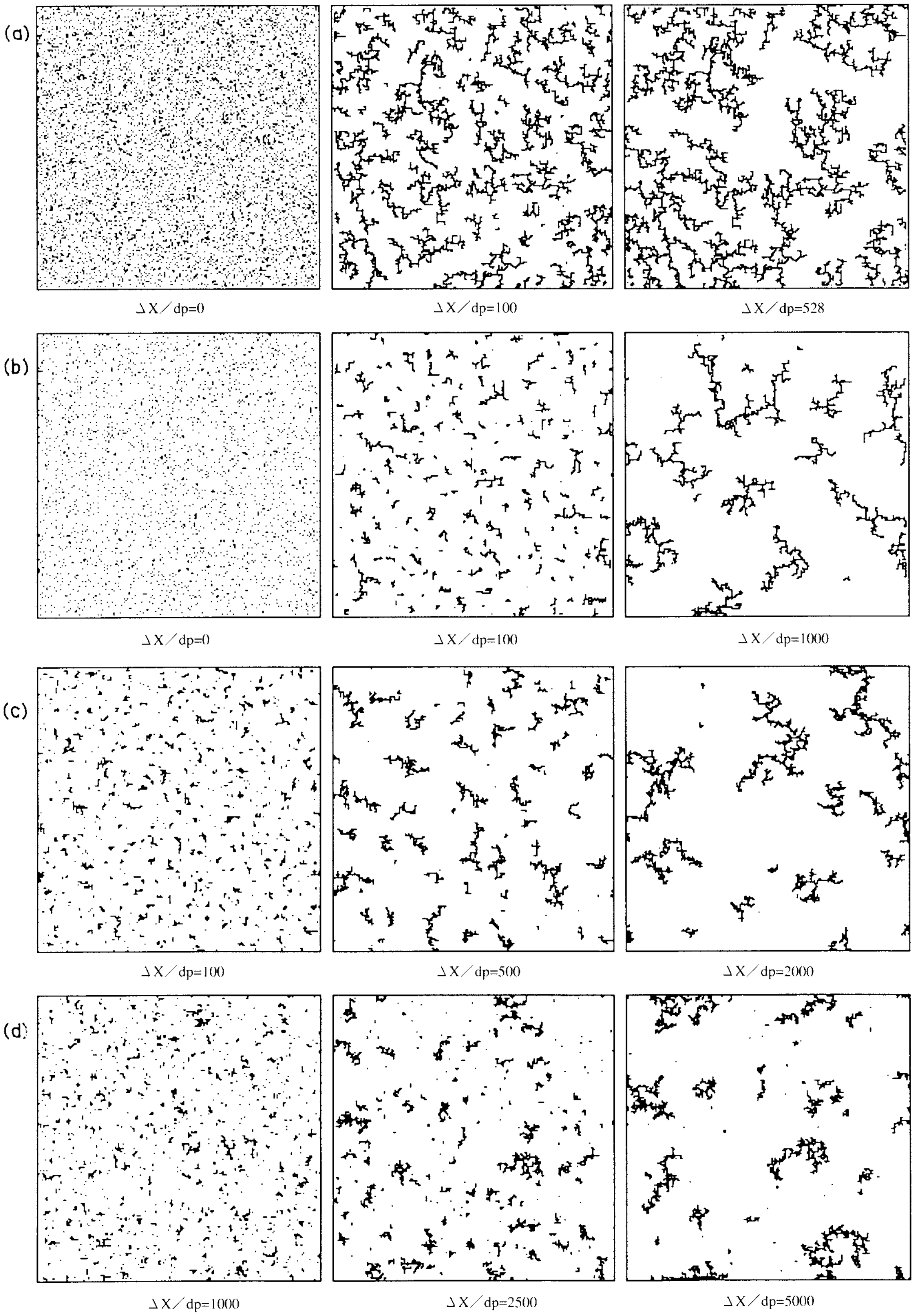

(a) $\Delta X/dp=0$ $\Delta X/dp=100$ $\Delta X/dp=528$

(b) $\Delta X/dp=0$ $\Delta X/dp=100$ $\Delta X/dp=1000$

(c) $\Delta X/dp=100$ $\Delta X/dp=500$ $\Delta X/dp=2000$

(d) $\Delta X/dp=1000$ $\Delta X/dp=2500$ $\Delta X/dp=5000$

Fig. 2 Effect of initial concentration (n_o) and adhesion probability (P_a) on aggregating process

(a) $n_0=0.185$, $P_a=1.0$ (b) $n_a=0.0772$, $P_a=1.0$
(c) $n_0=0.077$, $P_a=0.1$ (d) $n_0=0.0772$, $P_a=0.005$

$$R_g = N^{1/D} \quad (4)$$

Figure 3 (a) is determined for all conditions with initial concentration of primary particles (n_0) and adhesive probability (P_a) varied. The Fractal dimension (D) is calculated using Eq. (4), and the results are shown in **Figure 3 (b)**. It has been quantitatively confirmed that the higher the initial concentration of primary particles and the smaller the adhesive probability, the higher the Fractal dimension (D), and the dense structure of the aggregate was obtained. The tendency of the Fractal dimension to increase due to lowered adhesive probability differs depending on the initial concentration of primary particles. In the case of $n_0=0.185$, the Fractal dimension increases gradually, whereas in the case of $n_0=0.0077$, it increases only when $P_a=0.005$. Consequently, it has been determined that the aggregate structure varies in a complicated manner depending on the conditions.

Next, in order to quantitatively investigate the effect of the initial concentration of primary particles and of the adhesive probability on the aggregating speed, **Figures 4 (a)** and **(b)** were drawn to show one example of a decreasing process of monodisperse particles. The abscissa represents the number of calculation loops and the ordinate represents the concentration of monodisperse particles (n) expressed as a ratio to the initial concentration (n_0). The curve in the figure is approximated by Eq. (5), which is

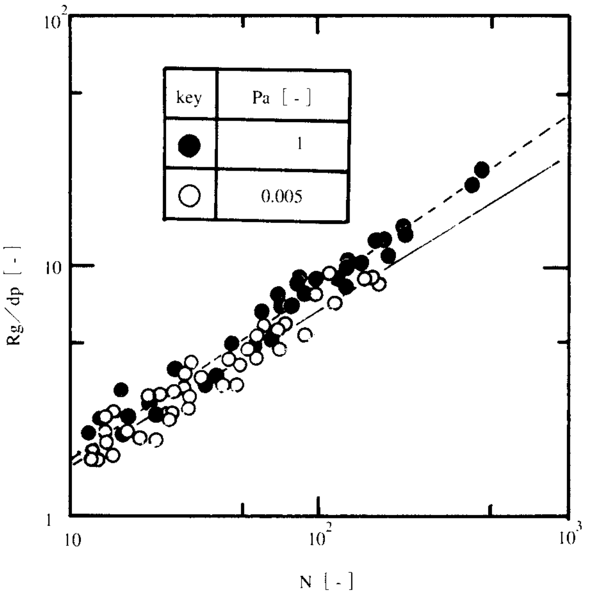

(a) An example of analyzed result

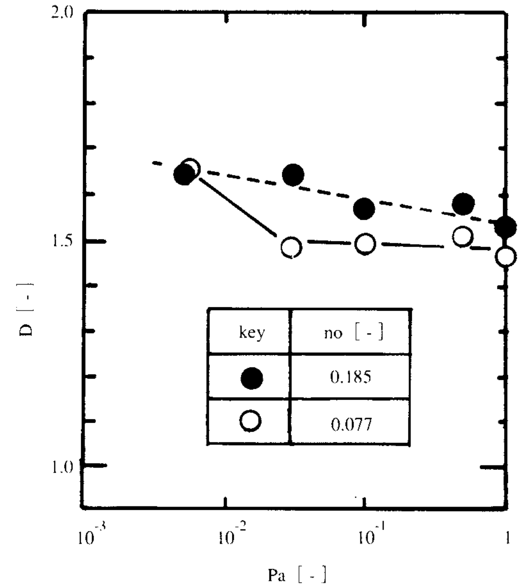

(b) Effect of adhesion probability (P_a) and initial concentration (n_0) on Fractal dimension

Fig. 3 Analysis of aggregate structure by Fractal dimension

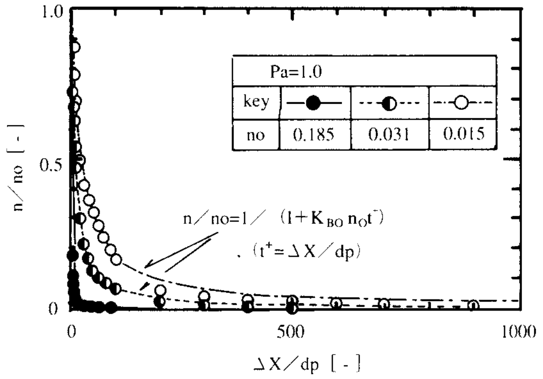

(a) Effect of initial concentration (n_0)

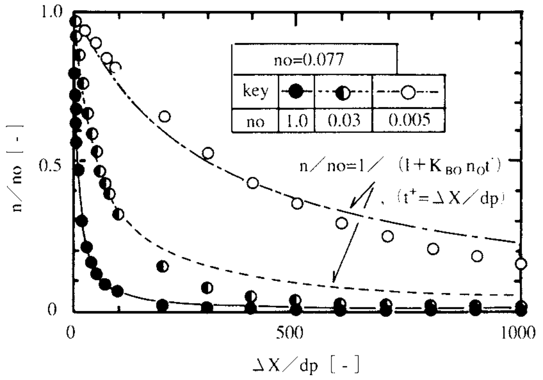

(b) Effect of adhesion probability (P_a)

Fig. 4 Examples of decreasing process of primary particle, and analyzed by Smoluchowski's equation deduced from the Smoluchowski's equation ($dn/dt=-K_{B0}n^2$)[3] of the aggregating speed.

$$\frac{n}{n_0}=\frac{1}{(1+K_{B0}n_0t)}=\frac{1}{\left\{1+\frac{K_{B0}^{+}n_0\Delta_x}{d_p}\right\}} \qquad (5)$$

where K_{B0}^+ corresponds to the coefficient K_{B0} when time t is replaced by the nondimensional time $\Delta x/d_P$. The Smoluchowski's equation is a relation which holds true for the initial aggregation stage of monodisperse particles in the three-dimensional space, but it was assumed to apply to a quantitative comparison of the aggregation process since it can be satisfactorily approximated by Eq. (5) in the range of $\Delta x/d_P < 1000$ even in two-dimensional conditions. Therefore, parameter K_{B0}^+ was estimated by the nonlinear least square method, the results of which are shown in **Figure 5**. **Figure 5 (a)** shows the results of plotting K_{B0}^+ versus the initial concentration of primary particles, and indicates that K_{B0}^+ exhibits a concentration dependency when the adhesive probability is particularly high. Conventionally, the Smoluchowski's equation was believed to hold true for the initial stage of the aggregation of monodisperse particles, but in the case of a high adhesive probability, the aggregation takes place immediately after the particle is generated as the particle concentration increases, and the particle becomes a polydisperse aggregating particle, possibly invalidating the Smoluchowski's equation.[2,6]

Figure 5 (b) shows the variation of constant K_{B0}^+ with respect to the adhesive probability. Under the condition of an adhesive probability of 0.1 or lower, the constant increases almost proportionally with the adhesive probability. In the Smoluchowski's equation, the number of collisions between particles per unit time (N_B) is related to Eq. (6), and the deceasing rate of monodisperse particles' is found by assuming that two monodisperse particles are eliminated per collision.[11]

$$N_B=8\pi D_B d_P\cdot n^2=K_B\cdot n^2 \qquad (6)$$

where, K_B is the coefficient corresponding to

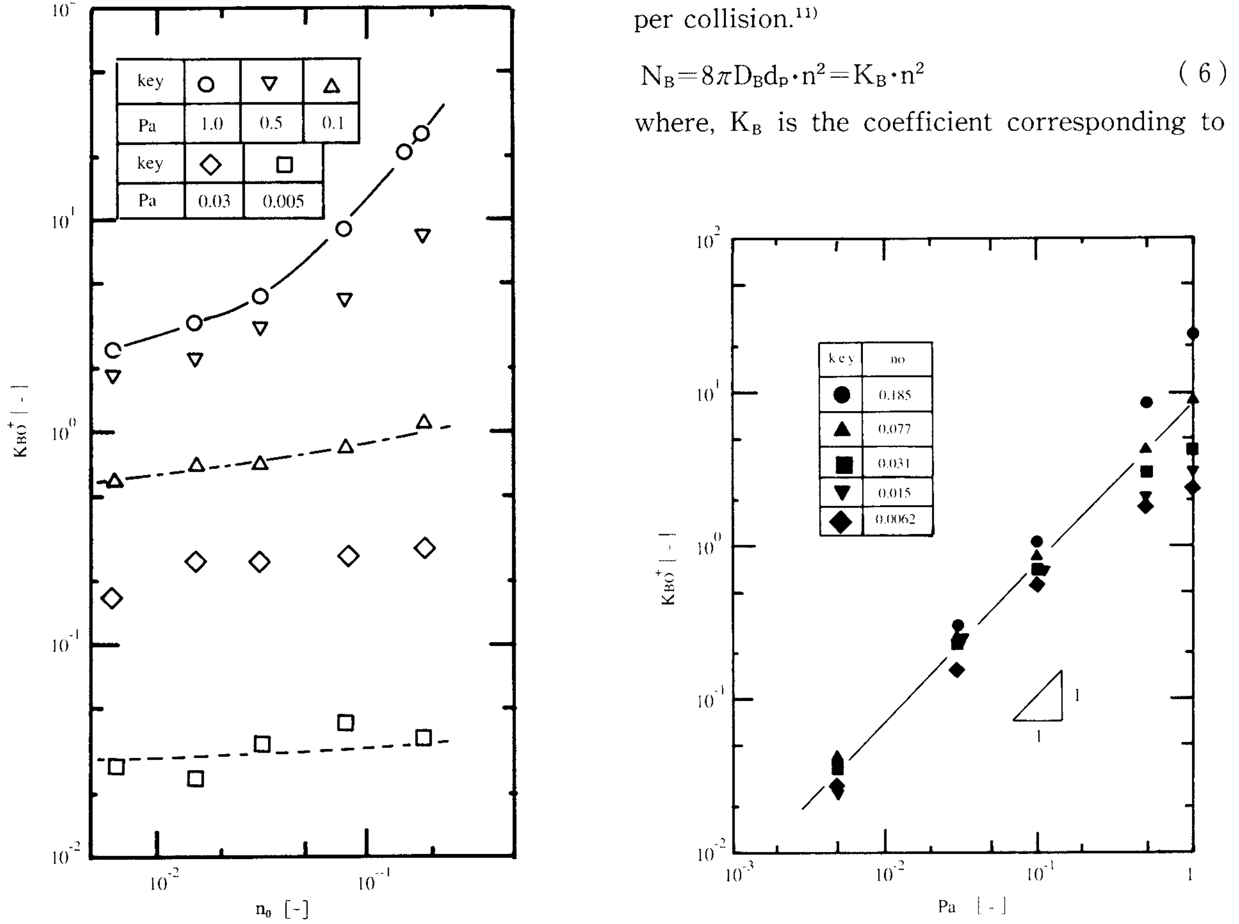

(a) Effect of initial concentration(n_0)

(b) Effect of adhesion probability(P_a)

Fig. 5 Parameter (K_{B0}^+) in Smoluchowski's equation obtained by Brownian dynamics method particle collision. Consequently, in the case of P of which the adhesive probability is lower than 1, the frequency of adhesion aggregation in all collisions becomes the frequency found by multiplying Eq. (6) by P_a, and therefore, the decreasing rate of monodisperse particles' is given by Eq. (7).

$$\frac{dn}{dt} = -2K_B \cdot P_a \cdot n^2 = -K_{B0}(P_a) \cdot n^2 \qquad (7)$$

Consequently, assuming that the number of collisions does not change if the frequency of the collisions is not varied even if the number of adhesion collisions varies, if coefficient K_{B0} (P_a) of the Smoluchowski's equation satisfied the conditions of monodisperse particles at the initial aggregation stage, it becomes proportional to the adhesive probability. **Figure 5 (b)** shows a case in which aggregating particles are not generated in a large quantity at the initial stage and the coefficient is nearly proportional to the adhesive probability, thus proving the adequacy of this simulation.

Figure 6 (a) shows one example of the aggregation process arranged with special emphasis on the change in the distribution of the number of constituent particles of the aggregate. This figure represents the distribution of the number of mass-based constituent particles in cluster or aggregate (Q) using the two-parameter Weibull's distribution when the initial concentration of primary particles is $n_0 = 0.0077$ and the adhesive probability is 1.0.

$$Q = 1 - \exp\{-(\frac{N}{Nc})^m\} \qquad (8)$$

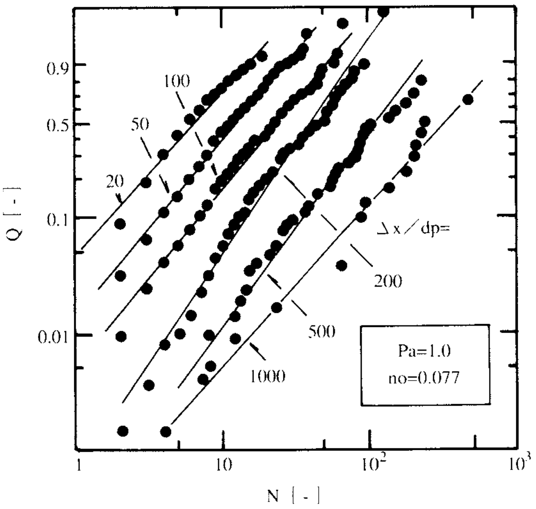

(a) Examples of analyzed result

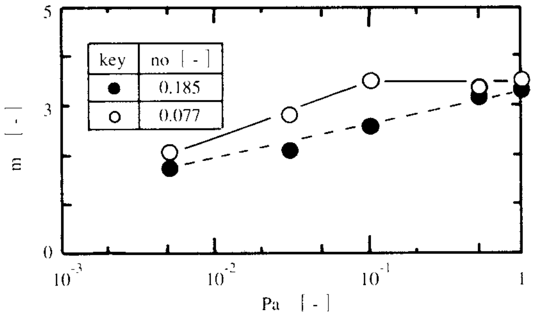

(b) Effect of adhesion probability(P_a) on mean value of shape parameter

Fig. 6 Analysis of cumulative distribution of particle number in each aggregate by Weibull's distribution function

On the Weibull's distribution graphic paper, the distribution of the constituent particles is approximated to an almost straight line, and the distribution can be represented by the scale parameter (N_c) which represents the number of constituent particles at a cumulative probability of 63.2% and the shape parameter (m) which represents the width of the distribution. Under the conditions used in the recent investigation, the scale parameter (N_c) increases almost proportionally with time except during the last stage of the aggregation in which the number of aggregates increases as shown in **Figure 6 (a)**, while the shape parameter (m) remains nearly constant, with a slight variation. In order to investigate the effect of the calculation conditions, the scale and shape parameters are plotted in **Figure 6 (b)** against the adhesive probability to find the mean value of m. The figure indicates that when the adhesive probability is close to 1, m is about 3 but as the adhesive probability decreases, m decreases and the distribution of the constituent particles expands. Analyzing the distribution with particle concentration taken into account, the same results as those of the Fractal dimension are obtained in the case of a concentration of 0.185. The distribution monotonously decreases as the adhesive probability decreases, but at $n_0 = 0.077$ a significant decrease is observed at an adhesive probability of 0.03 or lower. Consequently, it may be assumed that there is a correlation between the distribution of constituent particles and the aggregate structure.

2.2 Packing simulation results and discussion

A packing simulation was carried out using clusters with different distributions of constituent particles and structures obtained through an aggregation simulation. First, an example of the results is shown in **Figure 7** where the adhesive probability (P_c) during packing is fixed at 1. At a high adhesive probability, the aggregates were considered to grow large, and clusters of ultra-fine particles of which the scale parameter (N_c) of the distribution of constituent particles was of the order of several hundreds were assumed for the packing process. Regarding the conditions during aggregation, the adhesive probability (P_a) was fixed at 1, and **Figure 7 (a)** shows the result of packing clusters when the particle concentration (n_0) is 0.077 and $\Delta x/d_P$ =1000, while **Figure 7 (b)** shows the result when (n_0) is 0.185 and $\Delta x/d_P$ = 200. In both cases, large spaces are generated since the aggregates form bridging structures, resulting in extremely sparse structures having a porosity of over 90%. In the case o. f ultra-fine powders formed by an actual vaporization process, there exist cases with more numerous constituent particles, suggesting the possibility of a simulation of packed beds with a higher porosity and with a further increase in the number of constituent particles.

In order to investigate the effect of the number and structure of aggregate constituent particles on the packed bed structure, **Figure 8** is used to show the porosity when clusters obtained under various conditions are packed at an adhesive probability (P_c) fixed at 1.0. The abscissa represents the scale parameter (N_c) of the distribution of the constituent particles of

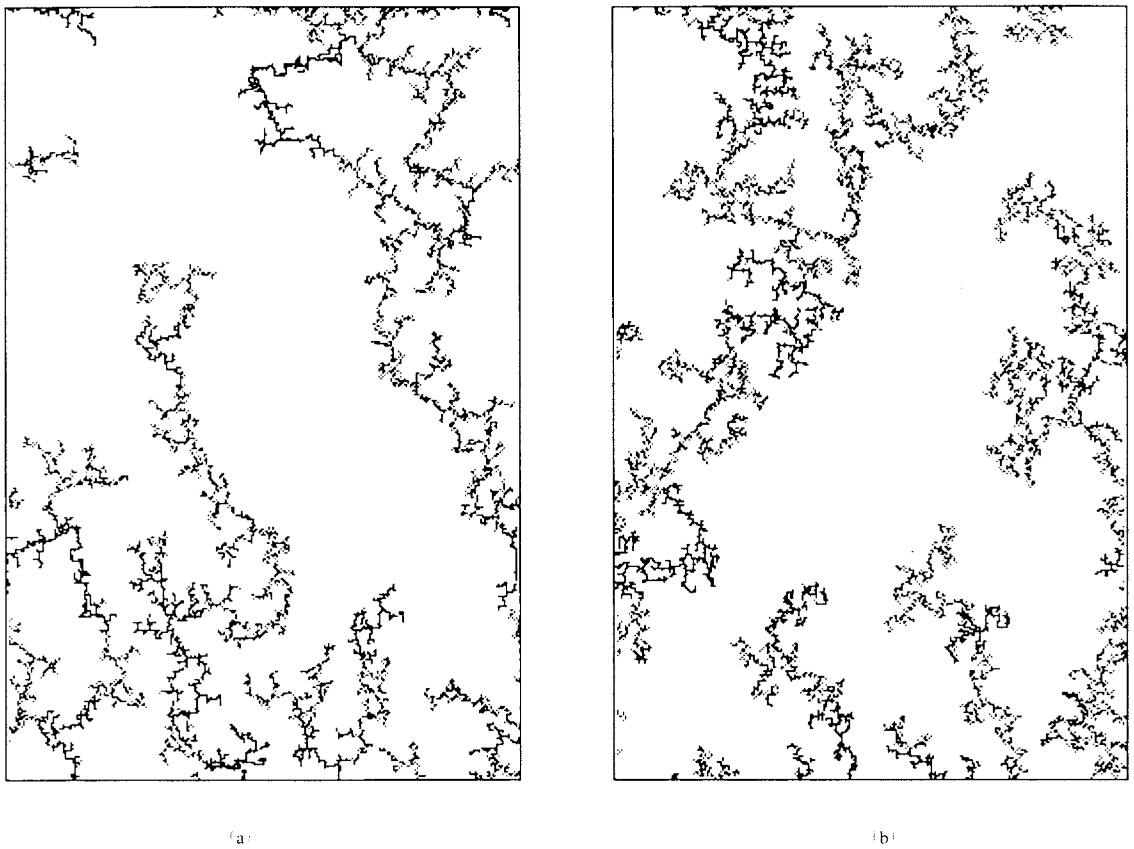

(a) Aggregated condition : $n_0=0.185$, $P_a=1$, $\Delta x/d_p=1000$, $N_c=395$, $m=3.30$, $D=1.47$ Packed result ; $\varepsilon=0.941$

(b) Aggregated condition : $n_0=0.185$, $P_a=1$, $\Delta x/d_p=200$, $N_c=858$, $m=3.32$, $D=1.54$ Packed result ; $\varepsilon=0.925$

Fig. 7 Structure of higt porosity packed bed obtained by packing simulation. Adhesion probability (P_c) on packing process is fixed 1.0. Aggregates which composed mean particle's number is more than 100 are used.

the aggregate and the ordinate represents the porosity of the packed bed. Under the condition of $P_c = 1$, the effect of the number of constituent particles on the porosity is comparatively small as compared to that at a low adhesive probability which is discussed later. An analysis of the effect of the aggregate's structure indicates that even at the same N_c value, the porosity tends to decrease as the Fractal dimension (D) increases and the shape parameter (m) of the distribution of constituent particles decreases.

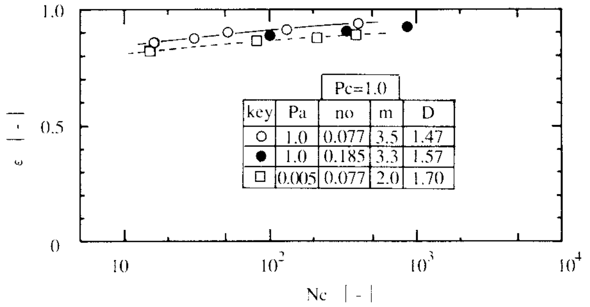

Fig. 8 Relations between porosity of packed bed and scale parameter in Weibull's distribution function. Adhesion probalility (P_c) in packing process is fixed 1.0.

Figure 9 shows one example of the results of packing at an adhesive probability (P_c) fixed at 0 when aggregates settle to enter the packed bed and are unable to move further. **Figure 9 (a)** shows the results of packing aggregate clusters similar to those used in **Figure 7 (a)**. Compared to the porosity of 0.941 indicated in **Figure 7 (a)**, the porosity slightly decreases to 0.910 when the adhesive probability during packing is fixed at 0, but a large bridging structure exists, resulting in an extremely high porosity. **Figure 9 (b)** shows the result of packing clusters at the initial aggregation stage $(\Delta x/d_P) = 50$ under the same aggregation conditions as those of **Figure 9 (a)**. A scale parameter of 15.9 and fine powders of about 1 nm with lower aggregation capabilities than those of ultra fine powders of several tens of nm used in (a) are used here, but the porosity has dropped to 0.688. However, through they are still smaller than those found in **Figure 9 (a)**, pores with diameters equivalent to dozens of particles are present. These pores may still remain even after compression forming or sintering, and may result in nonhomogeneous structures of sintered compacts. **Figures 9 (c)** and **(d)** show cases in which the adhesive probability (P_c) is set at 0.005 while the Fractal dimension and shape parameter of the distribution of constituent particles are varied. Indicating the results of packing clusters at the stage of $\Delta x/d_P = 5000$ and 1500, respectively, in which a scale parameter nearly similar to that of **Figures 9 (a)** and **(b)** can be achieved. Lowering the adhesive probability during aggregation increases the Fractal dimension, makes the aggregate structure denser, and expands the distribution of the constituent particles, thus lowering the porosity below that of (a) and (b).

To confirm this tendency, aggregates prepared under various conditions were packed at an adhesive probability of $P_c = 0$, the results of which are summarized in **Figure 10**. This figure is a plotting of the relationship between the scale parameter (N_c) of the distribution of constituent particles of clusters used for packing and the porosity, similar to that of **Figure 8**. When N_c is 100 or less the porosity rapidly decreases, and the adhesive probability during the packing of clusters shown with solid and dotted lines, the aggregate's shape at the initial concentration of primary particles as well as the Fractal dimension (D) and the shape of the distribution of the constituent particles (m) have more effects on the porosity than in the case of $P_c = 1$. When N_c exceeds 100, the effects of the shape of the aggregates and those of the adhesive probability during aggregation and packing decrease, resulting in about 90% porosity under any condition.

In order to investigate in detail the effect of the adhesive probability (P_c) during packing, P_c was varied from 0 to 1 for clusters of $N_c = 395$ and 15.9, respectively, which were used in **Figure 9 (a)** and **(b)**, and packing was carried out. The corresponding results are shown in **Figure 11**. In the case of clusters with a large scale parameter $N_c = 395$, the change in porosity is minor. On the other hand, in the case of clusters with a comparatively small scale parameter $N_c = 15.9$, the porosity rapidly decreases in the range from $P_c = 0.1$ to 0.01.

Finally, **Figure 12** shows the measurement results of the distribution of micropore diameters as a comparison between the structure of the packed bed obtained by simulation and that of actual ultra-fine powder packed compacts. **Figure 12 (a)** shows the measurement results of

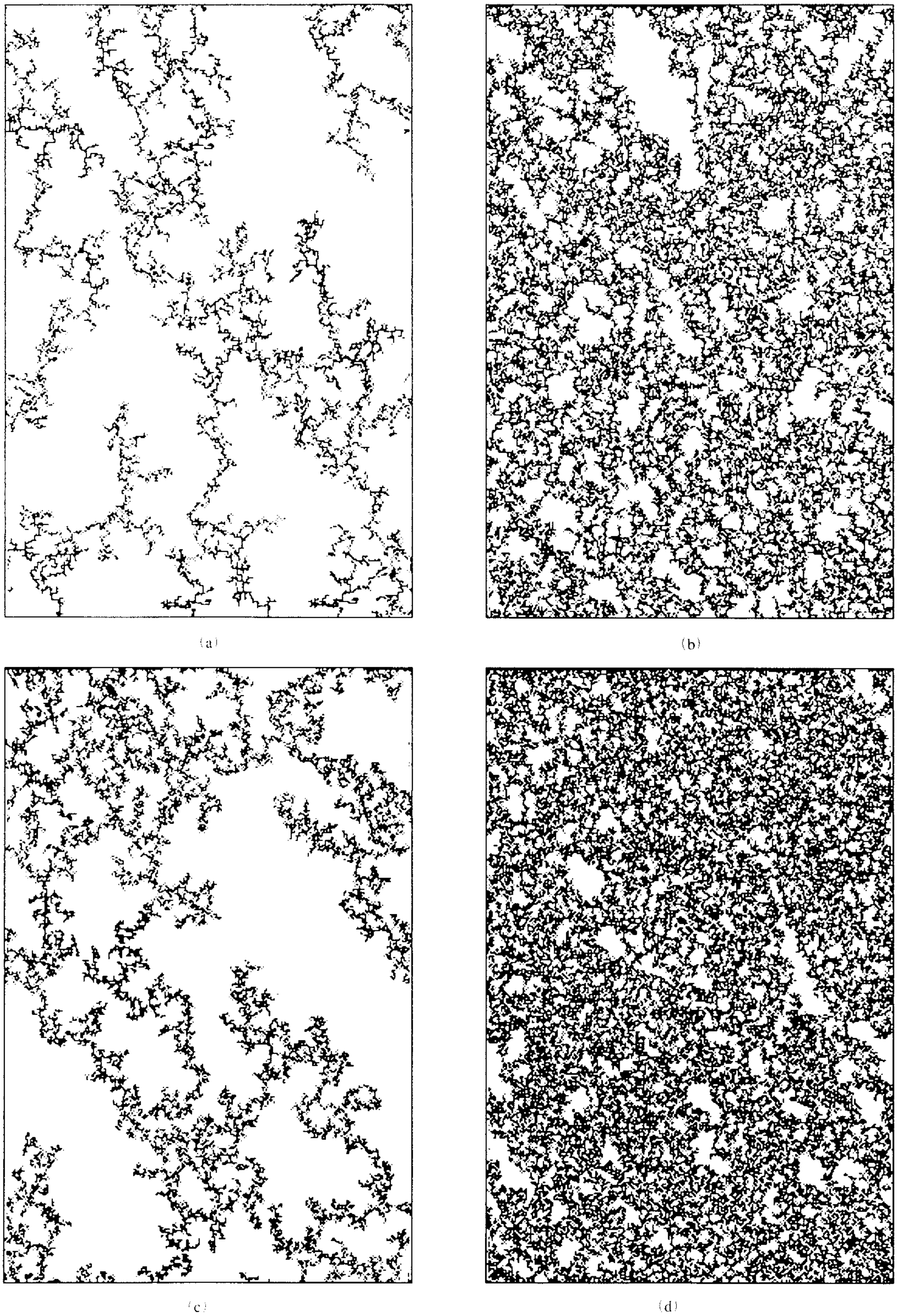

(a) Aggregated condition : $n_0=0.077$, $P_a=1$, $\Delta x/d_p=1000$, $N_c=395$, $m=3.30$, $D=1.47$
Packed result : $\varepsilon=0.941$

(b) Aggregated condition : $n_0=0.077$, $P_a=1$, $\Delta x/d_p=500$, $N_c=15.9$, $m=3.53$, $D=1.47$
Packed result : $\varepsilon=0.688$

(c) Aggregated condition : $n_0=0.077$, $P_a=0.005$, $\Delta x/d_p=5000$, $N_c=386$, $m=1.91$, $D=1.70$
Packed result : $\varepsilon=0.851$

(d) Aggregated condition : $n_0=0.077$, $P_a=0.005$, $\Delta x/d_p=1500$, $N_c=15.0$, $m=2.00$, $D=1.70$
Packed result : $\varepsilon=0.592$

Fig. 9 Structures of packed bed. Adhesion probability (P_c) on packing process is fixed 0.

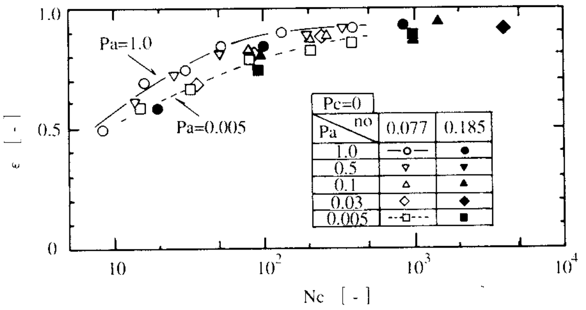

Fig. 10 Relations between porosity of packed bed and scale paramater. Adhesion probalility (P_c) on packing process is fixed 0.

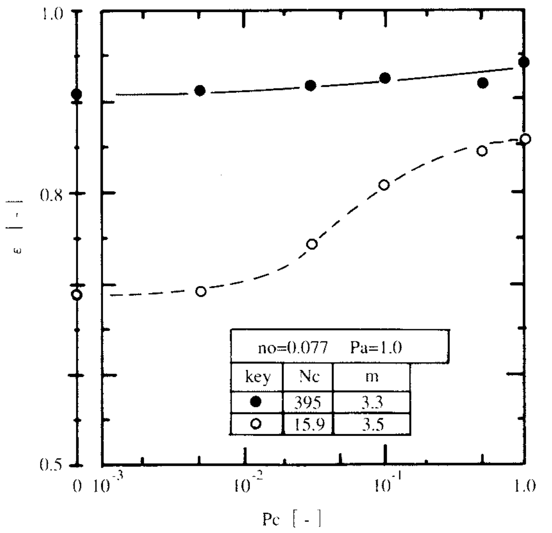

Fig. 11 Effect of adhesion probability at packing simulation on porosity of packed bed

micropore diameter distribution of ultra-fine silica powder packed beds and compacts molded at a pressure of 30 MPa by a uniaxial press using mercury porosimetry. For comparison purposes, results of silicon nitride compacts using 0.18 μm-diameter powders are shown. The micropore diameter (D_s) represented on the abscissa is made dimensionless by dividing it by the primary particle size (d_P) and the cumulative pore volume (V) represented on the ordinate is made dimensionless by dividing by the cumulative pore volume (V_{dp}) at a micropore diameter equal to the primary particle diameter. In the silica particle packed bed of a primary particle size of 20 nm and a porosity of 99%, micropores larger than 1000 times the particle size exist, and even if the bed is formed at 30 MPa to lower the porosity to 76%, micropores larger than 100 times the particle size remain. On the other hand, in the silicon nitride compacts with a primary particle size of 180 nm, only micropores several times the particle size are observed. A comparison of this result with that of the packed bed analysis by simulation shown in **Figure 12 (b)** indicates that the distribution profile of micropore diameters is quite similar to that obtained in the experiment. Consequently, it is confirmed that large pores formed by the bridging structures of aggregates, which have been identified by simulation, exist in actual ultra-fine powder packed beds, leading to packed beds with a porosity as high as 90% or above. However, the simulation space used in this investigation enables only the reproduction of micropores of several hundred times the primary particle diameter. In order to reproduce micropores structures in which the pores are larger than 100 times the particle size

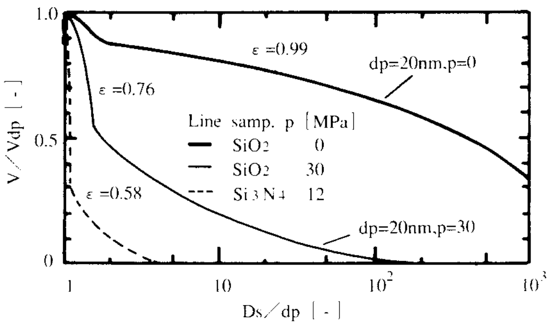

(a) Experimental results by mercury porosimetry

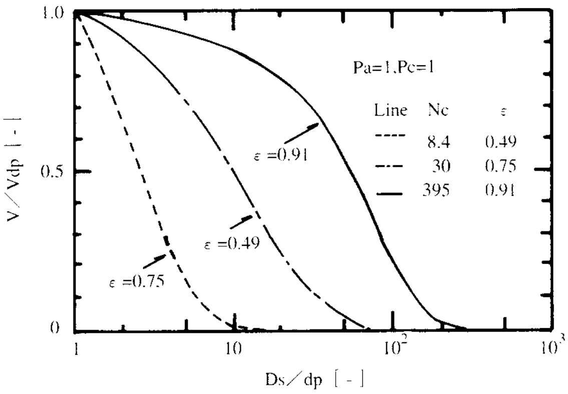

(b) Simulated results

Fig. 12 Cumulative distribution of pore diameter in packed bed obtained with ultra-fine silica powders of primary particle diameters of 20 nm, the simulation space must be expanded and three-dimensional simulation of clusters of a larger number of constituent particles is necessary. On the other hand, when the number of constituent particles is about 10, no micropores of which the diameter exceeds 10 times the particle size have been observed. Such micropores are nearly similar to those in silicon nitride powders. Consequently, even in packed beds and compacts of powders of size of the order of about submicrons, aggregates form small bridging structures, resulting in pores about several times the primary particle size, though such size is smaller than that formed with ultra-fine powders.

In future, in order to determine the mechanism at the preparation stage or pressure-forming and sintering stage of ultra-fine powders, the Brownian dynamics method shall be applied in the study of the behavior of the molecular level, the simulation shall be extended to the forming and sintering processes using the packed bed structure obtained in this report, and the results shall be analyzed and compared with the experimental results.

3. Conclusion

Using the Brownian Dynamics Methods, the aggregation process of ultra-fine powders was simulated by computer, the aggregation process and aggregates' shapes were analyzed, and the following conclusions were reached.

(1) From a quantitative analysis of the aggregates' shapes by Fractal dimension (D), it was discovered that by lowering the adhesive probability (P_a) during aggregation from 1 to 0.005 the Fractal dimension increased from 1.5 to 1.7, resulting in aggregates of dense structure. This increasing method differed depending on the initial concentration of primary particles (n_0).

(2) The aggregation process was analyzed using Eq. (5) based on the Smoluchowski's equation ($dn/dt = -K_{B0}n^2$) with special emphasis on the process of decreasing the initial concentration of primary particles. It was observed that the coefficient $K_{B0}{}^+$, when time (t) was replaced by the non-dimensional time ($\Delta x/d_P$), exhibited a concentration dependency, in particular, when the adhesive probability (P_a) is close to 1.

(3) The distribution of the constituent particles of an aggregate can be expressed by the two-parameter Weibull's distribution. The change due to the aggregation conditions was expressed by the scale parameter (N_c) and shape parameter (m).

Packing simulation was carried out for a cluster which had obtained a distribution of constituent particles and shape, and the results were compared with those of the analysis of ultra-fine powder packed beds using mercury porosimetry, and the following conclusions were reached.

(4) Following the packing of clusters having a scale parameter of 100 or larger, packed bed structures with a porosity exceeding 90%, which may be equated to that of ultra-fine powders of a size smaller than submicrons, could be reproduced. It was determined that this high porosity structure is attributed to the bridging structure formed by aggregates, which leads to the formation of large pores. When clusters of constituent particles numbering about 10 were packed, dispersed micropores of about 10 times the primary particle size, forming an extremely nonhomogeneous structure were observed.

(5) The results of the analysis of the micropore distribution in a packed bed of ultra-fine powder having a mean particle size of 20 nm measured by mercury porosimetry were compared with those of the distribution of micropore diameters of packed beds obtained by simulation and a similar distribution profile was obtained. In packed bed structures having a porosity of 90% of higher, micropores larger than 100 times the primary particle size were observed both in the experiment and through simulation, thus proving the adequacy of the ultra-fine powder packed bed structure obtained by simulation.

[Acknowledgment]

This research work was supported by the "1990 TEPCO Research Foundation" and the "1990 Grant-in-Aid (A) for General Scientific Research Subsidy of the Japanese Ministry of Education."

Nomenclature

A : length of side of square plane used on aggregating simulation [m]

B : width of rectangle plane used on packing simulation [m]

D : Fractal dimension of aggregate [−]

D_s : pore diameter in packed bed [m]

D_B : coefficient of diffusion [−]

d_P : diameter of primary particle [m]

d_{Pag} : representative diameter of cluster and aggregate [m]

H : height of rectangle plane used on packing simulation [m]

i : number of particle in aggregate [−]

K_B : parameter of number of collided times with particles by Brownian motion [−]

K_{B0} : parameter in Smoluchowski's equation [−]

K_{B0}^+ : parameter in Eq. (5) [−]

m : shape parameter in Weibull's distribution function [−]

N : numbers of particle in cluster or aggregate [−]

N_B : numbers of collided times with particles [−]

N_c : scale parameter in Weibull's distribution function [−]

n : concentration of primary particle [−]

n_0 : initial concentration of primary particle [−]

P_a : adhesive probability on aggregating process [−]

P_c : adhesive probability on packing process [−]

p : pressure at uniaxial press test of packed bed [MPa]

Q : cumulative probability of particle number in cluster or aggregate [−]

$R[0, 1]$: pseudo-random number between zero and unity [−]

R_g : mean radius of cluster or agglomerate [m]

r_i : displacement between i-th particle and gravity center of aggregate [m]

r_{max} : maximum radius of aggregate [m]

V : cumulative pore volume [m^3]

V_{dP} : cumulative pore volume at $D_s = d_P$ [m^3]

(x_{ag}, y_{ag}) : center gravity coordinate of aggregate [m]

y_{max} : maximum height of previous packed bed [m]

Δx : moving displacement of primary particle by Brownian motion [m]

ε : porosity ratio of packed bed [−]

Literature cited

1) Doi, M. and D. Chen: *J. Chem. Phys*, **90**, 5271 (1989)

2) Friedlander, S.K.: "Smoke, Dust and Haze", Wiely Interscience (1977)

3) Fuchs, N.A.: "The Mechanizum of Aerosols", Pergamon Press (1964)

4) Julin, R. and P. Meakin: *J. Collid Interface Sci.*, **127**, 265 (1989)

5) Kolb, M., R. Botet and R. Jullien: *Phys. Rev. Lett.*, **51**, 1123 (1983)

6) Lee, K.W.: *J. Colloid Interface Sci.*, **101**, 98 (1984)

7) Meakin, P.: *Phys. Rev. Lett.*, **51**, 1119 (1983)

8) idem: *Phys. Rev., Lett.*, **51**, 3722 (1984)

9) Mountain, R.D., G.W. Mulholland and H. Baum: *J. Colloid Interface Sci.*, **114**, 67 (1986)

10) Okuyama, K., H. Masuda, K. Higashitani, M. Chikazawa and T. Kanazawa: *J. Soc. Powder Tech. Japan*, **22**, 451 (1985)

11) Okuyama, K. and Y. Kousaka: *ibid.*, **23**, 180 (1986)

12) Sunada, H., A. Otsuka, Y. Kasashima and H. Takenaka: *Chem. Pharm. Bull.*, **29**, 273 (1981)

13) Sutherland, D.N.: *J. Colloid Interface Sci.*, **25**, 373 (1967)

14) Suzuki, M. and T. Oshima: *Pow. Tech.*, **36**, 181 (1983)

15) Wanke, S.E. and D.T. Lynch: *Chem. Eng. Technol.*, **12**, 103 (1989)

16) Witten, T.A. Jr. and L.M. Sander: *Phys. Rev. Lett.*, **47**, 1400 (1981)

Free Settling Cylindrical Particles in Stagnant Water †

Fumio Saito
*Institute for Advanced Materials Processing, Tohoku University**
Kazuyoshi Arai and Mitsuo Kamiwano
Department of Materials Science Chemical Engineering,
*Yokohama National University***

Abstract

The free settling behavior of cylindrical particles with densities ranging from 1.18 to 8.03 g/cm^3 *in stagnant water was observed with the aid of cameras and a stroboscope. The particles used ranged from 0.3 to 1.0 cm in diameter, and their size ratios of the diameter to the length were from 1.1 to 9.0. Particles having a size ratio over 1.2 sank with a periodic wobbling motion in the range of 700 to 15000 Reynolds number. This motion was simply expressed by a harmonic equation composed of several parameters. The parameters were expressed as functions of the size ratio, the density ratio between the particle and water and the Reynolds number. In the regular wobbling motion of the particles, the relationship between the drag coefficient and Reynolds number showed a hysteresis loop, of which the ranges of variation depended on the size of the particles, the density ratio and the Reynolds number.*

1. Introduction

Many processes used for the separation of particles of various sizes and shapes depend on the difference in the behavior of the particles when they are subjected to the action of a moving fluid. Further, many of the methods used for the determination of the sizes of particles in the sub-sieve range involve the relative motion between the particles and a fluid. Thus, the motion of particles in a fluid is closely related to the multiphase flow processes involving sedimentation, fluidization and particle size distribution measurement in gravitational and/or centrifugal fields. It is worthwhile to analyze the free settling motion of single particles, especially nonspherical ones, in order to understand the motion of particles and their mechanics in these flow processes. There have been many investigations dealing with this subject[1-6]. The motion of a single nonspherical particle in stagnant liquid has been reported to be dependent on the relative density ratio between the particle and the liquid, and the shape of the particle[7]. Our previous work on cylindrical particles provides some information regarding the free settling motion of particles in stagnant water[8,9]. That is, a cylindrical particle settling in stagnant water goes through a periodic wavering motion. However, the settling and wavering behavior of a nonspherical particle in stagnant liquid still has not been worked out.

The main purpose of this work is to analyze the phenomenon of the free settling and wavering behavior of single cylindrical particles falling freely in stagnant water.

2. Experiment

Bars and pipes made of four different materials, i.e., acrylic resin, bakelite, aluminum and brass were used as primary materials for the preparation of cylindrical specimens. Cylindrical particles were prepared from not only single materials but also from composite materials. Composite materials were made by inserting a

---

* 2-1-1 Katahira, Aoba-ku, Sendai 980 JAPAN
TEL: 022-227-6200

** 156 Tokiwadai, Hodogaya-ku, Yokohama 240 JAPAN
TEL: 045-335-1451

† This report was originally printed in *J. Soc. Powder Technology, Japan*, **27**, 673-679 (1990) in Japanese, before being translated into English with the permission of the editorial committee of the Soc. Powder Technology, Japan.

bar into a pipe, i.e., aluminum bar in a pipe of acrylic resin and brass bar in a pipe of acrylic resin. These single and composite materials were cut into cylindrical pieces having a predetermined length, then the two end-faces of the specimens were polished with emery paper. The density and geometrical size of these specimens are listed in **Table 1.** **Fig. 1** shows the schematic configuration of an experimental apparatus consisting of a settling vessel of rectangular cross section made of transparent acrylic resin, a stroboscope equipped with a counter and two sets of cameras. The settling vessel was filled with tap water (liquid density $\rho_l = 10^3$ kg/m^3, viscosity $\mu = 10^{-3}$ Pa•s, temperature 291K - 293K) and the depth of the water was kept at 1800 mm. The preliminary experiment suggested that the distance from the liquid surface to the observing area scanned by the cameras is maintained at least at 80 cm because the largest particles made of brass representing the highest Reynolds number in steady settling state shows a regular wavering motion below about 80 cm from the liquid surface. Therefore, the observing area was set at 1500 mm from the liquid surface in this experiment. The observation of the settling motion of specimens by cameras was carried out in a dark room with the aid of a stroboscope flashing at a fixed frequency precalibrated by means of the counter. The two cameras were placed at

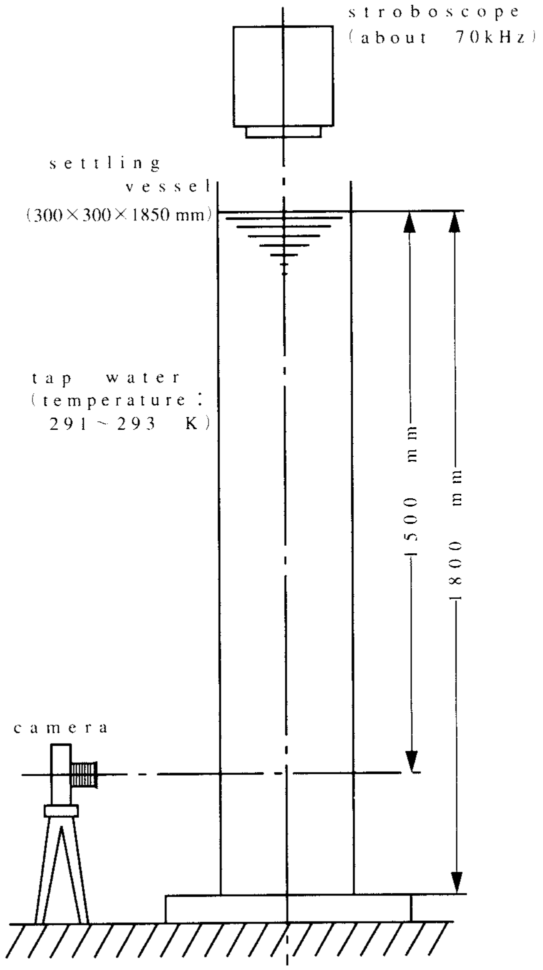

Fig. 1 Schematic configuration of an experimental apparatus.

Table 1 Density and sized of cylindrical particles

Material	ρ_p [g/cm^3]	d [cm]	l [cm]	l/d [-]
Acrylic resin	1.18	0.6~1.0	1.2~2.4	1.8~3.5
Bakelite	1.37	0.3~1.0	0.9~2.4	1.5~6.0
Aluminum-Acrylic resin	2.05	1.0	1.8	1.8
Aluminum	2.72	0.2~0.1	0.9~2.4	1.8~9.0
Brass-Acrylic resin	3.07	0.3	1.1~1.8	3.1~5.3
	3.65	1.0	1.8	1.8
	4.40	0.6	0.9~1.5	1.5~2.5
Acrylic resin-Brass	5.03	1.0	1.8~2.4	1.8~2.4
	5.56	0.5	0.9~1.2	1.8~2.4
Aluminum-Brass	6.11	0.5	0.9~1.2	1.8~2.4
Brass	8.03	0.3~1.0	0.9~2.4	1.8~4.0

different positions at the same height so as to be focused on the same observing area inside the vessel. When a single cylindrical specimen was placed gently on the liquid surface, it fell with its settling velocity increasing gradually inside the water. After few seconds, the particle started to settle with a regular fluttering motion. While the particle continued to settle with a regular fluttering motion and was about to come into the observing space, the shutters of the cameras were simultaneously pressed for one to three seconds to take pictures. The fluttering motion of a cylindrical specimen during settling is called a wavering motion in this paper. The settling locus of the particle on pictures and films was determined using an electric digitater, which enabled us to evaluate the changes in the settling and wavering behavior of the particle such as the angle of inclination and the change in the settling velocity with time.

3. Experimental Results and Discussion

3.1 Wavering motion

Fig. 2 shows the photographs indicating settling the loci of cylindrical particles having different geometrical sizes made of bakelite. The cylindrical particles in the figures were found to sink with a regular wavering motion. Further, it was found that the geometry of the particles affects not only their settling velocity but also the wavering period and the wavering angle. The reason for the occurrence of the regular wavering motion of a cylindrical particle during settling may be due to eddies generated by the separation of the liquid from the surface of the particle. **Fig. 3** shows the photograph indicating the vortices formed behind a cylindrical particle made of bakelite settling in stagnant water visualized by a condensed milk method. The visualization of vortices suggests that the wavering motion of a particle is closely related to the vortices generated alternatively near the two end-faces of the cylindrical particle sinking in water.

Fig. 4 shows the schematic settling locus of a cylindrical particle going through a regular wavering motion. In Fig. 4, θ_r is the wavering angle, V_h the velocity component in the horizontal direction and V_z the velocity component in the vertical direction. As these three values for


(A) (B)

Fig. 2 Settling loci of cylindrical particles with different geometrical sizes made of bakelite.
(A) dxl=0.3cmx0.9cm, $\bar{V}_z$=13.6 cm/s, f=19.9 s^{-1}
(B) dxl=0.5cmx1.8cm, $\bar{V}_z$=18.9 cm/s, f=19.9 s^{-1}

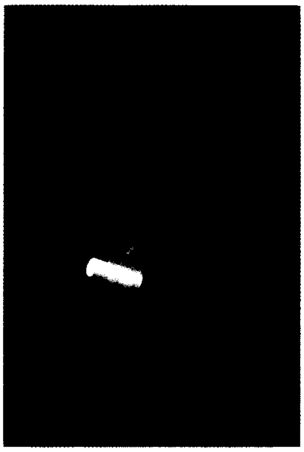

Fig. 3 Vortices formed behind a bakelite particle settling in stagnant water.

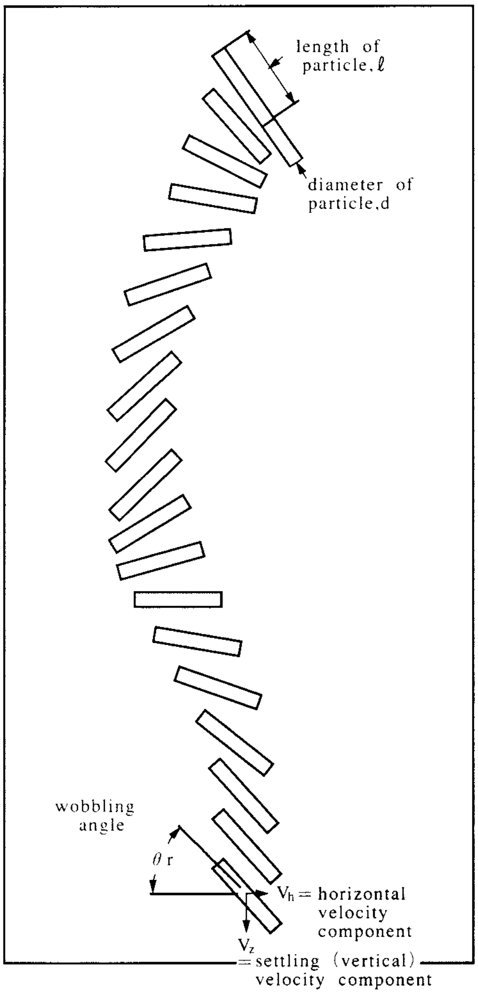

Fig. 4 Schematic setting locus of a cylindrical particle with regular wavering motion.

a settling particle vary cyclically with time, t, it can readily deduced that each of them may be expressed by a harmonic model equation, as follows;

$$\theta=\left(\frac{\theta_r}{(2\pi)}\right)=A_\theta \sin(\omega_{r1}t) \qquad (1)$$

$$V_z=A_{vz}\sin(\omega_{r2}t+\phi_1)+\overline{V_z} \qquad (2)$$

$$V_h=A_{vh}\sin(\omega_{r3}t+\phi_2) \qquad (3)$$

where, A is the amplitude, ω_{r1}, ω_{r2} and ω_{r3} are the angular frequencies for θ, V_z and V_h, ϕ_1 and ϕ_2 are the phase shifts of the settling velocity components based on the period of the sinusoidal equation for the wavering angle, θ, and subscripts z and h are the vertical and horizontal axes, respectively. **Fig. 5** shows θ_r, V_z and V_h as a function of time for a cylindrical particle (d×l =0.3cm×0.9cm) made of brass. The circles in the figures denote the observed values and the solid lines represent the values calculated using the equations (1) to (3) with the corresponding parameters, which were deter-

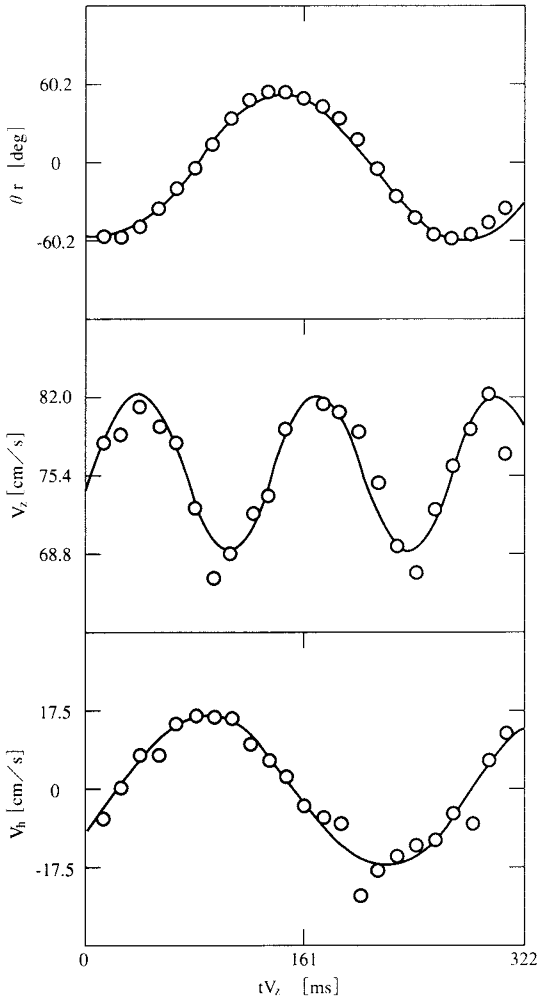

Fig. 5 Variation of θ_r, V_z and V_h with time for a cylindrical particle made of brass (dxl=0.3cmx0.9cm).

mined by matching the equations with experimental measurements. Thus it is found that θ_r, V_z and V_h can be approximately expressed by harmonic model equations.

In order to elucidate the variation of the period and angular frequency in the regular wavering motion of a cylindrical particle, the dimensional analysis is evaluated one step further as indicated below. Since the foregoing six factors, i.e., the diameter d, the length l, the density of the particle ρ_p, the liquid density ρ_l, the liquid viscosity μ and the mean settling velocity V_z are related to the angular frequency $\omega_1(=\frac{\omega_{r1}}{(2\pi)})$, the angular frequency is given by the following equation.

$$\omega_1 = F(d, l, \rho_p, \rho_l, \mu, \overline{V}_z) \qquad (4)$$

As d, μ and V_z are the fundamental physical terms, each term in Eq. (4) can be expressed in the independent non-dimensional form as follows.

$$\Pi_1 = \frac{\omega_1 l}{\overline{V}_z} \qquad (5)$$

$$\Pi_2 = \frac{l}{d} \qquad (6)$$

$$\Pi_3 = \frac{\rho_p}{\rho_l} \qquad (7)$$

$$\Pi_4 = \frac{\mu}{(d\rho_l \overline{V}_z)} \qquad (8)$$

Eq. (8) can be transformed when using the sphere equivalent diameter, as follows,

$$\Pi_4' = \left(\frac{\mu}{(d_s\rho_l \overline{V}_z)}\right)\left(\frac{l}{d}\right)^{\frac{1}{3}} = Re^{-1}\left(\frac{l}{d}\right)^{\frac{1}{3}} \qquad (9)$$

where, Re is the Reynolds number. Consequently, Eq. (4) can be rewritten as Eq. (10). Therefore, the dimensional analysis is performed by introducing the nondimensional constant K based on the definition of the following equation:

$$\frac{\omega_1 l}{\overline{V}_z} = K\left(\frac{l}{d}\right)^a\left(\frac{\rho_p}{\rho_l}\right)^b\left(\frac{\mu}{(d_s\rho_l \overline{V}_z)}\right)^c \qquad (10)$$

By substituting the various quantities into Eq. (10) and using arbitrary values for the three indices, the constant K can be calculated. In this calculation process, so as to keep the value of the constant K to a minimum the three indices a, b and c are determined by a trial-and-error method. Hence, the final equation of the dimensional analysis for ω_1 can be given by Eq. (11).

$$\frac{\omega_1 l}{\overline{V}_z} = 7.99\times10^{-2}\left(\frac{l}{d}\right)^{0.6}\left(\frac{\rho_p}{\rho_l}\right)^{-0.37}\left(\frac{d_s\rho_l\overline{V}_z}{\mu}\right)^{-0.02} \pm 0.080 \qquad (11)$$

The value of 0.080 with a symbol ± is a standard deviation (described in the following equations in the same manner). Similarly, the dimensional analysis for the mean settling velocity $\overline{V}z$ provides the following final equation:

$$\frac{d_s\rho_l\overline{V}_z}{\mu} = 6.02\times10^{-1}\left(\frac{l}{d}\right)^{-0.10}\left(\frac{\rho_p}{\rho_l}\right)^{0.98}\left(\frac{d_s^3\rho_l^2 g}{\mu^2}\right)^{0.49} \pm 0.214 \qquad (12)$$

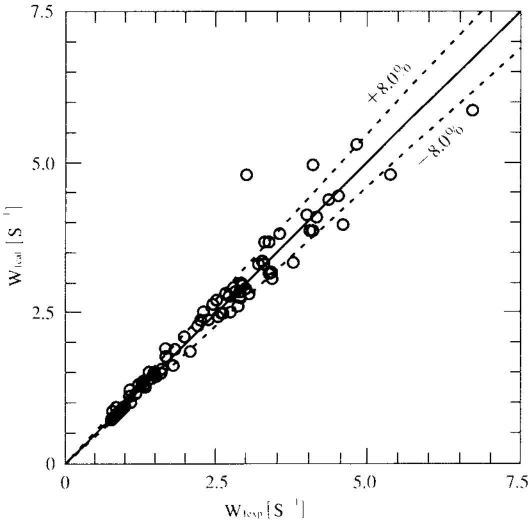

Fig. 6 Comparison of values of ω_1 calculated with those determined experimentally.

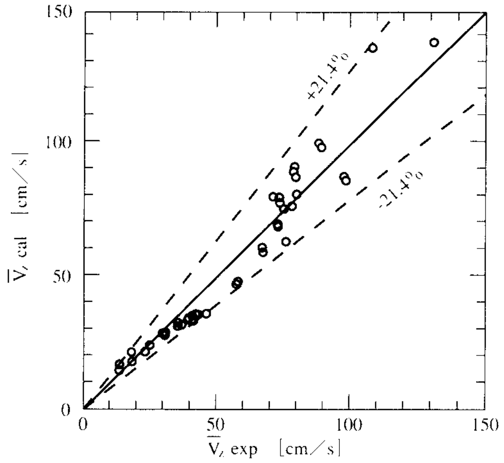

Fig. 7 Comparison of values of $\overline{V}_z$ calculated with those determined experimentally.

Figs. 6 and 7 show a comparison between the values of ω_1 and V_z calculated using Eqs. (11) and (12) and those determined experimentally. It is found from the figures that the calculated values are in fairly good agreement with those determined experimentally. The dimensional analysis for the amplitudes A_θ, A_{Vz}, A_{Vh} using the model equations provide the following final equations.

$$A_\theta=1.13\times10^{-1}\left(\frac{l}{d}\right)^{-0.18}\left(\frac{\rho_p}{\rho_l}\right)^{0.07}\left(\frac{d_s\rho_l\overline{V_z}}{\mu}\right)^{0.01}\pm0.177 \quad (13)$$

$$\frac{A_{Vz}}{\overline{V_z}}=2.01\times10^{-2}\left(\frac{l}{d}\right)^{1.12}\left(\frac{\rho_p}{\rho_l}\right)^{-0.11}\left(\frac{d_s\rho_l\overline{V_z}}{\mu}\right)^{0.02}\pm0.374 \quad (14)$$

$$\frac{A_{Vh}}{\overline{V_z}}=1.32\times10^{-1}\left(\frac{l}{d}\right)^{0.60}\left(\frac{\rho_p}{\rho_l}\right)^{-0.20}\left(\frac{d_s\rho_l\overline{V_z}}{\mu}\right)^{0.02}\pm0.229 \quad (15)$$

Figs. 8, 9 and 10 show a comparison between the calculated and the experimental values for this amplitude. The value of A_θ seems to be almost independent from the geometry of a particle and from the physical properties of a particle and a liquid. On the other hand, the values of A_{Vz} and A_{Vh} are found to be much influenced by $(\frac{l}{d})$ and $(\frac{\rho_p}{\rho_l})$ rather than by Re. All the same, it is found that these amplitudes can be expressed by the empirical equations (13) to (15). The interrelation between ω_1, ω_2 and ω_3 in Eqs. (1) to (3) is represented by Eq. (16) which is independent from the geometry of particles, as shown in **Fig. 11**.

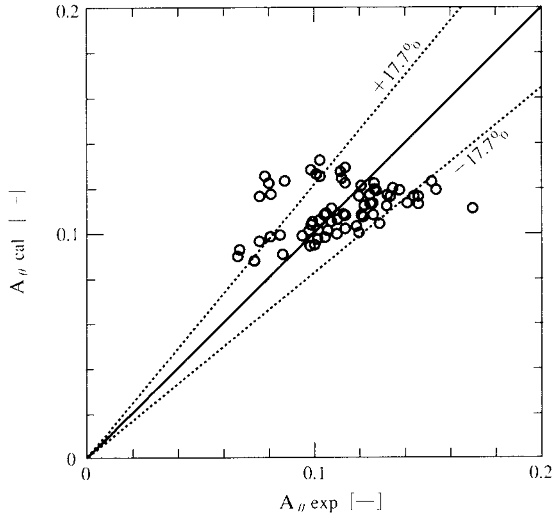

Fig. 8 Comparison of values of A_θ calculated with those determind experimentally.

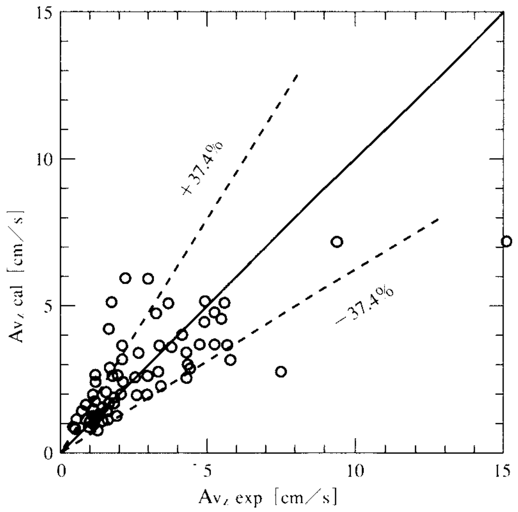

Fig. 9 Comparison of values of A_{Vz} calculated with those determined experimentally.

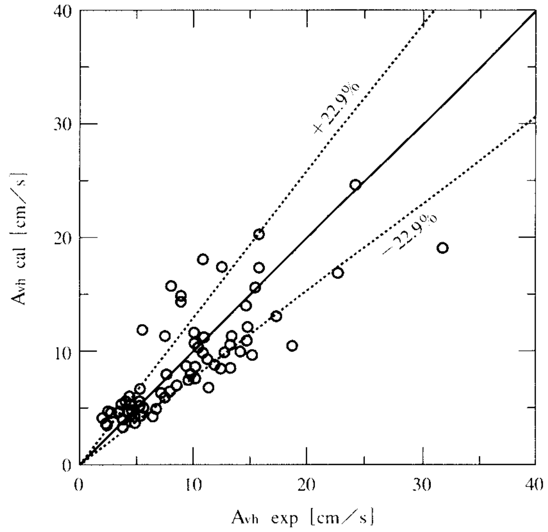

Fig. 10 Comparison of valuei of A_{Vh} calculated with those determined experimentally.

$$\omega_1=\frac{\omega_2}{2}=\omega_3 \quad (16)$$

It can be concluded that the settling and wavering behavior besides ϕ_1, ϕ_2 of a cylindrical particle in stagnant water can be estimated from its geometry, relative density and Reynolds number using the foregoing empirical equations. It should be noted that the regular wavering motion of a cylindrical particle occurs in the following ranges:

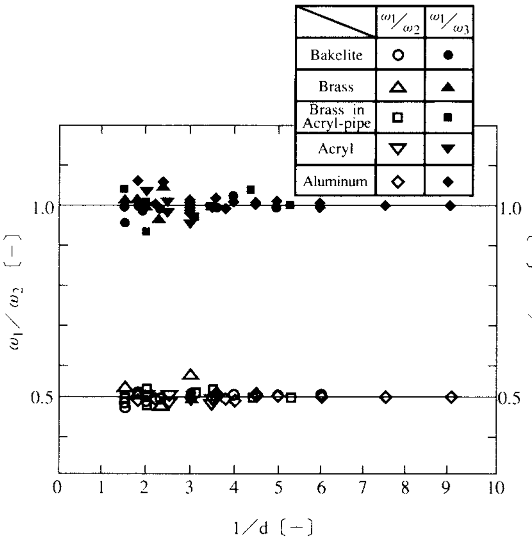

Fig. 11 Ratios of (ω_1/ω_2), (ω_1/ω_3) as a function of (l/d) for different materials.

$(\frac{l}{d})$: above 1.2

Re : about 700 − 15000

It was observed that a cylindrical particle in stagnant water settles with no wavering motion below about 700 for Re and with an irregular wavering motion above about 15000 for Re.

3. 2 Relation between drag coefficient and Reynolds number

The equation of motion for the settling of a cylindrical particle in stagnant water is given by substituting Eq. (2) as follows:

$$\frac{dV_z}{dt}=\frac{(\rho_p-\rho_l)g}{\rho_p}-\frac{C_D S V_z^2 \rho_l}{(2m)}$$

$$=A_{Vz}\omega_2\cos(\omega_{r2}t+\phi_1) \qquad (17)$$

Where, C_D is the drag coefficient, g the gravitational acceleration, m the mass of a particle and S the projection area of that particle. The value of S changes with the wavering angle, as given by Eq. (18).

$$S=dl\cos\theta+(\frac{\pi}{4})d^2\sin|\theta|$$

$$=dl\cos[A_\theta\sin(\omega_{r1}t)]+(\frac{\pi}{4})d^2\sin|A_\theta\sin(\omega_{r1}t)| \qquad (18)$$

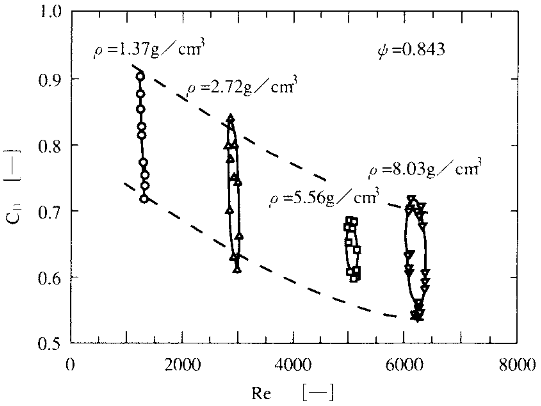

Fig. 12 Drag coefficient as a function of Reynolds number in one cycles of the regular wavering motion of cylindrical specimens made of different materials (dxl = 0.5cmx0.9cm).

Fig. 12 shows the drag coefficient as a function of Re for one cycle of the regular wavering motion of single cylindrical particles having the same geometry (d×l = 0.5cm×0.9cm, shape factor; ψ = 0.843) with different values for the density. It is found that the relation between C_D and Re in one cycle of the regular wavering motion of a settling particle represents a hysteresis loop, and the variation of C_D, with the highest value being about 20%, decreases gradually with the increase in the density of a particle (or Re). **Fig. 13** shows C_D as a function of Re in one cycle of the regular wavering motion of single particles made of bakelite having different lengths but the same diameter of 0.3 cm. C_D seems to increase with the increase in the length of cylindrical particles (ψ=0.666-0.779) without any remarkable change in the mean values of C_D. Moreover, the relation between C_D and Re with the values for the particle density (ρ_p = 2.72 g/cm^3) and its length (l = 1.2cm) kept constant and with the values for the particle's diameter varied (d = 0.2cm-0.5cm) is shown in **Fig. 14.** The drag coefficient seems to decrease

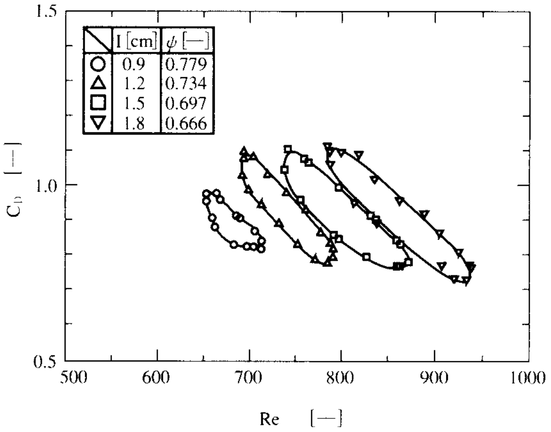

Fig. 13 Drag coefficient as a function of Reynolds number in one cycles of the regular wavering motion of brass specimens with d = 0.3cm.

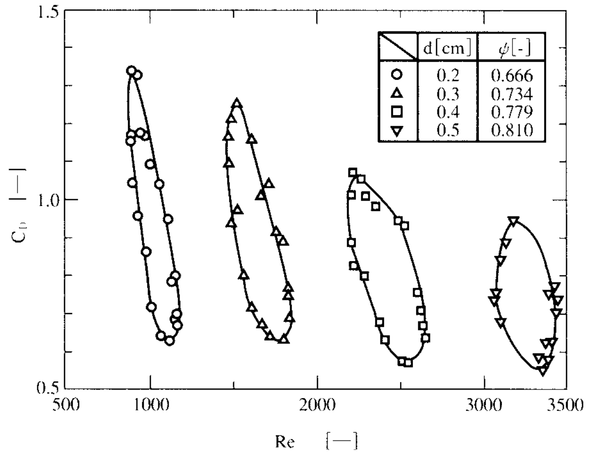

Fig. 14 Drag coefficient as a function of Reynolds number in one cycles of the regular wavering motion of aluminum specimens with $l = 1.2$cm.

gradually with the increase in Re, thus reducing their variation.

4. Concluding Remarks

Free settling experiment in stagnant water was carried out using single cylindrical particles having a diameter d = 0.3 - 1.0 cm and a size ratio $(\frac{l}{d}) = 1.5$-9.0 with a density difference between the particles and water $\Delta\rho = 0.18 - 7.03$ g/cm^3. The following concluding remarks were arrived at:

(1) The regular wavering motion during settling of a particle occurs at a size ratio $(\frac{l}{d})$ above 1.2 and at a range of the Reynolds number of about 700 to 15000.

(2) The regular wavering motion can be expressed by harmonic model equations, and the parameters with the exception of the phase shifts in the model equations can be represented as functions of the geometry of the particles, relative density and Reynolds number, as given by Eqs. (11) to (16). The ranges of parameters measured experimentally were as follows: 0.065 - 0.175 for A_θ, 0.05 - 0.10 for $(\frac{A_{Vz}}{V_z})$ and 0.3 - 0.4 for $(\frac{A_{Vh}}{V_z})$.

(3) The relation between the drag coefficient and the Reynolds number in one cycle of the regular wavering motion of a settling particle represents a hysteresis loop. The variation of the drag coefficient, which assumes the largest value of about 20%, depends on the Reynolds number.

Acknowledgements

The authors wish to express their appreciation to Miss. S. Oki, Mr. T. Kashiwagi and Mr. T. Ogawa for their invaluable contribution to the experiment.

Nomenclature

A_{Vh}	: amplitude in Eq. (3)	[cm/s]
A_{Vz}	: amplitude in Eq. (2)	[cm/s]
A_θ	: amplitude in Eq. (1)	[—]
a, b, c	: indices in Eq. (10)	[—]
C_D	: drag coefficient	[—]
d	: diameter of a cylindrical specimen	[cm]
d_s	: sphere equivalent diameter	[cm]
f	: frequency of flashing lamp of stroboscope	[s^{-1}]
g	: gravitational acceleration	[cm/s^2]
K	: nondimensional constant	[—]
l	: length of a cylindrical specimen	[cm]
m	: mass of a cylindrical specimen	[g]
Re	: Reynolds number	[—]
S	: projected area of a cylindrical specimen	[cm^2]
t	: time	[s]
V_z	: velocity component in vertical direction	[cm/s]
V_h	: velocity component in horizontal direction	[cm/s]
$\Delta\rho_0$	: relative density between particle and water	[g/cm^3]
θ	: non—dimensional wavering angle	[—]
θ_r	: wavering angle	[rad]
μ	: viscosity of liquid	[Pa s]
ρ_l	: liquid density	[g/cm^3]
ρ_p	: density of particle	[g/cm^3]
ϕ	: phase shift	[rad]
ψ	: shape factor	[—]
ω_1	: frequency defined by $\omega_{r1}/(2\pi)$	[1/s]
ω_2	: frequency defined by $\omega_{r2}/(2\pi)$	[1/s]
ω_3	: frequency defined by $\omega_{r3}/(2\pi)$	[1/s]
ω_{r1}	: angular frequency in Eq. (1)	[rad/s]
ω_{r2}	: angular frequency in Eq. (2)	[rad/s]

ω_{r3} : angular frequency in Eq. (3) [rad/s]

⟨Subscript⟩

— : average

References

1) Wadell, H.: J. Fran. Ins., **217** (1934), 415.

2) Lapple, C.E. and C.B. Shepherd: Ind. Eng. Chem., **32** (1940), 605.

3) Pettyjohn, E.S. and E.B. Christiansen: Chem. Eng. Prog., **44** (1948), 157.

4) Badger, W.L. and J.T. Banchero: "Intro. Chem. Eng.", Chap. 14, p. 618, Kogakusha Co. Ltd. (1955).

5) Metzmager, A., A. Saden and M. Shelef: Brit. Chem. Eng., **9** (1964), 314.

6) Brown, G. G., D. Katz, A. S. Foust and R. Schneidewind: "Unit Operation", Chap. 7, p. 72, John Wiley & Sons Inc. (1950)

7) Tanaka, Z. and K. Iinoya; J. Chem. Eng. Japan, **3** (1970), 261.

8) Kamiwano, M., T. Hikosaka, T. Saito and R. Aoki: Proc. Int. Symp. Pow. Tech., '**81**, (1981), 81.

9) Saito, F., M. Kamiwano and R. Aoki: Part. Sci. Tech., **2** (1984), 247.

Explanation of the Cover Photograph

—Nanodispersoid and Interface in Sintered Si_3N_4-SiC Nanocomposites—

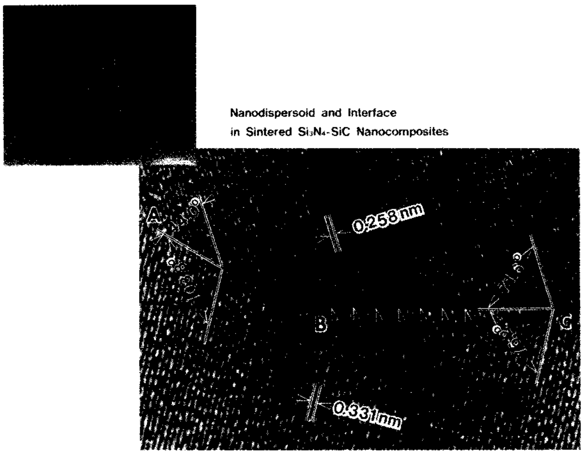

Recently, Si_3N_4-Sic nanocomposites, in which the nano-sized SiC particles were dispersed within Si_3N_4 matrix grains and/or at Si_3N_4 grain boundaries, were successfully prepared by sintering the mixtures of amorphous, fine Si-C-N powder precursors with various C/N ratio and sintering aids (2wt% Al_2O_3 and 6wt% Y_2O_3). This newly developed nanocomposites were found to exhibit the excellent mechanical properties. For instance, the fracture strength at room temperature and 1400°C were above 1500 and 1100MPa, respectively. Photo A shows an example of high resolution transmission electron micrograph of the facet-like structured SiC particle within the Si_3N_4 matrix grain.

Photo B indicates the lattice image of interface between the intragranular SiC particle and Si_3N_4 matrix. The Si_3N_4 and SiC are (101) and (200) planes, respectively. No interface layer is observed and both lattices are connected directly.

The lattice misfits at the interfaces between the point A and B (8%) and between the point B and C (20%) are accommodated by the way that every 5th and 12th lattice planes of SiC are extra planes, respectively. Although the 8wt% sintering aid was used, the similar observation was also obtained at the interface between the intergranular SiC and matrix Si_3N_4 grains. The above-mentioned tremendous improvement of mechanical properties was strongly related to these strong bonding at the interface between the intra/intergranular nano-sized SiC dispersions and matrix Si_3N_4 grains.

By courtesy of Professor Koichi Niihara, the Research Institute of Scientific and Industrial Research, Osaka University.

Measurement of the Contact Potential Difference between a Powder Bed and a Metal†

Hideto Yoshida and Toshihiko Fukuzono
*Dept. of Chem. Eng., Hiroshima Univ.,**
Hiroaki Masuda
*Dept. of Chem. Eng., Kyoto Univ.,***

Abstract

Experimental and theoretical studies have been conducted on the measurement of the contact potential difference between a powder bed and a metal. A new model was proposed for the analysis of the experimental data. The model analysis indicated that accurate contact potential differences are obtained only when the electric charge of the powder bed is assumed to be zero. It was found that the absolute value of the contact potential difference decreased with an increase in relative humidity. The contact potential changed with the particle surface-modification by methanol vapor. However the original contact potential difference was obtained again when the methanol evaporated completely from the particle surface.

1. Introduction

In the powder and granular material processing, inconveniences such as dust adhesion and production interference frequently occur due to the electrically-charged powder resulting from contact between particles and equipment wall surface during mixing, pulverizing, classification, and other dry powder handlings. However, detailed investigation has not been reported regarding accurate measuring methods and measured values of the contact potential difference between particles and a metal, which constitutes the basis of the charging mechanism. In the process of surface modification of powders, which has recently been attracting the attention of engineers and the industry, reliable values of contact potential difference[4)] between a powder and a metal become essential for the estimation of the charge signs and the amount of the charge of the particles.

Penny et al.[3)] measured the contact potential difference between a powder bed and a metal, but their experimental values contain problems since the time dependence of the measured values was not taken into account and no temperature and humidity control were carried out for the powder bed.

In this paper, an experimental apparatus measuring contact potential differences between powders and a metal was built as a device which provides reliable measured values. A new model was proposed to interpret the measurement results, and interesting findings have been obtained.

2. Experimental Apparatus

Figure 1 shows the experimental apparatus used for this investigation. The measuring apparatus is based on the Kelvin method.[1)]

The measuring apparatus consists of an upper vibrating electrode ③, a 3-mm-depth powder bed ⑤, a lower electrode ④, an external variable d.c. power supply ⑥, and an electrometer for electric current measurement (Advantest, TR8652) ①. The upper and lower electrode surfaces are gold-plated to eliminate the effects of the adhering impurities on the measurement errors.

The upper electrode has a diameter of 20 mm and the lower electrode a diameter of 30 mm, while the vibration frequency and amplitude of

---

* Higashi-Hiroshima, Kagamiyama, 724 JAPAN
TEL. 0824-22-7111

** Yoshida-Honmachi, Sakyoku, 606 JAPAN
TEL. 075-753-5565

† This report was originally printed in *J. Soc. Powder Technology, Japan*, **28**, 226-231 (1991) in Japanese, before being translated into English with the permission of the editorial committee of the Soc. Powder Technology, Japan.

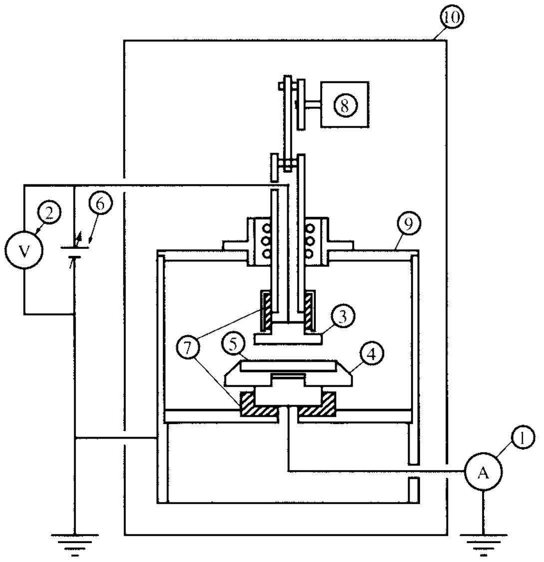

① Electrometer
② Voltmeter
③ Upper electrode
④ Lower electrode
⑤ Powder layer
⑥ Variable d.c. power supply
⑦ Insulator
⑧ Moter
⑨ Shield booth
⑩ Humidity and Temperature controlled room

Fig. 1 Experimental apparatus

the upper electrode are 120 rpm and 5 mm, respectively. An SiC powder (mass median diameter, 0.62 μm) is selected, compression-formed to a specified packing ratio, and subjected to the experiment.

Figure 2 shows the electric circuit of the measuring apparatus. The contact potential difference between the metal and the powder generates electric charges in the lower portion of the powder bed and at the lower electrode surface which induce charges at the upper electrode surface due to the influence of the lines of electric force from this charge. Varying the upper electrode periodically varies the charges on the upper electrode surface with time and allows the flow of current through the circuit.

Applying a voltage to the upper electrode, which does not generate current in the circuit even if the electrode is vibrated, equalizes the potential with that caused by the contact potential difference. Therefore, the magnitude of the current variation dèpends on the intensity of the d.c. current applied to the upper electrode, and the applied voltage at which the magnitude of the current becomes zero corresponds to the contact potential difference.

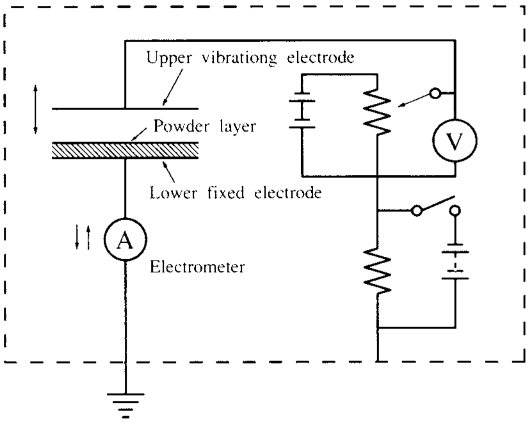

Fig. 2 Electric circuit of measuring system

3. Measuring Model

An investigation has been carried out to some extent on the surface potential using the Kelvin method, but the physical meaning of the measured values has not been interpreted accurately. In this paper, a new model shown below is used in a mathematical investigation.

Figure 3 shows a measuring system consisting of an upper electrode, a powder bed, and a lower electrode. Between the powder bed and the lower electrode, positive and negative charges are induced by the contact potential difference. Between the bottom of powder bed and the lower electrode, an extremely small clearance (about 4 Å[2)]) is assumed. Then, letting the surface charge density of the powder bed bottom and upper electrode be ρ_s and ρ_{se}, respectively, the upper electrode moves in accordance with the following equation.

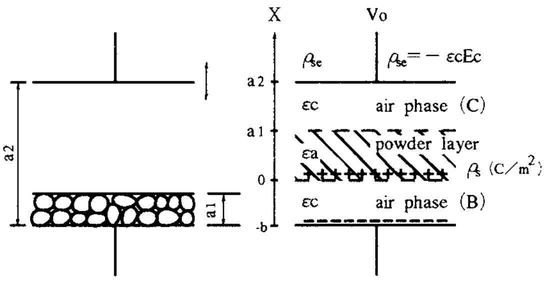

Fig. 3 Model of measuring system

$$a_2(t)=\alpha_1+\alpha_2\cos(\omega t) \qquad (1)$$

where, α_1 is a mean electrode spacing and α_2 the amplitude. Since there is no space charge in the air phase (C), (B), the potential is given by the following equations.

$$V_c=K_{c1}x+K_{c2} \qquad (2)$$

$$V_b=K_{b1}x+K_{b2} \qquad (3)$$

The constants K_{c1}, K_{c2}, K_{b1}, K_{b2} are determined by the potential boundary conditions.

The potential in the powder bed is given by the following equation.

$$V_a=-\frac{\rho_B x^2}{2\varepsilon_a}+K_{a1}x+K_{a2} \qquad (4)$$

where, ρ_B and ε_a are the volume charge density and the permittivity, respectively. Now, applying the Gaussian divergence theorem to the powder bed and powder bed bottom, we get

$$\left.\begin{array}{l} \varepsilon_c E_c S-\varepsilon_a E_a|_{x=0}S \quad =\rho_B a_1 S \\ \varepsilon_c(-K_{c1})-\varepsilon_a(-K_{a1})=\rho_B a_1 S \end{array}\right\} \qquad (5)$$

$$\left.\begin{array}{l} \varepsilon_a E_a|_{x=0}S-\varepsilon_c E_b|_{x=0}S=\rho_s S \\ \varepsilon_a(-K_{a1})-\varepsilon_c(-K_{b1})\ =\rho_s \end{array}\right\} \qquad (6)$$

where, S is the surface area of the electrode, ρ_s the surface charge density of the powder bed, and E the intensity of the electric field.

Since the potential is equal at the interface of each region, we get the boundary conditions for the following potentials.

$$V_c|_{x=a2}=V_0 \qquad (7\text{-}1)$$
$$V_a|_{x=0}\ =V_b|_{x=0} \qquad (7\text{-}2)$$
$$V_c|_{x=a1}=V_a|_{x=a1} \qquad (7\text{-}3)$$
$$V_b|_{x=b}\ =0 \qquad (7\text{-}4)$$

Because we have six equations (5), (6), (7-1)-(7-4) and six unknown variables K_{a1}, K_{a2}, K_{b1}, K_{b2}, K_{c1}, K_{c2}, we can determine the constants analytically as follows:

$$K_{a1}=\frac{\left[-\frac{\rho_B a_1{}^2}{2\varepsilon_c}+\frac{\rho_a b}{\varepsilon_c}+\frac{\rho_B a_1{}^2}{\varepsilon_c}-V_0-\frac{\rho_B a_1 a_2}{\varepsilon_c}\right]}{\left[\frac{\varepsilon_a a_1}{\varepsilon_c}-\frac{\varepsilon_a a_2}{\varepsilon_c}-a_1-\frac{\varepsilon_a b}{\varepsilon_c}\right]} \qquad (8)$$

$$K_{b1}=\frac{\varepsilon_a\left[-\frac{\rho_B a_1{}^2}{2\varepsilon_a}+\frac{\rho_s b}{\varepsilon_c}+\frac{\rho_B a_1{}^2}{\varepsilon_c}-V_0-\frac{\rho_B a_1 a_2}{\varepsilon_c}\right]}{\varepsilon_c\left[\frac{\varepsilon_a a_1}{\varepsilon_c}-\frac{\varepsilon_a a_2}{\varepsilon_c}-a_1-\frac{\varepsilon_a b}{\varepsilon_c}\right]}+\frac{\rho_B}{\varepsilon_c} \qquad (9)$$

$$K_{c1}=\frac{\varepsilon_a\left[-\frac{\rho_B a_1{}^2}{2\varepsilon_a}+\frac{\rho_s b}{\varepsilon_c}+\frac{\rho_B a_1{}^2}{\varepsilon_c}-V_0-\frac{\rho_B a_1 a_2}{\varepsilon_c}\right]}{\varepsilon_c\left[\frac{\varepsilon_a a_1}{\varepsilon_c}-\frac{\varepsilon_a a_2}{\varepsilon_c}-a_1-\frac{\varepsilon_a b}{\varepsilon_c}\right]} \qquad (10)$$
$$-\frac{\rho_B a_1}{\varepsilon_c}$$

Then, the charges induced in the upper vibrating electrode can be calculated using the following equation:

$$\rho_{se}=-\varepsilon_c E_c, \rho_{se}=\varepsilon_c K_{c1} \qquad (11)$$

In the above equation, ρ_{se} is the surface charge density on the upper electrode. From Eqs. (10), (11), the electric current can be calculated by Eq. (12).

$$i=S\left[\frac{d\rho_{se}}{dt}\right]=\frac{S\varepsilon_a{}^2\alpha_2\omega\sin(\omega t)\left[V_0-\frac{\rho_B a_1{}^2}{2\varepsilon_a}-\frac{\rho_B b a_1}{\varepsilon_c}-\frac{\rho_s b}{\varepsilon_c}\right]}{\left[\frac{\varepsilon_a a_1}{\varepsilon_c}-\frac{\varepsilon_a a_2}{\varepsilon_c}-a_1-\frac{\varepsilon_a b}{\varepsilon_c}\right]^2} \qquad (12)$$

From Eq. (12), the current fluctuates periodically and adjusting the applied voltage to satisfy the following equation at all times brings down the current value to zero.

$$V_0=\frac{\rho_B a_1{}^2}{2\varepsilon_a}+\frac{\rho_B a_1 b}{\varepsilon_c}+\frac{\rho_s b}{\varepsilon_c} \qquad (13)$$

Next, the contact potential difference $\Delta\tilde{V}$ corresponds to the potential difference between the lower electrode and the bottom of the powder bed can be calculated using the following equation together with Eq. (9).

$$\Delta\tilde{V}=\int_{-b}^{0}K_{b1}dx=\frac{\rho_s b}{\varepsilon_c}+\frac{b\rho_B a_1}{\varepsilon_c} \qquad (14)$$

A comparison between Eq. (13) and Eq. (14) leads to the relationship between the externally applied voltage V_0 and the contact potential difference $\Delta\tilde{V}$, which is given by the following equation.

$$V_0=\Delta\tilde{V}+\frac{\rho_B a_1{}^2}{2\varepsilon_a} \qquad (15)$$

From the above equation, the externally applied voltage V_0 becomes equal to the contact potential difference$\Delta\tilde{V}$ when there is no charge in the powder bed (that is $\rho_B \rightarrow 0$). Now applying the generally employed condenser model to the air phase (B) of **Figure 3**, we have

$$C=\varepsilon_c\frac{S}{b},\quad q=C\cdot\Delta V=\varepsilon_c\Delta V\frac{S}{b} \tag{16}$$

Hence, the potential difference ΔV is given by

$$\Delta V=\frac{qb}{\varepsilon_c S}=\frac{b\rho_s}{\varepsilon_c} \tag{17}$$

If there is no charge in the powder bed ($\rho_B=0$), the potential difference $\Delta\tilde{V}$ obtained by Eq. (14) would be equal to the potential difference ΔV of Eq. (17).

Next, an investigation of the potential of the powder bed top portion is carried out. Substituting Eq. (13) into Eqs. (8) and (9) gives the constants K_{a1} and K_{b1} as follows:

$$K_{a1}=\frac{\rho_B a_1}{\varepsilon_a},\quad K_{b1}=\frac{\rho_s}{\varepsilon_c}+\frac{\rho_B a_1}{\varepsilon_c} \tag{18}$$

The potential of the powder bed top portion is given as follows:

$$V|_{x=a1}=\int_{V(-b)}^{V(a1)}dV=\int_{-b}^{a1}(-E)dx=\int_{-b}^{0}(-E_b)dx+\int_{0}^{a1}(-E_a)dx \tag{19}$$

Now, using Eqs. (2), (3), (15), and (18), the potential of the powder bed top portion can be found from

$$V|_{x=a1}=\Delta\tilde{V}+\frac{\rho_B a_1^2}{2\varepsilon_a}=V_0 \tag{20}$$

Since the upper vibrating electrode is subjected to the externally applied voltage V_0, we have

$$V|_{x=a1}=V|_{x=a2}=V_0 \tag{21}$$

Though the surface area of the electrode between the bottom of powder bed and the lower electrode is S, it is assumed that the charged portion is concentrated primarily at the protruding area of the particles' surface. Therefore, let the area effectively taking part in the charging process be S'. Then, the surface charge density ρ_s is given by

$$\rho_s=\frac{q_s}{S}=\varepsilon_c\frac{\Delta VS'}{bS} \tag{22}$$

If the charge of the particle is zero, from Eqs. (13) and (22), we have

$$V_0=\frac{\rho_s b}{\varepsilon_c}=\frac{S'}{S}\Delta V \tag{23}$$

From the above equation, the externally applied voltage V_0 becomes equal to the contact potential difference ΔV only when S'/S is 1.

Figure 4 shows the variation of the electric current and the displacement of the upper electrode with time, which are calculated by use of Eq. (12) with the experimental conditions specified in **Table 1**. Needless to say, the electric current i becomes zero when the upper vibrating electrode is at the top end or at the bottom end. The varying electric current was extremely small, about $10^{-12}\sim10^{-14}$ (A) in the experimental conditions conducted for this report.

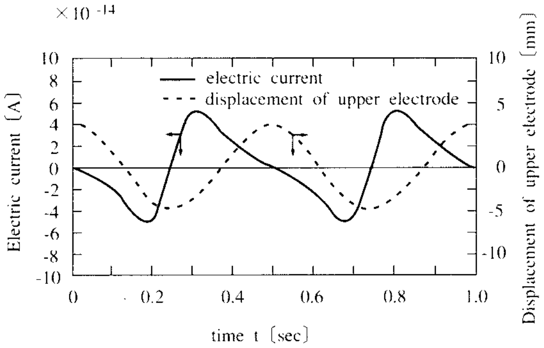

Fig. 4 Change of electric current and displacement of upper electrode with time

Table 1 Calculational conditions in Fig. 4

Applied voltage	V_0	1(V)
Frequency of vibrating electrode	ω	12.56(rad/s)
Thickness of powder bed	a_1	3(mm)
Thickness of air phase (B)	b	4(Å)
Pemittivity of air	ε_a	8.84×10^{-12}(F/m)
Permittivity of particle	ε_b	8.84×10^{-11}(F/m)
Charge density of particle layer	ρ_B	0(C/m³)
Surface charge density	ρ_s	−0.15(C/m²)
Area of electrode	S	7.06×10^{-4}(m²)
Amplitude of vibrating electrode	α_2	5(mm)

4. Results and Discussion

Figure 5 shows one of the experimental results on the relation between the amplitude of the electric current and the externally applied voltage V_0. In this case, the electric current becomes zero when V_0 is about -280 mV, which corresponds to the contact potential difference. The amplitude of the electric current was determined using an electrometer, which can automatically measure the electric current at 100

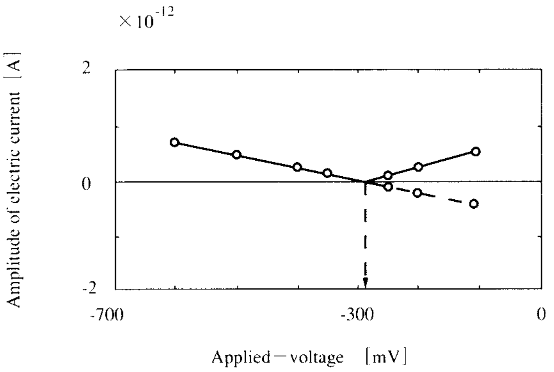

Fig. 5 Relation between amplitude of electric current and applied voltage

points per minute and indicate the maximum and minimum values.

The powder bed was adjusted in order to provide the specified packing ratio at the lower electrode and obtain the externally applied voltage which can nullify the electric current. The results indicated that the value V_0 varies in accordance with the measuring time. It is assumed that charges which the powder possessed at the initial stage of the measurement escaped through the grounding and the powder surface changed to the equilibrium surface condition adjusted to the environmental condition.

Figure 6 shows the relationship between the externally applied voltage which nullifies the electric current and the measuring time under various relative humidity conditions. The time within which V_0 exhibits a constant value increases as the relative humidity decreases.

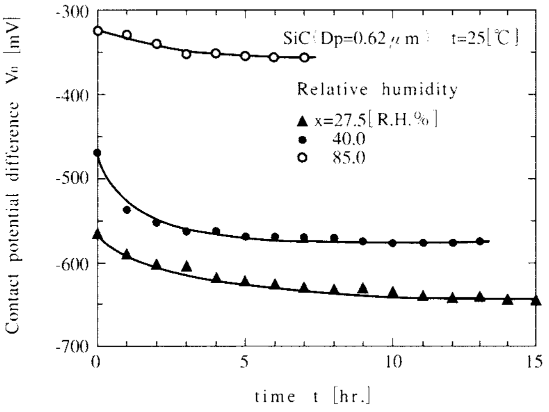

Fig. 6 Change of contact potential difference with time under different humidity conditions

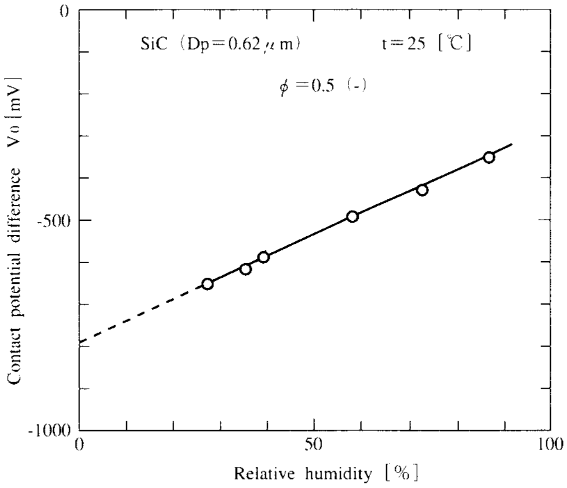

Fig. 7 Relation between contact potential difference and relative humidity

Figure 7 shows the relationship between the externally applied voltage V_0 and the relative humidity when there is no change with time. As the relative humidity increases, the absolute value of V_0 approaches zero. It is assumed that as the relative humidity increases, water molecules physically adsorbed at the powder bed top and lower electrode surface increase, thus lowering the original contact potential difference generated between the powder bed and the metal.

5. When the Powder Bed is Surface-modified with Alcohol:

An investigation of the changes in the contact potential difference when fine particles are methanol-modified to vary the surface electrical properties was carried out.

The powder was surface-modified by a technique in which the desiccator bottom was filled with a methanol solution, and the powder was set in a Petri dish for a long time.

Figure 8 shows the experimental results. In the figure, open circles indicate the experimental results when the nonmodified powder is dried at 110°C for 24 hours, indicating that V_0 is constant at about -500 mV. On the other hand, the powder modified with methanol for 24 hours (solid triangles) exhibits a constant V_0 value of -400 mV but shows a rapid change at the initial stage of the measurement. Based on these results, the powder of which the surface is modified with methanol has electrostatic characteristics which vary when methanol is adsorbed at the powder surface as compared to the conditions of nonmodified powder. In the experimental results in which the surface of the powder is modified over a period of 24 hours then dried again at 110°C for 12 hours (open triangles), the V_0 value scarcely varies but the constant value at the end of the measuring time nearly agrees with that of the powder of which the surface is modified over a period of 24 hours.

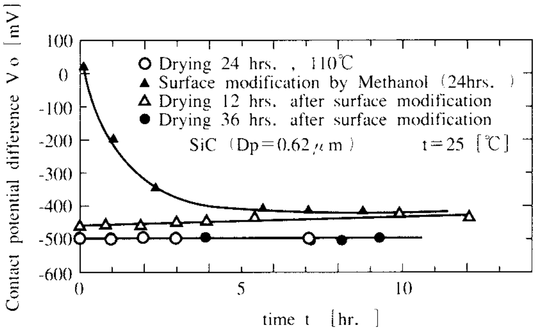

Fig. 8 Change of contact potential difference with time under different kinds of surface modification

However, the final value for the powder which is further dried at 110°C for 36 hours (solid circles) is nearly the same as that of the nonmodified powder. This may be attributed to the methanol molecules physically adsorbed by surface modification, which are desorbed by a long-period of drying. That · is, the surface modification method reported in this paper does not utilize reactions under high-temperature conditions, then methanol is easily desorbed from the powder surface because of weak bonding between the adsorbed methanol molecules and the powder.

As described above, the values measured by this technique enable the detection of subtle changes in the surface condition of the powder and may play an important role in the evaluation of the surface modification state of fine particles.

6. Conclusion

Experiments and a theoretical studies were carried out on the apparatus and the principle of measuring contact potential differences between powders and metals, and the following conclusions were obtained.

(1) New model was designed in order to interpret the experimental values of contact potential difference measurements. The study of the model has indicated that the contact potential difference between a powder and a metal can be measured only when the electric charge of the powder bed becomes zero.

(2) Because the electric charge of the powder bed decays and the powder surface shifts to a surface condition in equilibrium with the environmental conditions, a long time may be required to obtain a steady contact potential difference after the beginning of the measurement.

(3) The absolute value of the contact potential difference decreases as the relative humidity increases. This is attributed to a lowering of the contact potential difference originally existent between the powder and the metal due to the presence of water molecules between the two.

(4) The powder bed surface modified with methanol exhibits a contact potential difference different from that of the nonmodified powder. However, if adsorbed alcohol molecules are completely desorbed, the powder exhibits the same contact potential difference as that of the nonmodified powder.

Nomenclature

a_1	: thickness of powder bed	[m]
a_2	: position of upper vibrating electrode	[m]
b	: thickness of air phase between powder bed and lower electrode	[m]
C	: electrostatic capacity	[C/V]
D_p	: particle diameter	[m]
E_a, E_b	: electric field strength of powder and air phase, respectively	[V/m]
i	: electric current	[A]
K_i	: constants in Eqs. (2)-(4)	[V/m]
S, S'	: area of electrode and effective contact area	[m^2]
t	: time	[sec]
t_1	: temperature	[°C]
V, V_0	: electric potential and applied voltage	[V]
ΔV, $\Delta\tilde{V}$	: potential difference and contact potential difference	[V]
x	: position	[m]
α_1, α_2	: constants in Eq. (1)	[m]
ω	: frequency of upper vibrating electrode	[rad/s]

ε_a, ε_c : permittivities of particle and air, respectively [F/m]

ρ_B : volume charge density of powder layer [C/m^3]

ρ_s : surface charge density of powder layer [C/m^2]

ρ_{se} : surface charge density of upper vibrating electrode [C/m^2]

ϕ : packing fraction of particle [−]

χ : relative humidity [%]

References

1) Kelvin, L.: Phil. Mag., **46**, 82 (1898)

2) Krupp, H.: Advan. Collid Interface Sci., **1**, 111 (1967)

3) Penney, G.W. and E.H. Klingler: Elec. AIEE, 200 (1962)

4) Yoshida, H., T. Ninomiya and H. Masuda: J. Soc. of Powder Technology, Japan, **26**, 770 (1989)

A Method for Detecting Small Vibrations of Particles by LDV for Particle Size and Electrostatic Charge Measurements†

Yoji Nakajima
*Dept. of Chem. Process Eng., Hokkaido University**
Takashi Sato
*Dept. of Electrical Eng., Hokkaido Institute of Technology***

Abstract

A mathematical model based on an ideal LDV (Laser Doppler Velocimeter) signal indicates that the phase and amplitude of a light scattering particle vibrating sinusoidally within the interference fringes can be obtained from the Fourier integrals of the signal. Although actual LDV signals are distorted, it is found empirically that the use of a Hanning window is very effective for the removal of the undesirable effect of distortion. Hence the size and electrostatic charge of a particle being excited in an AC electric field can be calculated using the Fourier analysis of the LDV signal. A computer simulation shows that the phase can be determined very accurately, say, within 0.1° error if so desired. The lower limit of the amplitude measurement is ca. 0.2 μm within a few percent relative error. Therefore the present method is expected to provide a convenient device for measuring the size and the charge of particles of around 1 μm in diameter.

1. Introduction

Electrostatic and electrodynamic phenomena will hopefully be applicable to powder handling processes such as for classification, sorting, conveying, dispersion, mixing, coating, and so on. The most important properties of powder particles for such applications are of course the charge and the size. Various methods have been used for the measurement of the electrostatic charge of powders, however, most of them are not applicable to the measurement of the charge of single particles. Recently, a few devices used for simultaneous measurements of the charge and size of individual particles have been proposed[1], some of which are commercially available for practical use[2].

In a previous paper[3], the authors proposed one such device in which the waveform of a LDV signal emitted by a vibrating particle in the LDV fringes was geometrically analyzed to obtain the phase and amplitude of the particle vibration. Since the vibration of the charged particle in the device was induced by a controlled AC electric field, the phase and amplitude were converted into the size and charge of the particle. The accuracy of the measurement obtained with the device was satisfactory when the amplitude of the particle vibration was larger than the LDV fringe spacing. However, it becomes rather difficult to attain a sufficiently large amplitude with a moderate AC field when the device is applied to the measurements of aerosol particles usually encountered in the atmosphere.

In the present paper, a new method for analyzing LDV signals is proposed, with which particle amplitudes as small as one tenth the fringe size can be measured.

2. Theoretical background

2.1 Basic principle of size and charge measurements

Airborne particles with electrostatic charge

---

* N13 W8, Kita-ku, Sapporo 060 JAPAN
TEL. (011) 716 2111

** 7-Jo 15-Chome, Teine-ku, Sapporo 006 JAPAN
TEL. (011) 681 2161

† This report was originally printed in *Funsai* No.35, 11-20 (1991) in Japanese, before being translated into English with the permission of Hosokawa Micron Corporation, Japan.

flow through the measuring space between a pair of parallel plate electrodes, to which an AC high voltage having an angular frequency of ω is applied. As shown in **Fig. 1**, the particle is forced to vibrate in the x direction with an amplitude A under the effect of an AC electric field, E•sin (ωt).

Let the displacement of a vibrating particle in the measuring space be

$$x=A\sin(\omega t-\phi)+x_0 \qquad (1)$$

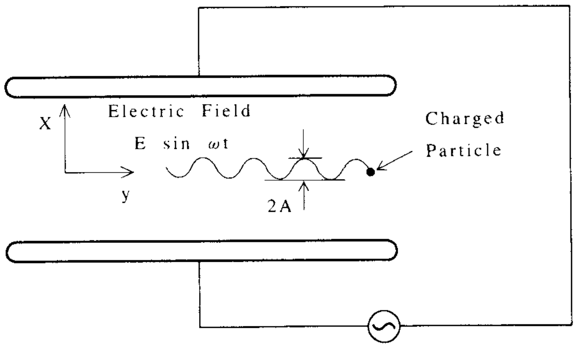

Fig. 1 AC electric field exerting on charged particle

As will be described later, the amplitude A and the phase lag ϕ can be obtained from the Fourier analysis of the LDV signal. The parameters of the vibration, A and ϕ are related to the following two parameters, which are characteristic to the particle, i.e., the electric mobility Z and the relaxation time τ.

$$A=\frac{ZE}{\omega\sqrt{(\tau\omega)^2+1}}=\frac{ZE}{\omega}\sin\phi \qquad (2)$$

$$\phi=\frac{\pi}{2}+\tan^{-1}(\tau\omega) \qquad (3)$$

We may assume a negative sign for Z and A if the particle charge is negative. Note that the phase lag ϕ is the phase difference between the applied AC electric field and the particle displacement (and not the particle velocity), and hence it is an angle between 90° and 180°.

The ratio of the two parameters, $\frac{Z}{\tau}$, gives the specific charge of the particle, namely, the charge per unit mass of the particle. Further, if the particle density is known, the particle diameter D_p and the charge q can be calculated from these parameters as follows:

$$D_p=\sqrt{\frac{18\mu\tau}{C\rho_p}} \qquad (4)$$

$$q=\frac{3\pi\mu D_p Z}{C} \qquad (5)$$

where μ is the viscosity of the surrounding medium (air), ρ_p is the density of the particle, and C is the Cunningham correction factor for molecular slip. The correction factor C is expressed by an empirical equation.

$$C=1+\frac{2\Lambda\left\{a_1+a_2\exp\left(\frac{-a_3D_p}{\Lambda}\right)\right\}}{D_p} \qquad (6)$$

where a_n's are the empirical constants, Λ is the mean free path of the medium; for normal air, $a_1=1.257$, $a_2=0.400$, $a_3=0.55$, and $\Lambda=0.065$ μm.

Eq. (4) requires an iterative method for obtaining D_p. Starting with $C=1$, the first approximation for D_p is calculated from Eq. (4), then a better value for C is estimated using Eq. (6). The iteration converges rapidly.

Eqs. (4) and (5) are derived from a steady Stokes' approximation, in which only the viscous term in the Navier-Stokes equation is taken into account. If the inertial term in the Navier-Stokes equation is included in the calculation (the Basset approximation), the corresponding expressions for Eqs. (4) and (5) may be written as follows:

$$D_p=\sqrt{\frac{18\mu\left\{(1+\sigma)\tau-\frac{\sigma}{\omega}\right\}}{C\rho_p}} \qquad (7)$$

$$q=\frac{3\pi\mu D_p Z(1+\sigma)}{C} \qquad (8)$$

where $\sigma=D_p\sqrt{\left(\frac{\omega\rho_g}{8\mu}\right)}$

(ρ_g, the density of surrounding gas). Our recent experiment, in which the measurement was carried out repeatedly many times with a single test particle, showed that D_p calculated from Eq. (4) depended on the vibrating frequency used for the measurement but D_p from Eq. (7) remained constant if the amplitude was not too large. Therefore, Eq. (7) is believed to be more accurate for calculating D_p than Eq. (4), though the use of the Cunningham correction factor in Eqs. (7) and (8) has not been justified yet.

2.2 LDV signal

As is well-known, the LDV fringes can be moved at a constant velocity using Bragg cells driven at two different frequencies. The LDV signal emitted by a particle in the moving fringes is an F-M wave[4)], of which the frequency is shifted from the carrier frequency (i. e., the difference between the drive frequencies of the Bragg cells) by an amount proportional to the particle velocity. Therefore, an F-M wave demodulator for the LDV signal, which tracks the instantaneous frequency of the LDV signal and transmits a continuous velocity signal, may be used for monitoring the velocity of the particle. Mazumder et al.[1)] successfully used such a conventional demodulator to measure the phase lag of a vibrating particle in the moving fringes.

In our opinion, however, conventional F-M wave demodulators may not be the best device for the present measurement, because they are not necessarily designed for the particular purpose of measuring the phase and amplitude of the sinusoidal motion of particles. In the present paper, LDV signals emitted by particles in pure sinusoidal motion with respect to the LDV fringes are mathematically examined to develop a more suitable method for the particular purpose of the present measurements. Here the words 'pure sinusoidal motion' also suggest that we will use stationary LDV fringes produced by a simpler optical system without Bragg cells. The beat signal emitted by a particle oscillating within stationary LDV fringes becomes a far different from a usual F-M wave. Therefore a digital computer, instead of a demodulator, will be used to analyze LDV signals in the new method.

Based on the diffraction theory, Roberds[5)] has reported a theoretical analysis of an LDV optical system shown in **Fig. 2**. The photo current or LDV signal, i, can be written as follows:

$$i \sim \exp\left\{-2\frac{\left(x^2+y^2+\frac{z^2\alpha^2}{4}\right)}{b_0^2}\right. \times\left\{\cosh\left(\frac{2xz\alpha}{b_0^2}\right)+V_0\cos(kx)\right\} \qquad (9)$$

where α is the intersection angle of the laser beams, b_0 the beam waist radius at the intersection, and k the fringe wave number, i.e., $\frac{2\pi}{\delta}$. The fringe spacing δ is expressed for laser beams of wave length λ as follows:

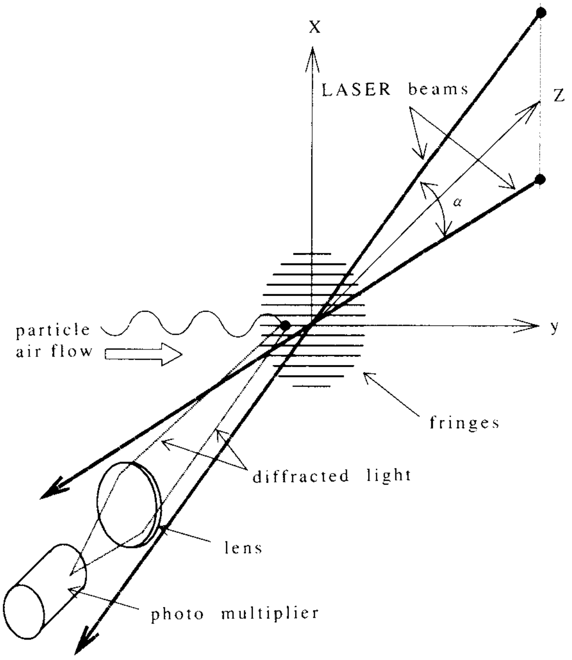

Fig. 2 LDV optical system

$$\delta=\frac{\lambda}{2\sin\left(\frac{\alpha}{2}\right)} \qquad (10)$$

Another parameter V_0 is a function of the light scattering particle size and optical parameters, but is independent of the coordinates (x, y, z). This parameter is related to the visibility of the LDV signal, i.e., $V=\frac{V_0}{\cosh\left(\frac{2xz\alpha}{b_0^2}\right)}$. When the particle size is much smaller than the fringe spacing, V_0 may be approximated to unity.

For simplicity, we assume an ideal case where the light scattering particle vibrates in the central portion of the LDV fringes with an amplitude much smaller than the beam radius. Then the exponential and the hyperbolic terms in Eq. (9) can be regarded as constants. The beat signal (AC component) may be written as

$$i_b=B\cos\{k(A\sin(\omega t-\phi)+x_0)\} \qquad (11)$$

where B is a constant depending on the optical system and the particle size. As stated in Eq. (2), we assume a negative sign for A if the particle charge is negative. However, Eq. (11) shows that it is impossible to determine the sign of A; the signal is exactly the same as that when the signs of both A and x_0 are reversed. Although we may be able to determine the sign if a very small velocity component in the x direction is added to the particle motion[3], we confine ourselves to the case where the polarity of the particle charge is known by some other means. In the following, A is assumed to be positive.

2.3 Fourier expansion of beat signal

The bottom curve in **Fig. 3** shows a typical example of a beat signal calculated using Eq. (11). The waveform is quite different from normal F-M waves. When the amplitude of the particle is comparable to or larger than the fringe spacing, we can find distinctive points denoted by a, b, ..., e, at which the direction of the particle motion is reversed. Hence ϕ can be determined from the time difference between a peak in the AC field and the nearest reverse point after the peak. Further, the number of peaks in a beat signal between two neighboring reverse points and their positions reflect the relationship between the particle relative location and the phase of oscillation. This information gives the particle amplitude. This is a brief explanation of the method proposed in the previous paper[3]. As may be seen from Eq. (11) and **Fig. 3**, however, the reverse points in a beat signal become difficult to pinpoint when the amplitude is too small.

Eq. (11) can be expanded[6] into an infinite series using Neuman expansion as follows:

$$
\begin{aligned}
i_b = & B\cos(kx_0)J_0(kA) \\
& -2B\sin(kx_0)\sum_{n=0}^{\infty}J_{2n+1}(kA)\sin\{(2n+1)(\omega t-\phi)\} \\
& +2B\cos(kx_0)\sum_{n=1}^{\infty}J_{2n}(kA)\cos\{(2n)(\omega t-\phi)\} \qquad (12)
\end{aligned}
$$

where J_n (kA) is the Bessel function of the first kind and of order n. Omitting the steady component and rearranging give:

$$
\begin{aligned}
i_0 = & A_1\{\cos(\phi)\sin(\omega t)-\sin(\phi)\cos(\omega t)\} \\
& +A_2\{\sin(2\phi)\sin(2\omega t)+\cos(2\phi)\cos(2\omega t)\} \\
& +A_3\{\cos(3\phi)\sin(3\omega t)-\sin(3\phi)\cos(3\omega t)\} \\
& +A_4\{\sin(4\phi)\sin(4\omega t)+\cos(4\phi)\cos(4\omega t)\} \\
& +\ldots \qquad (13)
\end{aligned}
$$

where the coefficients are defined by

$$
A_n=\begin{cases}-2B\sin(kx_0)J_n(kA) & n=1,3,5,7\ldots \\ 2B\cos(kx_0)J_n(kA) & n=2,4,6,8\ldots\end{cases} \qquad (14)
$$

The coefficient, A_n, represents the amplitude of the n-th harmonic wave in the beat signal. Since A_n may be positive or negative depending on the values of kA and x_0, we may call it the signed amplitude.

Mathematically, Eq. (13) together with Eq. (14) is equivalent to the Fourier expansion of an ideal beat signal, in which the fundamental angular frequency is assumed to be the same as that of particle oscillation, ω.

On the other hand, if actual beat signals are

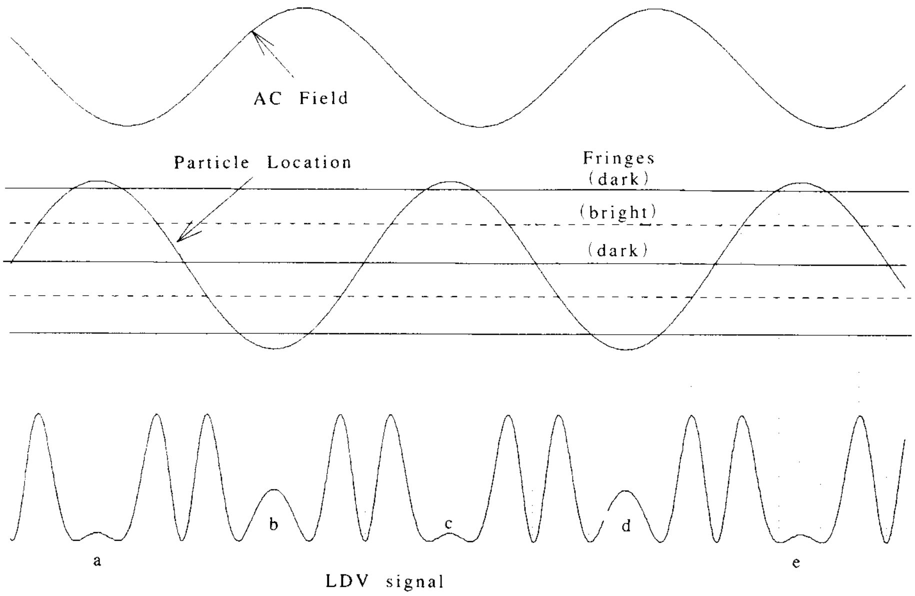

Fig. 3 Idel LDV beat signal

numerically expanded into harmonic series of sine and cosine waves having a fundamental angular frequency ω, the result may be written as follows :

$$i_0=\sum_{n=1}^{\infty}\{F_{sn}\sin(n\omega t)+F_{cn}\cos(n\omega t)\} \tag{15}$$

The coefficients in Eq. (15), F_{sn} and F_{cn}, can be calculated from the Fourier sine and cosine integrals of actual LDV signals, which may include a pedestal component. Taking the integration time T as a multiple of the period of the particle oscillation, we can evaluate the following complex integral by some suitable numerical method explained later in § 4.

$$F_n=\left(\frac{2}{T}\right)\int_0^T i\exp(jn\omega t)dt,\ j=\sqrt{-1},\ n=1,2,3\ldots \tag{16}$$

Then the real part and the imaginary part of F_n, respectively, give F_{cn} and F_{sn}.

2.4 Calculations for phase and amplitude measurements

By comparing Eq. (13) with Eq. (15), we obtain the following relations for the coefficients :

$$\left.\begin{array}{ll} F_{sn}=A_n\cos(n\phi),\ F_{cn}=-A_n\sin(n\phi) & n=1,3,5,\ldots \\ F_{sn}=A_n\sin(n\phi),\ F_{cn}=A_n\cos(n\phi) & n=2,4,6,\ldots \end{array}\right\} \tag{17}$$

Since ϕ is an angle between 90° and 180°, both the above equations for n=1 and 2 can be used to obtain a unique value for ϕ i.e.,

$$\left.\begin{array}{ll} n=1 & \phi=\tan^{-1}\left(\frac{-F_{c1}}{F_{s1}}\right)\ 90°<\phi<180° \\ n=2 & 2\phi=\tan^{-1}\left(\frac{F_{s2}}{F_{c2}}\right)\ 180°<2\phi<360° \end{array}\right\} \tag{18}$$

The method whereby ϕ can be obtained from two independent equations is quite advantageous because A_n (and hence F_{s1} and F_{c2} in the denominators of the above equations) becomes zero when the trigometric functions and/or the Bessel functions are equal to zero (see **Fig. 4**) in Eq. (14). In practical calculation, it is recommended to use one of the equations for n=1 or n=2 depending whether the absolute value of F_{s1} is greater than the absolute value of F_{c2} or not.

Equations (17) are then used to determine A_n's with their appropriate signs from F_{sn}'s and F_{cn}'s for several values of n. Further, from Eq. (14), the ratio of A_{n+2} to A_n is obtained as follows :

$$\frac{A_{n+2}}{A_n}=\frac{J_{n+2}(kA)}{J_n(kA)}=Q_n(kA) \tag{19}$$

This is a function of only kA, and the particle amplitude A can be obtained from this ratio. Since the Bessel functions are damped oscillating functions as shown in **Fig. 4**, however, the functions, Q_n's, defined by their ratios are not monotonous. As a result, the inverse functions, Q_n^{-1}'s, become multi-valued functions with innumerable branches. In **Fig. 5**, the first and second branches of Q_n's for several values of n are shown. Therefore, we will have an infinite number of values for kA even for a given single value of Q_n.

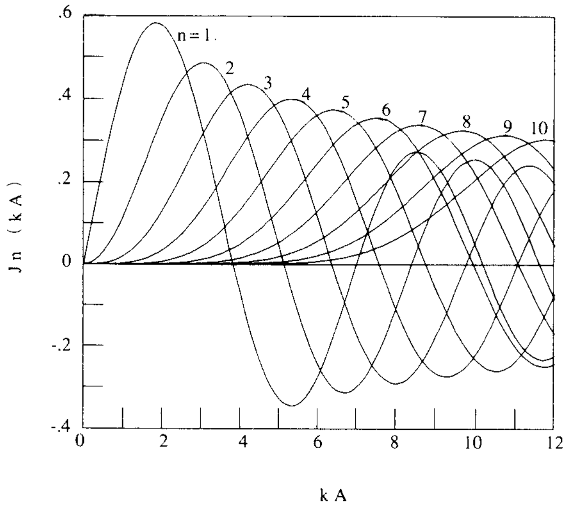

Fig. 4 Bessel function of the first kind

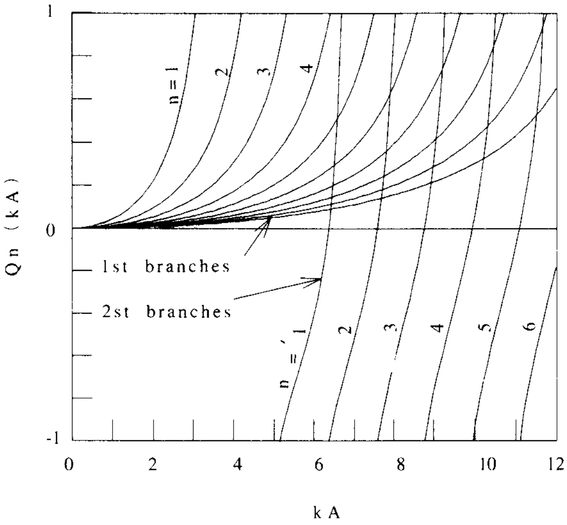

Fig. 5 First two branches of the Function Q_n (kA)

As can readily be seen from **Fig. 5**, the inverse function, Q_n^{-1}, gives a single value if the value of the inverse function is confined to the range between the first zero (i.e., $kA=0$) and the second zero of Q_n. We may call this range "the principal range" of Q_n^{-1}. Since the upper limit of the principal range becomes large for a large n, any large value of kA can be included in the principal range for n greater than a certain integer. Therefore, if we can select a suitable integer for n from the beat signal analysis, the proper value of kA can be uniquely found in the principal range for Q_n^{-1}. From the analysis of Eqs. (13) and (14) together with **Figs. 4** and **5**, the most suitable integer for n turns out to be of the order of the strongest harmonic wave in the beat signal.

This provides a simple method for determining kA : Find the strongest amplitude, A_n, among the signed amplitudes calculated using Eq. (16). Obtain the principal value (i.e., minimum value in the present calculation) for kA, which satisfies $\frac{A_{n+2}}{A_n}$, n being of the order of the strongest harmonic wave. The value of kA thus obtained gives the correct amplitude of the particle vibration.

3. Wave analysis of actual beat signal

The above theoretical results have been deduced with the assumption that the LDV signals are emitted from ideal fringes. Beat signals from actual LDV fringes are distorted by many sources, e.g., pedestal term, speckles, intensity fluctuations in laser beam, illuminated foreign particles, air flow disturbance in LDV fringes, and so on.

The authors have kept a good deal of LDV signal data digitally recorded in floppy disks obtained from the previous experiment[3]. The experiment was carried out with DOP droplets of 1.29 μm in radius, which were produced by an aerosol generator of the vibrating orifice type. The particle vibration frequency was approximately 6 kHz and therefore the phase lag was 127°. The LDV and the AC field signals were sampled by a two-channel, 8-bit digitizer for 1 ms duration at a sampling frequency of 1 MHz, and were recorded as a series of 2000 words binary data. An example of a reproduced AC field and LDV signals, respectively, is shown in the top and middle curves in **Fig. 6**. Reverse points (corresponding to points a, b, c, ... in **Fig. 3**) may be found in the LDV signal, although they are not very clearly noticeable. The particle amplitude for this LDV signal has been regarded as being at the sensible lower limit of the reverse points for the computer algorithm used in the previous method mentioned in § 2.3.

As stated in Eq. (16), the integration time, T, should be taken as a multiple of the period of the particle vibration, so that the LDV signal can be decomposed into a harmonic series of the fundamental frequency, i.e., the frequency of the particle vibration. This requirement is quite understandable for ideal LDV signals in which the fundamental frequency is really reflected in their waveforms as shown in **Fig. 3**. On the contrary, actual LDV signals may be so distorted that the fundamental wave cannot be recognized in LDV signals; in fact it is very hard to distinguish the fundamental wave in the actual LDV signal shown in **Fig. 6**.

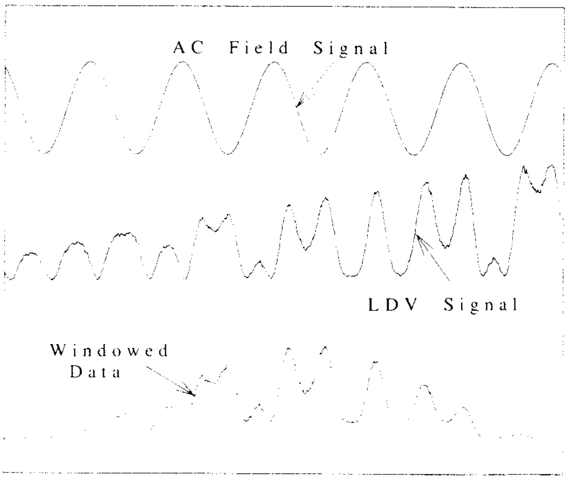

Fig. 6 Example of observed LDV signal

For the reason mentioned above, it is not certain that precise information for obtaining the phase and amplitude of a particle vibration can be extracted from actual LDV signals with the aid of Eq. (16), in which the fundamental wave plays an essential role. Nevertheless, the authors intend to analyze actual LDV signals on the basis of the mathematical discussions given in the preceding sections.

Here the mathematical role of the angular frequency, $n\omega$, in Eq. (16) is reconsidered so as to obtain a virtually continuous spectrum of the

LDV signal. Let's suppose a fictitious signal with long dummy data of zero (or constant) intensity attached before and after the actual recorded data of an LDV signal. The integration time T for this fictitious signal becomes very long for $\omega = (2\frac{\pi}{T})$ to approach zero, and $n\omega$ can actually be regarded as a continuous variable. Since relative values of F_n for various $n\omega$ are in question in the present calculation, the proportionality $\frac{2}{T}$ in Eq. (16) is not an essential factor. In this sense, the integration may be performed for an arbitrary angular frequency, Ω, regardless of the actual signal duration, T, by simply substituting Ω for $n\omega$ in Eq. (16), provided that Ω is fairly larger than $\frac{2\pi}{T}$.

The amplitude spectrum of the LDV signal shown in **Fig. 6** was calculated in this manner. If the LDV signal had been ideal, we would have had line peaks at several multiples of 6 kHz, the driving frequency of the particle oscillation. In contrast to the ideal case, the actual spectrum shown in **Fig. 7** displays an appreciable broadening and has dips at multiple frequencies of 6 kHz. The broadening is a result of a rather too short duration (1 ms) of the recorded LDV signal. This can be understood in terms of the boxcar window function discussed in the theory for spectrum analysis[7].

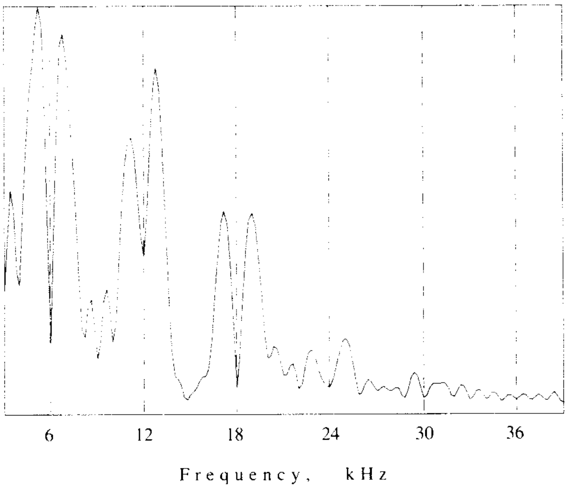

Fig. 7 Amplitude spectrum of the LDV signal in Fig 6

The dips can be explained by the effect of the particle drift velocity perpendicular to the fringe planes as follows : If the particle vibration in the fringes accompanies a steady drift velocity, the beat frequency becomes higher in the half period of the vibration where the particle velocity is enhanced by the drift velocity, and then becomes lower in the second half period. Such a frequency shift in the beat signal results in a separation of every peak in the spectrum of an actual LDV signal into pairs of peaks. The peak separation can be shown mathematically by simply replacing kx_0 with $k(x_0 + Ut)$ in Eq. (12). In the spectrum of an actual LDV signal with broadening, peak separation would display a dip at the middle frequency of every pair of peaks.

Judging from the above reasoning, **Fig. 7** may be acceptable as a reasonable LDV spectrum. Hence F_{sn} and F_{cn} for 6 kHz and 12 kHz were calculated using Eq. (16) to obtain ϕ from Eq. (18). However, the result (=121.7°) differed considerably from the expected value, 127°. Such calculations for 60 sets of data collected under the same experimental condition gave a rather unsatisfactory result. This is assumed to be caused by data truncation; as shown in **Fig. 6**, at the beginning and end of the recorded signal, there are sudden changes in signal intensity which may give rise to disturbances in the calculated spectrum.

In waveform data processing techniques, time series data are often multiplied by a function of time called window function before spectral analysis, so that the resultant data fade in and out smoothly at the beginning and ending portions of the truncated signal. It is well known that disturbances in a spectrum can be smoothed out using such a window function, which averages the spectrum intensity over a certain frequency width. In the present calculation, a Hanning window[7] is adopted, which takes the form $\frac{\{1-\cos(\frac{2\pi t}{T})\}}{2}$ where T is the signal duration and t is the time of the sampling point. $(t = 0 \sim T)$. Thus the original data shown in the middle curve in **Fig. 6** was transformed into the windowed data shown in the bottom curve.

The spectrum of the windowed data is shown in **Fig. 8**. We can see that many phantom peaks observed in **Fig. 7** completely disappeared. As a result of this improvement, the phase lag calculated from the windowed data gave a value very close to the expected value, 127°. Then phase lags for the 60 sets of recorded data were recalculated using this window technique. The phase distribution thus obtained was converted into the radius distribution of the monodisperse DOP droplets obtained from the aerosol generator. The average and the standard deviation of the radius distribution, respectively, were 1.289 μm and 0.0188 μm. These values coincided very well with the expected values for the operational conditions of the aerosol generator. In this way, the efficacy of the Hanning window is really advantageous for the phase measurement, although this fact doesn't necessarily mean that the spectrum calculated using the window function gives the true spectrum of the signal.

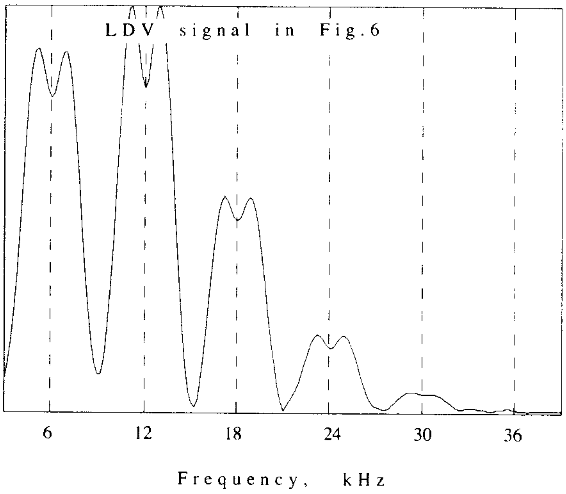

Fig. 8 Effect of Hanning window on the spectrum

It should be noted here that the frequency of the AC field, on which the phase calculation is based, must be measured precisely; only a few percent error in the frequency results in an unacceptable error in the phase measurement. And, another point for calculating the phase lag, one of the equations in Eq. (18) should be properly selected with due care as mentioned in the related section.

To obtain the amplitude of a particle vibration, the signed amplitudes of the harmonic waves, A_n's, were calculated using Eqs. (16) and (17) for n from 1 to 12. This range of n is suitable when $\frac{A}{\delta}$ is less than 2. For the measurement of a larger amplitude, the calculations must be extended to higher order harmonics. However, the present method loses its advantage over the previous method when the amplitude becomes greater than the fringe spacing. Therefore, in comparison with normal spectrum analyses, a very limited number of frequencies for the analysis will suffice for the present method.

The amplitude of a particle vibration depends on the particle charge. DOP droplets obtained from the aerosol generator used in the experiment were generated by breaking up periodically a liquid jet spouted from a vibrating platinum micro orifice. An experiment on electrostatic charges of particles obtained from the aerosol generator showed that the DOP droplets had a constant positive charge by spontaneous triboelectrification[8]. Therefore, it is not surprising that the particle amplitude calculated from the experimental data for the same operational conditions of the generator shows almost a constant amplitude; in fact, the average of $\frac{A}{\delta}$ (where $\delta=8.68$ μm) was found to be 0.431 with a standard deviation of 0.020 for the same data as those used in the phase measurement. Although we have no means to confirm the correctness of the above result, 47 sets of data out of 60 could be analyzed by the previous method[3] and a reasonable agreement with the above result was observed; the result obtained by the previous method was $\frac{A}{\delta}=0.426$ with a standard deviation of 0.012.

As stated before, the drift velocity of a particle gives rise to peak separation and yields dips in its LDV spectrum at the harmonic frequencies of the particle vibration. Since the present method totally relies on F_n's in Eq. (16) calculated for the harmonic frequencies, the depths of the dips greatly affect that accuracy of the measurement. We see from **Figs. 7** and 8 that the dips can be much flattened when a Hanning window is used. However, the efficacy of the window is of course limited to the case where the drift velocity is not too large. In the previous method, the drift velocity could be calculated from the LDV signal to compensate for its effect. Further, when the compensation was discriminated to be rather unsuccessful, the data was automatically abandoned. This is the major reason why only 47 data out of 60 could be analyzed, and as a result, the standard deviation obtained by the previous method was slightly smaller.

The peak separation shown in **Figs. 7** and 8 corresponds to a drift velocity of 0.78 cm/s. The maximum drift velocity in the experiment was found to be 1.5 cm/s. (The velocity is of course the velocity component perpendicular to the fringe planes.) Since the fringe planes are formed parallel to the plate electrodes, it may not be difficult to keep the drift velocity lower than this level.

4. Numerical integration

Eq. (16) is no other than the formula of the Fourier expansion for periodic functions. The only difference in the sign of the exponential term is not a matter of significance for the present discussion. In contrast to conventional LDV systems, a digital computer is used for the waveform data processing. As a consequence, the LDV signal is converted into a time series of digital data for the numerical processing, which naturally resembles very much the DFT (Discrete Fourier Transformation). Therefore techniques for the DFT such as the FFT algorithm may be applicable. In this section, however, it is pointed out that the calculated result using the DFT is not directly applicable to the present method.

In the DFT (and hence in the FFT) algorithm, the whole integrand in Eq. (16), i exp ($jn\omega t$), is approximated to a linear function in an interval between neighboring data points so as to obtain an approximate value of the integral for the single interval. When $n\omega$ is so small that exp ($jn\omega t$) remains almost constant in each interval, the sum of representative values for all intervals may give a value close to the integral of Eq. (16). However, for a large value of $n\omega$, the DFT algorithm may not be a reasonable approximation of the integral. Nevertheless the resultant DFT coefficients can exactly reproduce the original data, i, using the inverse DFT. Here we must remember the fact that the reproduction of original data using the inverse DFT is possible only for the moments which exactly correspond to the sampling points. If we calculate the data, i, for any moment between the sampling points, the result may give a quite unreasonable value for i. It follows that the DFT may not be regarded as a reasonable approximation of the Fourier integrals of the functions which vary with time smoothly and almost linearly between the sampling points.

To obtain acceptable values for F_n numerically from Eq. (16), only the LDV signal, i, and not i exp($jn\omega t$), should be approximated to a linear function between neighboring data points; $i = at + b$. The resultant integrand, $(at + b)\exp(jn\omega t)$, is integrated algebraically over a single data interval, and then the results are summed up to obtain the total integral of Eq. (16). The calculation is rather tedious but the final result can be summarized in the following simple conclusion :

The coefficient, F_n, calculated for Ω from the above approximation can be obtained by multiplying the coefficient of the DFT by a factor of $\frac{2\{1-\cos(\Omega\Delta t)\}}{(\Omega\Delta t)^2}$ where Δt is the sampling interval. The coefficients thus calculated coincide well with the Fourier coefficients in Eq. (15) for Ω ($= n\omega$) lower than $\frac{\pi}{\Delta t}$.

List 1 Example program of Fourier integrals for extracting the fundamental and harmonic waves from LDV signal.

```
          ** Fourier Sin/Cos Integrals **
          cosine=REAL(Zn),  sine=IMAG(Zn)

  note : pi=π,  j=√(-1)
          CEXP(j * θ)=cos(θ)+j * sin(θ)
          HanW(K) : Windowed data(real)
          HanW(0)=HanW(Kdata+1)=0
          FFreq : Fundamental Frequency
          St : Sampling time interval

  j=CMPLX(0.0, 1.0)
  Dth=2.0*pi*FFreq*St

  Do 200 Nf=1, NFourier
       ZDthNf=CEXP(Dth*Nf*j)
       ZW=ZDthNf
       Zsum=0.0

            Do 300 K=1, Kdata
                 Zsum=HanW(K)*Zw+Zsum
300              ZW=ZW*ZDthNf

                 (Zsum : DFT)

  linear interpolation between data points.
200 Zn(Nf)=(1.0-REAL(ZDthNf))/(Nf*Nf)*Zsum
```

List 1 is an example of a Fortran program used for the calculation, in which non-essential constants are omitted. In this program, the variables starting with Z together with j are complex variables. The loop enclosed by the statement number 300 is no other than the DFT.

The phase rotator is ZW. The complex variable, Zsum, is for the result calculated by DFT, and is multiplied at the statement 200 by a factor, $\frac{(1.0-\mathrm{REAL}(\mathrm{ZDthNf}))}{(\mathrm{Nf}\cdot\mathrm{Nf})}$, which corresponds to the factor, $\frac{\{1-\cos(\Omega\Delta t)\}}{(\Omega\Delta t)^2}$. The FFT algorithm is not used in this program because only a limited number of frequencies are required to be analyzed.

5. Simulated performance

5.1 Beat signal generation

In this simulation model, the same optical system as described in the previous paper[3] was considered; b_0, α, δ, and λ in Eqs. (9) and (10), respectively, were 200 μm, 0.0725 rad (4.18°), 8.68 μm, and 0.6328 μm. A particle to be traced in the simulation was initially located at a position (x_0, y_0, z_0) in **Fig. 2**; x and z_0, respectively, were randomly positioned within $\pm$ 1.5b_0 and $\pm 1.5\frac{b_0}{\sin(\frac{\alpha}{2})}$, while y_0 was a constant, i.e., $-1.5b_0$. This area for initial positions was wide enough to cover the whole measurement control volume of the simulated LDV system. From an initial position thus chosen randomly, a particle to be traced was transported in the y direction by a steady air flow with a velocity of 30 cm/s. The frequency of the particle vibration in the x direction was fixed at a constant value of 12 kHz; the phase lag was randomly given as an angle between 100° and 170°. The amplitude was set at a random value within a range between 0.05δ and 1.2δ; δ is the fringe spacing. The drift velocity in the x direction, which causes peak separation in the spectrum, was given randomly within $\pm$ 2 cm/s.

Under the above condition, beat signals for the simulation were calculated using Eq.(9) for the trajectories of about 42,000 particles. In the simulated system, an 8-bit digitizer was assumed to be used for recording the beat signal. Then the proportionality in Eq.(9) was assumed to be 128 so that the signals could be expressed in 8-bit integer data by omitting figures below the decimal point.

5.2 Trigger rate and count efficiency

The digitizer was triggered when the intensity of the signal exceeded a certain level, which was assumed to be 10% of the maximum intensity. The ratio of the number of particle trajectories which triggered the digitizer to the total number of particles traced is tentatively named 'trigger rate'.

As the digitizer was triggered whenever the signal intensity exceeded the threshold, some of the triggered signals had too poor visibility for the waveform data processing. For instance, when a particle passed across a single laser beam near its center axis but outside the fringe area, the signal was intense enough to trigger the digitizer but wholly void for the processing. Since the illuminating light intensity distribution in the beam cross section was assumed to be Gaussian (as usual in actual LDV optical systems), such a void signal was modulated by the frequency of the particle oscillation. This situation is true also in actual LDV systems.

It follows that a high-pass filter with a cut off frequency higher than the frequency of the particle oscillation is necessary for the removal of such void signals. However, the use of a high-pass filter would totally spoil the present method because one of the most important frequency components in normal signals comprises the frequency of the particle oscillation. Consequently, the computer program used for the waveform data processing should provide a function for the discrimination between acceptable signals and void signals for the processing. For this reason, not all of the triggered signals are supposed to be processed. The ratio of the signals adopted for the processing to the total triggered signals is tentatively termed 'count efficiency'.

The trigger rate and the count efficiency for the previous method depend appreciably on the particle amplitude when the amplitude is smaller than the fringe spacing. The trigger rate is of course affected by the area selected for the initial position of the particles. Therefore, only the relative change in the trigger rate in response to the amplitude is of significance. Referring to the changes in the trigger rate and the count efficiency, the measured amplitude distribution (and hence the charge distribution) can be corrected. However the particle size distribution must not be calculated from the measured phase lag distribution unless the breadth of the distribution is very narrow. This is because the actual signal intensity depends highly on the particle size ; this fact means that the trigger rate and the count efficiency depend also on the particle size.

5.3 Sampling frequency and number of sample points

As stated above, the frequency of the particle vibration in this simulation was 12 kHz and its maximum amplitude was assumed to be 1.2δ. These gave an estimation of the maximum frequency to be analyzed as follows:

The maximum kA is $2\pi \times 1.2 = 7.5$, and the absolute value of the signed amplitude A_n in Eq.(14) takes its largest value at $n=6$ or 7 for $kA=7.5$. Since we need A_{n+2} to obtain the particle amplitude, the possible maximum of the harmonic frequency to be analyzed is $(n+2) \times 12\text{kHz} = 108\text{kHz}$ for $n=7$.

The sampling frequency of the digitizer must be higher than twice this maximum frequency, i.e., 216 kHz. This is the minimum value for the sampling frequency required by the sampling theorem, therefore a 500 kHz sampling ($\Delta t = 2\ \mu s$) was selected for the simulation to avoid aliasing.[9)]

The signal time duration for the analysis, T, is proportional to the number of the sample points. Naturally, we may expect a better accuracy of the measurement with a larger number of sample points, N. Since T affects the window characteristics, however, an additional problem arises if a too large number of sample points is carelessly used without reducing the drift velocity of a lower level.

The window function averages the spectrum over a certain frequency range, which is inversely proportional to T. Therefore, a larger T or N yields a higher spectrum resolution. For the present method of analysis, however, a very high resolution is not necessarily favorable. This is because a high resolution exaggerates the dips in the spectrum caused by the drift velocity at the frequencies required for the analysis.

In the previous experiment, the signal time duration was 1 ms for a maximum drift velocity of 1.5 cm/s. Although these values might not be standard, T was tentatively chosen to be 1 ms (and hence $N=512$) for this simulation for a maximum drift velocity of 2 cm/s.

5.4 Discrimination of beat signal

As explained in § 5.2, not all the triggered signals were suitable for data processing. In this simulation, beat signals were discriminated in the following manner according to a measure for visibility of the beat signals.

The visibility defined by Roberds[5)] was $\frac{V_0}{\cosh(\frac{2xz\alpha}{b_0^2})}$; this definition can be understood from Eq.(9). However, it is not easy to evaluate the visibility thus defined from actual LDV signals. In this simulation, $V = \frac{\sum_{n=1}^{9}|F_n|}{|F_0|}$ was adopted for the visibility, where $|F_n|$'s are absolute values of the complex quantities calculated using Eq.(16) for n from 0 to 9. This definition of visibility may be considered as being the ratio of the sum of the intensities of the significant components to the total intensity of the signal.

The adoption of a small value for the visibility threshold increases the possibility of miscalculation, and decreases the accuracy and reliability of the measuring system. But the visibility becomes lower and lower as the particle amplitude decreases. When $\frac{A}{\delta} = 0.1$, V is less than 0.3 for the optimal condition; the visibility becomes optimal when the particle vibrates at the center of the fringes. Therefore, too large a value for the threshold decreases unacceptably the count efficiency for small amplitudes. The threshold was assumed to be 0.1 for the simulation.

Although this value might be too large for the measurement of small amplitudes, miscalculations still occurred with this value. When a particle passed through some portion of the fringes having a very weak contrast, the fundamental frequency component became highest when the particle amplitude was large enough to make some harmonics stronger than the fundamental if the particle had been in normal fringes ; this was an effect of the Gaussian distribution in beam intensity stated previously and led to miscalculation of the particle amplitude. To avoid this sort of miscalculation, the fundamental component was ignored if harmonics higher than the 4th had appreciable intensities.

5.5 Simulated results

About 42,000 particle trajectories were traced to examine the effect of their amplitude on the trigger rate and on the count efficiency. The result is shown in **Fig. 9**. The trigger rate depends little on the amplitude. In contrast to this, the count efficiency decreases considerably with a decrease in amplitude. This is an inevitable result of the discrimination of signals. However, the change occurs fairly smoothly down to $\frac{A}{\delta}=0.1$, and compensation for obtaining the amplitude distribution may be possible. This is an advantage over the previous method.

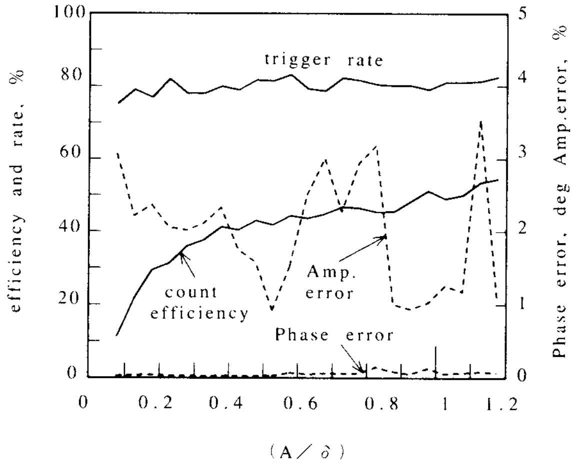

Fig. 9 Simulated results

In **Fig. 9**, the standard deviations of the error in the phase and of the relative error in the amplitude are also shown. The amplitude error varied widely with the amplitude; the error might have resulted from miscalculation caused by incomplete discrimination. Nevertheless, the error may well be considered to be within an acceptable level for normal purposes. On the other hand, the phase error was very small and was of the order of 0.05° on average. It follows that a fairly accurate particle size can be calculated from a rather small phase lag, caused by a rather too low frequency for the particle size. Or in other words, we may use a considerably low frequency even for small particles.

As explained before, the drift velocity of a particle in the x direction leads to peak separation and causes dips at the analyzed frequencies. As a result, LDV signals observed for large drift velocities tended to be classified as having too poor a visibility. **Fig. 10** shows the effect of the drift velocity on the count efficiency, i.e., the area below the curve over $U=U \sim U+dU$ gives the number of particles being processed of which the drift velocity was in the range between U and U + dU. Since the drift velocity was distributed uniformly in this simulation, it is observed from the figure that the count efficiency suddenly decreases for U greater than 1.6 cm/s.

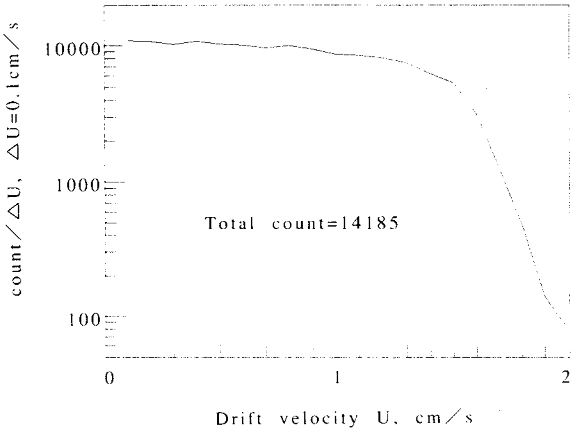

Fig. 10 Effect of drift velocity on count efficiency

The simulated results for U less than 1 cm/s were examined to determine whether the accuracy of the measurement could be improved for smaller drift velocities. However, no appreciable differences could be found in the amplitude and phase errors. Therefore we may conclude that the drift velocity affects mainly the count efficiency and slightly the accuracy of the measurement.

As stated in § 5.3, we can expect a better accuracy with longer signal time durations, which lead to a higher spectrum resolution as a by-effect. To maintain the count efficiency at a reasonable level for a high resolution of the spectrum, we must decrease the drift velocity. Keeping these points in mind, we carried out another simulation test for T=2 ms or 1024 sample points (i.e., twice the time duration of the first simulation). The maximum drift velocity was assumed to be 1 cm/s (i.e., half the maximum of the first simulation) and b_0, 400 μm (i.e., twice the radius of the first simulation). Other simulation parameters remained unchanged. The result showed that the effect of the amplitude on the trigger rate and on the count efficiency was almost the same as that shown in **Fig. 9**. However the errors in both the amplitude and phase measurements decreased to less than half the errors observed in the first simulation. The effect on the count efficiency was quite similar to that shown in **Fig. 10** except that the drift velocity should be read as being half that indicated in **Fig. 10**.

6. Conclusions

The Fourier analysis is applied to waveform data processing of the LDV signal emitted by an oscillating particle. The amplitude and the phase lag of the particle oscillation can be calculated using a spectrum analysis of the LDV signal. If a charged particle is forced to oscillate under the effect of an AC electric field, the size and the charge of the particle can be determined from the phase lag and the amplitude.

The accuracy of the phase lag measurement is believed to be so high that a frequency of the order of 10 kHz may be used for the measurement of a particle size as small as 0.3 μm. As for the amplitude measurement, the proposed method provides a convenient means for the determination of rather small amplitudes of around 1 μm. Both features mentioned above may be helpful for the measurement of small electrostatic charges on particles finer than 1 μm.

A longer signal duration can improve the accuracy of the measurement. The sensibility of the amplitude may be increased by decreasing the LDV fringe spacing. However, both modifications may lead to a drop in the count efficiency to a great extent because peak separation by drift velocity is exaggerated for longer signal durations and/or smaller fringe spacings. Consequently, the drift velocity caused by thermal convection and air flow turbulence should be eliminated as carefully as possible.

The polarity of a particle charge cannot be determined by the present method. Recently, we came upon a possible method to avoid this shortcoming by superposing on purpose a constant drift velocity on the vibrating motion of the particle.

Nomenclature

A : amplitude of particle oscillation, m

A_n : signed amplitude of n-th harmonic, Ampere

a_n : constants in Eq.(6), dimensionless

B : proportionality, Ampere

b_0 : radius of laser beam ($\frac{1}{e^2}$ point, m

C : Cunningham correction factor, dimensionless

D_p : particle diameter, m

E : amplitude of AC field, $\frac{V}{m}$

F_n : complex quantity for expressing Fourier sine and cosine integrals defined by Eq.(16), Ampere

F_{cn} : real part (cosine component) of F_n, Ampere

F_{sn} : imaginary part (sine component) of F_n, Ampere

i : output current, Ampere

i_b : beat signal current, Ampere

i_o : oscillating component in output signal, Ampere

J_n : Bessel function of the first kind and of order n

$j = \sqrt{-1}$

$k = \frac{2\pi}{\delta}$, fringe wave number, $\frac{1}{m}$

N : number of data points

n : order of harmonics

$Q_n(kA) = \frac{J_{n+2}(kA)}{J_n(kA)}$

q : particle charge, Coulomb

T : signal time duration or integration time, s

ΔT : sampling time interval of digitizer, s

t : time, s

U : drift velocity of particle in x direction, $\frac{m}{s}$

V : visibility, dimensionless

V_o : visibility parameter, dimensionless

x, y, z : coordinates of particle location, m

x_0 : center of particle oscillation in x, m

x_0, y_0, z_0 : particle initial position

Z : electric mobility of particle, $\frac{m^2}{Vs}$

α : intersection angle of laser beams, rad

δ : fringe spacing, m

Λ : mean free path of medium gas, m

λ : wave length of laser beam, m

μ : viscosity of medium gas, $\frac{\mathrm{kg}}{\mathrm{ms}}$

ρ_g : gas density, $\frac{\mathrm{kg}}{\mathrm{m}^3}$

ρ_p : particle density, $\frac{\mathrm{kg}}{\mathrm{m}^3}$

$\sigma = D_p \sqrt{\frac{\omega \rho_g}{8\mu}}$, dimensionless parameter in unsteady Stokes equation

τ : relaxation time for particle motion, s

ϕ : phase lag of particle oscillation, deg

Ω : angular frequency, $\frac{\mathrm{rad}}{\mathrm{s}}$

ω : angular frequency of particle oscillation = fundamental angular frequency for the analysis, $\frac{\mathrm{rad}}{\mathrm{s}}$

References

1) Mazumder, M. K., et al. : Rev. Sci. Instrum., **48**, 622 (1977) Renninger, R. G., et al. : ibid., **52**, 242 (1981)
2) Yokoyama, T., et al. : Preprint of 25th Symposium on Powder Science, p82 (1987, Sapporo)
3) Sato, T., Nakajima, Y. : Trans. I. E. E. of Japan, **110**, 473(1990)
4) Seely, S : “Electron Tube Circuit” 2nd ed., p603 (McGraw-hill Kougakusha, 1958 Tokyo)
5) Roberds, D. W. : Appl. Opt., **16**, 1861(1977)
6) Moriguchi, S., et al. : “Suugaku Koushiki III”, p211 (Iwanami Zensho, 1959 Tokyo) Gradshteyn, I. S., Ryzhik, I. M. : Table of Integrals, Series and Products, p974 (Academic Press, New York 1980)
7) Hino, M. : “Supekutoru Kaiseki (Spectrum Analysis)”, p167 (Asakura Shoten, Tokyo 1977)
8) Sato, T. : Trans. I. E. E. of Japan, **107**, 155 (1987)
9) Minami, S. ed. : “Hakei Deita Shori (Waveform Data Processing)”, p40 (CQ Shuppansha, Tokyo 1986)

Instantaneous Measurement of Particle Size and Flow Rate by the Prameters of Impact Sound between Particles and a Circular Plate †

Jusuke Hidaka, Atsuko Simosaka, Hideaki Ito and Shigeo Miwa.
*Dept. of chem. Eng., Doshishal Univ.**

Abstract

Effects of particle properties and number of particles on the parameters of sound from the collision between particles and a circular plate is discussed, in relation to measuring particle size and flow rate by the parameters of the impact sound.

The sound pressure is proportional to the number of particles colliding with the plate, and the characteristic frequency of the sound relates to the particle diameter. Moreover, particle size distribution can be measured by the intensity of the characteristic frequency component of each particle diameter.

These results show that the particle size distribution and the mass flow rate of particles can be measured instantaneously by the parameters of impact sound between particles and a circular plate.

Introduction

Since the sound generated by collisions between the wall of process equipment and particles provides a wide variety of information concerning the operating conditions of the equipment, the operator pays constant special attention to this sound. That is, it has been empirically known that there is a close relationship between the parameters of the sound of particle collisions and the physical properties, moving speed, and number of particles moving inside the equipment. It is, therefore, possible to utilize the impact for the measurement of fine particles, but no detailed investigation regarding this subject has been reported to date.

In investigating the sound of particles colliding against the fine-particle equipment wall, it is necessary to identify the sound generating mechanism of a single particle colliding against a plate. For this purpose, numerous studies[1,3,4,5,7,8,9,10,11] on the suppression of the sound of collisions between solids have been carried out. The authors have also identified the relationship existing between the sound pressure level of collisions against a circular disk and the particles' colliding speed as well as the particle properties, and have also determined the relationship existing between the frequency and the particle size.[2]

In this report, representing one of the basic studies of the sound of particles colliding against the fine-particle equipment wall, the investigation deals with the parameters of the particles' colliding noise against a circular disk, and the possibility of measuring the particles' properties, size, and flow rate simultaneously using the particles' impact sound is analyzed.

1. Estimation of the Frequency Spectrum of Particle Impact Force and Sound of Collision Against a Disk

1.1 Estimation of particles' impact force and sound pressure waveform of collisions against a circular disk

Now, let us consider the case of spherical particles having a uniform particle size colliding at the center of a circular disk at a constant mass flow rate Q. In this event, let the mass of

---

* Higashi-Imadegawa, Kamigyo-ku Kyoto 602 JAPAN
TEL. 075-251-3847

† This report was originally printed in *Kagaku Kougaku Ronbunshu*, **16**, 1067-1073 (1990) in Japanese, before being translated into English with the permission of the editorial committee of the Soc. Chemical Engineers, Japan.

one spherical particle be m. Then the number of colliding particles per unit time N_p is Q/m. That is, N_p particles per unit time collide against the disk at random time intervals. For simplification, let us suppose that the disk vibration is not affected by particles which have already collided with it; then, the particles' impact force and collision's sound pressure waveform can be determined as follows using the estimation technique[2)] for a single particle's impact force. First, the collision time is determined using the following method. As shown in **Figure 1**, the total observation time of a collision sound T_o is converted into a discrete form with a time increment Δt^* which is shorter than the duration of an impact between a particle and a disk T_c. The probability of a particle colliding against a disk within a discrete time Δt is given by $N_p \Delta t/T_o$. Therefore, random numbers from 0 to 1 were allotted to each collidable particle for every discrete time period, and particles of which the random number was below the collision probability value were designated as particles which would collide within that time. Once the collision initiation time of each particle is determined in the above manner, the particle impact force waveform is obtained, then, using the estimation method for collision sound pressure waveform, the sound pressure level emitted by each particle can be predicted. Therefore, adding the sound pressure levels emitted by each particle from hour to hour at observation points provides the sound pressure waveform of the collision sound of the particles.

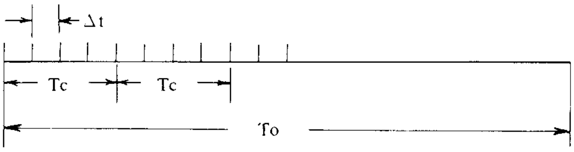

Fig. 1 Colliding time of each particle.

When the colliding particles have a particle size distribution, dividing the particles into micro particle diameter sections ΔD_p and performing the above-mentioned calculation for the particles of each particle size section provides an estimation of the impact force waveform and sound pressure level waveform produced by the particles.

1.2 Frequency spectrum of the waveform of the force of impact against a disk

The equation describing the vibration of a circular disk is linear and the frequency characteristics of a particle's colliding sound are determined by the frequency characteristics of the impact force.[2,9)] Therefore, an investigation of the relationship existing between the frequency spectrum of a particle's impact force and the colliding particle's size as well as the number of colliding particles shall be made.

[Collision of uniform-size particles]

As shown in **Figure 2**, let us suppose that spherical particles of uniform size collide against a disk at time intervals $(T_p + \tau_p)$ expressed as constant time intervals T_p and τ_p which satisfy the normal distribution of the standard deviation σ. The impact force waveform of particles and that of the disk at the time of collision of uniform-size particles are similar. Therefore, let the frequency spectrum of the waveform of the impact force due to a particle be $g(\omega)$, then the frequency spectrum $S(\omega)$ of a series of waveforms of impact forces due to $2N + 1$ particles can be expressed by the following equation.

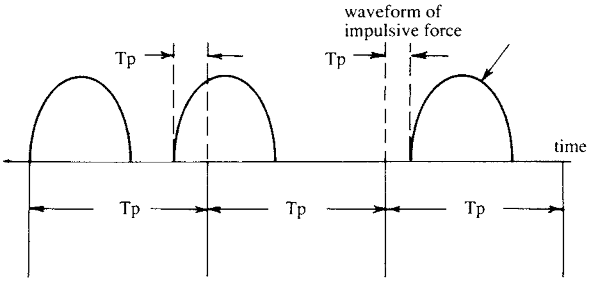

Fig. 2 Series of waveforms of impulsive force between particles and plate.

$$S(\omega)=g(\omega)\sum_{-n}^{n}\exp[j\omega(nT_p+\tau_p)] \qquad (1)$$

where, n is an optional coefficient and the distribution τ_p is expressed by the following equation.[6)]

$$q(\tau_p)=\frac{1}{\sigma\sqrt{2\pi}}\exp\left(-\frac{\tau_p^2}{2\sigma^2}\right) \qquad (2)$$

The power spectrum of a series of waveforms of impact forces G_N is given by

$$G_N(\omega)=\frac{|S(\omega)|^2}{(2N+1)T_p}$$
$$=\frac{|g(\omega)|^2}{T_p}\frac{1}{2N+1}[\{\sum_{-N}^{N}\cos\omega(nT_p+\tau_p)\}^2$$
$$+\{\sum_{-N}^{N}\sin\omega(nT_p+\tau_p)\}^2] \qquad (3)$$

Eq. (3) can be rewritten as follows:[6]

$$G_N(\omega)=\frac{|g(\omega)|^2}{T}[\{1-\exp(-\sigma^2\omega^2)\}$$
$$+\frac{\exp(-\sigma^2\omega^2)}{2N+1}[\{\sum_{-N}^{N}\cos(\omega nT_p)\}^2$$
$$+\{\sum_{-N}^{N}\sin(\omega nT_p)\}^2] \qquad (4)$$

where, $\Sigma\sin(n\omega T_p)=0$, and when N is sufficiently large, the following equation is verified using the unit impulse function δ and an optional coefficient n'.

$$\lim_{N\to\infty}\frac{1}{2N+1}\{\sum_{-N}^{N}\cos(\omega nT_p)\}^2=\frac{2\pi}{T}\delta(\omega-\frac{2n'\pi}{T_p}) \qquad (5)$$

Consequently, the power spectrum G_N of an impact force when particles of uniform size collide against a disk at time intervals $(T_p+\tau_p)$ is expressed by the following equation.

$$G_N(\omega)=\lim_{N\to\infty}G_N(\omega)=\{1-\exp(-\sigma^2\omega^2)+\exp(-\sigma^2\omega^2)$$
$$\frac{2\pi}{T_p}\delta(\omega-\frac{2n'\pi}{T_p})\}\frac{|g(\omega)|^2}{T_p} \qquad (6)$$

On the other hand, when the time intervals of the collisions between the disk and particles is completely random, $\sigma^2\to\infty$ and $\exp(\sigma^2\omega^2)\to 0$ in Eq. (6), then the frequency spectrum $S(\omega)$ of a series of waveforms of impact forces due to the particles can be expressed as follows using Eq. (4).

$$S(\omega)=\sqrt{(2N+1)T_pG_N(\omega)}=\sqrt{2N+1}\,|g(\omega)| \qquad (7)$$

That is, when spherical particles of uniform size collide against a disk at random time intervals, the frequency spectrum of the waveforms of the impact forces is the same as the profile of that due to a single particle and the value of the frequency component is proportional to the number of colliding particles N_p $[=2N+1]$ to the power 1/2.

Figure 3 shows the frequency spectrum of the impact force due to the collision between a disk and a single particle (**Fig. 3(a)**) obtained by the method described in Section 1.1 and the frequency spectra of a series of waveforms of impact forces due to the collisions between a disk and particles of uniform size (**Fig. 3(b)**). As can be seen from the frequency spectrum of

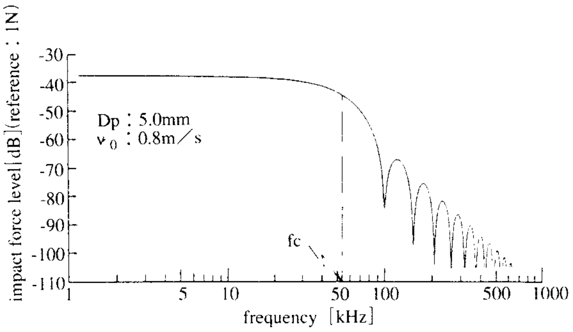

(a) collision between a particle and plate

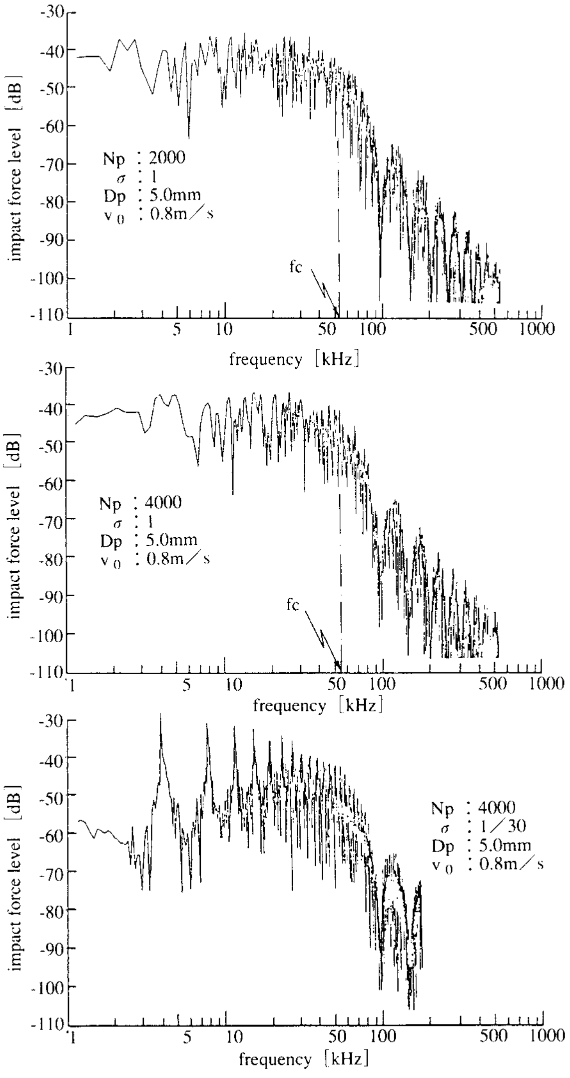

(b) collision between particles and plate

Fig. 3 Frequency spectra of impulsive force.

an impact force due to a particle shown in **Fig. 3(a)**, the frequency component above a certain frequency tends to rapidly decrease in the impact force frequency spectrum. In connection with this subject, in our previous report,$^{2)}$ the frequency of which a component rapidly decreases is called a characteristic frequency f_c and it has been determined that the characteristic frequency f_c is equal to the inverse $(1/T_c)$ of the impact duration T_c during a collision between a disk and a particle and the value depends on the particle size of the colliding particles.

In the calculation of the frequency spectra of a series of waveforms of impact forces due to particles of uniform size shown in **Fig. 3(b)**, the collision time intervals of the particles were set so as not to be completely random and the particles were allowed to collide at time intervals in which τ_p satisfies the normal distribution of the standard deviation σ. When the variation of τ_p is small (small σ value), a line spectrum appears in the frequency corresponding to an integer times the collision frequency as can be seen from Eq. (6). However, as the σ value increases and the collision time intervals grow irregular, the profile of the spectrum becomes similar to that of the frequency spectrum of the impact force due to a particle as shown in Eq. (7). This result indicates that the characteristic frequency f_c is constant irrespective of the number of colliding particles and the value is equal to the characteristic frequency f_c at the time of the collision of a particle. Consequently, in the collisions of multiple particles, this method enables the measurement of the particle size using the value of the characteristic frequency.

On the other hand, from Eq. (7) the following linear relationship between the level value $I(f_c)$ of the frequency component of the characteristic frequency f_c and the number of colliding particles N_p per unit time holds true.

$$I(f_c) = 10\log(N_p) + I_p \qquad (8)$$

where, I_p $[= 20 \log|g(\omega)|]$ is the level value in the frequency f_c of the frequency spectrum of the impact force due to a particle.

Now, the following relationship between the mass flow rate Q of the particles and the number of particles N_p can be verified.

$$N_p = 6Q/(\pi D_p^3 \rho_p) \qquad (9)$$

Hence, the following equation between $I(f_c)$ and the flow rate Q holds true.

$$I(f_c) = 10\log(Q) + I_{pp} \qquad (10)$$

where, $I_{pp} = I_p + 10 \log(6/\pi D_p{}^3 \rho_p)$.

These results suggest that it is possible to determine the particle size and the flow rate from the characteristic frequency of the collision sound and the intensity of the frequency component.

[Random collision of particles having different diameters]

The analysis of the characteristics of the frequency of an impact force due to particles having a particle size distribution is extremely complicated. Therefore, in this section, in order to reach some conclusions concerning the effects of particle size distribution on the characteristics of the frequency of an impact force, an investigation of the frequency spectrum of waveforms of impact forces was carried out when particles having different diameters collide against a disk randomly.

For particles having particle diameters D_{p1} and D_{p2}, let the number of collisions of the respective particles against a disk be N_{p1} and N_{p2}, and the spectra of the impact force waveforms be $g_1(\omega)$ and $g_2(\omega)$. In this case, the energy spectrum of a series of waveforms of impact forces due to particles consisting of N_{p1} and N_{p2} is the sum of the energy spectra of a series of waveforms of impact forces due to the corresponding particles and is given by

$$|S(\omega)|^2 = N_{p1}|g_1(\omega)|^2 + N_{p2}|g_2(\omega)|^2 \qquad (11)$$

Let the characteristic frequency for the corresponding size particles be f_{c1} and f_{c2}, then the energy spectrum values at these frequencies $|S(f_{c1})|^2$ and $|S(f_{c2})|^2$ can be calculated using the following equations.

$$|S(f_{c1})|^2 = N_{p1}|g_1(f_{c1})|^2 + N_{p2}|g_2(f_{c1})|^2 \qquad (12)$$

$$|S(f_{c2})|^2 = N_{p1}|g_1(f_{c2})|^2 + N_{p2}|g_2(f_{c2})|^2 \qquad (13)$$

That is, from Eqs. (12) and (13), the number of collisions N_{p1} and N_{p2} of the corresponding particles can be found using the following equations:

$$N_{p1}=\frac{|S(f_{c1})|^2|g_2(f_{c2})|^2-|S(f_{c2})|^2|g_2(f_{c1})|^2}{|g_1(f_{c1})|^2|g_2(f_{c2})|^2-|g_1(f_{c2})|^2|g_2(f_{c1})|^2} \quad (14)$$

$$N_{p2}=\frac{|S(f_{c2})|^2|g_2(f_{c2})|^2-|S(f_{c1})|^2|g_1(f_{c2})|^2}{|g_1(f_{c1})|^2|g_2(f_{c2})|^2-|g_1(f_{c2})|^2|g_2(f_{c1})|^2} \quad (15)$$

That is, this indicates a possibility of determining the number of particles having a specific size contained among particles of various sizes.

Figure 4 shows an example of calculation of the frequency spectrum of the waveforms of impact forces due to particles having different diameters D_{p1} and D_{p2} of 5 mm and 3 mm, respectively. In order to verify the relationship of Eqs. (14) and (15), a similar frequency spectrum was calculated by varying the number of colliding particles. Next, from these spectra, $|g_1(f_{c1})|^2$, $|g_1(f_{c2})|^2$, $|g_2(f_{c1})|^2$, and $|g_2(f_{c2})|^2$ were obtained, and from Eqs. (14) and (15), N_{p1}' and N_{p2}', the number of collisions of each particle was determined. **Table 1** is a comparison of the numbers of actual collisions determined by calculation of the waveforms of the impact forces N_{p1} and N_{p2} with N_{p1}' and N_{p2}', which indicates a remarkable relationship between the two.

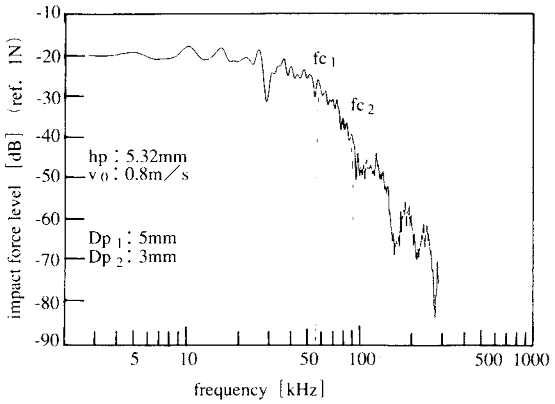

Fig. 4 Frequency spectrum of impulsive force between plate and particles having two different diameters (D_{p1}, D_{p2}).

Table 1 Colliding number between particles and plate

(hp ; 5.32mm, 0.8mm/D_{p1} ; 5.0mm, D_{p2} ; 3.0mm)

N_T	N_{p1}	N_{p2}	S (f_{c1})	S (f_{c2})	N'_{p1}	N'_{p2}
3000	1500	1500	0.0385	0.0091	1479	1485
4000	2800	1200	0.0506	0.0092	2985	1265
8000	2400	5600	0.0527	0.0171	2330	5852
10000	3000	7000	0.0597	0.0187	3066	6965

2. Experimental Apparatus and Methods

Figure 5 shows schematically the apparatus used for measuring the sound of collision of particles against a disk. A steel disk 395 mm in diameter was secured with bolts to the end surface of a steel cylinder of 350 mm inside diameter and 23 mm thickness. Particles in a hopper collide at the center of the circumferentially-fixed disk at a constant mass flow rate after emerging from an orifice located at the hopper bottom. The disk was arranged 33° aslant to prevent the particles which have collided against the disk from colliding against it again.[2] A condenser microphone (B&K, 4135) was installed 500 mm right above the disk surface center on the particles' collision side for collision sound measurement. The material of the disks used was SS41, with thicknesses h_p of 2.0, 5.32, and 10.0 mm. The particles were steel bearing balls, having diameters D_p of 3.0, 4.0, 5.0, and 7.0 mm. For the estimation of the sound pressure waveforms, Young's modulus $E_p = 2.06 \times 10^{11}$ Pa, density $\rho = 7.87 \times 10^3$ kg/m^3, and Poisson's ratio $\nu = 0.28$ were used as material characteristic values for the disks and steel balls.

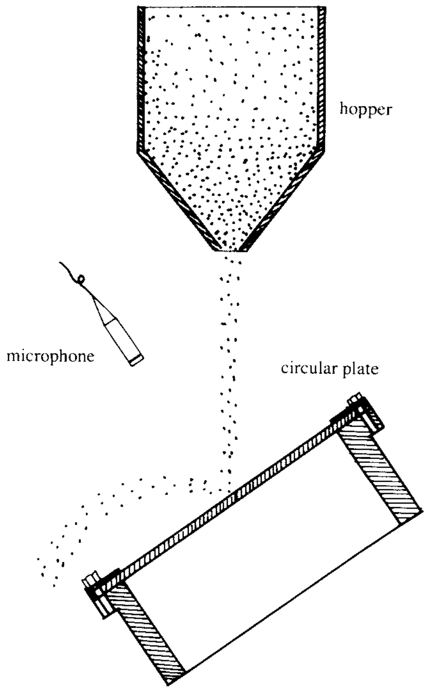

Fig. 5 Evperimental apparatus.

3. Experimental Results and Discussion

3.1 Parameters of collision sound due to particles of uniform size

Figure 6 shows the results of the measurement of the frequency spectrum of collision sounds due to particles of uniform size. The characteristic frequency observed in these measured spectra exhibited values smaller than those of the sound f_c when one particle collides perpendicularly with the disk (f_c =84 kHz (4 mm), f_c=113 kHz (3 mm)$^{2)}$). This is attributed to the tilting of the target disk so arranged for measuring the collision sound due to the particles. That is, **Table 2** shows the measured impact duration when one particle collides against the tilted target disk and the calculated impact duration when a single particle collides perpendicularly with the disk surface. In both cases, the impact duration increases when a particle collides against the tilted disk. However, the inverse ($1/T_c$) of the impact duration agrees with the characteristic frequency f_c which is observed on the spectra. In the case of a tilted disk, information on particle diameter can be obtained using this characteristic frequency f_c. The increased impact duration may be attributed to the slip experienced at the time of the collision between the particles and the disk. **Figure 7** shows the relationship which exists between the sound pressure level due to the particles $L_p(f_c)$ and the mass flow rate of the particles Q at f_c.

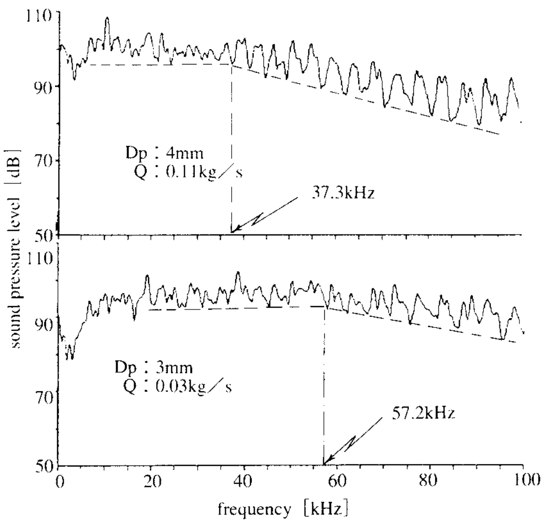

Fig. 6 Frequency spectra of the sound radiated from collision of uniform particles.

Table 2 Contact duration between a particle and inclined plate

(D_p= 5 mm, h_p= 2 mm)

v_o [m/s]	T_0 [μs]	f_c [kHz]	T_c [μs]	f_c [kHz]
	(measured values)		(calculated values)	
1.28	31.74	31.5	17.73	56.4
2.21	29.32	34.1	15.89	62.9
2.86	29.30	34.1	15.13	66.09

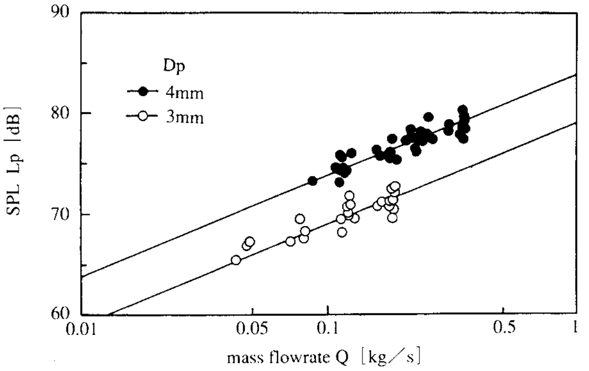

Fig. 7 Relationship between sound pressure level and mass flow rate of particles.

From these results, the relation expressed by the following equation which is similar to that of Eqs. (8) and (9) can be deduced.

$$L_p(f_c)=10\log N+K_1, K_1=20\log|P(f_c)| \qquad (16)$$

$$L_p(f_c)=10\log Q+K_2, K_2=10\log(6/\pi D_p^3\rho_p) \qquad (17)$$

where, $P(f_c)$ is the pressure of the collision sound due to a single particle.

3.2 Parameters of collision sound due to particles having different diameters

Figure 8 shows examples of calculation of the frequency spectra of collision sound due to particles of different diameters. In these frequency spectra, the level values of the characteristic frequencies f_{c1}, f_{c2} of the corresponding particles are related to the number of colliding particles as discussed in Section 1. On the other hand, when the number of particles colliding against a disk is small, or if the particle size is decreased, an intense frequency peak due to the disk's vibrating mode appears in the frequency spectrum, making it difficult to read the peak intensity in the characteristic frequency. Therefore, the remainder of this section shall deal

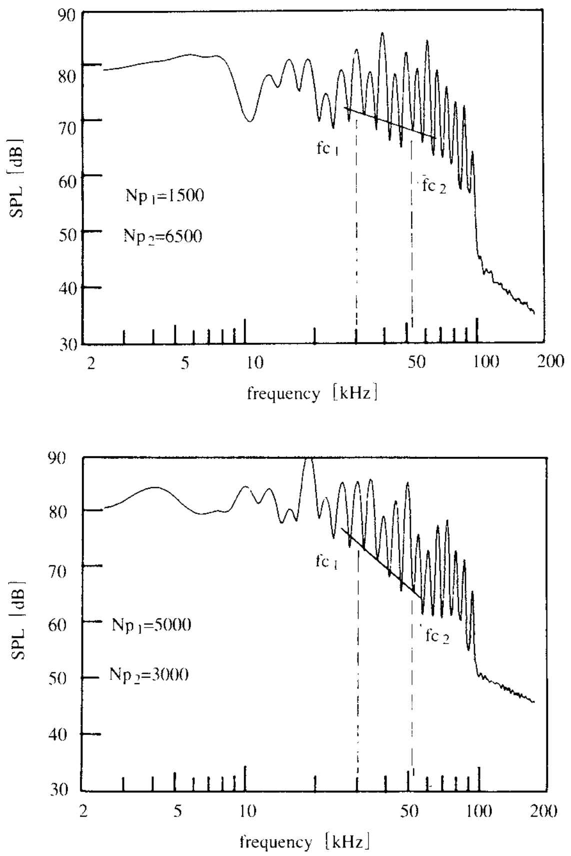

Fig. 8 Frequency spectra of impact sound from particles having two different diameter (D_{p1}, D_{p2}).

with the method used for determining the level values f_{c1}, f_{c2} based on the spectrum baseline. A comparison of two calculated spectra indicates that the level value of the characteristic frequency f_{c2} increases the relative intensity with respect to the level value of f_{c1} with an increase of the number of colliding particles N_{p2} of D_{p2} which is smaller than D_{p1}. The level values in the characteristic frequencies f_{c1}, f_{c2} are given by the sum of the sound energies due to the corresponding particles, which is equivalent to Eqs. (12) and (13) concerning the energy spectra of impact forces. Therefore, the gradient S^1 of a straight line joining the values f_{c1}, f_{c2} shown with broken lines in the figure has the following relation with the ratio of particles number κ_p (N_{p1}/N_{p2}) (Appendix-1).

$$S_1=\frac{L_P(f_{c1})-L_P(f_{c2})}{f_{c1}-f_{c2}}=\frac{1}{f_{c1}-f_{c2}}10\log \times\left\{\frac{K_P|P_1(f_{c1})|^2+|P_2(f_{c1})|^2}{K_P|P_1(f_{c2})|^2+|P_2(f_{c2})|^2}\right\} \qquad (18)$$

Figure 9 shows the relationship between S_1 and κ_p obtained from calculated and measured spectra.

It is possible to express the intensity $L_p(f_{c1})$ of the characteristic frequency f_{c1} as follows using the total number of colliding particles N_T ($=N_{p1}/N_{p2}$) and κ_p.

$$L_P(f_{c1})=10\log N_T+10\log \times\left\{\frac{K_P|P_1(f_{c1})|^2+|P_2(f_{c1})|^2}{K_P+1}\right\} \qquad (19)$$

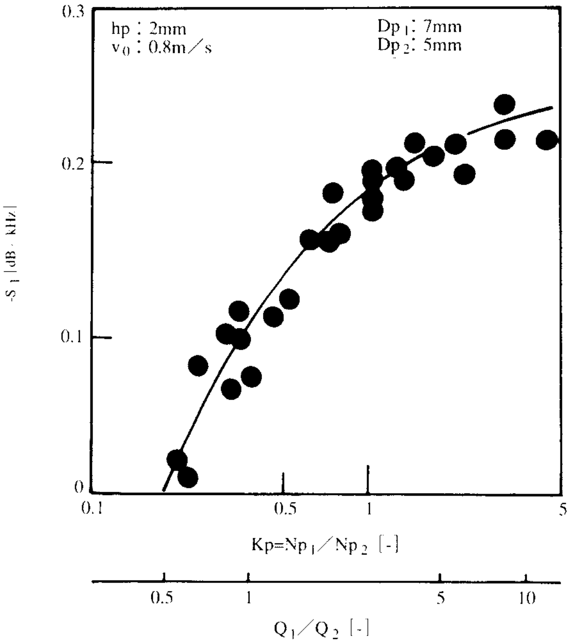

Fig. 9 Relationship between K_p and S_1.

Consequently, if κ_p is constant, the mass flow rate Q is proportional to $L_p(f_{c1})$. **Figure 10** is a relationship between the flow rate Q and $L_p(f_{c1})$ of particles of different diameters. It indicates a linear relationship with a gradient of 10 irrespective of the κ_p value. These results show that the particle size, flow rate, and flow rate ratio can be obtained from the frequency spectrum of the collision sound due to particles of different diameters.

On the other hand, from the discussion regarding the above-mentioned collision sound due to particles of different diameters, it is assumed that the gradient S_1 in the frequency spectrum of the collision sound of particles having different diameters is related to the particle size distribution. Using specimens

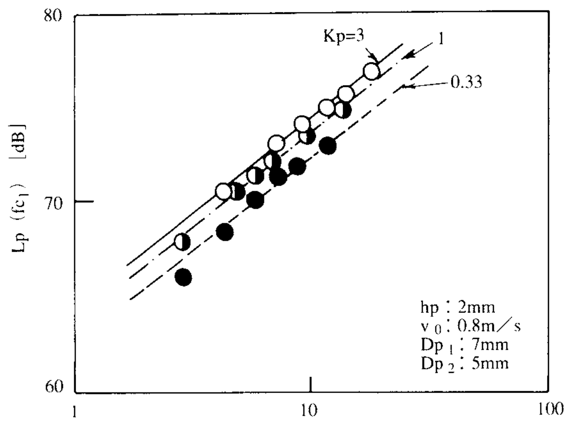

Fig. 10 Relationship between Q and $L_p(f_{c1})$.

adjusted in such a manner that the particle size distribution satisfies the logarithmic normal distribution, the relationship between S_1 and the geometric standard deviation σ_g was experimentally determined, the results of which are shown in **Figure 11**. These results indicate that the particle size distribution can be obtained from the collision sound due to the particles.

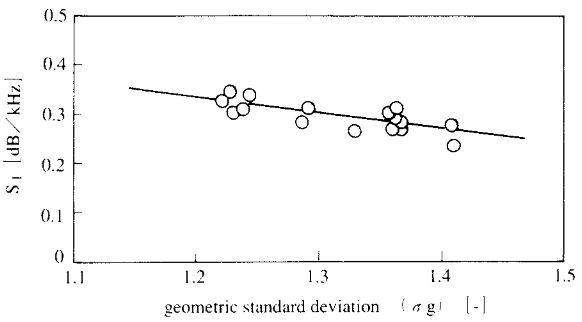

Fig. 11 Effect of σ_0 on S_1.

Conclusion

For basic research on the sound of particles colliding against a fine particle equipment wall, a relationship between a circumferencially-fixed disk and the parameters of collision sound due to the particles, particle properties, particle colliding speed, and number of colliding particles has been determined. The sound pressure level due to the particles is proportional to the number of colliding particles, and the characteristic frequency is constant irrespective of the number of colliding particles, and agrees with the value obtained for the collision sound due to a single particle. Consequently, it is possible to measure the number of colliding particles, particle size, and its distribution from the collision sound due to the particles.

Appendix-1 Deduction of Eq. (18)

The values of the characteristic frequency components $P_{\tau}(f_{c1})$, and $P_{\tau}(f_{c2})$ in the energy spectrum of the collision sound due to particles of different diameters are given by

$$P_T(f_{c1})=\{N_{p1}|P_1(f_{c1})|^2+N_{p2}|P_2(f_{c1})|^2\}^{1/2} \qquad (\mathrm{I})$$

$$P_T(f_{c2})=\{N_{p1}|P_1(f_{c2})|^2+N_{p2}|P_2(f_{c2})|^2\}^{1/2} \qquad (\mathrm{II})$$

where, $P_1(f_{c1})$, $P_2(f_{c2})$ are the values of the frequency components due to the colliding particles 1, 2. Consequently, their sound pressure levels are given by

$$L_p(f_{c1})=10\log\{N_{p1}|P_1(f_{c1})|^2+N_{p2}|P_2(f_{c1})|^2\} \qquad (\mathrm{III})$$

$$L_p(f_{c2})=10\log\{N_{p1}|P_1(f_{c2})|^2+N_{p2}|P_2(f_{c2})|^2\} \qquad (\mathrm{IV})$$

Therefore, the gradient S_1 of the straight line joining the level values f_{c1} and f_{c2} in the frequency spectrum of the collision sound can be expressed by the following equation.

$$S_1=\frac{L_p(f_{c1})-L_p(f_{c2})}{f_{c1}-f_{c2}}=\frac{1}{f_{c1}-f_{c2}}10\log \times\{\frac{N_{p1}|P_1(f_{c1})|^2+N_{p2}|P_2(f_{c1})|^2}{N_{p1}|P_1(f_{c2})|^2+N_{p2}|P_2(f_{c2})|^2}\} \qquad (\mathrm{V})$$

Substituting in Eq. (V) the ratio of the numbers of particles κ_p $(=N_{p1}/N_{p2})$ results in Eq. (18).

Nomenclature

D_p	: particle diameter	[m]
E_p	: Young's modulus	[Pa]
f_c	: characteristic frequency	[kHz]
G_N	: power spectrum of a series of waveforms of impulsive force	[N^2]
$g(\omega)$	: frequency spectrum of the impulsive force due to a particle	[N]
h_p	: thickness of plate	[m]
$I(f_c)$	: impulsive force level due to particles on a frequency spectrum	[dB]
i	: imaginary unit	[−]
$L_p(f_c)$	: sound pressure level due to particles	[dB]
m	: mass of a particle	[kg]
N_p	: number of particles (=2N + 1)	[−]
N_T	: total number of particles	[−]

n, n' : an integer [−]

$P(f)$: frequency spectrum of sound pressure due to a particle [Pa]

Q : mass flow rate [kg/s]

$q(\tau)$: distribution function of τ [−]

S_1 : gradient of frequency component of frequency spectrum [db/kHz]

$S(\omega)$: frequency spectrum of impulsive force due to particles [N]

T_c : impact duration between a particle and plate [s]

T_o : observation time of sound [s]

T_p : interval of collision between a particle and plate [s]

t : time [s]

v_0 : impact velocity [m/s]

Δt : increment time [s]

κ_p : ratio of particles number ($=N_1/N_2$) [−]

ν : Poisson's ratio [−]

ρ : density of a plate [kg/m^3]

ρ_p : density of particle [kg/m^3]

σ : standard deviation [−]

τ : time difference [s]

ω : angular frequency [rad/s]

<Subscripts>
1 =particle (1)
2 =particle (2)

Literature cited

1) Akay, A.: *J. Acoust, Soc. Am.*, **64**, 977 (1978)
2) Hidaka, J., A. Shimosaka and S. Miwa: *Funtaikogakkaishi* [to be published]
3) Igarashi, A., M. Goto and S. Kawasaki: *Nihon kikaigakkai Ronbunshu (C)*, **50**, 840 (1984)
4) Igarashi, A. and Y. Aimoto: *ibid*., **50**, 1799 (1984)
5) Igarashi, A. and S. Sasaoka: *ibid*., **51**, 3065 (1985)
6) Miyawaki, K.: "Zatsuon Kaiseki", p. 167, Asakurashoten (1978)
7) Nakagawa, N., R. Kawai and N. Nakamura: *ibid*., **51**, 1786 (1985)
8) Sakata, M., M. Nakagawa and M. Endou: *ibid*., **45**, 414 (1979)
9) Takahagi, T., M. Yokoi and M. Nakai: *J. Acoust. Soc. Jpn (E)*, **1**, 121 (1980)
10) Tokita, Y.: *Nihon Onkyogakkaishi*, **16**, 170 (1960)
11) idem: *ibid*., **17**, 116 (1961)

Separation of Asbestos Fibers by Length — Procedure for Obtaining Different-length Samples for Biological Experiments —†

Toshihiko Myojo and Norihiko Kohyama
*National Institute of Industrial Health, The Ministry of Labor,**

Abstract

A size-selective procedure has been developed in order to obtain samples of asbestos fibers of different lengths for use in biological experiments. Short chrysotile fibers less than 5 μm in length are widely suspected to be less carcinogenic than longer fibers. The bulk sample of U.I.C.C. standard asbestos (Chrysotile B) was aerosolized using a 2-component fluidized bed. It was then separated in a dry state by wire screens (200 mesh and 635 mesh) and a virtual impactor with a cut-off point of 2 μm.

0.1 g (sufficient weight for in-vitro tests) of a short-fiber fraction that passed through the wire screens and then onto the fine side of the virtual impactor, and 1.5 g of a medium fraction that passed through the 200 mesh screen but did not pass through the 635 mesh screen, were obtained from about 20 g of raw material. The length distribution of the short fiber fraction was 81% of fibers less than 5 μm long and 96 % of fibers less than 10 μm long. X-ray diffraction analysis revealed that the crystallinity of the separated chrysotile did not change markedly. The present dry and mild separation process that was developed thus successfully avoids any artificial change in the physicochemical properties of asbestos fibers.

1. Introduction

The Carcinogenesis of asbestos has been widely recognized and that of other fibrous materials has been suspected. At present, the causes have been only partly identified and it is considered that a search for the causes will directly determine the direction of the search for substitutes for asbestos, which is attracting the attention of engineers and the industry. Asbestos is a natural mineral, pound with various mineral species, and is available in a wide range of compositions and sizes depending on the production locations. As a promotion of the studies of the biological effects of asbestos, the international conference on the biological effects of asbestos held in New York in 1964 adopted a resolution advocating the preparation of standard reference samples of asbestos dust. At the request of the conference participants, by 1966 five types of U.I.C.C. standard reference samples (International Union against Cancer Standard Reference Samples), namely Chrysotile A (product of Rhodesia), Chrysotile B (product of Canada), Crocidolite, Amosite, and Anthophylite, were produced. Each of the five U.I.C.C. standard reference asbestos samples were prepared in 500 kg packages to meet the requirements of research organizations throughout the world, to which they are available in packages of 500 g or 50 g. In this way, the U.I.C.C. standard reference asbestos samples became standard samples for the studies of its biological effects and have been popularly used in *in vivo* and *in vitro* experiments. From these studies of the biological effects, which represent one of the causes of carcinogenesis, a hypothesis that "fibers which are long and thin, and remain in lungs unaltered are carcinogenic whether they are asbestos or not" has been advanced by Stanton[1,2] and Pott.[3] Stanton emphasized that fibers of 0.25 μm or less in diame-

---

* 6-21-1, Nagao, Tamaku, Kawasaki, 214, JAPAN
TEL. 044-865-6111

† This report was originally printed in *J. Soc. Powder Technology, Japan*, **27**, 804-810 (1990) in Japanese, before being translated into English with the permission of the editorial committee of the Soc. Powder Technology, Japan.

ter and 8 μm or more in length exhibit a particularly high carcinogenicity, and Pott also asserted that fibers of 0.5 - 2.5 μm in diameter and 3 - 20 μm in length are particularly carcinogenic. In order to carry out biological experiments to verify these hypotheses, such as they theory of Pott, samples of fibers of 3 μm or less in length and others of 20 μm or more in length are required in addition to the samples of 3 - 20 μm in length. This, in turn, requires a technique to separate the fibrous materials according to their length and diameter. Various methods have been tried to separate fibrous materials, but it has been difficult to obtain fine fibrous materials particularly of uniform length in a quantity (several grams) sufficient enough for biological experiments.

Stanton et al.[2] obtained samples of fibers of various lengths and diameters by varying the grinding time of their grinding machines such as ball mills and separating the fibers by sedimentation in water. Spurny et al.[4] made asbestos and glass fibers into fibrous aerosols by a vibrating type generator, and dispersed and separated them by sedimentation in water after a separation by elutoriator and cyclone. They reported that they were able to obtain several grams each of fine fibers containing 99% of 3 μm long or smaller fibers and others consisting of 100% of 10 μm long or smaller fibers. These methods are based on a separation by aerodynamic diameter of fibrous particles and are greatly dependent on the fiber diameter, and do not separate fibers directly according to their length.

On the other hand, Spurny et al.[4] indicated that in order to separate fibers by length it is most effective to use interception effects, together with the use of a uniform microsieve and to proceed in such a way that the fibers are as closely perpendicular to the flow direction as possible. They have even carried out parts of the experiments to that effect. However, Spurny et al.[4] concluded that their method involved a problem of reproducibility and needed improvements, suggesting that they could not obtain enough amount of fibers for the experiments with their methods.

A biological experiment was planned by separating fibers of 5 μm or shorter, which are supposed to be less harmful, and chrysotile of various fiber lengths from the U.I.C.C. standard reference Chrysotile B and comparing the toxicity of these fibers with that of the bulk sample. The research described in this paper was carried out as part of this experimental plan and was intended for the separation of fibers by length and obtaining the amount necessary for biological experiments. There were no specific requirements for the fiber diameter but fibers in splinter bundle form which are frequently encountered in aggregates of chrysotile fibers were eliminated.

In the plan of our biological experiment, about 1 gram of separated fiber sample is required for direct administration (*in vivo* test) to animals and about 0.1 gram for the cytotoxicity test (*in vitro* test). It is important for the samples not to be mixed with impurities during the separation process in order to obtain the same composition as that of the bulk sample, and to avoid the application of strong forces to destroy the whole or partial crystal structure. To satisfy these requirements, a fluidized bed was used to aerosolize the samples, stainless steel wire screens for sieves were used for the separation of the fibers by length, and a virtual impactor was used for the separation of fibers of small diameter. The whole method is based on dry type separation, which has the advantage of not changing the chemical composition, such as disolution of the cations. Because a physical force was applied to the samples, the crystal structure was investigated by X-ray diffraction analysis.

2. The Experimental method for Separating Fibrous Materials by Length

It has been said that it becomes very difficult to obtain the fairly amount of new U.I.C.C. standard reference asbestos now 20 years after its first appearance. In this experiment, a limited amount of the standard sample (Chrysotile B) was separated by length and a method to separate fine fibers was investigated.

2.1 Classification apparatus and method

As shown in the flow diagram of Bold Figure 1, the continuous classification apparatus used in the investigation consists of a fiber feeder (1), fluidized bed (2), wire screen for separation (4), and a virtual impactor (3). The fiber feeder (1) is of the same type as that used in our previous report[6] which chops fibers little by little in a grinder and transfers them pneumatically. The

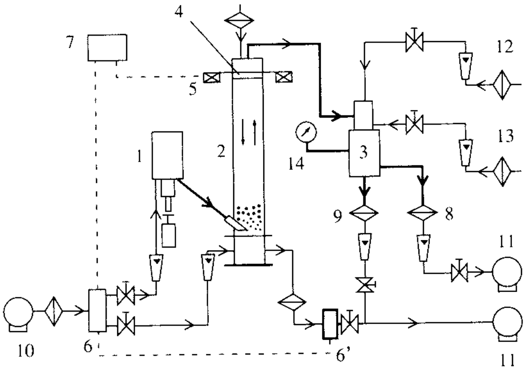

Fig. 1 Schematic diagram of classification apparatus of asbestos
(1) Fiber feeder, (2) Fluidized bed I, (3) Virtual impactor, (4) Wire screen, (5) Vibrator, (6) and (6)' Solenoid valve, (7) Controller, (8) Filter(fine), (9) Filter(coarse), (10) Compressor, (11) Vacuum pump, (12) Core air, (13) Sheath air, (14) Pressure gauge

feed rate was controlled by turning on and off the motor which pushed out the fibers towards the grinder.

The fluidized bed (2) is one of two types of fluidized beds I and II having different profiles. The fluidized bed I is of the same size as that used in our previous report[6] and is made of glass 50 mm in diameter and 500 mm high, which was used for evaluating the separation efficiency. As fluidizing particles, 100 g of 80 - 120 mesh glass beads were used after being washed sufficiently with water to prevent the migration of impurities from the glass beads to the asbestos aerosol. One wire screen (4) with openings of 78 μm (200 mesh) or 19 μm (635 mesh) was inserted in the upper part of the fluidized bed for separation.

The fluidized bed II was prepared for a continuous separation of chrysotile fibers. The inside diameter of the fluidized bed was made as large as 70 mm to provide a larger filtering area for the wire screen. In addition, because the amount of the standard sample fiber used was small, the fluidized bed was designed to produce two types of separated samples simultaneously through the use of two kinds of wire screens, which was of 78 to 19 μm and was of less than 19 μm which was further separated by the virtual impactor.

Figure 2 schematically shows the fluidized bed II. The fluidized bed is made of glass 500 mm high and contains 200 g of 80 - 120 mesh glass beads. The wire screen (1) has openings of 78 μm and the downstream wire screen (2) has opening of 19 μm. **Table 1** indicates the experimental conditions of the fluidized beds I and II.

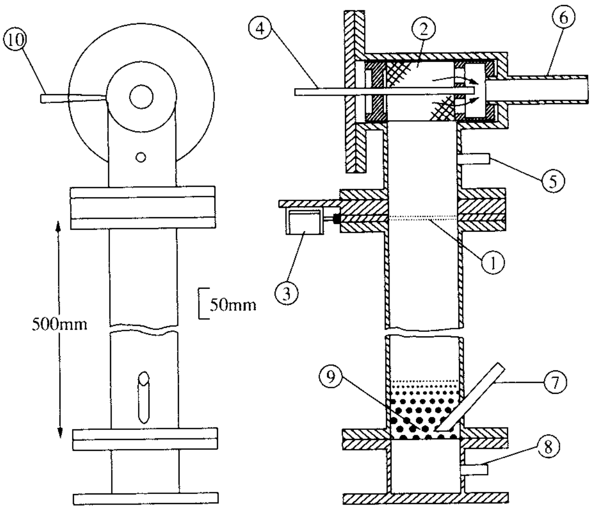

Fig. 2 Detail of Fluidized bed II.
(1) Wire screen(200 mesh)
(2) Wire screen(635 mesh), (3) Vibrator, (4) Motor shaft, (5) Clean air inlet, (6) Aerosol outlet, (7) Fiber inlet from feeder, (8) Clean air inlet for fluidizing, (9) Glass beads, (10) Fiber outlet

Table 1 Experimental conditions

Fluidized bed	I	II
Bed diameter(mm)	50	70
Air flow into F.B.(ℓ/min)	10	17.0
Air flow into feeder(ℓ/min)	6	7.5
Superfacial velocity in F.B.(m/s)	0.14	0.11
Glass beads(g)	100	200
Asbestos feed rate(mg/min)	1.8	1.4
Switching cycle of feeder ;	5s on/15s off	5s on/20s off
Fluidizing and cleaning cycle ;	110s/10s	110s/10s
Virtual impactor		
Nozzle diameter (mm)	4	
Nozzle gap (mm)	1	
Aerosol flow rate (ℓ/min)	26	
Core flow rate (ℓ/min)	29	
Sheath flow rate (ℓ/min)	9	
Fine flow rate (ℓ/min)	58.5	
Coarse flow rate (ℓ/min)	5.5	
100% cut diameter (μm)	2.0	

The aerosol was then directed to the virtual impactor (Variable Impactor manufactured by Sankyo Dengyo; hereinafter called "V.I.") indicated by numeral (3) in **Figure 1** and developed by Masuda et al.[7] and separated. The flow rate of the V.I. had been adjusted so as to obtain the particle of 2 μm in diameter for the 100% cut-off point with spherical particles having a density of 2.5 g/cm^3. These separated fibrous aerosols were trapped by membrane filters (8) and (9). The filter (8) corresponds to the fine side, where the finest fibers are collected. The flow rate between the fluidized bed and V.I. and the pressure difference were controlled by introducing clean air through the intermediate filter (5). The experimental conditions of the V. I. are also indicated in **Table 1**.

2.2 Wire screen for sieves

The wire screens of the sieves were used to separate the fibers. Compared to microsieves or nuclepore filters used by Spurny et al.,[4] wire screens with smaller openings are difficult to manufacture but they are stronger than microsieves and easy to use when shaking off the fibers, with the further advantage of a higher porosity than that of nuclepore filters. The wire screen with openings of 19 μm (635 mesh) was the finest screen available. With respect to wire screens, an investigation was made regarding the use of filtering material for spherical particles and the screening of cylindrical particles.[8] However, no investigation was made regarding the relationship between the wire screen openings and the penetration of fibrous aerosol per fiber length. In this investigation, the separated fibrous samples passing through the wire screen were confirmed by measuring the fiber sizes by scanning electron microscope (SEM).

2.3 Removal of fibers from wire screens

When filtering is continuously carried out by means of wire screens, the fibers gradually accumulate on the wire screens and lead to clogging, which requires the removal of such accumulated fibers to keep the wire screens in a regular condition. In the fluidized bed I shown in **Figure 1**, the solenoid valve (6) on the clean air supply side is closed and the valve (6') is opened to suck air into the bed and allow a temporary backflow of air in the fluidized bed. In addition, the wire screen frame is vibrated using the vibrator (5) to shake off accumulated fibers onto the fluidized particles.

In the fluidized bed II shown in **Figure 2**, fibers accumulated on the wire screens are shaken off onto the fluidized particles by allowing the air stream to flow in the reverse direction through the 200-mesh wire screen (1) as in the fluidized bed I while actuating the vibrator (3). Fibers on the 635-mesh wire screen (2) which is cylindrical and rotated by a motor are removed by the sucking force provided through the suction port (10) (Fiber outlet (10) in **Figure. 2**) on the side as described later. The fibers on the wire screen (1) are guided to the filter holder from the suction port (10) by the air stream. The fibers caught at this point are used for biological experiments designated as a sample pass through the wire screen (1) but do not pass through the wire screen (2). The connections between the Solenoid valves and the V.I. and the other overall configuration are the same as those shown in **Figure 1**. Both fluidized beds I and II repeat the process of a 110-second generation and a 10-second shake-off. The cyclic operation and condition monitoring of the whole apparatus were carried out by a microcomputer, and the apparatus was operated nearly unattended.

Figure 3 shows the air-stream direction at the time of generation (fluidizing) and shake-off (cleaning) of the fluidized bed II. In the fluidizing process (a), chrysotile fibers dispersed in the fluidized bed ascend at low speed together with the air stream and pass through the 78 μm-opening stainless steel wire screen 1 from the bottom, then pass through the cylindrical 19-μm opening wire screen 2 from the outside to the inside, and finally are sucked into the V.I. at a rate of 26 l/min. In this case, the fibers may be caught by the wire screens due primarily to the interception effects.

In the cleaning process (b), the air stream flow is reversed by the solenoid valve, and clean air is introduced into the bed through the clean air inlet (5) of **Figure. 2** and sucked from the fluidized bed bottom and through the fiber outlet (10) on the side of cylindrical wire screen. In this case, the frame holding the wire screen (1) is shaken several times by the vibrator. The fibers accumulated on the wire screen (1) drop onto the fluidizing particles. The fibers accumulated on the cylindrical wire screen (2) are caught on the filter in a filter holder connected to the fiber outlet (10). The wire screens are cleaned as described above and the fluidizing process is repeated.

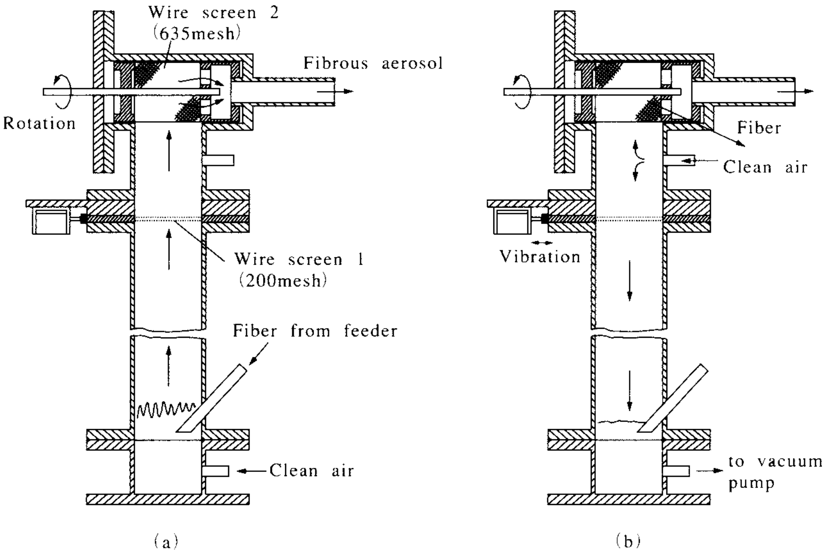

Fig. 3 Schematic diagram of Fluidizing process (a) and Cleaning process (b)

2.4 X-ray diffraction analysis

The separated chrysotile fibers were analyzed for mineral species, checked for crystallinity, and inspected for the presence and composition of contaminants. The measurement conditions were as follows:

(1) Voltage and current of a copper X-ray tube; 35 kV and 20 mA, respectively.

(2) The slit system; 1°- 1°- 0.3 mm with a graphite monochrometer.

(3) The radius of the goniometer; 185 mm, the step scanning width; 0.01°, and the scanning range; 2- 70°.

3. Results and Discussion

3.1 Experiment using fluidized bed I

The following results were obtained using the fluidized bed I through the evaluation experiments consisting of generation and separation. **Figure 4 (a)** shows a SEM photomicrograph of asbestos flowing out from the fluidized bed when no wire screens were used. Considerably long fibers or bundle-form fibers were seen and the long fibers were meandering, which are quite similar with the fibers contained in the bulk U.I.C.C. Chrysolite B. In addition, the distribution range of these fiber lengths was very wide, denying the accurate measurements by SEM.

Figure 4 (b) shows fibers which pass through 19 μm-opening wire screens and are caught on the coarse particle side of the V.I. Some fine fibers are included but fibers with large diameters and spherical particles are predominant.

Figure 4 (c) is a photomicrograph of the fine side of the V.I. Most of the fibers are shorter than 30 μm long. According to Burke and Esmen,[9] when the aspect ratio (length/diameter) is 10, the fibers are separated with a fiber diameter of about 1/3 the cut-off point of 2 μm of V.I. A comparison between **Figures 4 (b)** and **4 (c)** indicates that the V.I. separation greatly depends on fiber diameter. **Figure 4 (d)** represents a photomicrograph of fibers which pass through a wire screen of 78 μm-opening and caught on the fine side of the V.I. indicating the existence of long fibers exceeding 100 μm but there are no fibers nor fiber aggregates having both a big length and a large diameter.

Figure 5 shows the fiber length distributions measured on the fibers on **Figure 4 (c)** and **(d)**. The fibers on **Figure 4 (c)** passing through the 19-μm-opening wire screen are nearly of the desired size, in which a fiber length of less than 5 μm accounts for 81% and that of less than 10 μm for 96%. The fiber lengths distribution of the U.I.C.C. Chrysotile B measured by Timbrell[5] are also shown in this figure. These are the results obtained by optical microscope for bulk asbestos samples which were dispersed by alcohol and filtered, and the fibrous aerosol samples generated by the aerosol generator using a grinder were trapped on a filter. The fiber length distribution of the bulk samples is wide and slightly decrease after aerosolizing. This distribution is similar to that of the fibers

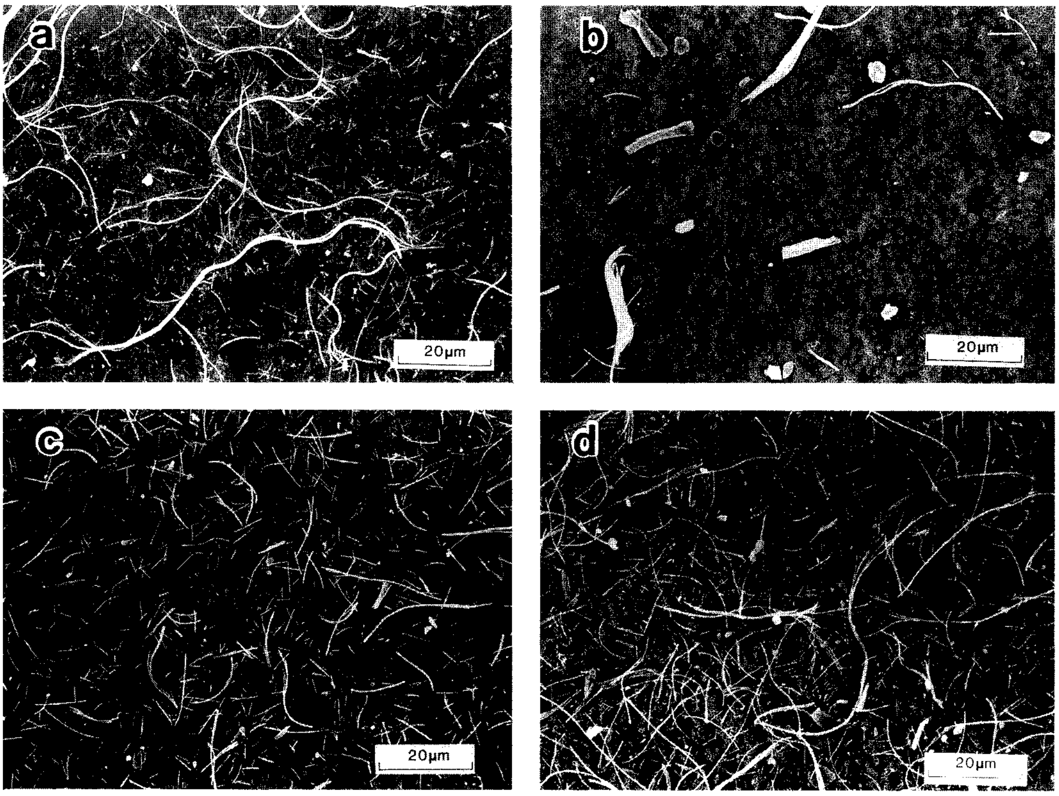

Fig. 4 SEM micrographs of asbestos (U.I.C.C. Chrysotile B)
(a) Fibers flow out fluidized bed.
(b) Fibers penetrating 635 mesh screen and V.I. coarse side.
(c) Fibers penetrating 635 mesh screen and V.I. fine side.
(d) Fibers penetrating 200 mesh screen and V.I. fine side.

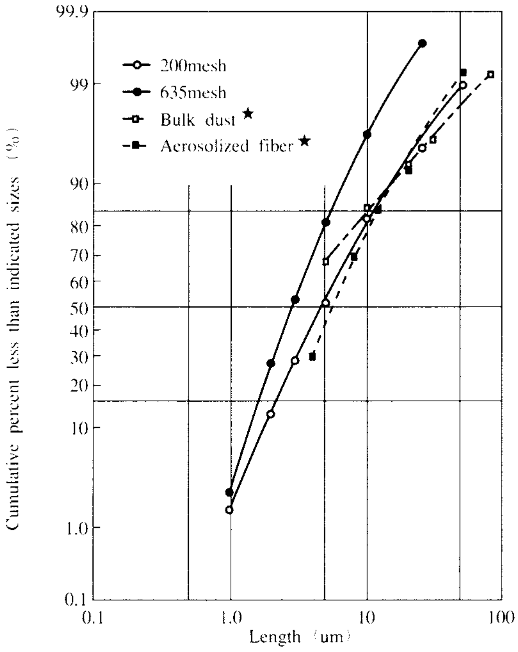

Fig. 5 Filer length distributions of U. I. C. C. Chrysotile B.
* : length distribution measured by Timbrell (5)

passing through the 78 μm opening wire screen of **Figure 4 (d)**, which was measured in this investigation. Comparing the distribution of bulk samples, that of the fibers passing through the 78 μm opening wire screen, and that of the fibers passing through the 19 μm opening wire screen, we came to the conclusion that it is possible to separate fibers by length using this method.

In order to estimate the separation efficiency, using the fluidized bed I, a 3-hour aerosol generation was carried out and the amount of asbestos caught at the lower reaches of the wire screen was measured. The generation efficiency was determined from the ratio of the amount of collected asbestos and the amount fed (0.331 g) for 3 hours estimated from the feed speed, the results of which are shown in **Table 2**. Because of the shortage of asbestos sample, results when no wire screens were used have not been obtained but considering the results for glass fibers reported earlier,[6] a generation efficiency of about 10% may be assumed, indicating that the amount of fibers passing through the wire screens is extremely small. When the V.I. is used for separation, the amount of asbestos trapped on the fine side would become further lower.

Table 2 **Generation efficiency of U.I.C.C. Chrysotile B**

No.	Screen (mesh)	Generated fiber (mg/3h)	E (%)
1	200	6.25	1.9
2	200	6.50	2.0
3	200	5.68	1.7
4	635	1.31	0.40
5	635	1.70	0.51

Fiber mass fed for 3 hours : 0.331g

3.2 Experiment using fluidized bed II

In the continuous operation using the fluidized bed II, about 0.1 g of fibers which passed through a 635 mesh wire screen and were caught on the fine side of the V.I. and 1.5 g of fibers which passed through a 200mesh wire screen but did not pass through the 635mesh were obtained using about 20 g of U.I.C.C Chrysolite B over a total period of 350 hours.

Figure 6 shows the X-ray diffraction patterns of separated fibers smaller than 635 mesh and from 200 mesh to 635 mesh, fibers in the fluidized bed, and bulk samples for Chrysotile B obtained in this investigation. Chrysotile B contains impurities of plate-form brucite and pyroaurite. The brucite and pyroaurite were collected in large quantities in the samples which passed through 200mesh screen and remarkably decreased in the samples which passed through the 635mesh screen, which was much less than that in the bulk sample. According to **Figure 4 (b)**, this may be attributed mainly to the separation process using the V.I.

In order to compare the crystallinity of each sample, the peak widths of the (002) and (004) diffraction lines observed in the vicinity of 12° (2θ) and 24° (2θ) were measured. For all samples, the decrease in crystallinity was scarcely observed as compared to that of the bulk sample as shown **Figure 7**. In particular, the fact that the crystallinity of the fibers remaining in the fluidized bed for a long time is not degraded indicates that the fluidized bed does not give any serious effect on the crystallinity unlike the grinder such as a ball mill.

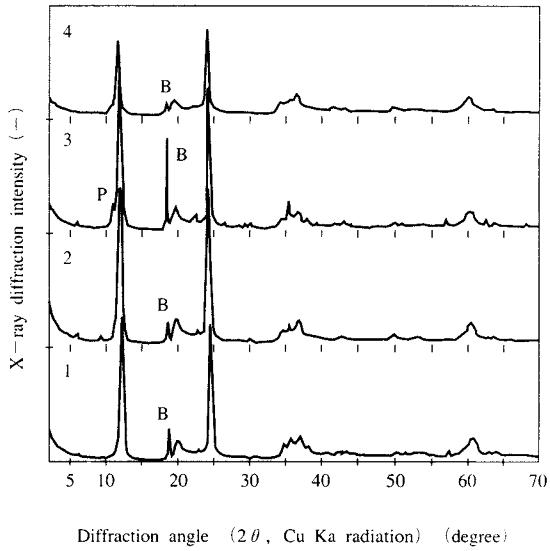

Fig. 6 X-ray diffraction pattern of Chsysotile B samples 1 : bulk sample, 2 : fibers in the bed materials, 3 : fibers penetrating 200 mesh screen, 4 : fibers penetrating 635 mesh screen and V. I. fine side, B : Brucite, P : Pyroaurite

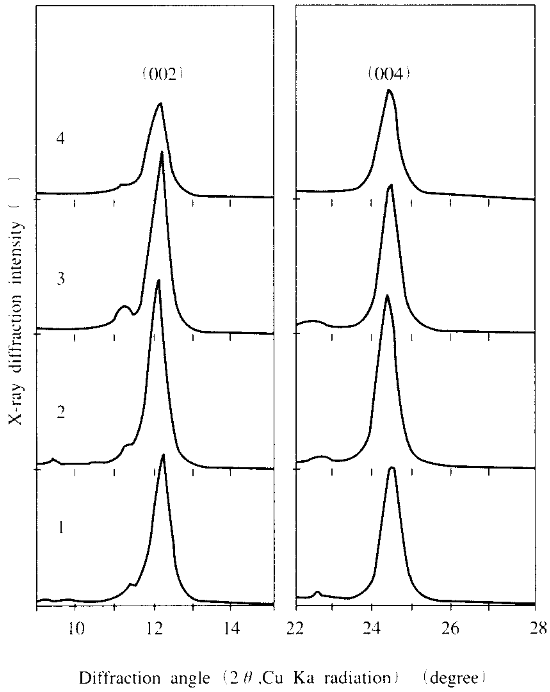

Fig. 7 X ray diffraction profile of Chrysotile B samples showing their crystallinity
(002): diffraction peak of (002) crystal plane.
(004): diffraction peak of (004) crystal plane
1 : bulk sample, 2 : fibers in the bed materials, 3 : fibers penetrating 200 mesh screen, 4 : fibers penetrating 635 mesh screen and V. I. fine side

4. Conclusion

A classification apparatus experimentally built for this investigation was operated nearly unattended, except when filling the fiber feeder with asbestos, for a total of about 350 hours and 0.1 g of asbestos fibers which passed through the 19 μm (635 mesh) opening screen and were caught on the fine side of the virtual impactor with a cut-off point of 2 μm and 1.5 g of asbestos which passed through the 78 μm (200 mesh) opening screen but were unable to pass through the 635 mesh screen were obtained from about 20 g of U.I.C.C. standard reference asbestos (Chrysotile B). The former consisted of short fibers was not enough amount for use in injection or inhalation experiments on animals but was offered for cytotoxicity tests (*in vitro* tests) and interesting results have been obtained.[10)]

Fibers obtained by this method are, in principle, not subjected to any alteration of their chemical composition since separation is carried out in a dry state, and the X-ray diffraction results have not indicated any obvious degradation in crystallinity, suggesting that the process is an superior separation method for fibrous samples to be offered for biological experiments. In addition, the fibers can be prepared as fibrous aerosols containing fine fibers, which can be directly used in inhalation tests.

In order to separate fibers using wire screens, a further quantitative investigation must be carried out in future regarding the fiber size and separation efficiency.

Acknowledgement

The authors wish to acknowledge the very substantial contribution of Dr. Kimiko Koshi, the former chief of the department of Occupational Diseases, and Dr. Kazuo Fukuda, the chief of the department of Experimental Toxicology, National Institute of Industrial Health, the Ministry of Labor, for their medicobiological advice. Additionally appreciated are the comments and suggestions of Professor Chikao Kanaoka, Material Chemical Engineering Department at Kanazawa University, on the separation technique and summarization.

References

1) Stanton, M.F., M. Layard, A. Tegeris, E. Miller, M. May and E. Kent : *J. Natl. Cancer Inst.*, **58**, 587 (1977)
2) Stanton, M.F., M. Layard, A. Tegeris, E. Miller, M. May, E. Morgan and A. Smith : *J. Natl. Cancer Inst.*, **67**, 965 (1981)
3) Pott, F. : *Staub Reinhaltung der Luft*, **38**, 486 (1978)
4) Spurny, K.R., W. Stöber, H. Opiela and G. Weiss : *Am. Ind. Hyg. Assoc. J.*, **40**, 20 (1979)
5) Timbrell, V. : Pneumoconiosis (Ed. H. Shapiro), Oxford Univ. Press, 28 (1970)
6) Myojo, T. : *Ind. Health*, **21**, 79 (1983)
7) Masuda, H., D. Hochrainer and W. Stöber : *J. Aerosol Sci.*, **10**, 275 (1979)
8) Endoh, S., J. Koga and K. Yamaguchi : *J. Soc. Powder Technol., Japan*, **20**, 8 (1983)
9) Burke, W.A. and N. Esmen: *Am. Ind. Hyg. Assoc. J.*, **39**, 400 (1978)
10) Koshi, K., N. Kohyama, T. Myojo and K. Fukuda : Environmental Research in Japan, Environmental Agency, Japan Vol. **11**, 94-1 (1986)

Fabrication of Al_2O_3/W Nanocomposites †

Tohru Sekino, Atsushi Nakahira and Koichi Niihara
*The Institute of Scientific and Industrial Research, Osaka University**
Masahiro Nawa
*Material Research & Development Laboratory, Matsushita Electric Works, Ltd.***

Abstract

The Mechanical properties and microstructure of Al_2O_3/W composites have been investigated. These composites were fabricated by hot-pressing a mixture of γ- or α-phase alumina (Al_2O_3) and fine tungsten (W) powders. In these composites, fine W particles were located both within the Al_2O_3 matrix grains and at the grain boundaries. The fracture strength of Al_2O_3/5vol%W composites sintered at 1400°C was 700 MPa, which is approximately 1.6 times higher than that of monolithic-Al_2O_3 prepared by way of the same processing method. But, the strength decreased with an increase in the sintering temperature. Although the interactions between cracks and W dispersion were partly observed, the fracture toughness was not significantly enhanced. It is believed that the presence of nanostructures do not sufficiently act on the mechanical properties of the composites because the grain boundary of the Al_2O_3 matrix where large W particles are located is not significantly strengthened by dispersion.

1. Introduction

In order to extend the range of application of ceramic materials which have high-strength and good thermal and/or chemical stabilities, it is necessary to further improve their mechanical properties. To this end, many efforts have been made to obtain an improved microstructural control of monolithic ceramics or to develop composites in which second phase was dispersed as particles, whiskers or fibers. However, most composite systems are ceramic/ceramic composites and only few reports deal with ceramic materials consisting of heterogeneous materials. In the present work, we examined the effect of the dispersion of a metal phase in ceramics for the improvement of their mechanical properties.

Cermet and/or functionally gradient materials are well known in the field of ceramic/metal composites[1-3]. However, metallic phases in these composites are mainly micrometer-level features and/or used as binding phases. For further extensions of such ceramic/metal composites to new applications, a significantly improved control of their microstructural development as well as the strength of the heterogeneous interfaces, are necessary.

Recently, oxide/non-oxide ceramic nanocomposites such as Al_2O_3/SiC[4], Al_2O_3/Si_3N_4[5] and MgO/SiC[6], and non-oxide/non-oxide nanocomposites, i.e. Si_3N_4/SiC[7] have been developed. It is reported that the mechanical properties of these nanocomposites, for example a fracture strength up to at high temperatures and fracture toughness, are significantly improved as a result of an improved control of both the nanostructure and the interface modification[4-8]. Following this newpoint, we applied such a technique, which has been developed for ceramic/ceramic composites, to a ceramic/metal composie system. It is expected for ceramic/metal nanocomposite systems, to

---

* 8-1 Mihogaoka, Ibaraki, Osaka 567, JAPAN
TEL. 06-877-5111 Ext. 3537

** 1048 Kadoma, Osaka 571, JAPAN
TEL. 06-908-6735

† This report was originally printed in *J. of Japan Society of Powder & Powder Metallurgy*, **38**, 326 (1991) in Japanese, before being translated into Englith with the permission of the editorial committee of the Soc. of Powder & Powder Metallurgy.

obtain not only the above-mentioned properties but also the contribution of the key-properties of the metal phase in the toughening and strengthening of the ceramic matrix.

In this work, we selected Al_2O_3 as a ceramic matrix, which is a well known material in the field of ceramic/ceramic nanocomposites, and tungsten (W) as a dispersed metallic phase. Hing[9-10] first reported the mechanical properties of Al_2O_3/W composites of various sizes of W particles' dispersion. These mechanical properties, however, were not significantly improved over the monolithic-Al_2O_3. In this work, we attempted to enhance the mechanical properties by using fine raw powders and combining them on a nanometer level with Al_2O_3 ceramics. The fabrication of Al_2O_3/W composites and the relationship between their mechanical properties and microstructures /will/ be discussed herein.

2. Experimental Procedure

Commercially available high-purity γ-Al_2O_3 powders (Asahi Chemical Co., particle-size less than 0.4 μm), α-Al_2O_3 powders (Sumitomo Chem. Co., AKP-30, particle-size less than 0.4 μm) and W powders (Nippon Tungsten Co., particle-size less than 0.6 μm) were selected as prime materials. The starting Al_2O_3 powder which contains 5% per volume of W was mixed using a conventional ball-milling technique with alumina balls immersed in ethanol or acetone for 24 hours. The mixture was thoroughly dried in vacuum by a rotary evaporator, and dry-ball-milled for 24 hours. During wet- and dry-milling, the pot was filled up with Ar gas to prevent the oxidation of the W powder. The mixture was hot-pressed at a temperature range of 1400 - 1800°C under an applied pressure of 30MPa for 1 hour in Ar atmosphere using a circular or rectangular graphite-die. The sintered bodies were cut, grounded with a diamond wheel and polished consecutively with 9 μm, 2 μm and 0.5 μm diamond pastes. The edges of the specimens were reveled at 45°. The final specimen size was $3 \times 4 \times 37$ mm.

The crystalline phases were identified by X-ray diffraction analysis (Cu-Kα radiation). The density of the specimens was measured by Archimedes method in toluene. The fracture strength was evaluated using a 3-point bending test at room temperature (span 30 mm and cross-head speed 0.5 mm/min). The fracture toughness was measured by indentation fracture (IF) method with Vickers indentation (144N-load applied for 15 sec.). The Young's modulus was determined by the resonance-vibration method using the 1st-mode resonance. Micro- and nanostructures, fracture surface and crack profiles introduced by Vickers indentation were observed by scanning electron microscopy (SEM).

Table 1 Fracture toughness (K_{IC}), Vickers hardness (H_V) and Young's modulus (E) of Al_2O_3/W composites.

Composition (vol%)	H.P.temp. (°C)	K_{IC} (MPa•m$^{1/2}$)	Hv (GPa)	E (GPa)
0.0	1400	4.37	19.6	389
	1500*	3.89	18.1	390
5.0	1400	4.63	16.3	389
	1400*	3.34	18.6	383
	1500*	3.73	17.9	387
	1600	4.57	17.6	392

Note : *Hot-pressed by rectanglar-die

3. Results and Discussion

Fig. 1 shows the X-ray diffraction patterns of Al_2O_3/5vol%W composites. When γ-Al_2O_3 was used as a prime powder and sintered at 1400°C, $AlWO_4$ and an unknown-phase were found as by-products as shown in **Fig. 1a**. At a hot-pressing temperature of 1500°C (**Fig. 1b**), the unknown-phase still remained in the composite although no formation of $AlWO_4$ was observed. The simple diffraction pattern of the unknown-phase may suggest that this phase is highly preferentially oriented in the specimen. Further experiments are required for the understanding of the crystallographic and morphological details of this unknown-phase. On the other hand, no by-products were observed in any hot-pressing conditions when α-Al_2O_3 was used as a prime material (**Fig. 1c**).

Fig. 2 shows the variation of density with the sintering temperature for the Al_2O_3/5vol%W composite. The density decreased with an increase in the hot-pressing temperature when γ-Al_2O_3 was used as a starting powder. This seems to be due to the formation of low-density by-products such as $AlWO_4$ and the unknown-phase. When α-Al_2O_3 was selected as a starting powder, however, a nearly full density (above 98.5% of the theoretical value) was

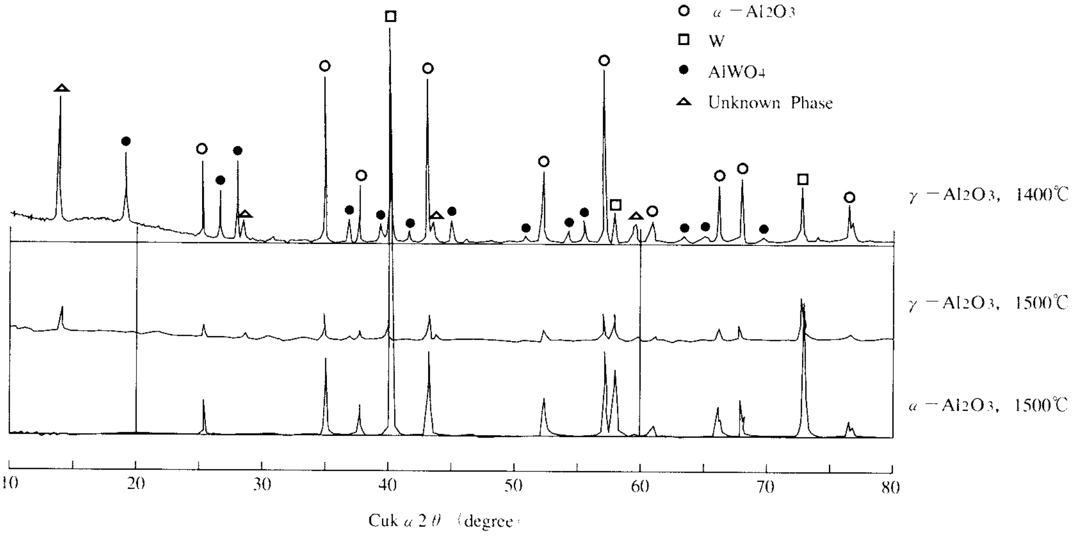

Fig. 1 Variation of the X-ray diffraction pattern with prime powders of Al_2O_3/5vol%W composites. The types of prime Al_2O_3 powders and sintering temperatures are, a: γ-Al_2O_3, 1400°C, b: γ-Al_2O_3, 1500°C and c: α-Al_2O_3, 1400°C.

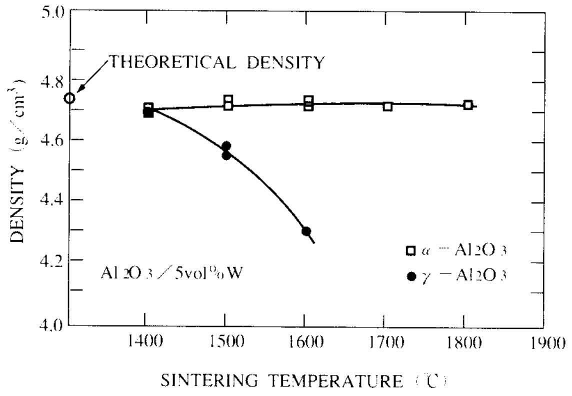

Fig. 2 Variation of density with sintering temperature and prime materials (γ- and α-Al_2O_3) of Al_2O_3/5vol%W composites.

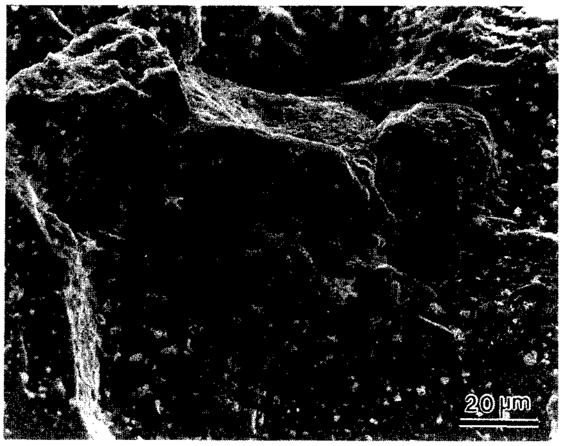

Fig. 3 Fracture surface of Al_2O_3/5vol%W composite fabricated with the use of γ-Al_2O_3 as a prime powder.

achieved.

Fig. 3 shows a SEM image of the fracture surface for the specimen which was prepared using a mixture of γ-Al_2O_3 and W. This composite was fairly fragile and fractured easily. The Al_2O_3 matrix grains grew up to several tens of microns. Although the dispersed W particles were located both within the matrix grains and at the grain boundaries, platelets or pillar-like species which might be produced during sintering were observed. Some cavities were also found around the W particles dispersed at the grain boundaries. It is suggested that the interface between the W particles and the Al_2O_3 matrix is not the most appropriate one. The formation of a liquid phase was also observed at the grain boundaries of this specimen. In the Al_2O_3-WO_3 binary system, bi-oxides which have eutectic temperatures of 1230°C and 1190°C have been reported[11]. Thus, it is speculated that such bi-oxides having low melting points are concerned with the formation of the liquid phase during sintering of this composite. The fact that Al-W-O bi-oxide was produced only when γ-Al_2O_3 was used as a prime material should be considered as follows: The W powder was much finer and has a higher activity. Consequently, the W particles were oxidized by the hydroxyl which was chemisorbed on the surface of the γ-Al_2O_3 powder depending on this larger specific surface area and the higher reactiveness of the γ-Al_2O_3. From the facts described above, the brittleness and low strength of the specimen fabricated by using γ-Al_2O_3 and W powders may be attributed to the formation of the Al-W-O bi-oxide and its existence at the grain boundaries of the composites.

Fig. 4 shows a SEM picture of the composite hot-pressed by using γ-Al_2O_3 and W mixed powders. In this specimen, the fine nanometer-sized W particles were located both within the Al_2O_3 matrix grains and at the grain boundaries. Larger particles (about 1 to 2 μm in diameter) were mainly located at the grain boundaries. Hence, it is speculated that the Al_2O_3/W composite has both micro- and nanostructures. Although by-products, which were observed when γ-Al_2O_3 was used, were not found in the composites prepared from α-Al_2O_3 and W powder mixtures, some pores were observed at the Al_2O_3/W/Al_2O_3 triple point.

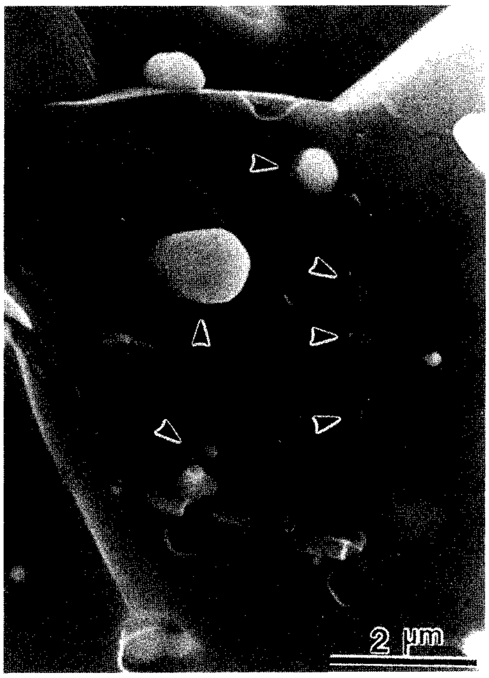

Fig. 4 SEM photograph of the Al_2O_3/5vol%W composite. Fine W particles are dispersed within the matrix grains and at the grain boundaries. Arrows indicate W particles.

The fracture strength was evaluated only for the composites fabricated from the mixture of α-Al_2O_3 and W powders because the specimens prepared by using γ-Al_2O_3 were highly fragile as described above. The sintering temperature dependence of the fracture strength for the Al_2O_3/5vol%W composites is shown in **Fig. 5**. An average strength value of 700 MPa (* maximum of 811 MPa) was achieved in specimens hot-pressed at 1400°C and was about 1.6 times higher than that of monolithic-Al_2O_3 prepared under the same condition. This strength is higher than that reported for Al_2O_3/W composites in previous works[9-10] (450 MPa). When the hot-pressing temperature was increased over 1700°C, however, the strength decreased until about 200 MPa.

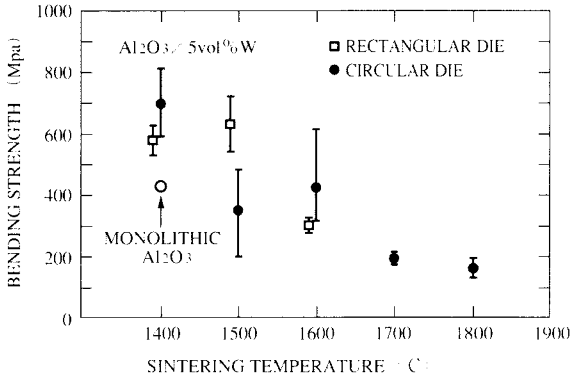

Fig. 5 Variation of fracture strength with sintering temperature for Al_2O_3/5vol%W composites.

Fig. 6 shows the fracture surfaces of the Al_2O_3/5vol%W composites hot-pressed at 1400 and 1600°C. The grain size distribution of the Al_2O_3 matrix in each composite was uniform. Both trans- and intergranular fractures were observed in specimens hot-pressed at 1400°C which also showed a high strength. On the other hand, the composite sintered at 1600°C had large matrix grains and exhibited only intergranular fractures (**Fig. 6b**).

The average grain size of the Al_2O_3 matrix, which was measured by a line-interception method, increased from 1 μm to about 8 μm with an increase in the hot-pressing temperature from 1400°C to 1800°C, while remaining unchanged at smaller respective values measured for monolithic-Al_2O_3. This effect is attributed to the fine W particle dispersion. In previous reports concerning Al_2O_3/SiC nanocomposites, the formation of a sub-grain boundary within the Al_2O_3 matrix grains due to the dispersion of nanometer-size SiC particles was reported[4,8]. Furthermore, it was also reported that the composites' high strength was maintained even when the matrix grains grew significantly because of some nano-dispersion effects such as the formation of the facet plane at the Al_2O_3-SiC interface[4,8]. In the Al_2O_3/W composite system, the specimens which were sintered at higher temperatures and had large matrix grains exhibited also the lowest fracture strength. The relation between strength and grain size of the composites almost complied with the Hall-Petch's law. A behavior similar to monolithic and/or micro-composites materials[12,13]. Thus, the increment of strength found only in composites sintered at low temperatures are mainly attributed to the inhibition of grain growth of the Al_2O_3 matrix in the presence of W dispersion. However it seems that the nano-dispersion effects are not significant in the present Al_2O_3/W composites.

The Al_2O_3/W composites fabricated in this work were difficult to polish in comparison with other ceramic composites, and the Al_2O_3 grains dropped out easily. This behavior is remarkable in specimens with large matrix grains. Mechanical property measurements were carried out for composites in which a sufficient polishing of the surfaces was obtained. **Table 1** shows the fracture toughness, hardness and Young's modulus of the Al_2O_3/5vol%W composites. Almost all of these values were nearly equal to those of the monolithic-Al_2O_3. The fracture toughness and hardness were, however, strongly affected by the shape of the graphite-die which was used during hot-pressing. The toughness of the specimens sintered by using a circular-die showed higher values than those when a rectangular-die was used.

Fig. 7 shows a SEM picture of crack propagation on a Al_2O_3/5vol%W composite introduced by Vickers indentation. In comparison with the monolithic-Al_2O_3, the crack propagated at the grain boundary with microscopical deflection. Furthermore, some interactions between cracks and dispersed particulates[14-16] such as pulling-out of the large W particles and crack-deflection by the W particles were observed.

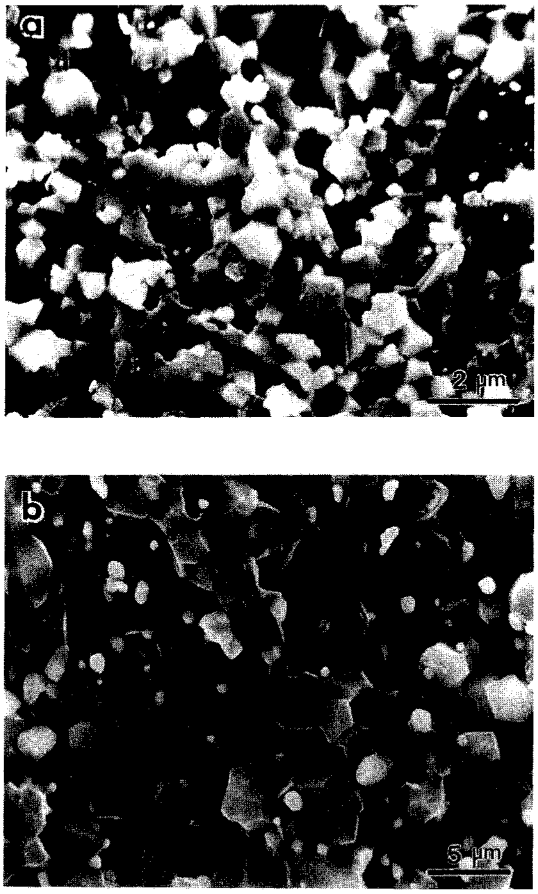

Fig. 6 SEM photographs of the fracture surfaces of Al_2O_3/5vol%W composites. a) Sintered at 1400°C and b) at 1600°C.

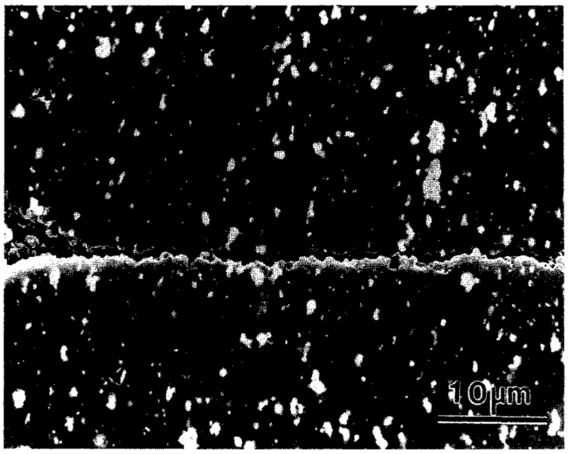

Fig. 7 Propagation behavior of cracks induced by Vickers indentation for Al_2O_3/5vol%W composites sintered at 1400°C.

From the above-mentioned results and the above-mentioned fact of an easy dropping-out of grains, it is belived that the bonding between Al_2O_3 matrix grains and large W particles is not strong enough. This indicates that a further control of the matrix-matrix and matrix-metal interfaces is required.

Although nanometer-size W particles dispersed within the Al_2O_3 matrix grains and W particles interacted with the propagating crack, the toughness in the present Al_2O_3/5vol%W composites was not significantly enhanced. It is considered that the effects of the nanocomposites[4-8], which are generated by the nanometer-size dispersion, such as crack attraction into the matrix grains, are inhibited by the weak interface bonding as in the above-mentioned results.

4. Conclusion

Low density and by-products were observed when Al_2O_3/W composites were fabricated using γ-Al_2O_3 and W powder mixtures. On the other hand, Al_2O_3/5vol%W composites with a nearly full density were fabricated by hot-pressing a mixture of α-Al_2O_3 and W powders. In these specimens, the fine W particles were dispersed both within the Al_2O_3 matrix grains and at the grain boundaries, while the larger ones were located only at the grain boundary. Thus, these Al_2O_3/W composites were found to have both micro- and nanostructures. It is recognized that ceramic/metal nanocomposites can be fabricated by the conventional powder-metallurgical method. A fracture strength of about 700 MPa was found for Al_2O_3/5vol%W composite which is 60% higher than that of monolithic-Al_2O_3. This increase in strength is mainly attributed to the grain-growth inhibition by the W dispersion. Interaction was observed between cracks and dispersed W particles, bonding at the Al_2O_3-W interface was, however, not strong. Thus, the nano-dispersing effects of metal particles into Al_2O_3 ceramics are not clearly observed in this composite system. For further improvement of the mechanical properties, it is required to disperse much finer metal particles within the Al_2O_3 matrix grains and at the grain boundaries, and to modify the interface structure, for example, by using sintering additives.

Acknowledgements

The authors acknowledge the financial supports of the Ministry of Education, Science, and Culture provided under a Grant-in-Aid for Scientific Research (Nos. 01647001 and 02205088), the Asahi Glass Foundation for their Grant-in-Aid for Research, and the Tanigawa Foundation for their Thermal Technology Promotion, for the achievement of this investigation. The authors wish to thank Mr. T. Ishibashi for his contribution in the TEM experiment, and also Dr. G. Pezzotti with his useful discussion.

References

1) A. K. Khaund and P. S. Nicholson, J. Mater. Sci., **15** (1980), 177.
2) M. Shinno, T. Hirai and R. Watanabe, J. of Composite Soc. of Japan, **13** (1987), 257.
3) M. Shinno, J. of Japan Soc. of Powder and Powder Metall., **37** (1990), 241.
4) K. Niihara, A. Nakahira, G. Sasaki and M. Hirabayashi, in Proc. of MRS Int'l. Mtg on Adv. Mater., (Plenum Press, Tokyo, 1988) p.129.
5) A. Nakahira, K. Niihara, J. Ohkijima and T. Hirai, J. of Japan Soc. of Powder and Powder Metall., **36** (1989), 239.
6) K. Niihara, A. Nakahira, H. Ueda, and G. Sasaki, in Proc. 1st Japan SAMPE Symp., (Plenum, Chiba, 1989) p. 1120.
7) K. Niihara, J. of Japan Soc. of Powder and Powder Metall., **37** (1990), 348.
8) K. Niihara, T. Hirano, A. Nakahira, K. Ojima, K. Izaki, and T. Kawakami, in Proc. of MRS Int'l. Mtg on Adv. Mater., (Plenum Pless, Tokyo, 1988) p. 107.
9) P. Hing, Sci. of Ceram., **10** (1980), 521.
10) P. Hing, Sci. of Ceram., **12** (1984), 87.
11) J. L. Warning, J. of Am. Ceram. Soc., **48** (1965), 494.
12) S. C. Carniglia, J. of Am. Ceram. Soc., **55** (1972), 243.
13) H. H. Bache, J. of Am. Ceram. Soc., **53** (1970), 654.
14) K. T. Faber and A.G. Evans, Acta. Metall., **31** (1983), 565.
15) A. G. Evans and T. G. Langdon, in Progress in Materials Science, Vol. 21, (Plenum Press, 1976), 275.
16) S. Wiederhorn, Ann. Rev. Mater. Sci., **14** (1984), 373.

Information Articles

Symposiums on Powder Technology

The 26th Symposium on Powder Technology, and the third Hosokawa Symposium on Powder Technology were held at the Sunshine Prince Hotel and the conference room of the Tokyo Sunshine Building, respectively, under the auspices of the Couneil of Powder Technology (Japan) and sponsored by Hosokawa Powder Technology Foundation during the period of August 26 to 27, 1992.

On the first day, the third Hosokawa Symposium on powder Technology was held. This time, the lectures and discussions focused upon "Powder Material Processing and Mechano-chemistry" as the main theme.

On the second day, the 26th Symposium on Powder Technology was held. As is well known, computer simulation techniques have recently become a popular vehicle for research and development, because of the advances made in computers and the drop in their price. Consequently, attention is being paid to computer simulation techniques as a flexible method for mathematical analysis, the application of which was difficult to powder technology in the past. In view of such a tendency, the "Application of Computer Simulation to Powder Technology" was adopted as the main theme, and five interesting lectures were delivered, followed by active discussions.

Both symposiums were very active and successful, thanks to the attendance by so many enthusiastic people.

The 3rd Hosokawa Symposium on Powder Technology
Powder Material Processing and Mechano-chemistry

Lectures and Discussions

Chairmanship : Toshio Oshima (Himeji Institute of Technology)

● Soft Mehcano-chemistry	Mamoru Senna (Keio University)
● Alloy Structure and Characteristic Control with Mechanical Alloying	Kenji Suzuki (Tohoku University)

Chairmanship : Tetsuo Yoshida (Hosokawa Powder Technology Foundation)

● Sintering Behavior of Ceramic Powder and Mechano-chemistry	Osami Abe (Ibaragi University)
● Phermaceuticals and Mechano-chemistry	Keiji Yamamoto (Chiba University)

- General Discussion

Chairmanship : Yoshitaka Kuwahara
(Goverment Industrial Research Institute, Nagoya)

The 26th Symposium on Powder Technology

Application of Computer Simulation to Powder Technology

Session I Application of Computer Simulation (1) (powder flow, collection)

Chairmanship : Yasuo Kousaka (University of Osaka Prefecture)

● Latest Development of Powder Granule Simulation : Phenomenon of Fluidized Granules (Lecture via animation film)	Yutaka Tsuji (Osaka University)
● Application of Computer Simulation for Particle Collection	Hideto Yoshida (Hiroshima University)

Session II Application of Computer Simulation (2) (molding, pulverizing, sound absorption)

Chairmanship : Kei Miyanami (University of Osaka Prefecture)

● Computer Simulation for Behavior of Powder Molding	Susumu Shima (Kyoto University)
● Appilication of Simulation for Pulverizing	Toyokazu Yokoyama (Hosokawa Micron Corp.)
● Simulation Using Sound Absorption Characteristics of Powder Bed and Distribution Constant Circuit	Yuzo Okuyama (Matsushita Electronic Works, Ltd.)

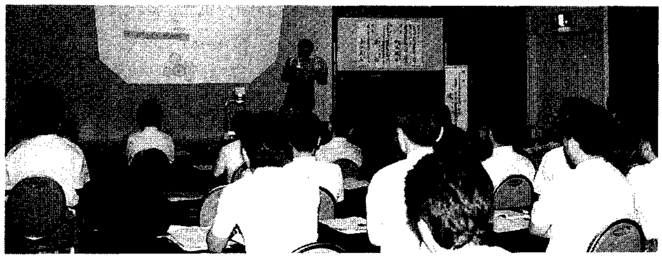

The 2nd KONA Award

The "KONA Award System" founded by Hosokawa Micron Corporation in 1990 has been inherited by Hosokawa Powder Technology Foundation. This time, the second KONA Award was given to Professor Hisakazu Sunada, Pharmacy Faculty of Meijo University, after the decision by the board of directors on the recommendation of the Award Committee.

The KONA Award is given to those scientists who have achieved excellence in research related to powder technology. This time, the Professor's long-term work regarding the packing and aggregation of powder particles, and granulation was highly evaluated.

On October 7, 1992, Mr. M. Hosokawa, President of Hosokawa Powder Technology Foundation, presented him with the KONA Award at the commemorative presentation ceremony for presenting funds and subsidies that was held at the R & D Center of Hosokawa Micron Corporation in Hirakata, Japan.

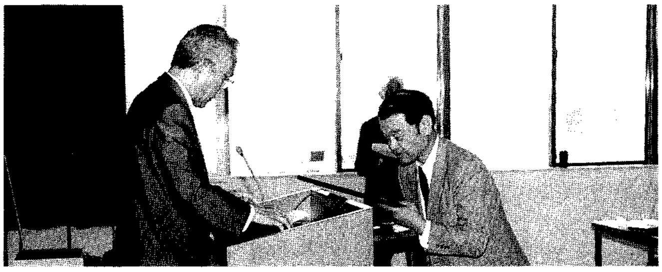

Academic publication concerning powder technology in Japan (1991)

Jouraul of the Society of Powder Technology, Japan Vol. 28 (1991)

Title	Author (s)	page
<**Original Report**>		
● Continuous Vibro Fluidized-bed for the Agglomeration of Milk Powder	S. Kudoh, I. Toyoda, J. Koga, S. Matsumoto and I. Inoue	11— 17
● On a Shape Index and Rolling Frictional Characteristics of Irregular Particles	K. Yamamoto, T. Hama and M. Sugimoto	18— 26
● On the Particle Cut Size of Cyclone Dust Collector (Part 3)—Relationship between the Particle Cut Size d_c and the Equilibrium Particle Size d_{R-E}—	K. Ikemori	27— 33
● Parameters of the Sound Due to the Impact of a Particle on a Circular Plate	J. Hidaka, H. Ito, A. Shimosaka. and S. Miwa	78— 84
● The Effect of the Fine Grinding of Additives on Sheet Formation and the Sintering of Ceramic Dielectrics	I. Koshika, K. Tanaka, I. Inada and K. Wakino	150— 154
● Computer Simulation of the Expansion of a Bed Packed with Different Particles	M. Nakamura, T. Akita, T. Yamagata T. Kimura and T. Togaya	155— 160
● Agitating Granulation and Coating under Reduced Pressure	K. Terashita, M. Kato, Y. Furuichi and K. Miyanami	161— 166
● The Operating Parameters and Powder Characterization of the Spray-bag-dryer	H. Takahashi, H. Masumura and S. Iwaya	167— 171
● Measurement of Contact Potential Difference between a Powder Bed and a Metal···	H. Yoshida, T. Fukuzono and H. Masuda	226— 231
● The Agglomeration Characteristics of Damp Powders in a Tapping Type Gyratory Agglomerator	I. Sekiguchi and Y. Ohya	232— 238
● The Simultaneous Operation of Granulation, Grinding and Separation by a Continuous Rotating Conical Vessel —The Effect of Operating Conditions on the Granule Shape—	M. Sugimoto, M. Sugihara N. Yokota and T. Hayashida	300— 306
● A Reduction in the Pulsating Wall Pressure Near the Transition Point in a Bin —The Effect of Widening the Bin Cylindrical Section—	R. Noriyama and T. Jotaki	307— 311
● Distribution of Void Fraction in a Powder Layer Formed on Filter Paper by Dust Collection	Y. Mori and T. Fujita	312— 317
● Continuous Feed and Dispersion for Fine Powder —Possibility of Dry-system for On-line Particle Size Analysis—	M. Ito and H. Ninomiya	368— 372
● Determination of the Moisture Content of Coal by Microwave Radiation	S. Matsuo and T. Inoue	373— 377
● On-line Measurement and Control of a Fluidized Bed	Z. Tanaka, H. Mitsuji and T. Takahashi	378— 383
● Study on the Deashing of Coal by the Oil Agglomeration Process —The Effect of Ground Coal Particle Size on Deashing Efficiency—	H. Takase, K. Higashi and M. Sugimoto	430— 436
● On the Particle Cut Size of Cyclone Dust Collector (Part 4) —Separation Grain Size Ratio as a Function of the Froude Number—	K. Ikemori	437— 442
● Cut Size Estimation in Centrifugal Air Classifiers	M. Ito	488— 494

● The Relationship Between Fiber Length and the Penetration Rate of Fibrous Aerosol Through Wire Mesh Screens —A New Method for Measuring Median Fiber Length—	T. Myojo	495— 500
● The Effect of Wet Ball Milling in the Production Process of YBaCu Composite Oxide on its Superconducting Properties	T. Yokoyama, Y. Yoshida, A. Kondo, M. Naito, M. Yoshikawa, H. Kamiya and G. Jimbo	501— 507
● The Grinding-Aid Effect of Phenylalanine on Talc Powder	A. Ikekawa and S. Hayakawa	544— 549
● Granulafing Characteristics of a Rotary Mixer with Rocking Motion	M. Satoh, Y. Ohnishi, K. Miyanami, S. Kondo and S. Ando	550— 554
● Stress-Voidage Relationship in the Uniaxial Compressive Packing Process of Ultrafine Powders and Change in the Internal Stucture of a Packed Bed	M. Mizuno and G. Jimbo	555— 561
● Particle Design of Adhesive Pharmaceutical Powders for Direct Tabletting by the Novel Emulsion-Solvent -Diffusion Method	Y. Kawashima, H. Takeuchi, T. Niwa, T. Hino, S. Ohmori, S. Furukawa, T. Suzuki and H. Sato	562— 566
● Influences of Bed Porosity on the Impact Efficiency of Air-borne Fine Particles to a Bed Particle	K. Ushiki, S. Yuu, S. Tanaka and W. Eguchi	612— 618
● An Examination of the Separation of Differently Shaped Particles·Based on Grindability	Y. Kondo and K. Enomoto	619— 623
● Air Flow and Pressure Loss in a Centrifugal Air Classifier	M. Ito	624— 631
● The Experimental Stress-Strain Rate Relationship of Granular Materials	S. Yuu and S. Kamimura	632— 637
● The Surface-treatment of Ceramic Powders through Pulverization in a Reactive Atmosphere by Means of Ball Mill (IV) —Surface-treatment of Silicon Carbide —	N. Suzuki, Y. Go, N. Baba, J. Ito, A. Endo and H. Utsugi	670— 678
● The Trajectory of a Particle—Inertial Classification	H. Ueno	679— 683
● The Relationship the Pore Characteristics and the Suctonability of a Gypsum Mold	L. Li, B. hwa wang and M. Arakawa	684— 688
● Production of Sustained Release Microspheres Coated with Inorganic Fine Particles	E. Abe, N. Yamada and H. Hirosue	689— 693
● Grinding Efficiency of an Agitation-Beads Mill (I) —Characteristics of the Particle Size Distribution of the Ground Product—	Y. Hashi and M. Senna	732— 737
● Grinding Efficiency of an Agitation-Beads Mill (II) —Relationship between the Media Flow Pattern and the Grinding Efficiecy—	Y. Hashi and M. Senna	738— 744
● Compressive Comminution of Single Particle and Particle Beds	J. Koo Park, Y. Okano and T. Inoue	745— 750
● The Grinding Equilibrium Size of In-Water Grinding of Silica Sand by a Planetary Ball Mill	T. Yokoyama, Y. Taniyama G. Jjmbo and Qion-Qiu Zhao	751— 758
● Model simulation of ball motion in a tumbling ball mill under high and low gravity	H. Hashimoto and R. waoanabe	4— 11
● Formation of Fine Particles of Slightly Soluble Medicines by Dry Ball-Milling	A. Ikekawa and E. Yoshino	12— 19
● Sintering of Superconducting Fine Particles in the Bi-Ca-Sr-Cu-O System Prepared by Spray Pyrolysis	K. Okuyama, M. Shimada, N. Tohge and M. Adachi	20— 29

● Enhancement of Solid Acid Strength and Stabilization of Constituent Particles of Zirconias and Other Oxides through Coordination with Inorganic Anions	K. Mukaida, M. Sato, A. Iijima, H. Ando and N. Ando	30—36
● Effects of Powder Roll Mixing to Cyclodextrin Molecular Complexation	Y. Nozawa, M. Kishimoto and M. Takeda	37—44
● Change in Density Distribution with Time Caused by Segregotion in a Continuous Fluidized Bed under Unsteady State	N. Yamada, E. Abe and H. Hirosue	1—7
● Air Separation Characteristics of Granular Molecular Sieving Carbon Produced from PVA/Phenolic Resin	C. Marumo, N. Shinmi and E. Hayata	60—66
● Evaluation of Contribution of Grid Zone in Silicon Production Via Fluidized Bed CVD —Monosilane argon system—	T. Kimura and T. Kojima	81—87
● Size Exclusion Characteristics of Porous Particle Mode of Cellulose Acetate	H. Ohya, K. Hiroishi, Y. Negishi and K. Matsumoto	950—954
● Residence Time Distribution of Fine Particles in a Powder Particle Fluidized Bed	K. Kato, T. Takarada, N. Matuo, T. Sato and N. Nakagawa	970—975
● Surface Modification of Fine Inorganic Powder by Use of Mechanochenical Polymerization	M. Hasegawa, T. Honma, S. Ishiyama and Y. Kanda	1019—1025
● A Numerical Analysis of Movement of Balls in a Vibration Mill	T. Yokoyama, K. Tamura, and G. Jimbo	1026—1034
● Preparation of Ultrafine Iron Particles by Chemical Vapor Deposition of $Fe(CO)_5$	Y. Sawada, Y. Kageyama and M.Iwata	1074—1079
● Falling Veltcity of a Particle in a Sinusoidally Oscillating Fluid	K. Takahashi, H. Miyazaki S. Mori and A. Tanimoto	1161—1167
● Control of Aerosol Particle Depostion on a Surface Composed of Different Kinds of Materials	H. Yoshida, T. Ninomiya, and H. Yamamoto	1187—1193
● Unsteady Particle-Reentrainment Model Based on the Internal Adhesive Strength Distribution of a Fine Powder Layer	S. Matsusaka, T. Ninomiya, and H. Masuda	1194—1200

New Product News

Hosokawa Micron Corporation presents two products.

☐ HOSOKAWA HIGH CLEAN UNIT

—Ultra cleaning and deodorizing unit—

Hosokawa High Clean Unit, developed recently by Hosokawa Micron Corporation, improved the circumstances as follows :

In order to reduce infection at hospital, it was required strongly to remove dusts and bacteria and also to meet demands of deodorizing by patients.

Meanwhile, demands for cleanness of working area aiming for improvement of product quality are raised by industrial field and also residential field.

Features

- The unit can be applied for clean room from class 10,000 to class 50,000.
- Portable type. Easy handling by making it small and light.
- Low noise level. Air volume can be selected by push button.
- Safety operations and easy maintenance.
- Two types are available ;
  HCU-10 Non deodorant function type.
  HCU-10N With deodorant function type.

Applications

- Hospital.
  Room for new-born baby, aged, recovery after operation, general and clinic.
- Research institute, laboratory and analysis room which require higher clean level than normal room.
- Experimental facility for animals, especially knife room.
- Office, smoking room and locker room.

☐ Fluidized Drying Granulator Lab. Type

Multi-purpose complex and batch processing type with sanitary construction for use in Lab. and capable of performing granulating, coating, drying, etc.

Features

- The machine can be used even for processing a small amount of material (0.25 to 1 liter).
- A wide range of granule properties can be obtained.
- The bag filter section is capable of continuously collecting particles with high efficiency and stability.
- The granule drying section allows the visual observation of a fluidized bed inside.
- The hot air supply section, exhaust section and control section are all housed in the machine body, and their operation mode can be easily set by adjusting the switches and dials on the machine front.
- The machine can also be used as a simple fluidized bed granulator.

Applications

- Granulation of pharmaceuticals
- Granulation of foodstuffs
- **Others**
  Toner, Powder metallurgic materials and ceramics, Agricultural chemicals, Catalysts, Cosmetics, Pigments and dyestuffs